An Investigation into Iron Isotope Systematics in Felsic Magmas and their Associated Magmatic-Hydrothermal Ore Deposits

Christine Mary Wawryk B.Sc (Hons)

Submitted in fulfilment of the requirements for the degree of Doctor of Philosophy

THE UNIVERSITY of ADELAIDE

School of Physical Sciences

April 2017

DECLARATION

I certify that this work contains no material which has been accepted for the award of any other degree or diploma in my name in any university or other tertiary institution and, to the best of my knowledge and belief, contains no material previously published or written by another person, except where due reference has been made in the text. In addition, I certify that no part of this work will, in the future, be used in a submission in my name for any other degree or diploma in any university or other tertiary institution without the prior approval of the University of Adelaide and where applicable, any partner institution responsible for the joint award of this degree.

I give consent to this copy of my thesis when deposited in the University Library, being made available for loan and photocopying, subject to the provisions of the Copyright Act 1968.

The author acknowledges that copyright of published works contained within this thesis resides with the copyright holder(s) of those works.

I also give permission for the digital version of my thesis to be made available on the web, via the University's digital research repository, the Library Search and also through web search engines, unless permission has been granted by the University to restrict access for a period of time.

I acknowledge the support I have received for my research through the provision of an Australian Government Research Training Program Scholarship.

Christine Wawryk

University of Adelaide

31 March 2017

ABSTRACT

The two possible valence states of the Fe ion have been shown to be a major control on the fractionation of Fe isotopes in both low and high temperature fluids. Magmatic-hydrothermal fluids can carry large amounts of Fe and economic metals leading to the formation of ore deposits, in which the metal association is determined by redox conditions of the magma chamber. This thesis examines the Fe isotope compositions of intrusive rocks and associated Fe-sulfides, oxides and carbonates, to assess whether a correlation exists between the oxidation state of magmas, and the isotope composition of hydrothermal minerals in ore deposits.

Chapter 2 presents a case study of the Fe isotope values of granite and mineral separates from the Renison tin deposit in north western Tasmania. This tin deposit is associated with a reduced, S-type magma. Samples of granite and separates of pyrrhotite, pyrite, arsenopyrite, magnetite, chalcopyrite and siderite were measured. The δ^{57}Fe values of mineral separates are consistent with theoretical predictions of equilibrium fractionation based on spectroscopic and other parametric calculations. Mineral-mineral pairs yield temperatures of formation that are in agreement with prior detailed fluid inclusion studies, but are spatially inconsistent with declining fluid temperature with distance from the causative intrusion, limiting the use of Fe isotopes as a potential geothermometer. Mineral separates from the Renison deposit are isotopically heavier than those from the Xinqiao Cu-Fe skarn, contradicting the hypothesis that magmatic-hydrothermal minerals should be isotopically lighter than the source intrusion.

Chapter 3 presents Fe isotope analyses from a differentiated series of magmatic intrusive rocks and coeval hypogene ore minerals from the Batu Hijau porphyry copper-gold deposit located on the Sunda Arc, Sumbawa, Indonesia. The variations of δ^{57}Fe with major and trace element concentration is consistent with crystallisation of clinopyroxene, amphibole and magnetite being the primary control on isotopic evolution of the melt. These isotopic trends are supported by thermodynamic (rhyolite-MELTS) modelling of crystal fractionation using published mineral-melt fractionation factors, and demonstrate that the isotopic evolution of these hydrous melts was controlled by crystal fractionation. Magnetite from the Batu Hijau ore deposit is

isotopically heavier than coexisting hypogene chalcopyrite and bornite, consistent with theoretical predictions. Models of Rayleigh type fractionation assuming an initial fluid composition that is isotopically light (between -0.5 and -0.1 ‰) produces mineral compositions that match our analytical data and are in agreement with experiments demonstrating that hypogene chalcopyrite has isotopic compositions reflecting that of the hydrothermal fluid. Chapter 4 presents results from the Río Blanco-Los Bronces deposit in Chile as a comparison to those of Batu Hijau. Despite the differences in tectonic setting (Andean margin and island arc, respectively), the results are strikingly similar, pointing to the local influence of fluid and mineral formation processes in determining the $\delta^{57}Fe$ values of minerals. The $\delta^{57}Fe$ values of chalcopyrite, when coupled with ^{34}S values result in grouping of minerals that highlight the potential of integrated studies to track metal formation processes.

Chapter 5 presents a case study from the giant Olympic Dam and Hillside Iron Oxide Copper Gold (IOCG) deposits located on the Gawler Craton, South Australia. Deposit formation is spatially and temporally associated with the 1.59 Ga voluminous, bimodal Gawler Range Large Igneous Province. Iron isotope analyses of bulk whole rock A-type granites of Hiltaba Suite intrusions, and magnetite, siderite, pyrite, chalcopyrite, bornite and hematite were measured. Hiltaba Suite intrusions are relatively isotopically heavy consistent with published results from the literature for evolved high silica magmatic rocks. Mineral separates such as siderite, magnetite, hematite, chalcopyrite and pyrite have isotopic values that are consistent with theoretical mineral-mineral fractionation factors. Siderite from Olympic Dam and bornite from Hillside are the minerals with the lightest $\delta^{57}Fe$ values. Pyrite and magnetite returned ranges that are similar between the deposits, however the opposing signs of $\Delta^{57}Fe_{py\text{-}mgt}$ are enigmatic and may be a result of preservation of isotopically light precursor minerals or quantitative dissolution of isotopically heavy precursor minerals. The $\delta^{57}Fe$ values of hematite and magnetite, sampled where clear overprinting relationships are evident at Olympic Dam, are isotopically indistinguishable within analytical error. This contrasts with previously published oxygen isotope results, demonstrating that Fe isotopes alone are unable to discriminate fluid mixing events at hydrothermal temperatures.

The data from all four deposits demonstrate that that the range of $\delta^{57}Fe$ values between minerals, up to 2‰, is much greater than the range of $\delta^{57}Fe$ values of suites of differentiated magmatic rocks (~0.3 to 0.7‰), suggesting that other mechanisms overprint and/or enhance fractionation controlled solely by temperature. Such mechanisms include Rayleigh-type precipitation, remobilisation of Fe^{2+} during coupled dissolution-reprecipitation reactions, and changing sulfur redox conditions in the fluid. Further experimental studies of precipitation mechanisms, coupled with in-situ Fe isotope analyses of zonation within minerals will help elucidate the complex overprinting of processes that render variability in natural samples difficult to interpret.

TABLE OF CONTENTS

LIST OF FIGURES

LIST OF TABLES

LIST OF APPENDICES

ACKNOWLEDGEMENTS

Thanks must go firstly to my supervisor, Emeritus Professor John Foden, for proposing the project and suggesting it to me. His unending support and advice have been instrumental in completion of the research. Professor David Giles cheerfully provided suggestions and practical advice for which I am grateful.

The research was in part funded by the Institute for Mining and Energy Resources, and I thank the Director, Stephen Grano, for his interest and enthusiasm for the project. Further funding came from the University of Adelaide in the form of the Eric Rudd Scholarship, which paid for conference attendance. A Visiting Researcher Grant from the Tectonics, Research and Exploration group facilitated collaboration with Dr Steven Garwin on the Batu Hijau deposit. I was fortunate to receive a Student Research Grant from the Society of Economic Geologists, which facilitated field work at, and preparation of samples from the Hillside deposit.

Samples for analysis were generously supplied by mining companies, and I thank the mine geologists for giving their time and knowledge, and the support staff for cutting drill core and arranging sample transport. These are; the Bluestone Tin Joint Venture for samples from the Renison tin mine, with support from Colin Carter, Carl Jackman and Jim Harvey; Rex Minerals for samples from the Hillside copper deposit, with support from Graham Teale, Marc Twining, Mike van Alphen and Mark May; samples from the Sur Sur and Río Blanco copper-molybdenum deposits were collected from the University of Tasmania (originally provided by CODELCO to AMIRA project P511) and I thank Dr Nathan Fox, Ms Isabel von Lichtan, Dr Jose Piquer and Professor David Cooke for support and discussion. Results have been presented at conferences and the companies are thanked for giving permission to publish.

I especially wish to thank Dr Steve Garwin for providing access to his personal collection of samples from the Batu Hijau deposit, and giving generously of his knowledge of the deposit and ore forming processes. His support, advice and friendship are gratefully acknowledged. Thanks are given to the PT Newmont Nusa Tengarra Company for permission to publish, and supplying samples.

Sampling and analysis of the Olympic Dam deposit would not have been possible without the logistical and financial support of BHP Billiton, and the assistance of Dr Kathy Ehrig. Dr Ehrig's knowledge of the deposit is incomparable, and I thank her for her generosity and support in sharing her knowledge and for many suggestions and

advice which improved my work. I thank Dr Cristiana Ciobanu for her assistance in reflected light ore microscopy of the Olympic Dam sampels, which facilitated selection of samples for isotopic analysis.

Sample preparation was conducted at the University of Adelaide, and Dr Katie Howard and Mr David Bruce are thanked for providing training and supervision in the use of mineral grinding and separation techniques, and isotopic clean lab procedures, respectively.

The project relied heavily on use of the Neptune Multicollector Mass Spectrometer housed at the Waite Campus. Training in the use of the instrument was provided by Drs Paolo Sossi, Kate Scheiderich and Galen Halverson; to them I offer my profound thanks. I also thank Claire Wright and Dr Justin Payne for additional assistance in running the instrument and much needed encouragement when all seemed broken, and Thurid Luetzeler of Thermo Scientific for her technical expertise.

Pam Eldridge is thanked for her thoughtful and constructive proofreading of the final manuscript.

My post graduate experience has been enriched by the friendship and support of my peers. Thank you to Ben Cooke, Fun Meeuws, Jade Anderson, Kat Lane, Laura Morrisey, Laura Rollison, Daniel Howlett, Rowan Hansberry and Alec Walsh for conversation, coffee and Monday morning analysis of the AFL fixtures.

CHAPTER 1. INTRODUCTION AND STRUCTURE OF THE THESIS.

Iron is the fourth most abundant element in the Earth's crust (FeO^T =6.71%; Rudnick and Gao, 2003), and has the highest production rate of all metals used in society (Sverdrup and Ragnarsdóttir, 2014). Iron may be one of the principal components of the ore minerals of other metals of importance to society such as copper, zinc and tin, or be present in gangue minerals within metal-bearing mineral assemblages. Hence, the chemical and physical properties of Fe-bearing minerals have been used to increase our understanding of the formation of ore deposits, and to explore for them.

There are four naturally occurring stable isotopes of Fe. They are shown in the table below:

Mass	54	56	57	58
Abundance	5.8%	92%	2.2%	0.25%

Iron isotope values of samples are reported in the "per mil" deviation from a standard of known composition, calculated by the following equation:

$$\delta^{57}Fe = 1000* [(^{57}Fe/^{54}Fe)_{sample} /(^{57}Fe/^{54}Fe)_{standard} -1]$$

The international reference standard is currently the iron wire IRMM-14, with a certified isotope value $\delta^{57}Fe = 0.09$ ‰. Isotopic values can also be reported as $\delta^{56}Fe$ values, and the literature review which follows illustrates that both conventions are used in the literature.

General factors that govern the equilibrium fractionation of stable isotopes have been summarised by Schauble (2004). These allow qualitative predictions to be made for the Fe system:

I. Inverse temperature dependence: The magnitude of isotope fractionation is inversely dependant on temperature, approximating $1/T^2$. At magmatic-hydrothermal temperatures the expected fractionation is small (~≤ 1‰) which underscores the necessity for sensitive analytical instrumentation.

II. Relative mass difference: The expected fractionation according to $\Delta m/m^2$, where m is the average isotopic mass of an element and Δm is the difference between a light and a heavy isotope. For Fe, with average atomic mass of 55.84, $\Delta m/m^2$ corresponds to a much smaller number than for light isotopic systems such as hydrogen or lithium, which again requires sensitive analytical instrumentation.

III. Bonding and Redox: At equilibrium, the heavy isotope is preferentially incorporated into the substance with the stiffest chemical bonds. Stiff chemical bonds are those that are short and strong. For Fe, this is seen in

   a. high oxidation state, e.g. Fe^{3+} such as in hematite (Fe_2O_3), rather than Fe^{2+} , .as in siderite ($FeCO_3$).
   b. low coordination numbers, i.e. tetrahedral coordination compared to octahedral coordination e.g. fayalite compared to magnetite (Shahar et al., 2008).
   c. the presence of highly covalent bonds, such as those with sulfur (e.g. pyrite FeS_2; Polyakov et al., 2007)

The geochemical behaviour of Fe is governed by its capacity for 2 valence states, either Fe^{2+} or Fe^{3+}. Thus, the fractionation of Fe isotopes owing to valence state has been investigated as a potential tracer of redox processes in the geosphere and biosphere (see Dauphas and Rouxel, 2006, for a review). These studies have demonstrated large fractionation (> 2-3 ‰) at ambient temperatures (Anbar, 2004).

However, at higher magmatic (>700 °C) or magmatic-hydrothermal temperatures (200-600 °C), isotope fractionation is only fractions of the per-mil unit (Dauphas and Rouxel, and references therein). The development of modern mass spectrometers with multiple detectors (the “multi-collectors”), means that analysts can simultaneously measure the abundance of isotopes with mass 54, 56 and 57 at sensitivies of ±0.03‰ (e.g. Weyer and Schweiters 2003), thus opening the field of high temperature Fe isotope geochemistry. A recent review by Young et al. (2015) summarises advances in understanding of the behaviour of Fe isotopes at high temperatures with applications to geochemistry and planetary science.

Fe isotopes systematics in magmatic rocks.

The $\delta^{57}Fe$ values of igneous rocks have been measured by researchers since the development of MC-ICPMS instruments to quantify the isotopic reservoir of the crust

(e.g. Beard and Johnson, 2004; Anbar 2004; Poitrasson and Freydier, 2005). The seminal paper by Poitrasson and Freydier (2005) demonstrated that granites with high SiO_2 content (>70 wt %) can have $\delta^{57}Fe$ values of up to 0.6‰, which is heavier than that of "mean mafic Earth", which has a $\delta^{57}Fe$ value of 0.1‰. The focus of the paper was to refine the MC-ICPMS analytical technique, but the authors proposed a mechanism to explain their results: that intrusive rocks released magmatic-hydrothermal fluids upon cooling, and that the light iron isotope is fractionated into the fluid owing to the prevalence of Fe^{2+} in the exsolved volatile phase. Poitrasson and Freydier's (2005) study was followed up by Heimann et al. (2008), who analysed both plutonic and volcanic rocks, with SiO_2 contents ranging from 58 to 77 wt%. Biotite, chlorite and magnetite were also analysed. The authors combined solubility models of Fe in chloride solutions, with predicted fractionation factors for silicates, magnetite and the $FeCl_2$ complex, to predict that sub solidus isotope exchange with magnetite results in isotopically light fluids, leaving behind an isotopically heavy bulk rock.

Heimann et al. (2008) discounted the process of fractional crystallisation as a process for ^{57}Fe enrichment in siliceous bulk rock samples on the basis of trace element chemistry. However, studies of natural systems where magmatic differentiation is well demonstrated, such as the Hekla volcano in Iceland (Schuessler et al., 2008), the Jurassic dolerite sills in Tasmania (Sossi et al., 2012) and the Kilauea Iki lava lake (Teng et al., 2008) clearly demonstrate that magmatic differentiation by crystal fractionation can result in isotopically heavy melts owing to partitioning of the light isotope into Fe^{2+} bearing silicate minerals. Furthermore, the experimental work by Dauphas et al. (2014) on synthetic glasses of basalt, andesite, dacite and rhyolite composition clearly demonstrated the force constants[1] of both Fe^{2+} and Fe^{3+} in rhyolite glass is much higher than that of magnetite, resulting from change in coordination number in a polymerised melt. That Fe^{3+} remains in the silicate melt is also supported by the analyses of leucosomes in migmatite complexes by Telus et al. (2012) who reported $\delta^{56}Fe$ values of 0.25 to 0.48‰.

Fe isotope fractionation can also be a result of temperature gradients in a melt. An experiment conducted by Huang et al. (2009), placed USGS standard andesite rock AGV-1 in a piston cylinder apparatus held at a sustained temperature gradient (350

[1] The Force constant comes from Hooke's Law, F=*k*x which states that the force (F) required to stretch or compress a spring by a distance x is related to the stiffness of the spring, *k*. The 'spring' in this context is chemical bonds in the melt.

°C at the cold end and 950 °C at the hot end), in the presence of 4% H_2O. The starting andesite powder was differentiated mineralogically into a melt at the hot end, and a crystalline mass of bulk granite composition at the cold end. Measured $\delta^{56}Fe$ values had a range of 2.8‰, with the hotter end enriched in the light isotope. Thermal diffusion was also used to explain the distribution of $\delta^{56}Fe$ values across a natural sequence of erupted lavas from the Cedar Butte volcano, ranging from basaltic trachyandesite to rhyolite in composition (Zambardi et al., 2014). These authors also sampled a silicic granophyric sill of A-type affinity from the Duluth Complex. The authors concluded that neither crystal fractionation nor fluid exsolution could explain progressively heavier isotope compositions with mineral assemblages that suggested cooler temperatures of crystallisation, and thus concluded that a thermal gradient is the dominant process.

The effect of magma chamber processes on Fe isotope evolution in the context of the S-, I- and A-type classification is discussed in Foden et al. (2015) who showed that the fractionation of Fe isotopes in evolving magmatic systems is strongly dependent on the oxidation state of the magma as well as on its mode of buffering. Whilst relatively reduced magmas may fractionate to yield isotopically heavy Fe in the most evolved felsic end members, oxidized systems tended to show less fractionation towards heavy Fe or may even evolve towards isotopically slightly lighter end members. As Foden et al. (2015) point out, the other key influence was the mode of buffering of the magma. Closed (unbuffered) systems tend to evolve to heavy products, while buffered “open-system” behaviour can suppress trends towards final relative enrichment in $\delta^{57}Fe$ and $\delta^{56}Fe$.

The light fluid hypothesis discussed previously is of interest to researchers because of the capacity of ferrous-chloride rich magmatic-hydrothermal fluids to transport economic metals (e.g. Candela and Holland, 1984). Coupled with the known association between magma oxidation state and ore mineral assemblages, this thesis poses the question of whether the Fe-isotope value of the melt at the time of fluid saturation impacts the isotopic value of the exsolved fluid, i.e. is the fluid exsolved from an isotopically light melt, such as an andesite (65 wt% SiO2) isotopically lighter than the fluid exsolved from an evolved, silicic S-type granite (~70 wt% SiO_2)? In turn such fluids deposit Fe-bearing sulfides, oxides and carbonate minerals: if the starting fluids have very different $\delta^{56}Fe$ values, will this result in clustering of hydrothermal minerals in different groups?

Magma oxidation state and metal association in ore deposits

The metallogeny of granites and their associated deposit styles has been known since the seminal definition of ilmenite- and magnetite-series granites by Ishihara (1977), and studies by foremost researchers such as Blevin and Chappell (1992), Blevin (2004) and Candela and Holland (1985). Tin-tungsten deposits are associated with highly differentiated, reduced (~FMQ to FMQ -2) ilmenite series granites (e.g. Černy et al., 2005). Porphyry style Cu-Mo-Au deposits are associated with arc magmas in collisional tectonic settings; host rocks are intermediate to felsic in composition, magnetite rich and have oxidation states generally 1 to 2 log units above the fayalite-quartz-magnetite (FMQ) buffer (e.g. Seedorff et al., 2005).

A third type of magma, the A-type granites, are alkalic, Fe-rich, generally have low water contents and have experienced protracted, closed system fractional crystallisation (Foden et al., 2015). Voluminous A-type plutonism within the Gawler Craton is intimately associated with a widespread tectonothermal event during which large Iron-Oxide-Copper-Gold ('IOCG') deposits were formed (e.g. Reeve et al., 1990, Skirrow et al., 2007), and this deposit style was included in this project.

Each of the following chapters of the thesis documents the results of a case study of a well-understood deposit, representing the type magma- ore deposit associations described above.

Chapter 2 presents a case study of a tin-tungsten (Sn-W) deposit associated with a reduced ilmenite series granite. The Renison Sn-W deposit, a world-class replacement-style Sn deposit in western Tasmania, was formed when magmatic-hydrothermal fluids, accumulated in a probable cupola structure on the upper surface of the cooling Meredith Granite pluton, were tapped and ascended along the controlling major fault depositing tin ores as a result of replacement of carbonate units in the host sedimentary succession. An outer siderite alteration halo surrounds the deposit, and represents the outer limit of ore fluid percolation. Samples of stratabound massive pyrrhotite-cassiterite ore, fault controlled arsenopyrite-pyrrhotite-chalcopyrite-pyrite ore and the outer siderite halo were collected and analysed by MC-ICPMS. Samples of fresh, unaltered Renison granite were collected from drill core.

The study revealed that Fe isotope compositions of Fe-bearing sulfides and oxides are consistent with theoretical predictions. Mineral-mineral pairs yielded temperatures of formation that are in agreement with prior detailed fluid inclusion studies, but are spatially inconsistent with declining fluid temperatures with distance from the causative intrusion. Comparison of our data with published data from other deposits clearly demonstrates that pyrite, magnetite and chalcopyrite from the hottest ore fluids (>300-400 °C) at Renison are isotopically heavier than minerals sampled from a deposit formed at similar temperatures (Wang et al., 2011), but associated with a more oxidised and less differentiated intrusion. This case study has been published in *Geochimica Cosmochimica Acta,* and was the first published case study of a tin deposit.

Chapter 3 presents a case study from the Batu Hijau Cu-Au deposit in Indonesia. This deposit is situated within an oceanic island arc setting, and thus is a natural laboratory to study magmatic evolution in a hydrous, oxidised (NNO≤fO_2≤ NNO+2; Garwin, 2000) magma, which became volatile saturated and deposited Cu and Au in a porphyry-style system. In the Batu Hijau area, a suite of intrusive magmas that have evolved from andesite to tonalite are exposed, thus the effect of melt differentiation by crystal fractionation upon iron isotope evolution can be studied. The mineral associations within quartz vein sets from the earliest mineralising event are simple, comprising co-precipitated bornite-magnetite and bornite-chalcopyrite, which allows comparison with published spectroscopic isotope fractionation factors, and Rayleigh modelling of fractionation during magnetite-sulfide formation. Samples of hypogene magnetite, bornite and chalcopyrite mineral separates were analysed, and our data show that δ^{57}Fe for hypogene chalcopyrite from porphyry copper deposits are significantly lighter than composition of chalcopyrite separates from the Renison deposit. The results have been published in *Chemical Geology,* and are the first published results of co-precipitated hypogene bornite and chalcopyrite.

Chapter 4 reports the Fe-isotope values of intermediate and felsic igneous rocks from the later stages of evolution of the giant Río Blanco-Los Bronces Cu-Mo deposit in Chile. The deposit is associated with potassic magmatism in the Andean margin tectonic setting, with coarse-grained Cu-Fe sulfides and oxides deposited as infill within hydrothermal tourmaline-rich breccias. The tectonic setting and Cu-Mo association contrast with the island arc and Cu-Au rich nature of Batu Hijau. The results are written in journal article format for submission to a journal, yet to be decided upon. The results are consistent with those at Batu Hijau, suggesting that

fluid processes are similar between the two deposits despite their differing tectonic setting and styles.

Chapter 5 compares and contrasts Fe-isotope compositions of Fe-bearing sulfides and oxides from two IOCG deposits on the Gawler Craton, South Australia. Samples were collected from the Olympic Dam deposit, the archetypal IOCG deposit; samples were chosen from fresh Roxby Downs Granite, the host rock to the deposit, through the spectrum of increasing Fe-metasomatism and brecciation to the core of the deposit. Samples of paragenetically early magnetite-pyrite alteration, chalcopyrite-hematite ore and the siderite halo were sampled. Samples from variably mineralised satellite prospects were also analysed to elucidate the behaviour of Fe isotopes distal to Olympic Dam. The Hillside deposit in the Moonta-Wallaroo district offers the opportunity to compare and contrast Olympic Dam with an IOCG skarn deposit that formed at higher temperatures.

The Gawler Craton experienced a widespread tectonothermal event at 1.59 Ga, resulting in bimodal volcanism, which produced the voluminous Gawler Range Volcanics, and plutonism, which produced the Hiltaba Suite, as well as IOCG deposits such as Olympic Dam. Samples of A-type intrusive rocks were collected from the Olympic Dam deposit and the Hillside skarn, and from exposures of Hiltaba Suite rocks from Port Riley on the Yorke Peninsula. The aim of this study was 2-fold:

1. To ascertain if hydrothermal fluids that had equilibrated with isotopically heavy A-type granites precipitated hydrothermal minerals that were relatively isotopically heavy themselves, compared to minerals from Renison and Batu Hijau.

2. To compare the Fe-isotope values of the early magnetite-pyrite alteration stage (with siderite at Olympic Dam), to the overprinting hematite-chalcopyrite-sericite mineralising event. If hematite is formed by quantitative replacement of magnetite, then we would expect the isotopic values to be similar; however, if new Fe is introduced into the system we could expect to see hematite with different isotopic compositions to magnetite. This case study is written in journal article format for submission to a journal.

Chapter 6 provides a comparison of the analyses of intrusions and mineral separates on the basis of metallogeny, and discusses what may be interpreted from the analyses given constraints provided by recent published experiments. The field of iron-isotope geochemistry is relatively new in economic geology, and the thesis

suggests some future research directions to elucidate iron isotope fractionation in ore-forming processes that remain poorly understood.

References

Anbar, A. (2004). Iron stable isotopes: beyond biosignatures. Earth and Planet. Sci. Lett. 217, 223-236.

Beard, B. L., Johnson, C. M. (2004). Fe isotope Variations in the Modern and Ancient Earth and other Planetary Bodies. In: Johnson, C. M., Beard, B. L., Albarede, F. (Eds.), Geochemistry of Non-Traditional Stable Isotopes, vol. 55. Mineralogical Society of America, Washington, DC, pp. 319–357.

Blevin, P. L., Chappell, B. W. (1992). The Role of Magma Sources, Oxidation-States and Fractionation in Determining the Granite Metallogeny of Eastern Australia. Transactions of the Royal Society of Edinburgh-Earth Sciences 83, 305-316.

Blevin, P. (2004). Redox and compositional parameters for interpreting the granitoid metallogeny of Eastern Australia: implications for gold-rich ore systems. Resource Geol. 54, 241-252.

Candela, P. A., Holland, H. D. (1984). The partitioning of copper and molybdenum between silicate melts and aqueous fluids. Geochim. Cosmochim. Acta 48, 373-380.

Černý, P., Blevin, P. L, Cuney, M., London, D. (2005). Granite related ore deposits. Econ. Geol. 100, 337-370.

Dauphas, N. and Rouxel, O. (2006). Mass spectrometry and natural variations of iron isotopes. Mass Spectrometry Reviews, 25, 515-550.

Dauphas, N., Roskosz, M., Alp, E., Neuville, D., Hu, M., Sio, C., Tissot, F., Zhao, J., Tissandier, L., Médard, E., Cordier, C. (2014). Magma redox and structural controls on iron isotope variations in Earth's mantle and crust. Earth Planet. Sci. Lett. 398, 127-140.

Foden, J., Sossi, P., Wawryk, C. M. (2015). Fe isotopes and the constrasting petrogenesis of A-, I- and S-type granite. Lithos. 212-215, 32-44.

Garwin, S. G. (2000). The setting, geometry and timing of intrusion-related hydrothermal systems in the vicinity of the Batu Hijau copper-gold deposit, Sumbawa, Indonesia. PhD thesis, University of Western Australia.

Heimann A., Beard, B. L., Johnson, C. M. (2008). The role of volatile exsolution and sub-solidus fluid/rock interactions in producing high 56Fe/54Fe ratios in siliceous igneous rocks. Geochim. Cosmochim. Acta 72, 4379-4396.

Huang, F., Lundstrom, C. C., Glessner, J., Ianno, A., Boudreau, A., Li, J., Ferré, E. C., Marshak, S., DeFrates, J. (2009). Chemical and isotopic fractionation of wet andesite in a temperature gradient: Experiments and models suggesting a new mechanism of magma differentiation. Geochim. Cosmochim. Acta 73, 729-749.

Ishihara, S. (1977). The magnetite-series and ilmenite-series granitic rocks. Min.Geol. 27, 293–305.

Poitrasson, F., Freydier, R. (2005). Heavy iron isotope composition of granites determined by high resolution MC-ICP-MS. Chem. Geol. 222, 132-147.

Polyakov, V. B., Clayton, R. N., Horita, J., Mineev, S. D. (2007). Equilibrium iron isotope fractionation factors of minerals: reevaluation from the data of nuclear inelastic resonant X-ray scattering and Mössbauer spectroscopy. Geochim. Cosmochim Acta 71, 3833-3846.

Reeve, J. S., Cross, K. C., Smith, R. N., Oreskes, N. (1990). Olympic Dam copper-uranium-gold-silver deposit, in Hughes, F.E. (Ed) Geology of the Mineral Deposits of Australia and Papua New Guinea, 1009-1035, AusIMM. Melbourne.

Rudnick, R. L.,Gao, S. (2003). Composition of Continental Crust. In. Rudnick, R.L., Holland, H. D., Turekian, K. K. (Eds), Treatise on Geochemistry, Volume 3, Elsevier, pp. 1-64.

Schauble, E. A. (2004). Applying stable isotope fractionation theory to new systems. Rev. Min. Geochem. 55, 65-111.

Shahar, A., Young, E. D., Manning, C. E. (2008). Equilibrium high-temperature Fe isotope fractionation between fayalite and magnetite: an experimental calibration. Earth Planet. Sci. Lett. 268, 330–338.

Skirrow, R. G., Bastrakov, E. N., Barovich, K., Fraser, G. L, Creaser, R. A. Fanning, C. M., Raymond, O. L., Davidson, G.J. (2007). Timing of iron oxide Cu-Au-(U) hydrothermal activity and Nd isotope constraints on metal sources in the Gawler Craton, South Australia. Economic Geology, 102, 1441-1470.

Schuessler, J., Schoenberg, R., Sigmarsson, O. (2008). Iron and lithium isotope systematics of the Hekla volcano, Iceland-Evidence for Fe isotope fractionation during magma differentiation. Chem. Geol. 258, 78-91.

Seedorf, E., Dilles, J. H., Proffett, J. M., Einaudi, M. T., Zurcher, L., Stavast , W. J. A., Johnson, D. A., Barton, M. D. (2005). Porphyry deposits: characteristcs and origin of hypogene features. Econ. Geol. 100, 251-298.

Sossi, P. A., Foden, J. D., Halverson, G. (2012). Redox-controlled iron isotope fractionation during magmatic differentiation. Contrib. Mineral. Petrol. 164, 757-772.

Sverdrup, H. and Ragnarsdóttir, K. (2014). Natural Resources in a Planetary Perspective. Geochemical Perspectives, 3. 129-341.

Teng, F-Z., Dauphas, N., Helz, R. (2008). Iron isotope fractionation during magmatic differentiation in Kilauea Iki Lava Lake. Science 320, 1620-1622.

Telus, M., Dauphas, N., Moynier, F., Tissot, F., Teng, F., Nabelek, P., Craddock, P., Groat, L. (2012). Iron, zinc, magnesium and uranium isotopic fractionation during continental crust differentiation: The tale from migmatites, granitoids and pegmatites. Geochim. Cosmochim. Acta 97,247-265.

Wang, Y., Zhu, X., Mao, J., Li, Z., Cheng, Y. (2011). Iron isotope fractionation during skarn formation - case study of Xinqiao Cu-S-Fe-Au deposit in Middle-Lower Yangtze Valley. Ore Geology Reviews 43, 194-202.

Young, E. D., Manning, C. E., Schauble, E. A., Shahar, A., Macris, C. A., Lazar, C., Jordan, M. (2015). High-temperature equilibrium isotope fractionation of non-traditional stable isotopes: experiments, theory, and applications. Chem. Geol. 395, 176-195.

Zambardi, T., Lundstrom, C., Li, X., McCurry, M., (2014). Fe and Si isotope variations at Cedar Butte volcano; insight into magmatic differentiation. Earth and Planet. Sci Lett. 405, 169-179.

Statement of Authorship

Title of Paper	Fe-isotope fractionation in magmatic-hydrothermal mineral deposits: A case study from the Renison Sn-W deposit, Tasmania.
Publication Status	☑ Published ☐ Accepted for Publication ☐ Submitted for Publication ☐ Unpublished and Unsubmitted work written in manuscript style
Publication Details	Wawryk, C.M and Foden, J.D (2015). Fe-isotope fractionation in magmatic-hydrothermal mineral deposits: A case study from the Renison Sn-W deposit, Tasmania. Geochimica et Cosmochimica Acta, 150, 285-298.

Principal Author

Name of Principal Author (Candidate)	Christine Wawryk
Contribution to the Paper	Collected samples from the field and mine site. Performed all sample preparation, analyses and interpretation. Wrote the manuscript and acted as corresponding author.
Overall percentage (%)	90
Certification:	This paper reports on original research I conducted during the period of my Higher Degree by Research candidature and is not subject to any obligations or contractual agreements with a third party that would constrain its inclusion in this thesis. I am the primary author of this paper.
Signature	Date 31/3/2017

Co-Author Contributions

By signing the Statement of Authorship, each author certifies that:

i. the candidate's stated contribution to the publication is accurate (as detailed above);

ii. permission is granted for the candidate in include the publication in the thesis; and

iii. the sum of all co-author contributions is equal to 100% less the candidate's stated contribution.

Name of Co-Author	John D Foden
Contribution to the Paper	Supervised collection of samples. Assisted with manuscript evaluation.
Signature	Date 4 April

Name of Co-Author	
Contribution to the Paper	
Signature	Date

Please cut and paste additional co-author panels here as required.

CHAPTER 2. FE-ISOTOPE FRACTIONATION IN MAGMATIC-HYDROTHERMAL MINERALS: A CASE STUDY FROM THE RENISON SN-W DEPOSIT, TASMANIA

Christine M. Wawryk*,[a] and John D. Foden[a]

[a]Centre for Tectonics, Research and Exploration, University of Adelaide, North Tce, South Australia, 5005, Australia

*corresponding author. Tel: +61 8 8313 1717. E-mail address: christine.wawryk@adelaide.edu.au

ABSTRACT

We present 50 new iron isotopic analyses of source granite and mineral separates from the Renison tin deposit in north western Tasmania. The aim of the study is to characterise the composition of minerals within a tin deposit associated with a reduced, S-type magma. We have analysed bulk samples of granite, and separates of pyrrhotite, pyrite, arsenopyrite, magnetite, chalcopyrite and siderite by multi-collector inductively coupled mass spectrometry. The isotopic compositions of mineral separates are consistent with theoretical predictions of equilibrium fractionation based on Mössbauer spectroscopy and other parametric calculations. Mineral-mineral pairs yield temperatures of formation that are in agreement with prior detailed fluid inclusion studies, but are spatially inconsistent with declining fluid temperatures with distance from the causative intrusion, limiting the use of Fe isotopes as a potential geothermometer, at least in this case. Comparison of our data with published data from other deposits clearly demonstrates that pyrite, magnetite and chalcopyrite from the hottest ore fluids (>300-400 °C) at Renison are isotopically heavier than minerals sampled from a deposit formed at similar temperatures, but associated with a more oxidised and less differentiated intrusion.

Keywords: iron isotopes, iron isotope fractionation, Multi Collector ICPMS, magmatic-hydrothermal minerals

2.1. INTRODUCTION

The use of Fe-isotope variation in tracking redox processes in Earth systems has resulted in a steadily increasing body of literature in the last decade. Thanks to the development of sensitive analytical equipment, it is now possible to characterise the isotopic composition of igneous rocks and minerals, formed from processes that have

fractionated iron isotopes at high temperatures. The iron isotope literature now reports the composition of an increasingly diverse array of igneous systems. These include; mantle xenoliths (e.g. Williams et al., 2002), ocean basalts (e.g. Teng et al., 2008; Teng et al., 2013), mafic volcanics (e.g. Schuessler et al., 2008), dolerites (Sossi et al., 2012) and granites (e.g. Poitrasson and Freydier, 2005; Telus et al., 2012)

Researchers investigating the fractionation of magmas (e.g. Schuessler et al., 2008; Teng et al., 2008; Sossi et al., 2012) have found that the most evolved differentiates often have heavy iron isotope enriched compositions. These studies demonstrate measurable Fe-isotopic fractionation at magmatic temperatures. Although fractional crystallisation is now clearly demonstrated as one mechanism that drives felsic differentiates towards heavy iron isotopic compositions, it has also been proposed by Poitrasson and Freydier (2005) and Heimann et al. (2008) that fluid exsolution from cooling siliceous plutons (>70 wt% SiO_2) may also lead to heavy isotopic enrichment; discharged Cl-bearing fluids preferentially stripped these granites of isotopically light Fe^{2+} driving the residual magmas to heavy iron isotope composition. A third mechanism of fractionating Fe isotopes, thermal diffusion, is demonstrated in the experiment of Huang et al. (2009), who melted the geostandard AGV-1 (a homogenous andesite powder) under hydrous conditions, with a steady temperature gradient between 350 and 950 °C. The run products showed that significant Fe-isotope fractionation of 2.8‰ had occurred, with the hotter region being isotopically lighter than the cold end.

The “light fluid” hypothesis is supported for some systems by the results from combined Fe and Zn isotopic studies (Telus et al., 2012) which demonstrate a correlation between high ^{66}Zn and high ^{56}Fe in pegmatites and some granitic rocks. The Zn^{2+} ion, being divalent, shows similar geochemical behaviour to Fe^{2+}, but is unaffected by redox processes being monovalent. Zn is highly mobile in chloride-bearing hydrothermal fluids, and studies (e.g. Gagnevin et al., 2012 and references therein) infer that kinetic Raleigh fractionation is one explanation for isotopic evolution of Zn from light to heavy (i.e. positive $\delta^{66}Zn$) isotopic compositions in cooling fluids. Telus et al. (2012) analysed pegmatites from the Black Hills in Dakota, where the reaction between exsolved fluids and reacted country rock were well documented. The authors used thermodynamic modelling to show that fractional crystallisation alone cannot account for the large dispersion of Zn/Fe ratios observed

in the samples and concluded that fluid exsolution does control iron isotope fractionation to some extent in magmatic processes.

It has long been recognised that cooling and crystallising magmas may exsolve chloride-rich, metal-bearing fluids that form economic ore deposits (e.g. Lindgren, 1906; Candela and Holland 1984; Eugster 1985). However important questions still await resolution. In particular, how can we link key variables that govern the evolution of the magmas that generate these ore fluids to characteristics of the ore minerals themselves? One such key variable is oxidation state. In this study we demonstrate that there is a strong relationship between the iron isotope systematics of cooling plutons and the iron isotope composition of associated hydrothermal sulfide ores. Furthermore it appears that this Fe-isotopic signature is particularly a function of the oxidation state of the magma.

Magmatic-hydrothermal fluids that are released from cooling and crystallising plutons may carry high concentrations of economic metals such as Cu, Au, Mo, Sn and W (e.g. Heinrich 1990; Simon et al., 2004; Webster 2004; Černy et al., 2005; Williams-Jones and Heinrich, 2005; Zajacz et al., 2007; Audétat et al., 2008; Frank et al., 2011). Suites of economic metals that occur together in magmatic-hydrothermal deposits have a well-known association with magma oxidation state (Blevin and Chappell 1992; Blevin 2004; Černy et al., 2005; Vigneresse 2007). Tin and Sn-W deposits are often associated with weakly to strongly peraluminous, reduced or ilmenite-series granites using the terminology of Ishihara (1977), whilst Cu- Au ± Mo ± W are associated with oxidised, magnetite-series intermediate to felsic intrusives often found in magmatic arc terranes (Černy et al., 2005; Seedorf et al., 2005; Sillitoe 2010 and references therein).

To date, published case studies of iron isotope systematics in magmatic-hydrothermal deposits (e.g. Graham et al., 2004, Li et al., 2010) do not have results for both magmatic suites and associated Fe-bearing ore minerals. In this paper we present 50 iron isotope values of bulk granite (sensu stricto) and mineral separates, from different structural and stratigraphic positions in the Renison Sn-W deposit. The Renison deposit is a world class example of a stratabound carbonate replacement Sn deposit associated with reduced S-type granitic intrusion, and therefore represents one end of the magma oxidation state spectrum. Our results are compared to theoretical predictions for equilibrium mineral-mineral fractionation. We also compare our results to published data from the Xinqiao Cu-Fe-S-Au skarn,

associated with a quartz-monzodiorite stock (Wang et al., 2011), to examine the effect of magma oxidation state on the isotopic composition of fluids that later deposited the magmatic-hydrothermal minerals. Our results contribute a large new empirical dataset to a rapidly expanding field of research, and further illustrate the complex interplay of processes that fractionate iron isotopes.

2.2. GEOLOGY

2.2.1 Regional Geology

The geological setting and detailed descriptions of the Renison Sn-W deposit has been described by many authors (e.g. Patterson et al., 1981; Kitto, 1994; Bajwah et al., 1995; Walshe et al.,1996; Walshe et al., 2011), covering decades of research, and is summarised below.

The deposit is located in the Dundas Region in western Tasmania (Patterson et al., 1981). The Dundas region comprises a linear basin of Late Proterozoic to Early Paleozoic sedimentary sequences, allochthonous ultramafic to mafic sequences, and the Cambrian Mt Read Volcanics (Patterson et al., 1981). The Trough is bound to the northwest and southeast by blocks of Proterozoic metasediments (Fig. 2.1).

The oldest sedimentary sequence in the mine area is the Upper Neoproterozoic Success Creek Group (Fig. 2.1). The Success Creek Group comprises shallow water to subaerial siliceous clastic sediments, shales and dolostones (Patterson et al., 1981). The Crimson Creek Formation overlies and is in faulted contact with the Success Creek Group (Patterson et al., 1981). The Crimson Creek formation comprises a shelf sequence of siltstones, shales and volcaniclastics with minor dolostones. (Patterson et al., 1981; Kitto, 1994).

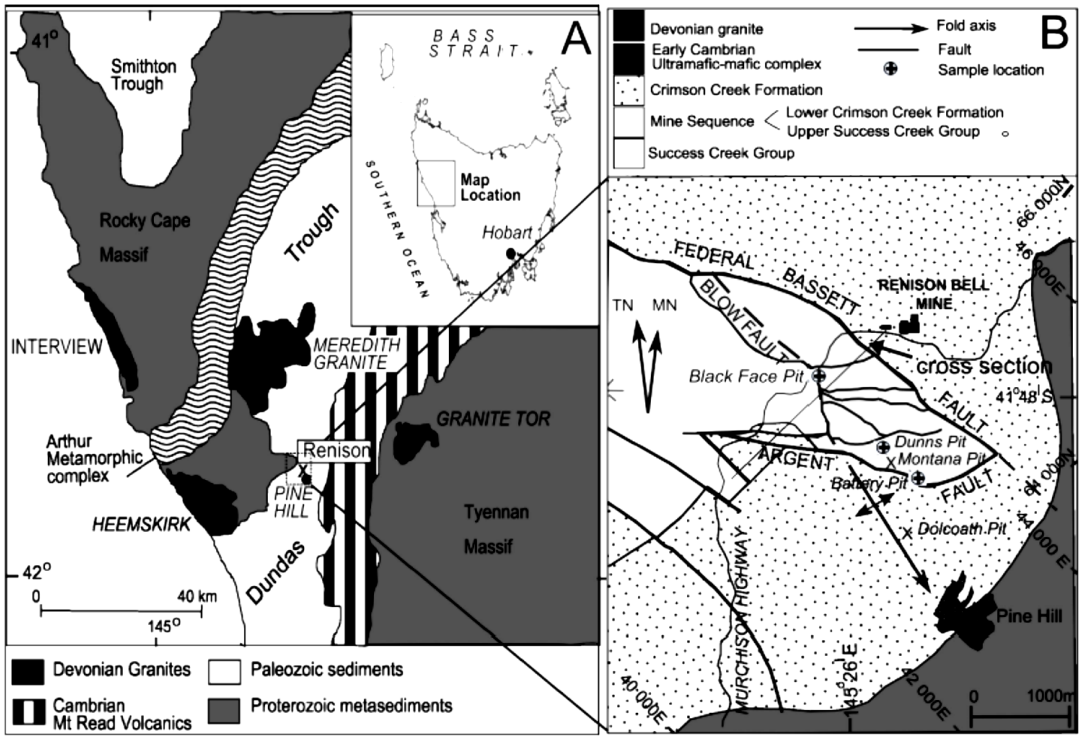

Figure 2.1 Location and geology of the Renison Sn-W deposit. A: major tectonostratigraphic elements of western Tasmania (after Patterson et al., 1981). B: geological map of the Renison Sn deposit Mine area (after Kitto, 1994).

The contact between the Success Creek Group and Crimson Creek Formation is marked by the Red Rock Member (Fig. 2.2), a variably hematitic unit comprising siltstones and volcaniclastics, conglomerates and greywackes, cherty ironstones and thin dolostones (Patterson et al., 1981; Kitto, 1994). Strata comprising the upper Success Creek Group and lower Crimson Creek Formation are termed the Mine Sequence by mine geologists

Polyphase folding in Middle Devonian resulted in north-west trending open folding (Patterson et al.,1981; Kitto, 1994) Syn- to post kinematic I and S-type granites intruded at around 390 Ma, during the later stages of the Taberabberan orogeny (Black et al., 2005).

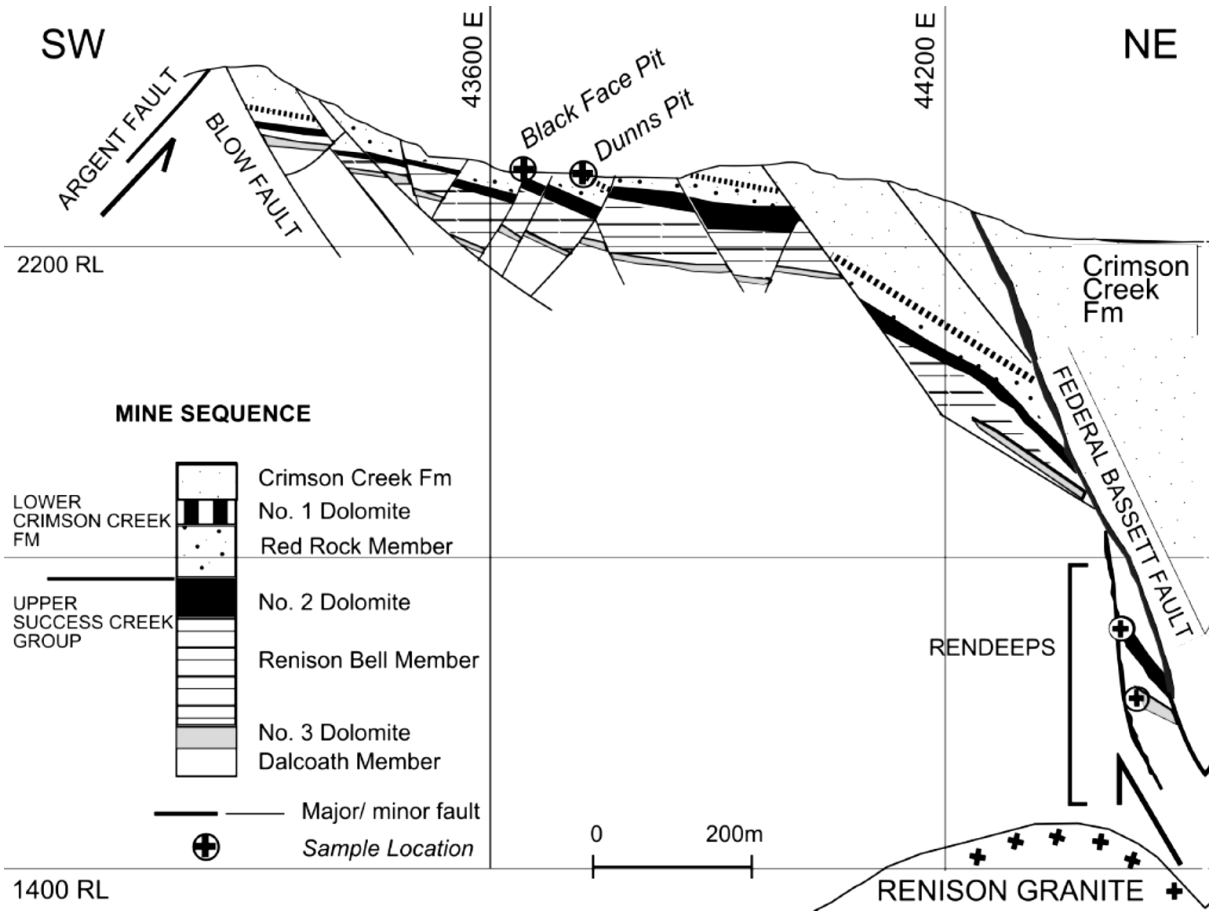

Figure 2.2 Cross section looking northwest through the Renison Sn deposit. Positions of Black Face and Dunn's pits have been projected onto section to graphically illustrate the stratigraphic position of samples (after Kitto, 1994). Coordinates are local Mine Grid. Section line is shown in Figure 2.1B

2.2.2 Deposit Geology

The Renison deposit is controlled by the NW striking, normal Federal Bassett Fault ('FBF'), located on the north east limb of a south east plunging anticline (Fig. 2.1 and 2.2). Intrusion of the Renison granite caused brittle fracturing and normal fault reactivation in the intruded Late Neoproterozoic Success Creek and Crimson Creek Formations. This allowed magmatic fluids accumulated in a probable cupola structure on the upper surface of the cooling Meredith Granite pluton, to be tapped and ascend along the FBF and invade the sedimentary strata depositing base metal and tin ores, as a result of replacement of carbonate units. Stratabound, massive pyrrhotite-cassiterite with minor pyrite and base metals (e.g. galena, sphalerite and chalcopyrite) replaced 3 dolomite horizons within the Success Creek Group and Crimson Creek Formation (Fig. 2.2). Although the bulk of the mineralisation is replacement style, fault controlled veins are also economically exploited. Faulted

blocks of the Mine Sequence are mined within the FBF and are referred to as ‘Stratafault’ Ore.

Normal faults located within 1km of the mine area also provided a conduit for mineralising fluids, as evidenced by the numerous historical workings that lie along them (Figs. 2.1, 2.2). The stratabound ore surfaces are structurally complex (Fig 2.3), being controlled by structures both sub-parallel and transverse to the FBF (Kitto, 1994).

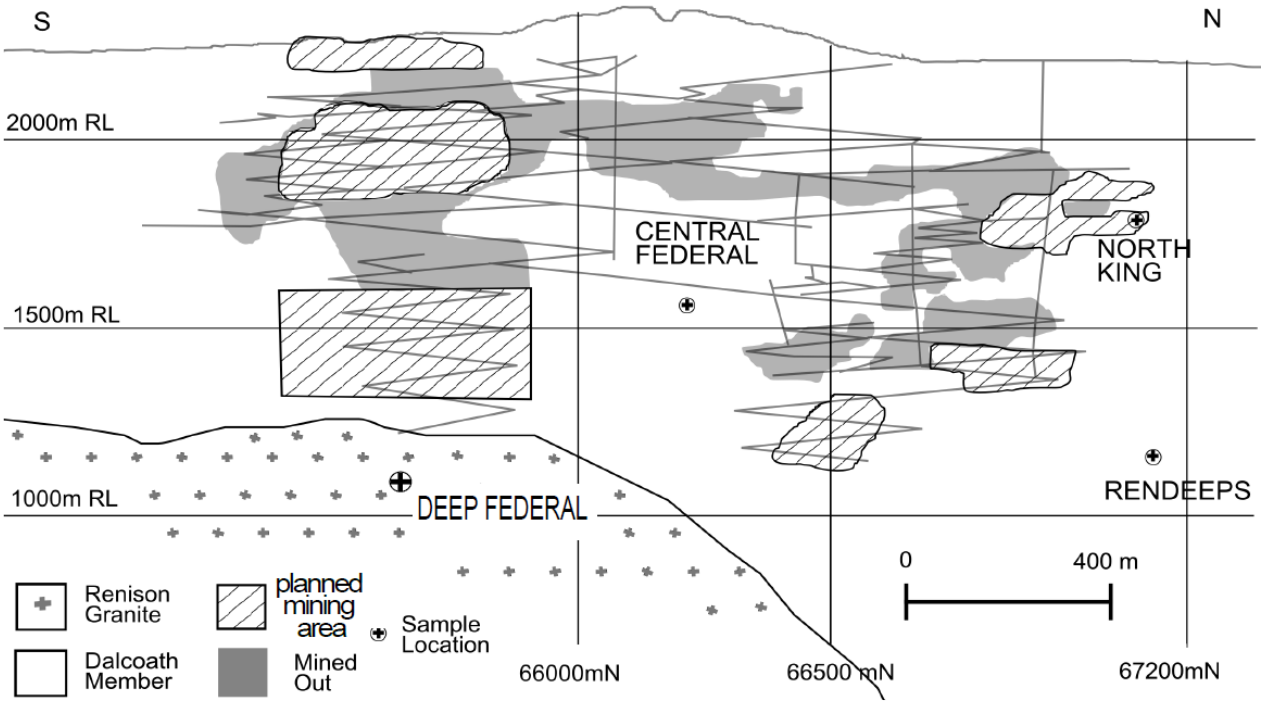

Figure 2.3 Long section along the Federal Bassett Fault projected from the footwall, showing sample locations from the North King, Central Federal, Deep Federal and Rendeeps ore surfaces. Coordinates are local Mine Grid. “mRL”= metres Relative Level and refers to height referenced to a datum, usually sea level (diagram sourced from MetalsX Quarterly Activities Report for the December Quarter, 2013).

2.2.3 The Renison Granite

The Renison granite is a fractionated, shallow (2-4 km) S-type intrusion, ranging in composition from adamellite to alkali-feldspar granite (Sawka et al., 1990; Bajwah, 1995; Black et al., 2005). Interpretation of gravity data by Richardson and Leaman (1989, referenced in Kitto, 1994) shows that the Renison Granite forms part of the larger Meredith Pluton which includes the Heemskirk intrusion to the west and Granite Tor to the east (Kitto, 1994; Fig. 2.1).

The Renison granite is a grey, medium to coarse grained biotite granite (Fig. 2.4). Bajwah et al. (1995) describes four texturally distinct types; K-feldspar porphyry, fine-grained porphyritic granite, fine grained non-porphyritic granite and medium to coarse grained equigranular granite. Unaltered granite comprises quartz, K-feldspar, plagioclase and biotite, with ilmenite, monazite, apatite, zircon, fluorite, topaz, tourmaline and rare allanite as accessory phases. Phenocrysts in the porphyritic varieties are either quartz or K-feldspar up to 1 cm across. Plagioclase phenocrysts are recorded in the quartz-feldspar porphyry. These types are interpreted, on the basis of geochemistry and petrography (Bajwah et al., 1995; Walshe et al., 2011) to be related by fractional crystallisation.

The Renison granite has been variably albitised, sericitised and tourmalinised via boron-fluorine metasomatism from hydrothermal fluids (Patterson et al., 1981; Kitto, 1994; Bajwah et al., 1995).

2.2.4 Mineralogy and paragenesis

Researchers (e.g. Patterson et al., 1981; Kitto, 1994) have documented several different paragenetic stages. We use the interpretation and terminology of Kitto (1994), which places alteration and paragenesis in a temporal context of structural evolution and declining fluid temperatures, as summarised in the next section.

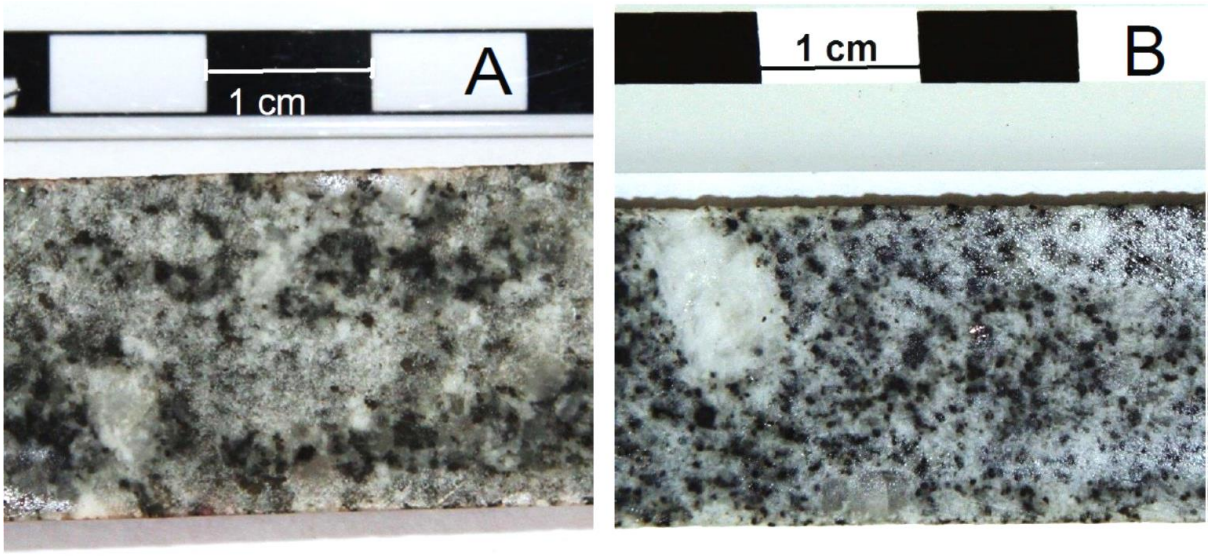

Figure 2.4 Hand specimens of the feldspar porphyry unit of the Renison Granite from Deep Federal underground diamond drill core. A: coarse-grained K-feldspar porphyry. B: fine-grained porphyritic granite.

2.2.4.1 Oxide –Silicate stage

Rare assemblages of carbonate and magnetite may represent the earliest magmatic fluid (Kitto, 1994; Fig. 2.5), followed by quartz-arsenonopyrite ± cassiterite ± wolframite ± pyrrhotite-pyrite-chalcopyrite-ilmenite-rutile (Fig. 2.6C). This stage is interpreted by Kitto (1994) to be coincident with the onset of normal-dextral movement along the FBF system. Fluid inclusion studies showed minimum formation temperatures of 340-420 °C, and salinity varied between 8-12 equivalent wt% NaCl.

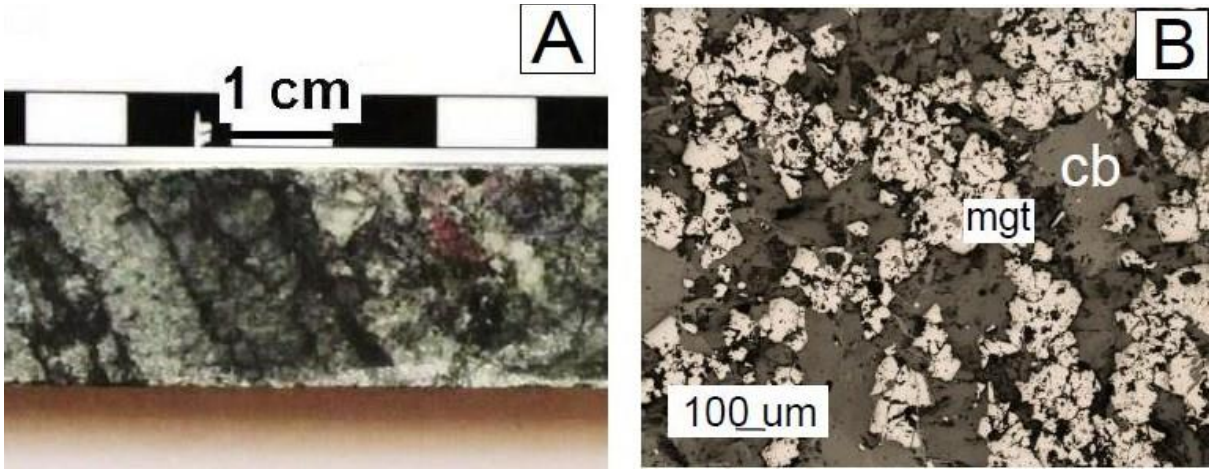

Figure 2.5 Magnetite altered Dolomite #2 from the North King ore surface, possibly representing the earliest ore fluid. Mineral abbreviations as in Table 2.1. A: hand specimen, scale bar divisions are 1cm wide B: photomicrograph showing subhedral fine grained magnetite, scale bar at bottom left is 500µm wide.

2.2.4.2 Main Sulphide stage

This stage is the dominant carbonate replacement stage and is characterised by pyrrhotite- cassiterite -± arsenopyrite ±pyrite ± quartz-fluorite (Figs 2.6B, C). Base metal phases such as chalcopyrite-sphalerite-galena-bismuth-argentite-chlorite may also be present, typically interstitial to pyrrhotite-arsenopyrite. Chalcopyrite is more common within the FBF where Cu grades of up to 0.3% occur. These stratabound bodies are interpreted to have been deposited in dilational zones along structures in the FBF caused by dextral wrench reactivation. This stage is recognised in thin section by brittle deformation of arsenopyrite, with fractures infilled by chalcopyrite

and pyrrhotite (Fig. 2.6F). Fluid inclusion studies results in minimum formation temperatures of 170-300 °C, and salinity varied between 0-14 equivalent wt% NaCl.

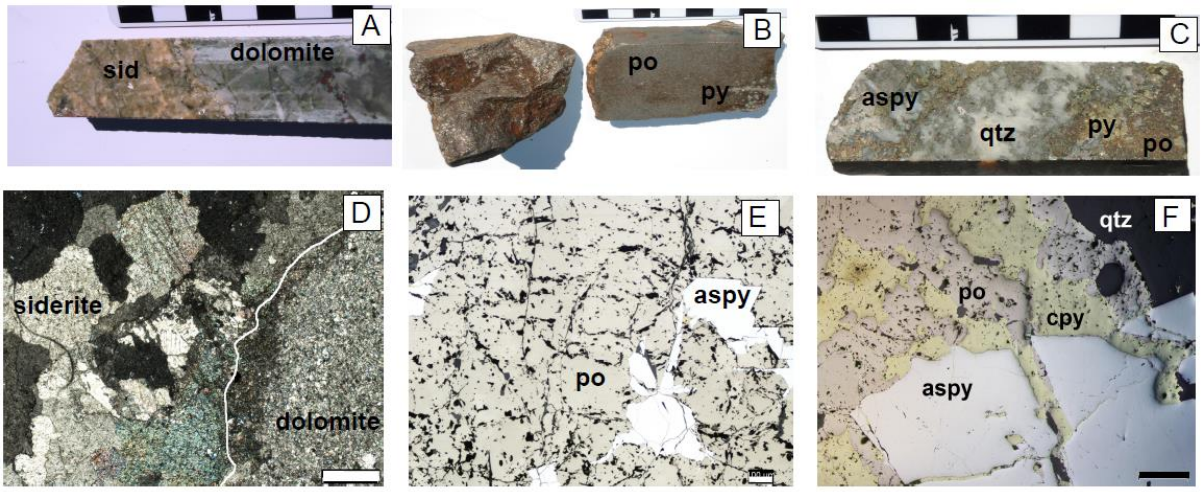

Figure 2.6 Type examples of samples from the Renison deposit. Mineral abbreviations as in Table 2.1. Scale bars shown next to hand specimens are divided into 1cm divisions. A: Siderite alteration of dolomite (sample RB011). Note the very sharp reaction front. B: massive replacement pyrrhotite ore from Black Face pit (sample 40612-5). C: Early Oxide Stage aspy in quartz vein is overprinted by Main Stage po-py (sample RB030). D. Photomicrograph of A, showing fine grained dolomite replaced by coarse, recrystallised siderite. Scale bar shows 500µm. E: reflected light photomicrograph of massive po replacement ore from Black Face pit, overprinting early aspy. Scale bar shows 100µm. F: reflected light photomicrograph showing Oxide Stage aspy-qtz fractured and infilled by Main Stage po-cpy. Scale bar shows 500µm.

2.2.4.3 Late Base Metal Stage

Crustiform rhodocrosite-lined veins are characteristic of this stage. Vein mineralogy comprises sphalerite- galena- quartz- -pyrrhotite- pyrite-chalcopyrite-fluorite-calcite-chlorite. The interpretation of this stage being associated with brittle reactivation is based on textural features such as syntaxial crack-seal veins and micro folding (Kitto, 1994 and references therein). Fluid inclusion studies record lower temperatures (150° -210°C) and bimodal salinities (2 or 10 wt% NaCl equivalent), suggesting mixing of magmatic-hydrothermal fluids with meteoric groundwaters (Patterson et al., 1981; Kitto, 1994; Walshe et al., 1996).

2.2.4.4 Carbonate Stage

Dolomite, fluorite, clear quartz, chalcopyrite and calcite comprise a carbonate-dominant mineral assemblage infilling brecciated sediments or vugs and fault cavities.

A hydrothermal magnesian siderite halo surrounds the stratabound ore surfaces (Patterson, 1981; Kitto, 1994), and is interpreted to form via dissolution of the host dolomites by magmatic fluid. The limit of the reaction front is usually very sharply defined as an abrupt transition to largely unaltered sedimentary rock (Figs. 2.6A, D).

Sulfur isotope, oxygen and hydrogen isotope studies have been carried out by previous workers (e.g. Patterson et al., 1981; Kitto, 1994 and references therein). The $\delta^{34}S$, $\delta^{18}O$ and δD values of minerals from the Oxide-Silicate and Main Stages are 6‰, +10‰ and ~-90‰, respectively, interpreted to represent magmatic sulfur and water sources. However, Walshe et al., (1996) present an alternative model of reduced, sedimentary sulfur–bearing meteoric waters homogenizing at depth with magmatic fluids, prior to ascent through fault conduits.

2.3. ANALYTICAL METHOD

2.3.1 Sample Selection

Sample locations and descriptions are described in Table 2.1, and illustrated in Figures 2.1, 2.2 and 2.3. Samples of stratafault ore, which contain both arsenopyrite-pyrrhotite-chalcopyrite-pyrite assemblages and massive pyrrhotite, were sampled from the Central Federal and Rendeeps mine areas. Siderite alteration of host dolomite units was sampled from core drilled in the North King mine area. Dolomite-hosted replacement ore was sampled from several historic mines along the Black Face Fault, adjacent to the Blow Fault. Samples thus encompass a strike length of approximately 1.2km, and vertical extent of about 1km from surface.

The Late Base Metal and Carbonate stages were not analysed as part of this study, to eliminate variability owing to multiple vein crack-seal events and lower temperature fluid mixing.

Samples of fresh, unaltered Renison granite were collected from drill core, and tourmalinised granites were sampled from outcrop at Pine Hill.

Mineral separates were obtained by crushing samples in an agate mortar and pestle, then passing a hand magnet over crushed samples to separate magnetite. Pyrrhotite,

pyrite, arsenopyrite, chalcopyrite and siderite were separated by hand-picking under a binocular microscope. Composition of siderite was verified by X-ray diffraction. Mineral separates were cleaned with ethanol prior to dissolution.

2.3.2 Preparation for Fe-isotope analysis

Fresh, unaltered, unmineralised granite samples were crushed and milled in their entirety, to produce a whole rock powder. These were dissolved in a mixture of concentrated HNO_3-HCl-HF overnight at 80°C. Sulfide mineral separates were dissolved in HNO_3-HCl only. Samples were then dried, following further additions of concentrated HNO_3 to drive off the HF. The samples were converted to chloride in 6M HCl, dried again, and finally taken up in 6M HCl and centrifuged to remove insoluble cassiterite or silicate mineral inclusions prior to ion-exchange chromatography.

Iron in the samples was purified using Bio-Rad AG 1X4 200-400 mesh anion exchange resin, and HCl, following the method of Poitrasson and Freydier (2005).

2.3.3 Mass spectrometry

Iron isotope measurements were performed at the University of Adelaide on a Thermo Finnigan Neptune Multi-Collector ICP-MS. Measurements were performed in medium resolution mode, with H-geometry skimmer cones. Some samples were measured with X cones on high resolution mode, owing to degradation of the entrance slit precluding satisfactory peak resolution in medium resolution mode.

Sample introduction was via a glass spray chamber and Scott double pass assembly, together with a low flow, self-aspirating PFA nebulizer (between 50-70 µl/min).Samples were analysed in a 0.05M HCl solution. Iron was set to a concentration of 3.5 ppm to give a sensitivity of ~1V on ^{57}Fe. Ni spiking was set to a concentration of ~8 ppm, to give a signal of ~1V on 61Ni.

Sample take-up time to achieve a stable signal was set at 45s. A measurement consisted of 35 cycles of 8s integration time in static mode. A baseline measurement was done before each sample measurement. Each sample was run a minimum of 3 times.

Delta values were corrected for mass bias using the Ni-spiking method described by Poitrasson and Freydier (2005). Data quality control was assured through the running of a hematite internal standard every 10th analysis, in addition to running replicates of geostandard GSP2. Our long term average for GSP2 is 0.176 ± 0.13‰ (2σ) for

$\delta^{56}Fe$ and 0.29 ± 0.17‰ (2σ) for $\delta^{57}Fe$, which compare well with the published composition of 0.159 ± 0.013‰ for $\delta^{56}Fe$, and 0.23 ± 0.021‰ for $\delta^{57}Fe$ (Craddock and Dauphas, 2011).

All data are reported using delta notation, in units of per mil (‰)

$\delta^{56}Fe = [(^{56}Fe/^{54}Fe_{sample}) / (^{56}Fe/^{54}Fe_{IRMM14}) - 1] \times 10^3$

2.4. RESULTS

The isotope data for different minerals and whole rock granite samples are presented in Table 2.1 and Figure 2.7, and discussed below.

Table 2.1 Iron isotopic compositions of granite and magmatic-hydrothermal mineral separates.

Sample Number	Description	Mineral	Paragenetic Stage	$\delta^{57}Fe$	2SD	$\delta^{56}Fe$	2SD
Black Face Pit							
40612-01	massive py in stratabound lode Dolomite #1	py	Main Sulfide	0.89	0.01	0.61	0.00
40612-03	massive py in stratabound lode	py	Main Sulfide	1.30	0.06	0.84	0.07
40612-04	massive po replacement lode	po	Main Sulfide	-0.40	0.09	-0.28	0.08
40612-05	massive po replacement lode	po	Main Sulfide	-0.36	0.08	-0.25	0.06
40612-07	massive py in stratabound lode	py	Main Sulfide	1.13	0.01	0.75	0.00
40612-09	massive po replacement lode	po	Main Sulfide	-0.34	0.05	-0.23	0.07
Dunns Pit							
40612-12	massive po replacement lode	po	Main Sulfide	-0.34	0.08	-0.26	0.03
40612-13	massive po replacement lode	po	Main Sulfide	-0.36	0.04	-0.25	0.04
The Battery Pit							
40612-17	intergrown py-po veins in siltstone	po	Main Sulfide	-0.46	0.08	-0.33	0.04
40612-17		py	Main Sulfide	1.46	0.00	0.93	0.02
40612-21	massive po replacement lode	po	Main Sulfide	-0.50	0.03	-0.37	0.04
40612-21		py	Main Sulfide	1.46	0.14	1.11	0.02
Pine Hill							
40612-31	greisenised Pine Hill granite	whole rock		0.34	0.10	0.24	0.10
40612-32	tourmalinised Pine Hill granite	whole rock		0.32	0.02	0.21	0.05
40612-33	greisenised Pine Hill granite	whole rock		0.45	0.10	0.31	0.05
Deep Federal							

Sample Number	Description	Mineral	Paragenetic Stage	$\delta^{57}Fe$	2SD	$\delta^{56}Fe$	2SD
RB001	fresh Renison granite	whole rock		0.43	0.01	0.27	0.01
RB002	fresh Renison granite	whole rock		0.27	0.09	0.18	0.03
RB003	fresh Renison granite	whole rock		0.29	0.09	0.19	0.05
RB004	fresh Renison granite	whole rock		0.38	0.07	0.26	0.07
King Surface							
RB009	siderite- altered dolomite	sid		-0.07	0.12	-0.04	0.10
RB010	siderite- altered dolomite	sid		0.05	0.02	0.04	0.00
RB011	mgt altered dolomite	mgt	Oxide-silicate	1.00	0.06	0.70	0.06
RB013	sid intergrown with py-po in Fault ore	po	Main Sulfide	-1.00	0.09	-0.72	0.06
RB013		sid	Main Sulfide	-0.01	0.09	-0.01	0.09
RB013		py	Main Sulfide	1.39	0.04	0.94	0.09
366mgt	mgt altered dolomite	mgt	Oxide-silicate?	1.01	0.04	0.50	0.04
Rendeeps							
RB016	as-cpy-po vein	aspy	Main Sulfide	1.01	0.08	0.68	0.08
RB016		cpy	Main Sulfide	0.59	0.04	0.39	0.04
RB017	as-cpy-po vein	po	Main Sulfide	-0.55	0.04	-0.39	0.04
RB017		cpy	Main Sulfide	1.06	0.05	0.71	0.08
RB018	as-cpy-po vein	po	Main Sulfide	-0.72	0.07	-0.48	0.05
RB019	massive po replacement lode	po	Main Sulfide	-0.77	0.09	-0.52	0.04
RB020	massive po replacement lode	po	Main Sulfide	-0.51	0.07	-0.32	0.05
Central Federal							

Sample Number	Description	Mineral	Paragenetic Stage	$\delta^{57}Fe$	2SD	$\delta^{56}Fe$	2SD
RB021	cb-py-aspy-cpy-po vein in Fault ore	aspy	Main Sulfide	1.04	0.02	0.73	0.01
RB021		cpy	Main Sulfide	0.55	0.06	0.37	0.01
RB022	massive po replacement lode	po	Main Sulfide	-0.15	0.01	-0.09	0.01
RB023	cb-mg altered dolomite host rock	po	Oxide-silicate	0.00	0.10	-0.02	0.06
RB024	quartz vein hosted aspy-po in Fault ore	aspy	Main Sulfide	1.19	0.08	0.80	0.02
RB024		po	Main Sulfide	-0.52	0.00	-0.34	0.01
RB024		cpy	Main Sulfide	1.32	0.07	0.86	0.04
RB025	massive po-aspy-cpy in Fault Ore	aspy	Main Sulfide	0.85	0.06	0.60	0.03
RB025		po	Main Sulfide	-0.67	0.06	-0.43	0.04
RB027	cpy-aspy-py-cb vein in Fault Ore	aspy	Main Sulfide	1.08	0.03	0.74	0.02
RB027		po	Main Sulfide	-0.87	0.01	-0.60	0.00
RB027		py	Main Sulfide	1.59	0.01	1.14	0.03
RB027		cpy	Main Sulfide	0.28	0.10	0.18	0.05
RB028	aspy-cpy-cb vein	aspy	Main Sulfide	0.96	0.08	0.57	0.04
RB030	sid(?)-cpy-po vein	aspy	Main Sulfide	1.11	0.06	0.77	0.01
RB030		po	Main Sulfide	-0.39	0.02	-0.28	0.03
RB030		cpy	Main Sulfide	0.60	0.03	0.39	0.02

aspy=arsenopyrite
cb= carbonate
cpy=chalcopyrite
mgt=magnetite
po=pyrite
py=pyrite
sid=siderite

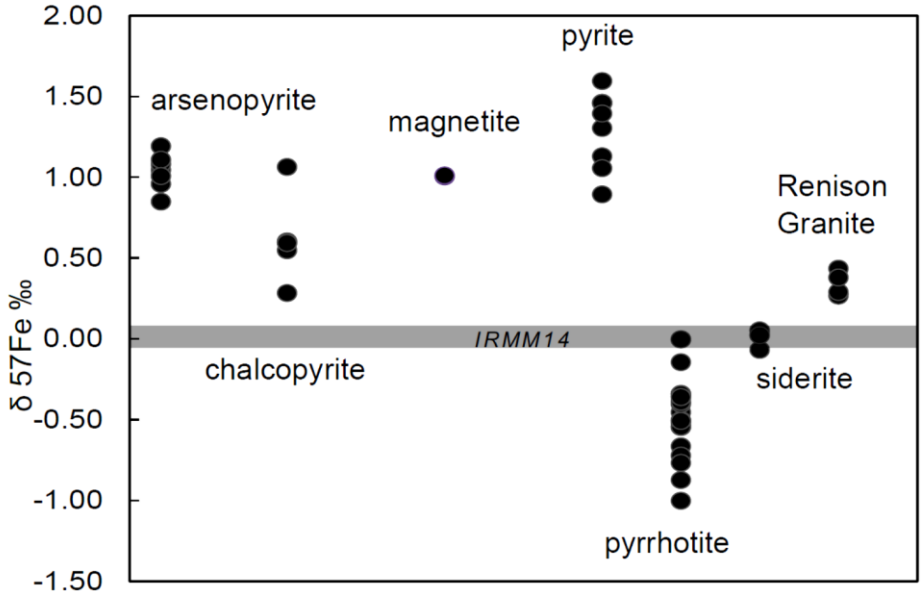

Figure 2.7 Iron isotope ratios of magmatic hydrothermal minerals and bulk granite from the Rension deposit.

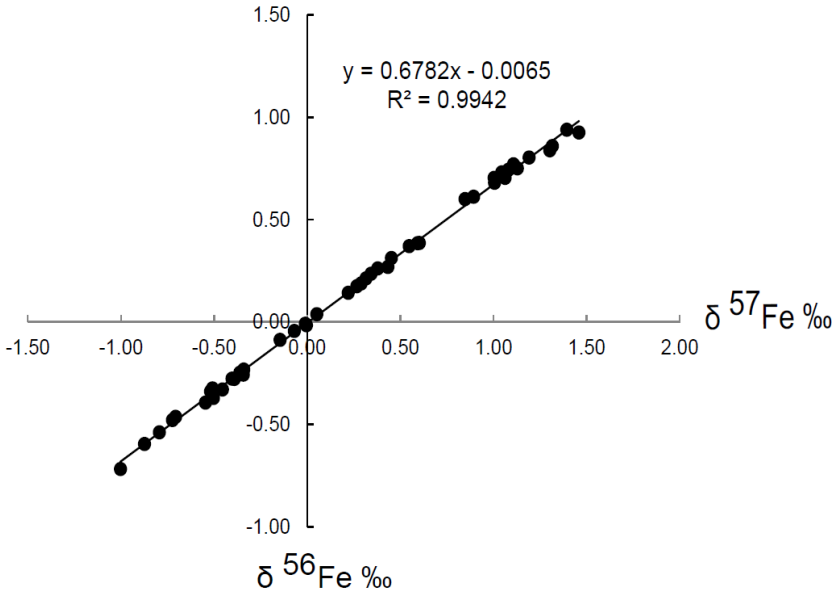

Figure 2.8 Plot of $\delta^{56}Fe$ v $\delta^{57}Fe$ of samples analysed. The slope of the line is close to the theoretical mass dependent fractionation of 0.672, showing that spectral interferences from Ar-O and Ar-N species have effectively been resolved in medium and high resolution modes. Deviation from the theoretical line may be a results of matrix effects from different batches of 2% nitric acid used over time

2.4.1 Isotopic composition of whole rocks

The $\delta^{57}Fe$ of fresh Renison granite (n=4) vary between +0.27 ± 0.09‰ (2σ) and +0.43 ± 0.01‰ (2σ) as shown in Table 2.1 and Fig. 2.7. They are similar in composition to isotopically heavy felsic (>65-70 wt% SiO_2) igneous rocks reported by Poitrasson and Freydier (2005), which ranged between 0.137 ± 0.027‰ (2SE) and 0.584 ± 0.034‰ (2SE). In comparison, $\delta^{57}Fe$ of mafic igneous geostandards range from 0.074 ± 0.077‰ to 0.247 ± 0.022‰ (Craddock and Dauphas, 2011), and a wide ranging study of oceanic basalts (~48-60 wt% SiO_2) by Teng et al. (2013) report $\delta^{57}Fe$ ranging from -0.017 ± 0.04‰ (95% confidence interval, CI) to 0.269 ± 0.047‰ (95% CI).

2.4.2 Isotopic composition of minerals separates

Sulfides, magnetite and siderite results are detailed in Table 2.1 and Figure 2.7. The $\delta^{57}Fe$ of arsenopyrite (n=7) analyses vary between +0.85 ± 0.06‰ (2σ) and +1.11 ± 0.06‰ (2σ). Pyrite results (n=7), are very similar to arsenopyrite, varying between +0.89 ± 0.01‰ (2σ) and +1.59 ± 0.01‰ (2σ). The two magnetite samples returned +1.0 ± 0.06‰ (2σ) and +1.01 ± 0.04‰ (2σ), so are also isotopically heavy. Chalcopyrite analyses (n=6) vary between +0.28 ± 0.1‰ (2σ) and +1.32 ± 0.07‰ (2σ). Pyrrhotite analyses (n=16) are the isotopically lightest of all the minerals analysed, varying between -1.0 ± 0.09‰ (2σ) and 0.00 ± 0.10‰ (2σ). Siderite analyses (n=3) vary between -0.07 ± 0.12‰ (2σ) and +0.05 ± 0.02‰ (2σ).These results are very close to that those reported for a skarn carbonate of -0.07‰ by Dideriksen et al. (2006).

2.5. DISCUSSION

2.5.1 Mineral-Mineral Fractionation

There are few published experimental measurements of mineral-mineral or mineral-fluid pairs that have formed at magmatic-hydrothermal temperatures, although the number of experiments being published in the literature is increasing (e.g. Saunier et al., 2011, and Syverson et al., 2013). In the absence of empirical data, theoretical fractionation factors are calculated using the relationship:

$$\Delta A\text{-}B = \delta^{56}Fe_A - \delta^{56}Fe_B \approx 10^3 \ln\alpha^{56}Fe_{A\text{-}B} \quad (1)$$

where

$$10^3 \ln\alpha^{56}Fe_{A\text{-}B} = 10^3 \ln\beta_A - 10^3 \ln\beta_B , \quad (2)$$

The variable $10^3 \ln\beta$ is termed the “reduced partition function’, and can be calculated by Mössbauer Spectroscopy (e.g. Polyakov and Mineev, 2000; Polyakov et al., 2007; Polyakov and Soultanov, 2011). Other calculations of theoretical equilibrium Fe-isotope fractionation between minerals and fluids have been reported by researchers using a variety of methods such as Density Functional Theory (Blanchard et al., 2009; Rustad et al., 2010), infrared, Raman and vibrational spectroscopies (e.g. Polyakov and Mineev, 2000; Schauble et al., 2001) and inelastic nuclear resonant X-ray scattering (Polyakov et al., 2007). A review of these methods is contained in Schauble (2004).

At equilibrium, the fractionation of iron isotopes is governed by several factors. Heavy isotopes are incorporated into sites wherein vibrational energy is minimised i.e. short, strong chemical bonds (Schauble, 2004). The formation of a stiff chemical bond is made more favourable by several parameters. To summarise from Schauble et al. (2001), these include (1) the oxidation state of Fe; Fe^{3+} compounds preferentially incorporate the heavy isotopes; (2) the ligand bond strength; for example, chloride complexes have weaker bonds than CN- or H_2O complexes so are isotopically lighter, and (3) the coordination number of Fe in the compound in question; for example, 4-fold coordination versus 6-fold coordination. Polyakov and Mineev (2000) also reported the effect of covalent bonds for pyrite, which has a high β factor, despite being a ferrous compound.

Theoretical Fe-isotopic fractionation between minerals as a function of temperature can be calculated using published reduced partition functions (e.g. Blanchard et al., 2009; Polyakov and Soultanov, 2000; Polyakov and Soultanov, 2011). For a typical magmatic-hydrothermal temperature of 350°C, it can be predicted that $10^3 \ln\beta$ mgt~py>cpy>sid~po (Fig 2.9A). The isotopic compositions of the different minerals we analysed form distinct and consistent groupings implying a relationship governed by coherent partitioning. Our data are clearly consistent with the prediction that pyrite, magnetite and chalcopyrite are isotopically heavier than siderite and pyrrhotite. The pyrrhotite and siderite data is also consistent with the prediction that ferrous minerals preferentially incorporate the light iron isotope. We also note that the Fe isotope compositions for pyrrhotite (Fig 2.7 and Table 2.1) cannot be distinguished on the basis of spatial position within the deposit, which suggests that equilibrium fractionation has been reached in part.

Our results are consistent with results reported by Graham et al. (2004), Markl et al. (2006) and Wang et al. (2011) who also found magnetite and pyrite to be isotopically heavier than siderite and chalcopyrite. In contrast, pyrite deposited from rapidly quenched sea floor hydrothermal fluids is isotopically light (e.g. Rouxel et al., 2004; Rouxel et al., 2008), with fractionation dominated by kinetic processes. Another possibility is that pyrite is preserving the isotopic composition of a FeS precursor, where fractionation is dominated by kinetic processes (Rouxel et al., 2008). Syverson et al.'s (2013) precipitation experiments, conducted at hydrothermal conditions (300–350°C, 500 bars) resulted in fractionation of the light isotope first, perhaps as a result of kinetic or Rayleigh processes, with deposited minerals getting isotopically heavier with time. We observe fractionation between pyrite and pyrrhotite of up to ~2‰, which suggests that pyrite at Renison does not preserve the isotopic composition of a lighter precursor so perhaps kinetic processes are not the dominant process in longer lived magmatic-hydrothermal systems.

2.5.2 Mineral-Fluid Fractionation

Figure 2.9B illustrates theoretical Fe fractionation between minerals and an Fe(II)-bearing fluid using the reduced partition function for the species $[Fe(II)Cl_2]^0$, calculated by experimental work (e.g. Simon et al., 2004; Saunier et al., 2011 and references therein), which shows that this is the predominant complex at magmatic-hydrothermal conditions. This diagram shows that we would predict magnetite and pyrite to be isotopically heavier than the fluid, and siderite and pyrrhotite to be lighter. However, this diagram ilustrates the complications that can arise when choosing which theoretical fractionation factor to use for the fluid. The difference between possible values for $10^3 \ln\beta$ arises owing to the choice of basis sets (see Hill et al., 2010 for details) used in the computation, and indeed, the choice of computational approach (see Saunier et al., 2011 for more detailed discussion about sources of uncertainty). Two dashed lines are plotted for theoretical chalcopyrite-fluid fractionation. The shaded wedge between the two possible lines shows the range of fractionation that could be expected, depending on whether $10^3 \ln\beta$-factor 1 is used, or whether $10^3 \ln\beta$-factor 2 is used. In this case the choice clearly affects whether we would predict chalcopyrite to be isotopically heavy or light compared to a fluid, with the impact being greater at lower temperatures. Although not plotted in the figure, similar differences in fractionation factors were observed for all our analysed minerals, depending on the choice of $10^3 \ln\beta$ for ferrous fluid species. Continuing

research to gather experimental and empirical data will be important for refining theoretical models.

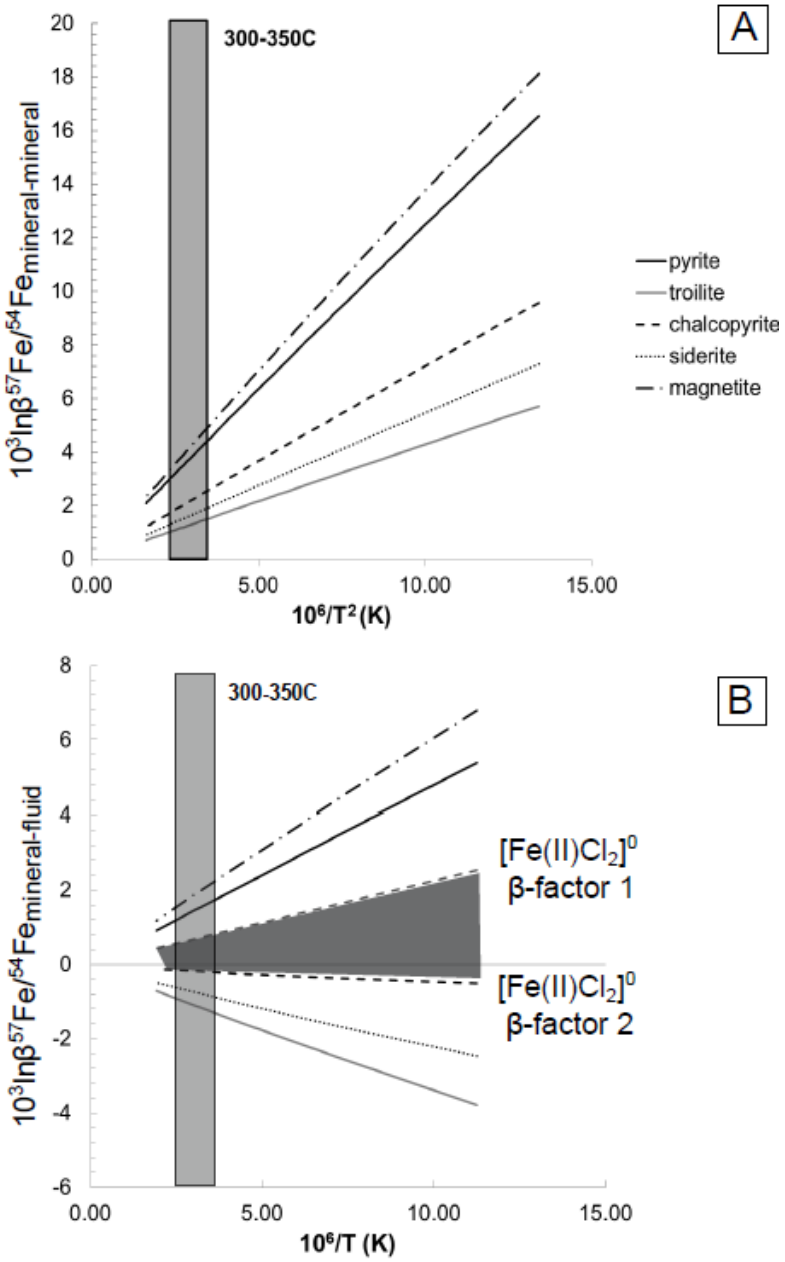

Figure 2.9 Theoretical iron isotope fractionation using reduced partition functions for ^{57}Fe. A: iron isotope fractionation between minerals.Troilite is stoichiometric pyrhhotite.The reduced partition function from Blanchard et al. (2009) was used for pyrite. The shaded area shows the minimum temperatures in Celsius estimated from fluid inclusions for formation of Oxide-Silicate and Main Sulfide stage minerals at Renison. B: theoretical isotopic fractionation between minerals and a Fe(II)-Cl bearing aqueous solution. For Fe(II)-Cl bearing fluid, the reduced partition function calculated by (Schauble 2001) was used. Mineral abbreviations as in Table 2.1.

2.5.3 Fe- isotopes as a geothermometer

The theoretical curves in Figure 2.9 imply that if isotopic equilibrium is achieved between minerals during precipitation, then any pair of minerals could be used to calculate the temperature of their formation. From our mineral pairs listed in Table 2.2, we have calculated an apparent fractionation factor, according to Equation (1), then estimated the temperature of formation from Figure 2.9A. It must be stated that although we have used mineral pairs that have co-precipitated, we have not observed any unequivocal equilibrium textures. The apparent fractionation factors for each pair give results that are consistent overall with fluid inclusion work for formation temperatures (Kitto, 1994), however, there are two clear inconsistencies:

Fluid inclusion isotope work by Kitto (1994) demonstrated that the fluid temperatures in the Main Sulfide Stage cooled from 350 °C at depth to 200 °C, at upper levels of the mine. However, our pyrite-pyrrhotite pairs from the Central Federal Mine Area (RB027) yield temperatures 180 °C cooler than those from historic open-pits (40612-17 and 40612-21) which are further away from the intrusion at a stratigraphically higher position; the opposite of that indicated by fluid inclusion work. The sample from deepest in the mine (RB017) from the Rendeeps yields a temperature of 160 °C from co-precipitated chalcopyrite-pyrrhotite pairs, again about 200 °C lower than homogenisation temperatures of fluid inclusions.

Furthermore, mineral pairs from the same sample give very different temperatures. For example, RB013 yield temperatures from 70 °C to 510 °C, for siderite, pyrite and pyrrhotite from the same paragenetic stage. The 70 °C result is not supported by other evidence; the lowest temperatures recorded in fluid inclusions at Renison is ~100 °C for the Late Base Metal and Carbonate stages of mineralisation.

This raises an interesting dichotomy of results, that at the deposit-scale, Fe isotopes fractionate between magmatic hydrothermal minerals and fluids in a distribution predicted by theoretical equilibrium factors, yet natural mineral-mineral pairs yield highly variable results (e.g. Dziony et al., 2014), limiting the use of Fe-isotopes as a geothermometer at the present time. It is possible that other mineral deposition processes, for example, wall rock reaction, may overprint the fractionation controlled by temperature.

Detailed in-situ studies using micro-drilling (e.g. Gagnevin et al., 2012), UV femtosecond laser (e.g. Horn et al., 2006; Dziony et al., 2014), and Secondary Ion

mass Spectrometry (SIMS; e.g. Marin-Carbonne et al., 2011) have shown variability of >1‰ within individual zoned minerals. Studies with high degrees of spatial resolution may be needed to resolve fractionation at the mineral scale as a result of processes such as wall-rock interaction, and repeated dissolution-precipitation reactions.

Table 2.2 Apparent iron isotope fractionation between mineral pairs. We used calculated temperatures of formation using the theoretical fractionation curves in Figure 2.9A.

Sample Number		Δ57 Fe (‰)	Calculated T
		Δpy-po	
40612-17		1.46	490
40612-21		1.46	490
RB013		1.39	510
RB027		2.47	310
	average	*1.695*	*430*
		Δpy-cpy	
RB027		1.31	370
		Δcpy-po	
RB027		1.16	230
RB030		0.6	440
RB024		1.835	130
RB017		1.609	160
	average	*1.301*	*210*
		Δsid-po	
RB013		0.99	70
		Δpy-sid	
RB013		1.4	450

2.5.4 Comparison of Renison mineral compositions with Xinqiao skarn and the effect of magma oxidation state on magmatic-hydrothermal minerals

The literature contains other case studies of Fe isotope data from magmatic-hydrothermal ore deposits as diverse as seafloor hydrothermal vents (e.g. Rouxel et al., 2004), hydrothermal iron oxide (Markl et al., 2006) and base metal deposits (Gagnevin et al., 2012), porphyry coppers and skarns (e.g. Graham et al., 2004; Wang et al., 2011) and magmatic Ni-Cu sulphides (Fiorentini et al., 2012). Of these

case studies, Xinqiao is the only case study where both the source/host plutons and magmatic-hydrothermal minerals have been analysed. This deposit provides an interesting contrast with Renison, because of the different petrology and geochemistry of the associated plutons.

The Xinqiao Cu-Fe-S-Au deposit is associated with the Jitou quartz-monzodiorite ('QMD') stock, emplaced during Mesozoic late syn- to post-orogenic high-K, calc-alkaline magmatism (Xu and Zhou 2001; Wu et al., 2008). The mineralogy of plagioclase-alkali feldspar-amphibole-quartz with accessory magnetite (Wu et al., 2008) indicates a hydrous, oxidised magma. The deposit comprises a carbonate replacement skarn and a stratiform sulphide deposit. We consider only the minerals reported to be sourced from the skarn at Xinqiao, so as to compare only higher temperature magmatic-hydrothermal minerals between the two deposits. Xu et al. (2001) report 2 populations of fluid inclusion homogenisation temperatures; one group formed at temperatures of 380-420 °C and a second population at 220-300°C. Thus the temperatures of formation of sulphides in both Renison and Xinqiao are very similar.

Figure 2.10 illustrates comparison of our Renison data for magnetite, chalcopyrite and pyrite with the Xinqiao data. There are clear differences in iron isotope compositions between minerals from each deposit, with chalcopyrite, pyrite and magnetite from Renison being isotopically heavier than those from Xinqiao.

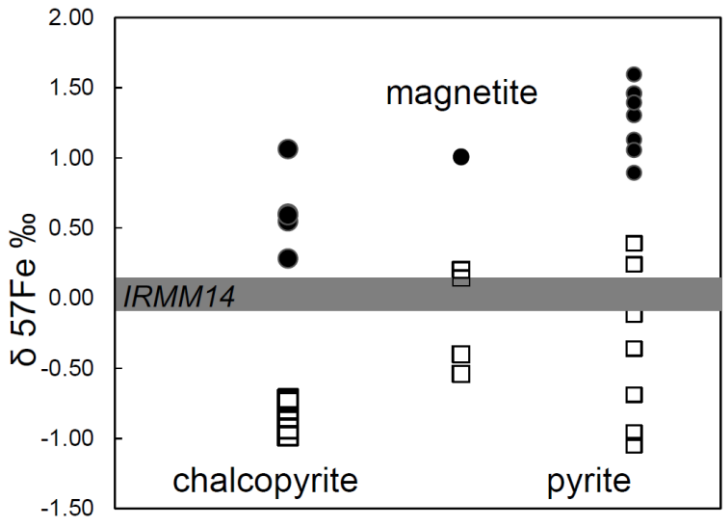

Figure 2.10 Comparison of iron isotope compositions of pyrite, magnetite and chalcopyrite between the Renison deposit (closed circles) and Xinqiao deposit (open squares).

The Jitou QMD, hosting the skarn deposit (Wang et al., 2011), has $\delta^{57}Fe$ compositions of −0.15‰ to 0.29‰, and is therefore isotopically lighter than the Renison granite (0.27‰ - 0.43‰). The difference in isotopic composition between the two intrusions can be explained qualitatively by the control exerted by the crystallisation of magnetite, as follows:

The behaviour of iron isotopes is governed in part by the redox state of the iron; Fe (III) bearing phases fractionate the heavier isotopes, and Fe (II) bearing phases fractionate the lighter isotope (Schauble, 2004). We therefore expect that an oxidised magma crystallising magnetite—which has 2x Fe (III) and 1xFe (II)—will remove more ^{56}Fe and ^{57}Fe from the melt than ^{54}Fe, resulting in a melt with isotopically light composition. Sossi et al. (2012), have demonstrated this control that magnetite crystallisation exerts on the Fe-isotope composition of a melt, in their study of a differentiating dolerite sill acting as a closed system. It is also likely that lack of differentiation also plays a part, as monzodiorites have significantly less SiO_2 (<70 wt %) than that of highly fractionated felsic magmas (70-77 wt %)

In contrast, in an S-type granite, both anatexis and fractional crystallisation mechanisms may control the isotopic composition; these have been examined by Foden et al. (2014, submitted). The petrogenesis of S-type granites is dominated by partial melting of protoliths containing reduced minerals such as sulphides or graphite (e.g. Clemens, 2003). Telus et al. (2012) have shown the effects of partial melting by their analyses (reported as $\delta^{56}Fe$) of leucosomes (+0.246 ± 0.031‰ to +0.480 ± 0.029‰) in migmatites which are systematically heavier than the melanosomes (+0.077 ± 0.029‰ to+0.302 ± 0.028‰). The difference between melanosome-leucosome pairs ranges from +0.038 ± 0.056‰ to +0.196 ± 0.058‰. If such a melt is transported to shallow levels and undergoes fractional crystallisation, then we would expect the melt to remain isotopically heavy because the main Fe-bearing minerals are Fe(II)- bearing minerals such as biotite (Paveseti et al., 2007; Vigneresse, 2007), garnet and ilmenite, which preferentially incorporate the light isotope. Although thermal diffusion cannot be discounted, given the models of pluton assembly by discrete additions of magma (e.g. Petford et al., 2000, Vigneresse, 2007), the vast bulk of the Renison granite is unexposed, which precludes detailed examination of contacts and relationships of any discrete magma batches which may be present.

Our interpretation is that the Renison ore minerals are isotopically heavier than those from Xinqiao because the magmatic fluid exsolved from an isotopically heavy,

reduced S-type magma, rather than an isotopically light, less differentiated oxidised I-type magma. The range of isotopic ratios within our data is -1.0 ± 0.09‰ for the lightest pyrrhotite to +1.59 ± 0.01‰ for the heaviest pyrite, which is much larger than the range in granites (0.0 to +0.6‰; Foden et al, submitted; Poitrasson and Freydier, 2005), so it is likely that additional mechanisms have operated.

2.6. ORE FLUIDS AS ISOTOPICALLY LIGHT RESERVOIRS

The Jitou QMD, hosting the skarn deposit, is isotopically heavier than chalcopyrite-pyrite and magnetite. Wang et al. (2011) used these data to support the “light fluid” hypothesis put forward by Poitrasson and Freydier (2005) and Heimann et al. (2008), that Fe(II)-Cl rich fluids exsolved by magmas are isotopically lighter than the melt, because the valence state of Fe in Fe-Cl fluids is almost always Fe(II) (Simon et al., 2004; Saunier et al., 2011 and references therein), therefore will preferentially fractionate the light isotope. Minerals deposited from such a fluid would be isotopically lighter than the source granite.

However, at Renison, the isotopic composition of the granite is located midway between the heavy minerals (pyrite-arsenopyrite-magnetite) and the light minerals (siderite-pyrrhotite; Fig. 2.7). Our data clearly do not support the hypothesis that the first minerals in a paragenetic sequence will be isotopically lighter than the granite, although mass balance calculations to assess the contribution of host rocks, and all mineral phases to the isotopic signature of the analysed minerals, and to compute a composition of ore fluids is necessary to provide a more quantitative discussion. There is evidence from the δH/D and $\delta^{18}O$ work of Patterson et al. (1981) that the earliest fluids equilibrated with the granite at ~600C, and a review of tin deposits by Heinrich (1990) shows that this is often the case. At least on a qualitative basis, reduced melts crystallise ferrous Fe-bearing phases, leaving the heavy isotope behind in the melt. Therefore isotopic equilibration with the melt would result in an initially isotopically heavy ore fluid.

The isotopic composition of hydrothermal fluids has been measured at seafloor conditions (e.g. Sharma et al., 2001; Rouxel, et al., 2008) and experimentally at hydrothermal conditions (Syverson et al., 2013; Saunier et al., 2011). However, techniques that can routinely measure the iron isotope ratios of ore fluids contained in fluid inclusions in natural magmatic-hydrothermal minerals are still undeveloped. In-situ measurement of iron isotope compositions in fluid inclusions and zoned

minerals will shed light on processes that are difficult to unravel using an average composition of the hand-picked sample.

2.7. CONCLUSION

We have analysed magmatic-hydrothermal minerals and bulk granite from the Renison Sn-W deposit to characterise the Fe isotopic composition of minerals associated with a reduced, S-type granite. Pyrite, magnetite and chalcopyrite are isotopically heavier than pyrrhotite and siderite, results which are consistent with theoretical equilibrium fractionation factors. However, the use of iron isotopes as a geothermometer is complicated by the variability of results within single samples, and that calculated temperatures of formation are spatially inconsistent with the results from detailed fluid inclusion work.

Pyrite, chalcopyrite and magnetite from the Renison deposit, are isotopically heavier than those from the Xinqiao skarn. These results are consistent with the hypothesis that a magmatic-hydrothermal fluid exsolved from, or equilibrated with, an isotopically heavy, reduced magma could deposit isotopically heavy ore minerals. In contrast, oxidised magmas crystallise magmatic magnetite which sequesters heavy Fe, resulting in an isotopically lighter melt, and hence a lighter magmatic-hydrothermal fluid. Our results also contradict the hypothesis magmatic-hydrothermal minerals should be isotopically lighter than the source intrusion, although the overall range of isotopic compositions suggests that other mechanisms may overprint and/or enhance fractionation controlled solely by temperature.

Magmatic-hydrothermal ore deposits result from complex physicochemical interactions between magmas, fluids, and host rocks. The rapidly developing capability to measure isotope ratios at the nanometer scale may help to unravel processes at the mineral scale. More experimental data exploring mineral deposition processes at high temperatures (>300°C) such as wall-rock reaction and mineral dissolution-precipitation are also needed to calibrate theoretical fractionation curves.

Acknowledgements

This project was funded by the Institute for Mineral and Energy Resources, University of Adelaide, and is TRAX Publication Record 288. The geologists of Bluestone Tin Joint Venture at Renison are thanked for providing samples, on-site support and

discussion. The first author gratefully acknowledges K.Scheiderich, G. Halverson, P.Sossi and F. Poitrasson for their help and advice in running the Neptune MC-ICPMS. We thank A. Simon, F. Poitrasson and R. Smernik for comments that greatly improved the manuscript.

References

Bajwah, Z. U., White, A.J.R., Kwak, T.A.P., Price, R.C. (1995). The Renison granite, Northwestern Tasmania: A Petrological, Geochemical and Fluid Inclusion Study of hydrothermal alteration. Econ. Geol. 90, 1663-1675.

Beard, B. L., Johnson, C. M. (2004). Fe isotope Variations in the Modern and Ancient Earth and other Planetary Bodies. In: Johnson, C.M., Beard, B.L., Albarede, F. (Eds.), Geochemistry of Non-Traditional Stable Isotopes, vol. 55. Mineralogical Society of America, Washington, DC, pp. 319–357.

Black, L. P., McClenaghan, M. P., Korsch, R. J., Everard, J. L., Foudoulis, C. (2005). Significance of Devonian-Carboniferous igneous activity in Tasmania as derived from U-Pb SHRIMP dating of zircon. Australian Journal of Earth Sciences: an International Geoscience Journal of the Geological Society of Australia 52, 807-820.

Blanchard, M., Poitrasson, F., Meheut, M., Lazzeri, M., Mauri, F., Balan, E. (2009). Iron isotope fractionation between pyrite (FeS_2), hematite (Fe_2O_3) and siderite ($FeCO_3$): A first-principles density functional theory study. Geochim. Cosmochim. Acta 73, 6565-6578.

Blevin, P. L. (2004). Redox and Compositional Parameters for Interpreting the Granitoid Metallogeny of Eastern Australia: Implications for Gold-rich Ore Systems. Resource Geology 54, 241-252.

Blevin, P. L., Chappell, B. W. (1992). The Role of Magma Sources, Oxidation-States and Fractionation in Determining the Granite Metallogeny of Eastern Australia. Transactions of the Royal Society of Edinburgh-Earth Sciences 83, 305-316.

Candela, P. A., Holland, H. D. (1984). The partitioning of copper and molybdenum between silicate melts and aqueous fluids. Geochim. Cosmochim. Acta 48, 373-380.

Černy, P., Blevin, P. L, Cuney, M., London, D. (2005). Granite Related Ore Deposits. Econ. Geol. 100, 337-370

Clemens, J. D. (2003). S-type granitic magmas-petrogenetic issues, models and evidence. Earth Sci. Rev, 61, 1-18

Craddock, P. R., Dauphas, N. (2011). Iron Isotopic Compositions of Geological Reference Materials and Chondrites. Geostandards and Geoanalytical Research 35, 101-123.

Dziony, W., I., Horn, I., Koepke, J., Steinhoefel, G., Schuessler, J., Hotz, F. (2014). In-situ Fe isotope ratio determination in Fe-Ti oxides and sulfides from drilled gabbros and basalt from the IODP Hole 1256D in the eastern equatorial Pacific. Chem. Geol. 363, 101-113.

Eugster, H. P. (1985). Granites and Hydrothermal Ore-Deposits - a Geochemical Framework. Min. Mag. 49, 7-23.

Fiorentini, M. L., Bekker, A., Rouxel, O., Wing, B. A., Maier, W., Rumble, D. (2012). Multiple Sulfur and Iron Isotope Composition of Magmatic Ni-Cu-(PGE) Sulfide Mineralization from Eastern Botswana. Econ. Geol. 107, 105-116

Foden, J. D., Sossi, P.A., Wawryk, C. M. (2015). Fe isotopes and the contrasting petrogenesis of A-, I- and S-type granites. Lithos. 212-215, 32-44.

Gagnevin, D. B., Boyce, A. J., Barrie, C.D., Menuge, J. F., Blakeman, R. J. (2012). Zn,-Fe-and-S-isotope-fractionation-in-a-large-hydrothermal-system. Geochim. Cosmochim. Acta 88, 183-198.

Graham, S., Pearson, N., Jackson, S., Griffin, W., O'Reilly, S. Y. (2004). Tracing Cu and Fe from source to porphyry: in situ determination of Cu and Fe isotope ratios in sulfides from the Grasberg Cu-Au deposit. Chem. Geol. 207,147-169.

Heimann, A., Beard, B. L., Johnson, C. M. (2008). The role of volatile exsolution and sub-solidus fluid/rock interactions in producing high $^{56}Fe/^{54}Fe$ ratios in siliceous igneous rocks. Geochim. Cosmochim. Acta 72, 4379-4396.

Heinrich, C. A. (1990). The Chemistry of Hydrothermal Tin (-Tungsten) Ore Deposition. Econ. Geol. 85, 457-481.

Hill P. S., Schauble E. A., Shahar A., Tonui E., Young, E. D (2010). Effects of changing solution chemistry on Fe^{3+}/Fe^{2+} isotope fractionation in aqueous Fe-Cl solutions. Geochim. Cosmochim. Acta 74, 6669-6689.

Horn, I., von Blanckenburg, F., Schoenberg, R., Steinhoefel, G., Markl, G. (2006). In situ iron isotope ratio determination using UV-femtosecond laser ablation with application to hydrothermal ore formation processes. Geochim. Cosmochim. Acta 70, 3677-3688.

Huang, F., Lundstrom, C. C., Glessner, J., Ianno, A., Boudreau, A., Li, J., Ferré, E. C., Marshak, S., DeFrates, J. (2009). Chemical and isotopic fractionation of wet andesite in a temperature gradient: Experiments and models suggesting a new mechanism of magma differentiation. Geochim. Cosmochim. Acta 73, 729-749.

Ishihara S. The magnetite-series and ilmenite-series granitic rocks. (1977). Min.Geol. 27, 293–305.

Marin-Carbonne, J., Rollion-Bard. C., Luais B. (2011). In-situ measurements of iron isotopes by SIMS: MC-ICP-MS intercalibration and application to magnetite crystal from Gunflint chert. Chem. Geol. 285, 50-61.

Kitto, P. A. (1994). Structural and geochemical Controls on Mineralisation at Renison, Tasmania. PhD thesis, University of Tasmania.

Li, W., Jackson, S.E., Pearson, N. J., Graham, S. (2010). Copper isotopic zonation in the Northparkes porphyry Cu-Au deposit, SE Australia. Geochim. Cosmochim. Acta. 74, 4078-4096.

Lindgren, W. (1906). Ore deposition and deep mining. Econ. Geol., 1, 34-46.

Markl, G., von Blanckenburg, F., Wagner, T. (2006). Iron isotope fractionation during hydrothermal ore deposition and alteration. Geochim. Cosmochim. Acta 70, 3011-3030.

Patterson, D. J., Ohmoto, H., Solomon, M. (1981). Geologic Setting and Genesis of Cassiterite-Sulfide Mineralization at Renison Bell, Western Tasmania. Econ. Geol. 76, 393-438.

Pavese, A., Curetti N., Diella, V., Levy, D., Dapiaggi, M., Russo U. (2007). P-V and T-V Equations of State of natural biotite: An in-situ high-pressure and high-temperature powder diffraction study, combined with Mössbauer spectroscopy. American Mineralogist 92, 1158-1164.

Petford, N., Cruden, A. R., McCaffrey, K. J. W., Vigneresse, J.-L. (2000). Granite magma formation, transport and emplacement in the Earth's crust. Nature, 408, 669-673.

Poitrasson, F., Freydier, R. (2005). Heavy iron isotope composition of granites determined by high resolution MC-ICP-MS. Chem. Geol. 222, 132-147.

Polyakov, V. B., Mineev, S.D. (2000). The use of Mossbauer spectroscopy in stable isotope geochemistry. Geochim. Cosmochim. Acta 64, 849-865.

Polyakov, V. B., Clayton R. N., Horita, J., Mineev, D. D. (2007). Equilibrium iron isotope fractionation factors of minerals: Reevaluation from the data of nuclear inelastic resonant X-ray scattering and Mössbauer spectroscopy. Geochim. Cosmochim. Acta 71, 3833-3846.

Polyakov, V. B., Soultanov, D. M. (2011). New data on equilibrium iron isotope fractionation among sulphides: Constraints on mechanisms of sulfide formation in hydrothermal and igneous system. Geochim. Cosmochim. Acta 75, 1957-1974.

Rouxel, O., Fouquet, Y., Ludden, J. N. (2004). Subsurface processes at Lucky Strike hydrothermal field Mid-Atlantic Ridge: Evidence from sulfur, selenium and iron isotopes. Geochim. Cosmochim. Acta 68, 2295-2311.

Rouxel, O., Shanks, W. C., Bach, W., Edwards, K. J. (2008). Integrated Fe- and S-isotope study of seafloor hydrothermal vents at East Pacific rise 9-10°N. Chem. Geol. 252, 214-227.

Rustad, J. R., Casey, W. H., Yin, Q.Z., Bylaska, E .J., Felmy, A. R., Bogatko, S. A., Jackson, V. E., Dixon, D. A. (2010). Isotopic fractionation of Mg^{2+}(aq), Ca^{2+}(aq), and Fe^{2+}(aq) with carbonate minerals. Geochim. Cosmochim. Acta 74, 6301-6323.

Saunier, G., Pokrovski, G. S., Poitrasson, F. (2011). First experimental determination of iron isotope fractionation between hematite and aqueous solution at hydrothermal conditions. Geochim. Cosmochim. Acta 75, 6629-6654.

Sawka, W. N., Heizler, M. T., Kistler, R. W., Chappell, B. W. (1990). Geochemistry of highly fractionated I- and S-type granites from the tin-tungsten province of western Tasmania. In Ore-bearing granite systems; Petrogenesis and mineralising processes. H. J. Stein & J. L. Hannah (Eds). Geological Society of America Special Paper, v. 246, p. 161-179.

Schauble, E. A. (2004). Applying Stable Isotope Fractionation Theory to New Systems. In: Johnson, C.M., Beard, B.L., Albarède, F. (Eds.), Geochemistry of Non-Traditional Stable Isotopes, vol. 55. Mineralogical Society of America, Washington, DC, pp 65-111.

Schauble, E. A., Rossman, G. R., Taylor, H. P. (2001). Theoretical estimates of equilibrium Fe-isotope fractionations from vibrational spectroscopy. Geochim. Cosmochim. Acta 65, 2487-2497.

Schuessler, J. A., Schoenberg, R. and Sigmarsson, O. (2008). Iron and Lithium isotope systematics of the Hekla volcano, Iceland-Evidence for Fe isotope fractionation during magma differentiation. Chem. Geol. 258, 78-91.

Schuessler, J. A., Schoenberg, R., Behrens, H., von Blanckenburg, F. (2007). The experimental calibration of the iron isotope fractionation factor between pyrrhotite and peralkaline rhyolitic melt. Geochim. Cosmochim. Acta 71, 417-433.

Seedorf, E., Dilles, J. H., Proffett, J. M., Einaudi, M. T., Zurcher, L., Stavast, W. J. A., Johnson, D. A., Barton, M. D. (2005). Porphyry deposits: Characteristics and origin of hypogene features. Econ. Geol. 100, 251-298.

Sharma, M., Polizzotto, M., Anbar, A. D. (2001). Iron isotopes in hot springs along the Juan de Fuca Ridge. Earth Planet. Sci.Lett. 194, 39-51.

Sillitoe, R. H. (2010). Porphyry Copper Systems. Econ. Geol. 105, 3-41.

Simon, A. C., Pettke, T., Candela, P. A., Piccoli, P. M., Heinrich, C. A. (2004). Magnetite solubility and iron transport in magmatic-hydrothermal environments. Geochim. Cosmochim. Acta 68, 4905-4914.

Sossi, P. A., Foden, J. D., Halverson G. (2012). Redox-controlled iron isotope fractionation during magmatic differentiation. Contrib. Mineral. Petrol.164, 757-772.

Syverson, D. D., Borrok, D. M., Seyfried, W. E. (2013). Experimental determination of equilibrium Fe isotopic fractionation between pyrite and dissolved Fe under hydrothermal conditions. Geochim. Cosmochim. Acta 122,170-183.

Telus, M., Dauphas, N., Moynier, F., Tissot, F., Teng, F., Nabelek, P., Craddock, P., Groat, L. (2012). Iron, zinc, magnesium and uranium isotopic fractionation during

continental crust differentiation: The tale from migmatites, granitoids and pegmatites. Geochim. Cosmochim. Acta 97,247-265.

Teng, F.-Z., Dauphas, N. (2013). Iron isotopic systematics of oceanic basalts. Geochim. Cosmochim. Acta 107, 12-26.

Teng, F.-Z., Dauphas, N., Helz R. T. (2008). Iron Isotope Fractionation during Magmatic Differentiation in Kilauea Iki Lava Lake. Science 320, 1620-1622

Vigneresse, J.-L. (2007). The role of discontinuous magma inputs in felsic magma and ore generation. Ore Geology Reviews 30, 181-216.

Walshe, J. L., Halley, S. W., Anderson, J. A., Harrold, B. P. (1996). The interplay of groundwater and magmatic fluids in the formation of the cassiterite-sulfide deposits of western Tasmania. Ore Geology Reviews 10, 367-387.

Walshe, J. L., Solomon, M., Whitford, D. J., Sun, S-S., Foden, J. D. (2011). The role of the mantle in the genesis of tin deposits and tin provinces of Eastern Australia. Econ. Geol. 106, 297-305.

Walshe, J. L., Heithersay, P. S (1995). Toward an Understanding of the Metallogeny of the Tasman Fold Belt System. Econ. Geol. 90, 1382-1401.

Wang, Y., Zhu, X., Mao, J., Li, Z., Cheng, Y. (2011). Iron isotope fractionation during skarn formation - case study of Xinqiao Cu-S-Fe-Au deposit in Middle-Lower Yangtze Valley. Ore Geology Reviews 43, 194-202.

Webster, J. D. (2004). The exsolution of magmatic hydrosaline chloride liquids. Chem. Geol. 210, 33-48.

Williams, H., Lee D. C, Levasseur, S., Teutsch, N., Poitrasson, F., Rehkamper, M., Halliday, A. N. (2002). Iron isotope composition of mid-ocean ridge basalts and mantle peridotites. Geochim. Cosmochim. Acta 66(15A): A838-A838.

Wu, G. G., Zhang, D., Di, Y. J., Zang, W. S., Zhang, X. X., Song, B., Zhang, Z. Y. (2008). SHRIMP zircon U-Pb dating of the intrusives in the Tongling metallogenic cluster and its dynamic setting. Science in China Series D-Earth Sciences 51, 911-928.

Xu, G., Zhou, J. (2001). The Xinqiao Cu-S-Fe-Au deposit in the Tongling mineral district, China: synorogenic remobilization of a stratiform sulfide deposit. Ore Geology Reviews 18, 77-94.

Statement of Authorship

Title of Paper	Iron isotope systematics from the Batu Hijau Cu-Au deposit, Sumbawa, Indonesia.
Publication Status	☐ Published ☐ Accepted for Publication ☑ Submitted for Publication ☐ Unpublished and Unsubmitted work written in manuscript style
Publication Details	Wawryk, C.M., and Foden, J.D (2017) Iron isotope systematics from the Batu Hijau Cu-Au deposit, Sumbawa, Indonesia. Submitted to Chemical Geology

Principal Author

Name of Principal Author (Candidate)	Christine Wawryk
Contribution to the Paper	Performed all sample preparation, analyses and interpretation, with the exception of petrological modelling. Wrote the manuscript and acted as corresponding author.
Overall percentage (%)	85
Certification:	This paper reports on original research I conducted during the period of my Higher Degree by Research candidature and is not subject to any obligations or contractual agreements with a third party that would constrain its inclusion in this thesis. I am the primary author of this paper.
Signature	Date 31/3/2017

Co-Author Contributions

By signing the Statement of Authorship, each author certifies that:

i. the candidate's stated contribution to the publication is accurate (as detailed above);

ii. permission is granted for the candidate to include the publication in the thesis; and

iii. the sum of all co-author contributions is equal to 100% less the candidate's stated contribution.

Name of Co-Author	John D Foden
Contribution to the Paper	Contributed to interpretation of the data, performed the petrological modelling. Assisted with manuscript editing.
Signature	Date 4 Apr. 17

Name of Co-Author			
Signature		Date	

Please cut and paste additional co-author panels here as required.

CHAPTER 3. FE ISOTOPE SYSTEMATICS FROM THE BATU HIJAU PORPHYRY CU-AU DEPOSIT, SUMBAWA, INDONESIA

Christine M. Wawryk[*,a], John D. Foden[a].

[a]*Centre for Tectonics, Research and Exploration, University of Adelaide, North Tce, South Australia, 5005, Australia*

**corresponding author. Tel: +61 8 8313 1717. E-mail address: christine.wawryk@adelaide.edu.au*

ABSTRACT

This study examines the fractionation of iron isotopes as a reflection of processes that govern the co-magmatic formation of a hydrothermal ore system of a classic porphyry copper deposit. We present iron isotope analyses, measured using multi-collector ICPMS, of magmatic intrusive rocks and coeval hypogene ore minerals from the Batu Hijau porphyry copper-gold deposit in Sumbawa, Indonesia. Isotopic analysis were made of the intrusive magmatic host rocks to the deposit, ranging from sub-volcanic andesite and quartz diorite to tonalite, and of hypogene chalcopyrite, bornite and magnetite ore mineral separates.

Iron isotope values of andesite and quartz diorite range from $\delta^{57}Fe$ = 0.17±0.05‰ to 0.26±0.05‰. The more felsic, differentiated dacite and tonalite have heavier iron isotope values ($\delta^{57}Fe$ = 0.27 ±0.08‰ to 0.32 ±0.08‰) than the intermediate and mafic rocks. Heavy iron isotopes are positively correlated with SiO_2 and negatively correlated with MgO, CaO, TiO_2 and V suggesting that crystallisation of clinopyroxene, amphibole and magnetite is the primary control on isotopic evolution of the melt. These isotopic trends are supported by thermodynamic (rhyolite-MELTS) modelling of crystal fractionation using published mineral-melt fractionation factors, and demonstrate that the isotopic evolution of the Batu Hijau melts was controlled by crystal fractionation.

Magnetite from the Batu Hijau ore deposit is isotopically heavier ($\delta^{57}Fe$ range from 0.24 ±0.14‰ to 0.74±0.14‰) than coexisting chalcopyrite ($\delta^{57}Fe$ range from -0.62 ‰ ± 0.04‰ to -0.16 ± 0.05‰) and bornite ($\delta^{57}Fe$ from -0.72 ± 0.23‰ to -0.08 ± 0.03‰), consistent with theoretical fractionation factors derived from spectroscopy. Comparison of our mineral data with data from other deposits defines a range of $\delta^{57}Fe$ values for hypogene chalcopyrite from porphyry copper deposits from -1.26‰ to 0.29‰. Models of Rayleigh type fractionation assuming an initial hydrothermal fluid

composition which is isotopically light ($\delta^{57}Fe$ between -0.5 and -0.1 ‰), produces mineral compositions that match our analytical data. The modelled isotope values are in agreement with experiments demonstrating that hypogene chalcopyrite has isotopic compositions reflecting the isotopic value of the hydrothermal fluid. However, hypogene chalcopyrite from this study is significantly lighter than values of chalcopyrite separates from the Renison tin deposit which span a range of 0.28 ±0.06‰ to 1.32 ±0.06‰. We propose that the presence or absence of pyrrhotite influences the relative differences in $\delta^{57}Fe$ values of chalcopyrite between porphyry copper and tin deposits, because of its preference for isotopically light iron, which in turn is controlled by both oxygen and sulfur redox conditions in the fluid.

Keywords: iron isotopes, redox, hydrothermal fluid, porphyry copper-gold deposits, Batu Hijau

3.1. INTRODUCTION

Previous studies have shown that magmatic differentiation in a variety of settings can fractionate iron isotopes (Poitrasson and Freydier, 2005; Teng et al., 2008, 2013; Schuessler et al., 2009; Sossi et al., 2012; Chen et al., 2014; Foden et al., 2015, Sossi et al, 2016). Granitoids containing > 70 wt% SiO_2 commonly have heavy iron isotope ratios (e.g., $\delta^{57}Fe$ ~0.3 - 0.5‰) compared to most mafic rocks that contain <55 wt% SiO_2 ($\delta^{57}Fe$ ~0.1‰; Poitrasson and Freydier, 2005; Heimann et al., 2008; Foden et al., 2015).

Foden et al. (2015) demonstrated that the fractionation of iron isotopes in evolving magmatic systems is strongly dependent on the oxidation state of the magma as well as on its mode of buffering (Foden et al., 2015). Relatively reduced magma bodies, such as the ilmenite-series granitoids (Ishihara, 1977; fO_2 ~ FMQ to FMQ-1) may fractionate to yield isotopically heavy Fe, around ~0.4 ‰ to 0.5‰ in the most evolved felsic endmembers. However, oxidised systems (fO_2 ~NNO or above) tend to show less fractionation towards heavy Fe or may even evolve towards isotopically slightly lighter endmembers. Closed (unbuffered) systems tend to evolve to heavy final fractionates, while buffered “open-system” behaviour can dampen trends towards final relative enrichment in iron isotopes. Magmatism in the Batu Hijau area is characterised by juvenile, low-K_2O calc-alkaline, sub-volcanic basaltic andesite, quartz diorite and tonalite (Foden and Varne, 1980; Garwin, 2000). The magmatic

suite thus provides an opportunity to study fractionation of iron isotopes in an oxidized (fO_2 ranges from NNO to NNO+2), differentiating calc-alkaline magmatic series.

If granitic (*s.l*) melts become fluid saturated during cooling and crystallisation, magmatic fluids are exsolved, and these fluids transport Fe and other dissolved economic metals such as Cu, Mo and Ag (e.g., Shinohara, 1994; Candela and Holland, 1984; Webster, 2004; Simon et al., 2004; Yardley, 2005; Audétat et al., 2008; Zajacz et al., 2012). These hydrothermal solutions precipitate Fe-bearing sulphide, carbonate and oxide minerals. The isotopic values of the precipitated minerals ultimately reflect; 1. The initial magmatic fractionation up until the melt became fluid –saturated, 2. The fractionation due to the partitioning of Fe between the fluid and the co-existing silicate melt, and then 3, the isotopic partitioning between the hydrothermal fluid and the co-precipitating Fe bearing oxides, sulfides and carbonates.

To investigate whether there is an observable relationship between magma oxidation state and magmatic-hydrothermal minerals, Wawryk and Foden (2015) reported iron isotope values from a Tasmanian Sn-W deposit associated with a reduced, S-type granite, and associated Fe-bearing hydrothermal sulfide and carbonate minerals. In this paper, we report iron isotope values from oxidized magmatic intrusions and associated magmatic-hydrothermal minerals from the Batu Hijau deposit. The Batu Hijau deposit is a porphyry copper-gold deposit located in an island-arc setting (Garwin, 2002).). The deposit thus provides an opportunity to study fractionation of iron isotopes where cooling and crystallising dacite to tonalite melts released hydrothermal fluids and formed an associated porphyry system. In the first part of the paper, we report δ^{57}Fe values of magmatic rocks, and assess the controls that fractional crystallisation exert on iron isotope signatures of differentiated rocks. In the second part of the paper, we compare our iron isotope analyses of hypogene magnetite and chalcopyrite at Batu Hijau to analyses of magnetite and chalcopyrite from the Renison Sn-W deposit, to assess the effect of magma oxidation state on the iron isotope values of minerals deposited in different styles of ore deposit. We also compare empirical inter-mineral fractionation factors with theoretical predictions to examine the applications of iron isotopes as a geothermometer.

3.2. DEPOSIT GEOLOGY

3.2.1 Tectonic setting and magmatic intrusions

The Indonesian Sunda Arc lies on the Eurasian plate, underthrust by subduction of the Indian Ocean plate. The Batu Hijau deposit is on Sumbawa island, at the eastern end of the arc which is formed on oceanic crust approximately 14 to 23 km thick (Barbieri et al., 1987) and records a subduction history from the early Miocene. At Sumbawa, the Indian Ocean plate is transporting the northeastern extension of the buoyant Roo Rise oceanic plateau into the subduction zone. This is inferred by Garwin (2002) to control a crustal scale arc-transverse oblique-slip fault zone, which subsequently controls the distribution of the basement volcanosedimentary succession and younger plutonic magmatic rocks. An alternative interpretation is that these NE-SW across-arc sinistral transpressional structures are controlled by the oblique convergence of the Indian oceanic plate at the subduction zone at the Asian margin. This leads to effective along arc extension and fault-block segmentation of the arc.

The Batu Hijau area (Fig 3.1A) consists of an early to mid-Miocene andesitic volcanosedimentary succession cut by several phases of igneous intrusions (Meldrum et al., 1994; Irianto and Clark, 1995; Clode et al., 1999; Garwin, 2000; 2002). The series of intrusions are: (1) mid to late Miocene hypabyssal andesites, (2) late Miocene to mid Pliocene (5.9 to 3.7Ma; U-Pb SHRIMP zircon ages; Garwin, 2000; 2002) quartz diorite (‘QD’) plutons, and late stage tonalite to granodiorite dykes and (3) porphyritic tonalite stocks and dykes (3.7 Ma; U-Pb SHRIMP zircon ages). At least three phases of equigranular quartz diorite intrusion are documented (Garwin, 2000). In the mine area, a NE-elongate stock of plagioclase-hornblende-phyric dacite (‘porphyritic dacite’) is intruded by the youngest of the equigranular quartz diorites (‘QD3’). The intrusions associated with the copper-gold mineralization in the Batu Hijau deposit consist of a series of three semi-cylindrical, nested porphyritic tonalite intrusions (Fig 3.1B) termed the Old, Intermediate and Young Tonalites (‘Batu Hijau tonalites’). Detailed mapping of intrusive contact relationships, petrography, vein density, alteration and copper grade demonstrate that the greatest vein density and bulk of the copper were synchronous with emplacement of the Old Tonalite (Clode et al., 1999).

Northwest of the deposit, hypabyssal dykes of post-mineralisation porphyritic andesite, diorite and quartz diorite cross cut the Santong diatreme breccia, and post-date the youngest mineralizing magmatic events (Clode et al., 1999). This porphyritic andesite is thus inferred to be younger than the Batu Hijau Tonalite complex (Garwin, 2002).

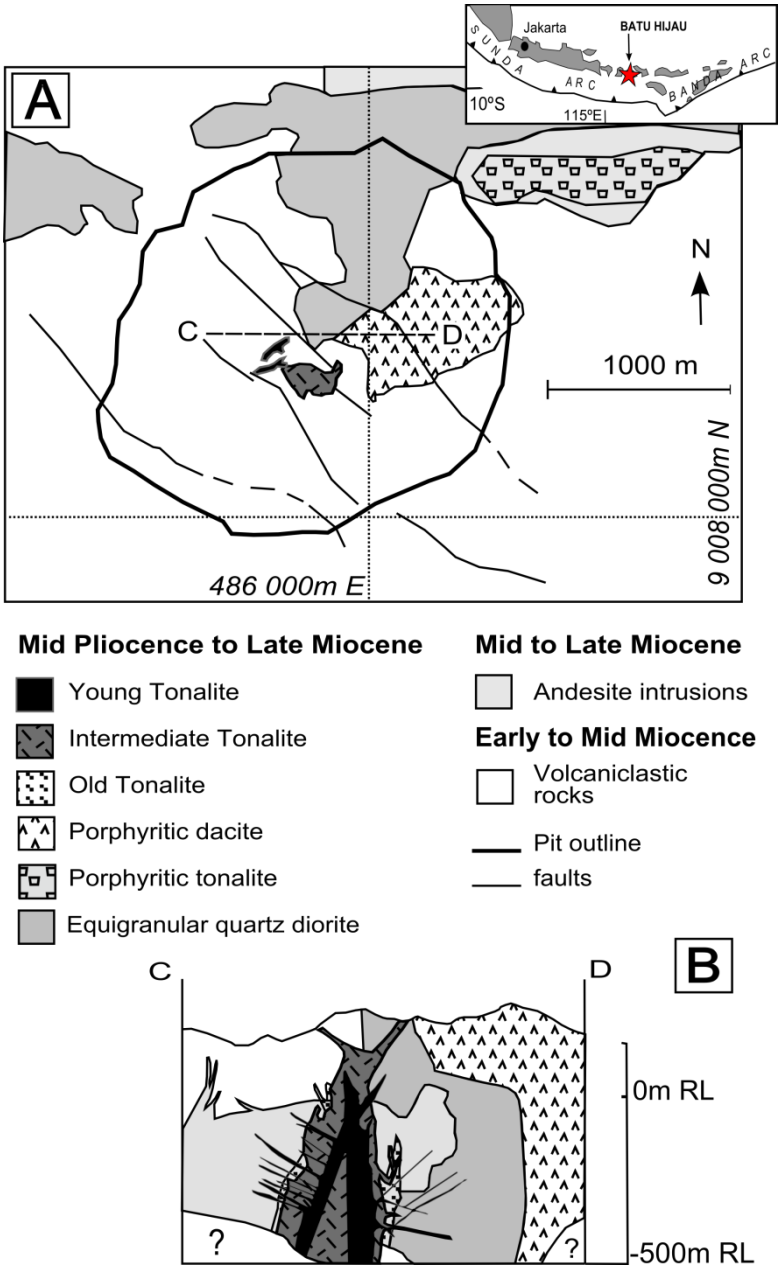

Figure 3.1 Location and geology of the Batu Hijau deposit Simplified geological map (A) and east-west cross section (B) of the Batu Hijau Cu-Au deposit (after Garwin, 2000).

Whole rock and trace geochemical data show a differentiation trend from low-K andesitic rocks through low-K to medium-K felsic intrusions (Garwin, 2000). Radiogenic isotope data (Sm-Nd, Rb-Sr, Pb-Pb), and in-situ amphibole geochemistry with hydrogen isotope analyses (Fiorentini and Garwin, 2010) demonstrate that arc

magmatism has a juvenile mantle-dominant signature, suggesting a component from asthenospheric mantle upwelling through a tear in the subducting slab, without a large input of sediment (<0.1%).

Amphibole-plagioclase thermobarometry provides evidence for the presence of a magma chamber(s) at 6-8 km below the paleosurface, with the uppermost sections of the mineralising tonalite intrusions undergoing *in situ* fractional crystallization and fluid exsolution at shallow crustal levels (~2 km; Garwin, 2000, 2002; Idrus et al., 2007; Vasyukova et al., 2013).

3.2.2 Alteration, Vein Types and Mineralogy

A central core of hydrothermal biotite-oligoclase-magnetite alteration is coeval with intrusion of the Batu Hijau Tonalite complex (Clode et al., 1999; Garwin, 2000; 2002; Idrus et al., 2007; Idrus et al., 2009). Alteration grades outwards to inner- and outer-propylitic zones, defined by chlorite-actinolite and chlorite-epidote assemblages. The inner biotite zone contains the greatest density of fracturing and quartz veins, which host hypogene copper sulfides. The principal ore minerals are chalcocite-bornite-digenite, precipitated with magnetite, in thin (<2cm), wispy, early veins which are termed “A veins” (Fig 3.2A and C; Clode et al., 1999, vein terminology of Gustafson and Hunt, 1975). The A-veins are cross-cut by wider (~2cm), regular “B” veins which have centre-lines filled with chalcopyrite and lesser bornite, also formed with magnetite (Fig 3.2C; Clode, *op cit).* Examination of polished thin sections show that bornite and chalcopyrite typically exhibit simple or amoeba-type interlocking grain boundaries, (Fig 3.2B).Equilibrium crystallization textures such as graphic intergrowth (Fig 3.2D) and triple points were observed between bornite and chalcopyrite.

3.2.3 Temperatures of ore fluids

Garwin (2000) reported homogenization temperatures (‘T_h’) of 440-513°C from brine-rich inclusions in veins that are transitional between A type and B type (’AB’ veins) in the centre of the deposit. The inference is that earlier A veins must have homogenization temperatures (T_h of >500°C. Garwin (2000) also summarises unpublished microthermometric studies and these are listed in Table 3.1. Armstrong (2012), measured T_h in brine-rich inclusions between 310 and 490 °C. However it must be noted that the study had a working limit of 500 °C. Thus the lower overall average T_h measured by Armstrong may be an artefact resulting from experimental set up, rather than the data representing a true distribution of temperatures.

The stability fields of phases within Cu-Fe-S space have been extensively studied (see Fleet, 2006, for a review). The coexistence of magnetite-bornite-(digenite)-chalcopyrite is in the Low to Intermediate Sulfidation state of Einaudi et al. (2003; their Figure 7), and these minerals precipitate together at magmatic-hydrothermal temperatures of between ~800°C and 400° C. The experiments of Simon et al. (2000) imply that for gold carried by chloride fluids to partition into Cu sulfides existing with magnetite, fluids followed a temperature path from ~620°C in A veins to ~450°C in B veins (Garwin, 2000). Furthermore, recent gas-brine interaction experiments by Blundy et al. (2015) have demonstrated the formation of magnetite-bornite assemblages at magmatic temperatures (700° to 850°C; fO_2 NNO+1.6, 120-175 MPa) providing a further possible temperature constraint for the context of our isotope data.

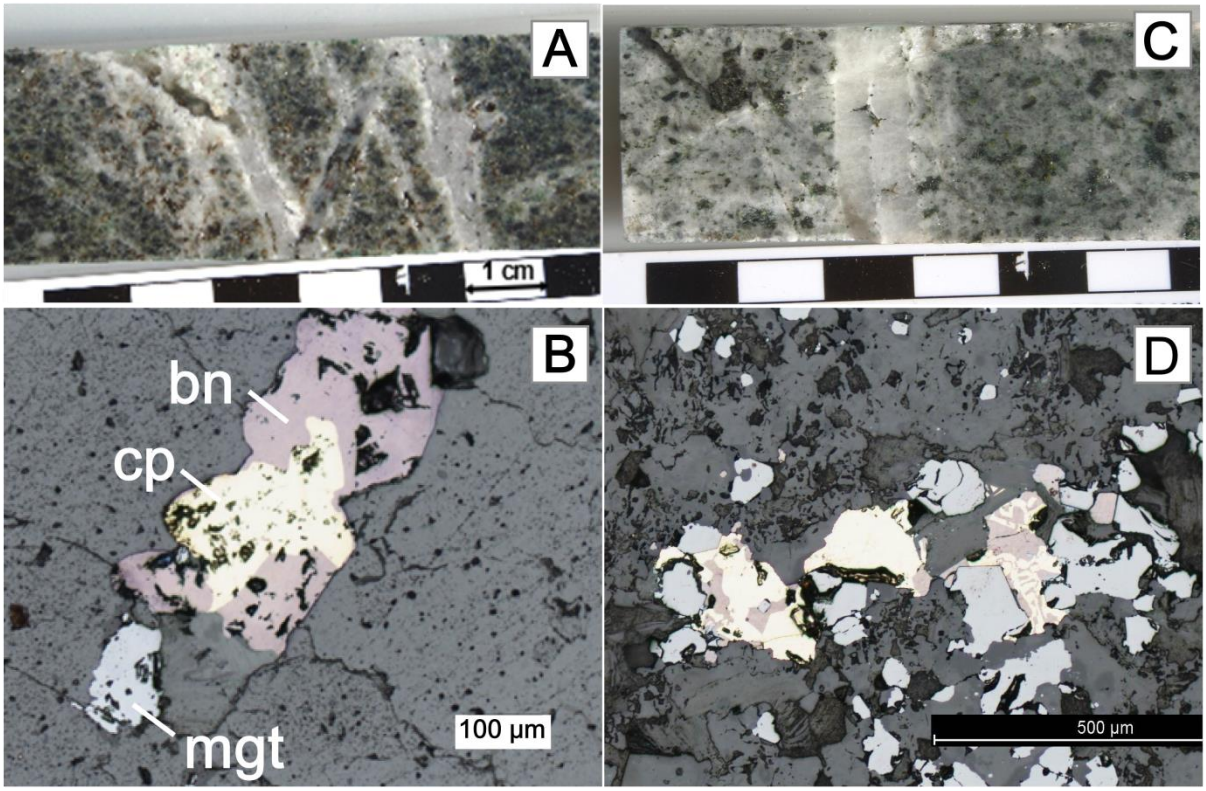

Figure 3.2 Representative photographs of Batu Hijau vein samples and sulfides for analysis: Wispy A-veins with bornite-magnetite mineralisation hosted in biotite-magnetite altered Intermediate Tonalite (sample SBD59E-652m). B: Reflected light photomicrograph of bornite-chalcopyrite-magnetite vein from sample SBD59E-652m. C: A regular B-vein (centre) with a centre-line of bornite-chalcopyrite±magnetite, in chlorite-epidote-biotite altered Intermediate Tonalite (sample SBD103-485m). Scale bar divisions are 1 cm. D: Reflected light photomicrograph of magnetite-chalcopyrite-bornite in a B vein (SBD103-184). Note graphic intergrowth of bornite-chalcopyrite to the right of centre.

Author	Nomenclature	Description	T_h (°C)	Salinity (wt% NaCl equivalent)	Vein type
Garwin (2000) reporting unpublished studies for PT Newmont Nusa Tenggara	Type III	Liquid rich, abundant daughter minerals, vapour bubble ~20 of volume	263-462	34-54	cpy-bn bearing A and AB
Garwin (2000)	Type III	As above	440-513	37-54	cpy-bn bearing AB
Armstrong (2012)	VB20H	Brine inclusion with 20% vapour and 80% liquid with a halite daughter crystal	310-490	36-48	A and AB? Vein type not specified against individual microthermometric measurements. Brine phase of immiscible fluids deposits most copper.
Armstrong (2012)	VB60	Vapour (60%)+liquid (40%)	330-490*	0-11	Represents first fluid pulse, deposits minor copper

Table 3.1 Summary of fluid inclusion studies at Batu Hijau. Abbreviations: cpy=chalcopyrite, bn=bornite, mgt=magnetite. *Homogenises to vapour, thus these temperatures are minimum estimates

3.3. SAMPLING AND ANALYTICAL METHODS

Samples of igneous rock were selected to cover the magmatic range of SiO_2 from 55-70 wt%, and were taken from milled powders previously prepared by Garwin, (2000), as samples of unaltered rock types. Unaltered hornblende tonalite and equigranular quartz diorite is defined by the presence of magmatic amphibole in textural equilibrium with plagioclase and/or biotite (Clode, 1999; Garwin, 2002; Idrus et al., 2009). The Young Tonalite exhibits magmatic biotite rimming hornblende and secondary biotite rimming magmatic magnetite. The Old and Intermediate Tonalities retain primary porphyritic texture, but show some alteration of “mafic clots” (Clode, 1999) to secondary biotite±magnetite (Clode 1999; Garwin, 2002; Idrus et al., 2009).

In order to capture the earliest, hottest magmatic-hydrothermal fluid that deposited sulfides and magnetite, we have sampled A and B veins from drill cores which intersect the centre of the deposit. As mentioned in the previous section, intergrowth textures such as triple points indicate co-precipitation of magnetite and sulfides at near equilibrium (Ramdohr, 1980) Wall rock was cut away from veins using a GEMMASTA mini rock saw, to ensure only minerals contained within quartz veins were sampled. Magnetite and sulfide phases were separated using a combination of milling, heavy liquids and magnetic separation. Minerals were examined by binocular microscope before dissolution, and purity estimated at 90%. The protocol is fully summarized in Appendix A.

3.3.1 Sample dissolution

Whole rock powders were dissolved in a mixture of concentrated HNO_3-HCl-HF overnight at 140°C. Mineral separates were dissolved in HNO_3-HCl only. Samples were then dried, following further additions of concentrated HNO_3 to drive off the HF. The samples were dissolved in 6M HCl, dried again, and finally taken up in 6M HCl and centrifuged prior to ion-exchange chromatography.

Iron in the samples was purified using Bio-Rad AG 1X4 200-400 mesh anion exchange resin, and HCl, following the method of Poitrasson and Freydier (2005). Fe was eluted using 0.05M HCl. Samples were evaporated and taken up in 2% HNO_3 for mass spectrometry.

To check the separation of transition elements such as copper from iron, the aliquots from each elution step were retained, and the base metal and iron concentration measured by ICP-OES. The data and elution graphs are detailed in Appendix B.

3.3.2 Mass spectrometry

Iron isotope ratios were measured on a Thermo-Finnigan Neptune Plus MC-ICPMS at the Research School of Earth Sciences at the Australian National University. Measurements were performed in medium resolution mode, with H-geometry skimmer cones. Sample introduction was via a glass spray chamber and Scott double pass assembly, together with a low flow, self-aspirating PFA nebulizer (between 50-70 µl/min). Samples were analysed in a 2% HNO_3 solution. Iron was set to concentration of ~4 ppm to give a signal of between 0.95 V and 1.1 V on ^{57}Fe. Ni spiking was set to a concentration of ~8 ppm, to give a signal of ~1V on ^{61}Ni.

Solution take-up time to achieve a stable signal was set at 120s. A baseline measurement was done before each solution measurement. A measurement consisted of 35 cycles of 8s integration time in static mode, with 60s washout time between each measurement. Each solution was measured a minimum of 3 times.

Data are corrected for mass bias using the Ni-spiking method of Poitrasson and Freydier (2005). All data are reported using delta notation, in units of per mil (‰) relative to the international isotopic reference standard IRMM-014:

$$\delta^{57}Fe\ (‰) = [(^{57}Fe/^{54}Fe_{sample}) / (^{57}Fe/^{54}Fe_{IRMM\text{-}014}) - 1] \times 10^3$$

Uncertainties are reported as 2 times standard deviation (2SD) of replicate analyses of the same sample. The long-term reproducibility is monitored by preparation and analysis of geostandard GSP2 with each batch of samples. Our average δ^{57}Fe for GSP2 was 0.24‰ ± 0.05‰ (95% confidence interval), within analytical error of the published δ^{57}Fe value for GSP2 of 0.23‰ reported by Craddock and Dauphas (2009). A procedural blank was prepared with each batch of 12 samples, and the average iron concentration is 3 ppb.

3.4. RESULTS

Iron isotope results are listed in Table 3.2 and illustrated in Figure 3.3. The δ^{57}Fe values of the magmatic rocks (supplied as bulk rock milled powders) range between

0.21 ± 0.05‰ and 0.32 ± 0.02‰. The iron isotopic value of the youngest igneous rock sample, the post-mineralisation porphyritic andesite is 0.17 ± 0.02‰.

The iron isotopic values of mineral separates show clear groupings (Fig. 3.3B). Bornite samples vary between -0.72 ± 0.23‰ and -0.08 ± 0.03‰. Chalcopyrite ratios vary from -0.62 ‰ ± 0.04‰ and -0.16 ± 0.05‰. Magnetite samples are iron isotopically heavier than bornite and chalcopyrite with $\delta^{57}Fe$ values between 0.24 ± 0.15‰ and 0.74 ± 0.18‰.

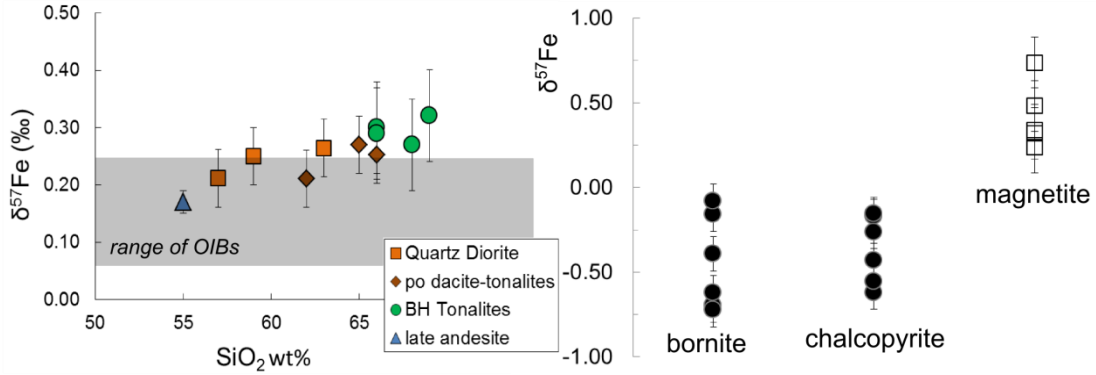

Figure 3.3 Results of iron isotope analysis from Batu Hijau. Left: Iron isotope ratios of whole rock powders from intrusive rocks around the Batu Hijau deposit, plotted against SiO_2 wt% as an index of differentiation. SiO_2 data from Garwin (2000), supplied in Electronic Annexe Table EA1. The grey shaded area is the range of OIB analysed by Teng et al. (2013) shown for comparison. Right: Fe isotope ratios of mineral separates from A and B veins at Batu Hijau. See Table 3.2 for data.

Table 3.2 Iron isotope ratios of whole rocks and magnetite, bornite and chalcopyrite separates from the Batu Hijau deposit.

Sample Number	Description	Mineral	$\delta^{57}Fe$	2sd	$\delta^{56}Fe$	2sd
97101143	porphyritic hornblende tonalite	whole rock	0.25	0.04	0.16	0.02
97101144	porphyritic hornblende tonalite	whole rock	0.21	0.05	0.13	0.01
SBD120/404m	porphyritic dacite	whole rock	0.27	0.05	0.17	0.03
99050902	Quartz Diorite (QD3)	whole rock	0.26	0.05	0.17	0.03
97101030	Quartz Diorite (QD3)	whole rock	0.25	0.04	0.16	0.04
99050502	Quartz Diorite (QD3)	whole rock	0.21	0.14	0.16	0.06
BH12	Young Tonalite	whole rock	0.30	0.08	0.21	0.03
BH7	Young Tonalite	whole rock	0.32	0.02	0.21	0.01
SBD004-157	Intermediate Tonalite	whole rock	0.29	0.11	0.22	0.05
BH4	Old Tonalite	whole rock	0.27	0.06	0.23	0.00
98070736	porphyritic late andesite	whole rock	0.17	0.02	0.13	0.02
SBD086-293bn	A vein	bornite	-0.16	0.10	-0.10	0.06
SBD086-293mgt	A vein	magnetite	0.34	0.07	0.23	0.06
SBD086-293cpy	B vein	chalcopyrite	-0.26	0.10	-0.18	0.06
SBD59E-652bn	A vein	bornite	-0.70	0.10	-0.49	0.06
SBD59E-652cpy	A vein	chalcopyrite	-0.17	0.21	-0.11	0.14
SBD59E-652mgt	A vein	magnetite	0.74	0.18	0.48	0.14
SBD086-714bn	A vein	bornite	-0.72	0.23	-0.47	0.14
SBD086-714cpy	A vein	chalcopyrite	-0.43	0.03	-0.29	0.03
SBD086-714mgt	A vein	magnetite	0.48	0.14	0.31	0.10
SBD103-379bn	AB vein	bornite	-0.39	0.16	-0.24	0.12
SBD103-379cpy	late cp	chalcopyrite	-0.16	0.05	-0.13	0.04

Sample Number		Description	Mineral	$\delta^{57}Fe$	2sd	$\delta^{56}Fe$	2sd
SBD103-184bn		B vein	bornite	-0.62	0.14	-0.43	0.06
SBD103-184cpy		B vein	chalcopyrite	-0.62	0.04	-0.44	0.00
SBD103-184mgt		B vein	magnetite	0.24	0.15	0.18	0.07
SBD103-485bn	B vein		bornite	-0.08	0.06	-0.06	0.07
SBD103-485cpy		B vein	chalcopyrite	-0.55	0.15	-0.36	0.11
SBD103-485mgt		B vein	magnetite	0.32	0.07	0.21	0.00

bn=bornite

cpy=chalcopyrite

mgt=magnetite

3.5. DISCUSSION

3.5.1 Fe-isotope evolution in melt by crystal fractionation

On the basis of whole rock and trace element geochemical data, Garwin (2000) interpreted that the differentiation of magmas emplaced in the Batu Hijau area primarily resulted from crystal fractionation. Variation diagrams for MgO, CaO, TiO_2, and V, using SiO_2 as an index of differentiation, are shown in Figure 3.4.The data are contained in electronic annexe EA1. Major oxide compositional trends to about 65 wt% SiO_2 result from crystallisation of pyroxene, amphibole and calcic plagioclase. The Batu Hijau Tonalites (>65 wt% SiO_2) crystallized amphibole, biotite and sodic plagioclase. Magnetite crystallized throughout differentiation (Garwin, 2002), reflected in the compositional trend of TiO_2 and V in whole rocks.

We observe a trend of increasing $\delta^{57}Fe$ with increasing SiO_2 (Fig 3.3A), and decreasing MgO and CaO (Fig 3.4B, D). The $\delta^{57}Fe$ then returns to lighter initial isotopic values (0.17‰) with the onset of a new cycle of andesitic magmatism. This increasing $\delta^{57}Fe$ with indices of differentiation is consistent with other studies of *in situ* magmatic differentiation (eg Schuessler et al., 2009; Teng et al., 2008; Foden et al., 2015).The interpretation by Garwin (2000) and by Vasyukova et al. (2013) of magmatic evolution through fractional crystallization is thus inferred to be responsible for the relatively isotopically heavy Fe isotopic values of the tonalities.

Our results are similar to models of isotope fractionation reported by Dauphas et al. (2014). The authors measured the force constants of Fe-O bonds in basalt, andesite and dacite glasses at magmatic temperatures. Using fractionation factors derived from different force constants for Fe^{2+} and Fe^{3+} in the melt, their model of fractional crystallisation of an anhydrous andesite melt (see their Fig 9) shows a steady increase in iron isotope values, reported as $\delta^{56}Fe$, to about 75 wt% SiO_2. Thereafter, structural properties of the melt control Fe-isotope evolution to heavy values. Our measured isotope ratios follow the same isotopic evolution trend for differentiation from andesite to tonalite.

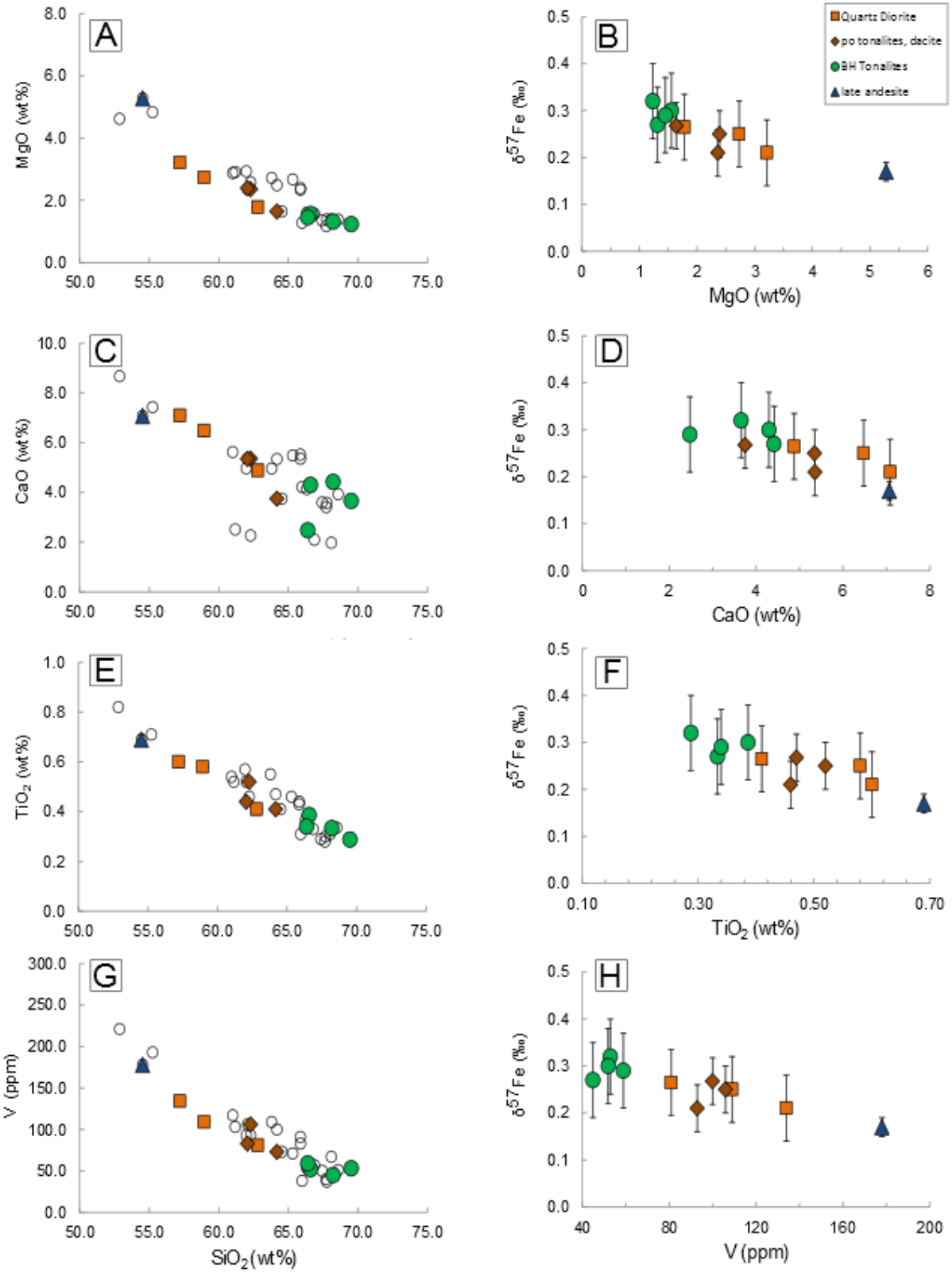

Figure 3.4 Variation diagrams of MgO (wt%), CaO (wt%), TiO_2 (wt%) and V (ppm) with SiO_2 (wt%; A,C, E and G), and variation of $\delta^{57}Fe$ (‰) with MgO wt%, CaO wt%, TiO_2 (wt%) and V (ppm; B,D, F and H). Open circles are geochemical data of unaltered igneous intrusions, from Garwin (2000) and the University of Adelaide collection. Geochemical data are provided in Electronic Annexe Table EA1, iron isotope data from Table 3.2.

3.5.2 Modelling Magmatic Fractionation Trends at Batu Hijau

In modelling the evolution of isotopically heavy A-type granite magmas, both Dauphas et al. (2014) and Foden et al. (2015) set oxygen fugacity to the fayalite-magnetite-quartz ("FMQ") buffer, i.e., $3Fe_2SiO_4 + O_2 = 2Fe_3O_4 + 3SiO_2$, and low water contents. In comparison, the magmatic rocks at Batu Hijau are hydrous and oxidized (fO_2>NNO; Garwin, 2000). Early magnetite crystallization (Garwin, 2000; 2002), restricts early Fe enrichment during differentiation thus generating the calc-alkaline differentiation trend (e.g., Fudali, 1965; Zimmer et al., 2010). We have used the amphibole-based geothermooxybarometer of Ridolfi et al. (2010), to calculate the fO_2 and pressure of the Batu Hijau magmas (see Appendix C). These calculations show that the early andesite melts had fO_2= NNO+1, and amphibole crystallization temperatures of >1000°C. This is within the range of fO_2 values for arc magmas of NNO to NNO+4 (Matjuschkin et al., 2016). The oxidation state of the melt had increased by 1 log unit when the Batu Hijau tonalite magmas were emplaced. This increase in fO_2 could result from autooxidation of the melt owing to exsolution of a magmatic volatile phase containing Cl (Bell and Simon, 2011) and degassing of O-H-S species (Burgisser and Scaillet, 2007).

The importance of intensive parameters in controlling iron isotope trends during fractional crystallisation of mafic magmas can be assessed by comparing three suites of natural samples. We have plotted the Batu Hijau data and the Hekla volcano (Iceland) data (Schuessler et al., 2009) in Figure 3.5, to compare the difference in Fe-isotopic evolution of a calc-alkaline suite with that of an anorogenic transitional alkali suite. Both the Batu Hijau and the Hekla suites were fractionated in shallow magma chambers (~8km depth; Garwin, 2000; Schuessler et al., 2009) before extraction of melts to shallow crustal levels, to form intermediate and felsic intrusives (Batu Hijau), and mafic to felsic lavas (Hekla). We have also plotted the Red Hill differentiating dolerite sill data (Sossi et al., 2012), to compare the isotopic evolution of a closed, fractionating tholeiitic system.

All three natural systems show depletion of MgO content with increasing SiO_2 interpreted to result from fractional crystallisation (Fig 3.5A) of clinopyroxenes. The obvious difference in Fe-isotopic evolution is the contrast between the closed system (Red Hill) and the two open systems (Batu Hijau and Hekla). At ~62 wt% SiO_2, the late onset of magnetite crystallisation in the relatively reduced Red Hill magma depletes the melt in Fe^{3+}, and drives the melt to isotopically light values (Sossi et al.,

2012). In contrast, the Hekla volcanics show little fractionation up to ~66 wt% SiO_2 (during evolution of basalt to dacite), above which there is a relatively rapid increase in isotopic ratios as magma evolves from dacite to rhyolite (Schuessler et al., 2009). The Batu Hijau suite shows a steady increase in $\delta^{57}Fe$ throughout the crystallisation sequence. Hydrous, mafic subduction-related magmas, such as those parental to the Batu Hijau complex, will experience more extended early crystallisation of Fe-Mg silicates and Fe-oxide at the expense of delayed appearance of plagioclase. The control that clinopyroxene crystallisation exerts on Fe-isotope value of a melt can be illustrated by the $\delta^{57}Fe$ vs CaO variation diagram (Teng et al., 2013, their Fig 7b and our Fig 3.5D).The QD3 at Batu Hijau shows early clinopyroxene crystallisation (Garwin, 2002), but crystallisation of Ca-bearing hornblende and magnesio-hastingsite also control depletion of Ca from the melt (Fig 3.5D).

We conclude that fractional crystallisation is the principal control on the evolution of $\delta^{57}Fe$ in this calc-alkaline suite, and note that our results are in agreement with those of Williams et al. (2014) who reported similar overall $\delta^{57}Fe$ for samples from the intra-oceanic Mariana Arc. This interpretation can be tested, using thermodynamic modelling. We used the thermodynamic free energy minimisation software, Rhyolite-MELTS (Gualda et al., 2012; http://melts.ofm-research.org/), to model a feasible differentiation path originating from a likely mafic parental melt. The starting composition was taken as that of the most mafic co-magmatic micro-gabbro (sample 98100301, Fig 3.5D; data in EA1), an olivine-two pyroxene-magnetite assemblage. The success of this modelling was judged by the comparison between modelled whole-rock trends and that of the Batu Hijau suite. The results were optimised by varying pressure, fO_2 and the water content of the parent magma. We achieved an excellent match between the modelled and the natural rock trends (Fig 3.6A, B) using “fractional crystallisation” mode with fO_2 = 2 log units above the quartz-fayalite-magnetite buffer (‘QFM+2’), pressure =1.2 kbar and a starting water concentration in the melt of 2.5 wt% H_2O. The modelling predicts that the starting melt composition has a liquidus temperature of 1155 ˚C with liquidus phase magnetite joined by pyroxenes from ~1115 ˚C. The model then predicts continued precipitation of magnetite with clinopyroxene + plagioclase, then plagioclase plus orthopyroxene and clinopyroxene (Fig 3.6C).The modelled crystallisation sequence is in close agreement with the detailed thin section petrography of described by Garwin (2000). The starting magmatic intensive variables in the model are similar to those estimated

using geooxythermobarometry, discussed in section 5.2. Water saturation was reached at about 4.45% H_2O (SiO_2 = 68 wt% and T = 879 ˚C).

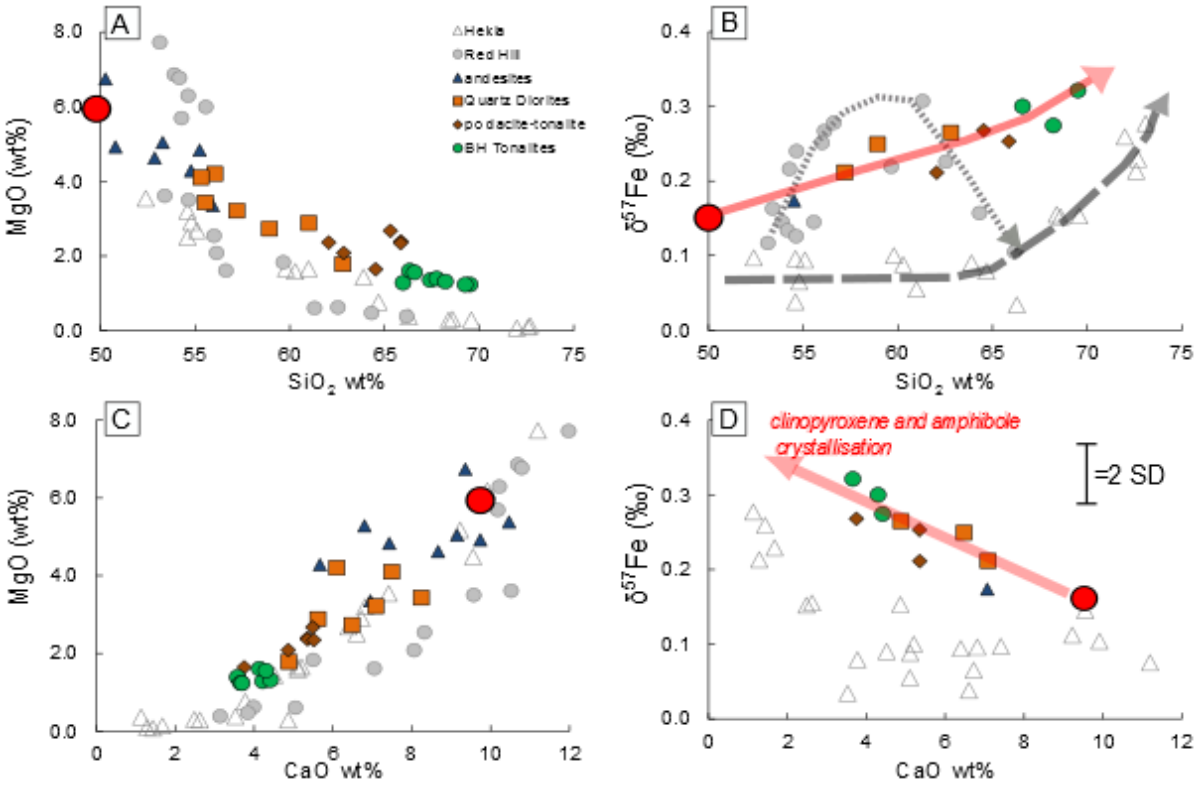

Figure 3.5 Comparison of whole rock geochemistry and iron-isotope evolution trends for Batu Hijau, Hekla and the Red Hill Dolerite Sill. Data from Batu Hijau are from this study; (symbols as in Figs 3.3 and 3.4); Hekla data (open triangles; from Schuessler et. al. 2009) and Red Hill dolerite data (closed grey circles; from Sossi et al. 2011). The large red circle shows the composition of a micro gabbro sampled by Garwin (2000; sample # 98100301, Table EA1) from the Batu Hijau area, which we have taken as the starting composition of a melt from which the Batu Hijau Tonalites evolved via fractional crystallisation A: MgO wt% v SiO_2 wt% as an index of differentiation. B: iron isotope composition against SiO_2 wt%. C: Variation diagram of MgO wt% v CaO wt% D: iron isotope composition v CaO wt%. Black bar in (D) is the 2 times standard deviation of iron isotope ratios measured in this study.

The main purpose in developing the Rhyolites-MELTS model was to use the output as a mineralogical basis to model the fractionation of the Fe-isotopes. Our modelling of isotope evolution incorporated isotope fractionation factors calculated by Sossi et al. (2012) and published theoretical constraints (Polyakov and Mineev, 2000; Polyakov et al., 2007). We used a weighted isotope fractionation factor in our model,

which accounts for both Fe^{2+} and Fe^{3+} bearing phases. For fractionation of isotopes between ferrous-iron bearing phases (pyroxenes and ilmenite) and melt, we used a $\Delta^{57}Fe_{mineral\text{-}melt}$ fractionation factor of -0.25‰ x $10^6/T_2$ (1). We assumed that magnetite is the only phase that incorporated Fe^{3+}, and used a magnetite-melt fractionation factor of 0.2‰ x $10^6/T^2$ (2). A single weighted fractionation factor was derived for each crystallisation stage by multiplying (1) and (2) by the percentage of minerals in the rock mass. Note that the $\Delta^{57}Fe_{magnetite\text{-}melt}$ value was slightly adjusted from published values to account for some substitution of ulvöspinel in magnetite in the quartz diorite rocks.The amount of ulvöspinel solid solution is important because the $\Delta^{57}Fe_{magnetite\text{-}melt}$ values change as a direct function of the activity of magnetite in solid solution, declining from positive to negative values as the amount of Ti substitution (as ulvöspinel) increases (Sossi et al., 2012). Based on petrographic and microprobe results of Garwin (2000), magnetite at Batu Hijau has generally low ulvöspinel content, ranging from <2 mol% in micro gabbro and basaltic andesite, to < 1 mol% in dacites and tonalities. There is more variability in the quartz diorites, with ulvöspinel content of magnetite varying between 1 and 17 mole%. But generally, we would expect that our $\Delta^{57}Fe_{magnetite\text{-}melt}$ should remain virtually unchanged during crystallisation.

Results of the Rhyolite-MELTS modelling are shown in Figure 3.6D. The predicted $\delta^{57}Fe$ achieved a very close fit to the measured variation of $\delta^{57}Fe$, taking the most mafic Batu Hijau micro gabbro as a starting composition with a $\delta^{57}Fe$ value of 0.15‰. The trend can be explained in terms of the crystallisation sequence of minerals, seen in Fig 3.6C. First, when magnetite alone is crystallising at SiO_2 between 50 and 52 wt%, the heavy isotope is removed from the melt, and the $\delta^{57}Fe$ value of the melt gets lighter. Then pyroxene co-crystallises with magnetite at 1115 $^{\circ}$C, followed by an interval of plagioclase-clinopyroxene-magnetite crystallisation. At this point, the $\delta^{57}Fe$ of the melt starts to get heavier, because the abundant Fe^{2+} bearing silicates remove the light isotope from the melt at a rate much greater than the rate at which 2-3% magnetite can remove the heavy isotope. Thus, the calculated bulk weighted fractionation factors are always negative, leading to the observed general trend of

^{57}Fe-enrichment.

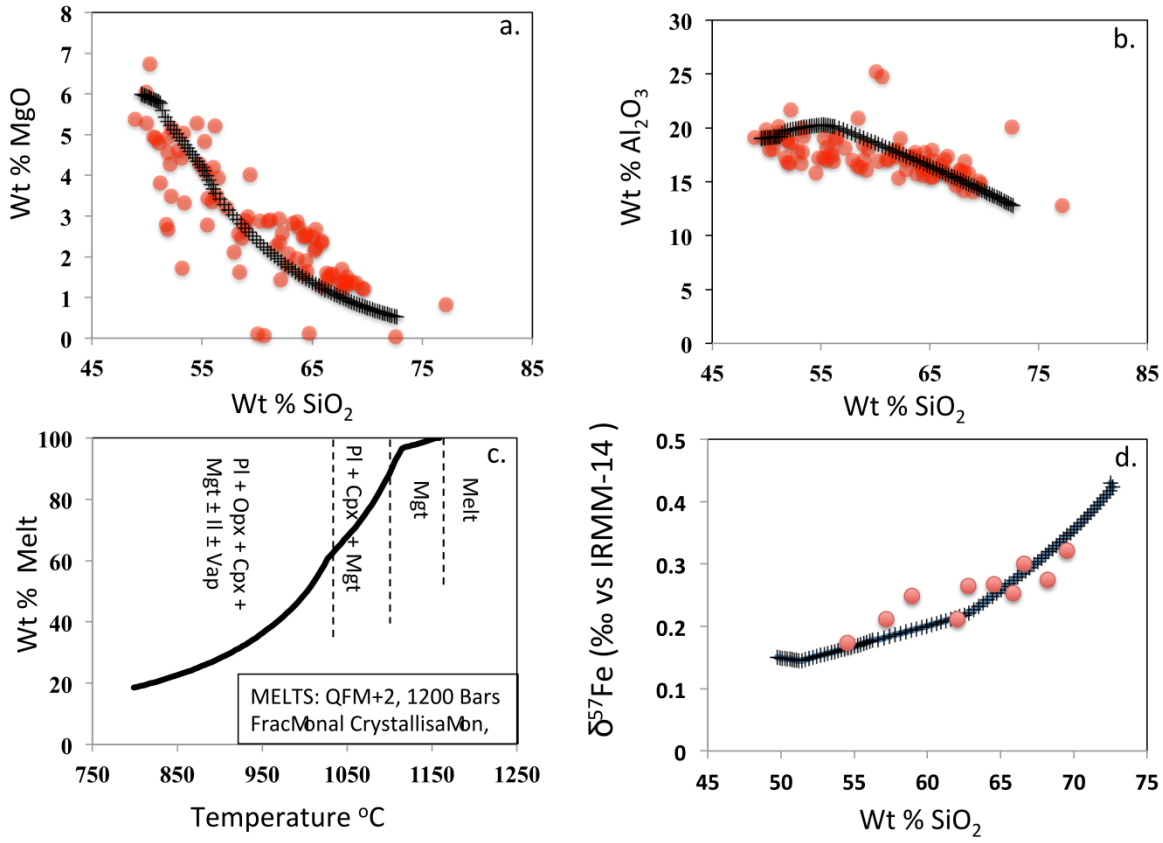

Figure 3.6 Results from thermodynamic modelling of magmatic evolution of the Batu Hijau suite by fractional crystallisation, using Rhyolite-MELTS (Gualda et al., 2012; http://melts.ofm-research.org/) software. The model assumed fractional crystallisation at fO_2 = QFM +2, at 1.2 kbar pressure and that the parental mafic magma (sample # 98100301, Table EA1) had 2.5wt% H_2O. A and B. show the modelled liquid trend (at 4 °C cooling intervals) superimposed on the Batu Hijau whole rock trends. C. shows the temperature v. wt% melt variation generated by the model, and modelled appearance of magmatic minerals D. shows measured variation of δ^{57}Fe in the Batu Hijau samples and the modelled trend, which assumed the initial parent magma had δ^{57}Fe = 0.15‰. Average error of the iron isotope measurements is ±0.07‰. See text for details of the fractionation factors used. Abbreviations: Mgt=magnetite, Pl=plagioclase, Cpx=clinopyroxene, Opx=orthopyroxene, Il=ilmenite, Vap=vapour

3.5.3 Mineral-mineral fractionation in hydrothermal quartz veins

Theoretical considerations of Fe-isotope fractionation (e.g., Schauble, 2004) predict that heavy isotopes are incorporated into Fe^{3+}-bearing minerals, or where Fe occupies coordination sites with the shortest, stiffest chemical bonds. An alternative

way of writing these predictions results from the consideration of crystal chemical controls on fractionation presented by Young et al. (2015), i.e., 1) heavy isotopes concentrate where coordination number is low, and 2) heavy isotopes concentrate where valence is high. Therefore magnetite, with its inverse spinel structure, will incorporate heavy iron isotopes because half of the Fe^{3+} ions are located in tetrahedral coordination (Fleet, 1981).

In both bornite and chalcopyrite, Fe is in the 3+ state (Goh et al., 2006), thus similar isotopic values are unsurprising. However, these minerals are both isotopically lighter than magnetite, despite the similar oxidation state. Fe also has similar coordination number in the sulfide minerals; chalcopyrite has Cu and Fe in IV-fold coordination with S (Mikhlin et al., 2004) and high bornite (the polymorph stable above ~235 °C) has metals in VI-fold coordination in the S lattice (Mikhlin et al., 2005). The covalent nature of the Fe-S bonds in these minerals result in electron sharing, so that Fe valence is between Fe^{2+} and Fe^{3+} (Goh et al., 2006) which may be a possible explanation for why magnetite is isotopically heavier than sulfides.

3.5.3.1 Iron isotope fractionation between magnetite and iron-copper sulfides

An apparent fractionation factor between magnetite and chalcopyrite can be calculated according to:

$$\Delta^{57}Fe_{mgt\text{-}cpy} = \delta^{57}Fe_{mgt} - \delta^{57}Fe_{cpy} \quad (1)$$

If the experimentally determined fractionation factors for magnetite (Polyakov et al., 2007), and chalcopyrite (Polyakov and Soultanov, 2011) are used to predict a fractionation curve (shown by the dashed red line in Fig 3.7) we would expect a fractionation at 450 °C of 0.40‰. However, using our 4 magnetite-chalcopyrite pairs, we calculate magnetite-chalcopyrite fractionation factors of 0.86 ± 0.16‰, 0.87 ± 0.17‰, 0.91 ± 0.14‰ and 0.91 ± 0.0.28‰ (Table 3.3). These four points give a range of temperatures from 200 to 210 °C, significantly lower than temperatures indicated by fluid inclusion homogenization temperatures and ore petrography summarized in section 2.3. This contradicts the many studies of A veins in other porphyry copper deposits, which show hypogene formation temperatures of ~600 °C (Seedorff et al., 2005). Notably, a temperature of formation of 600 °C is obtained when our measured results are compared to the theoretical fractionation curve calculated using a factor for magnetite obtained by Mössbauer Spectroscopy (Polyakov and Mineev, 2000;

solid blue line in Fig 3.7). This temperature is more consistent with the fluid inclusion results of Garwin (2000).

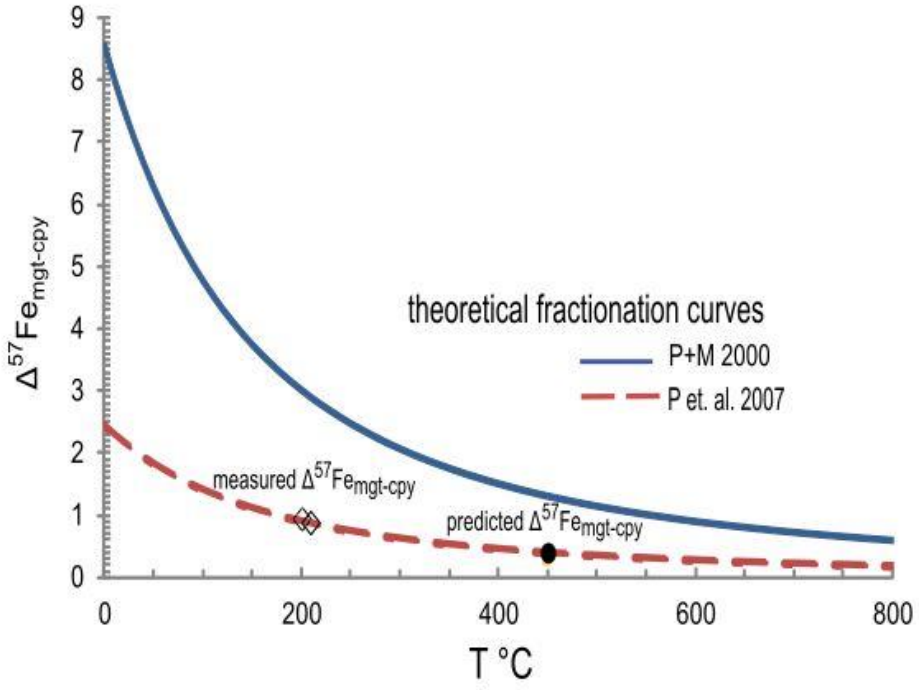

Figure 3.7 Comparison between empirical fraction factors for iron isotopes between magnetite and chalcopyrite at Batu Hijau measured in this study (open diamonds), and published theoretical fractionation curves, as a function of temperature. The solid blue theoretical curve is calculated from Polyakov and Mineev ("P+M"; 2000), and the red dashed curve is calculated from Polyakov et al. ("P et. al."; 2007). The solid circle is the equilibrium fractionation between magnetite and chalcopyrite expected at 450 °C.

This discrepancy perhaps points to the difficulty of applying experimental and spectroscopic fractionation factors, which apply to pure minerals phases, to natural systems where solid solution is common. Alternatively, a simple explanation for the difference between the predicted and measured $\Delta^{57}Fe_{mgt-cpy}$ values may be that minerals were not initially deposited at equilibrium, and therefore a kinetic fractionation process predominates. Furthermore, mineral-mineral isotope fractionation may be overprinted by fluid-mineral fractionation effects. The experimental work of Hill et al. (2010) demonstrated that the number of chloride ligands complexing Fe ions in solution, and coordination geometry, can cause significant iron isotope fractionation. We qualitatively discuss the isotope fractionation between magnetite and Fe-bearing aqueous species in the following section.

Sample	Apparent fractionation (‰)		
	$\Delta^{57}Fe_{mgt-cpy}$	$\Delta^{57}Fe_{bn-cpy}$	$\Delta^{57}Fe_{mgt-bn}$
SBD086E-293			0.50±0.12
SBD086E-714	0.91±0.14	-0.29±0.23	1.21±0.27
SBD103-184	0.86±0.16	0.00±0.15	
SBD103-379		-0.23±0.17	
SBD103-485	0.87±0.17	0.47±0.16	
SBD59E-652	0.91±0.28	-0.53±0.23	1.43±0.21

Table 3.3 Empirical calculations of fractionation factors for magnetite-chalcopyrite, bornite-chalcopyrite and magnetite-bornite mineral pairs, using δ^{57}Fe ratios measured by MC-ICPMS. Mineral abbreviations as in Table 3.2

3.5.4 The effect of magma oxidation state and fluid exsolution

The association that magma oxidation state exerts on metallogeny is well documented (e.g., Ishihara, 1977; 1998; Blevin, 2004; Czerny et al., 2005; Sillitoe, 2010). Hydrous arc magmas with fO_2 between NNO and NNO+4 are the source of porphyry-style Cu ± Au ± Mo deposits (e.g., Seedorff et al., 2005; Sillitoe 2010). By contrast, reduced, highly differentiated silicic magmas with $fO_2 \leq$ FMQ may give rise to Sn-W deposits (e.g., Blevin, 2004; Czerny et al., 2005). However, at present, the fractionation of iron isotopes between magmatic-hydrothermal fluids and co-existing silicate melt is not well understood. In the next section, we briefly review published models and experimental constraints, and compare them to the isotopic values of our natural mineral samples.

3.5.4.1 Review of theoretical and experimental data

Fe is transported in magmatic-hydrothermal fluids as chloride complexes (eg Webster 2004), in the Fe^{2+} oxidation state (eg Simon et al., 2004). It was thus postulated by Poitrasson and Freydier (2008) and Heimann et al. (2008), that light iron isotopes would be fractionated into a Fe-Cl bearing magmatic-volatile phase, and the pluton would retain a residual isotopically heavy signature Heimann et al's

model, using Fe solubility and a mass balance approach, concludes a fluid would be isotopically lighter by ~0.4‰ than the magnetite with which it had equilibrated.

However, three-isotope technique experiments conducted by Bilenker (2015) contradict the models of Heimann et al, (2008), and demonstrate the complex interaction between fluids, melts and magnetite. The following fractionation factors at 800 °C, reported as $\Delta^{56}Fe$, were calculated; $\Delta^{56}Fe_{mgt\text{-}fl} = 0.75‰ \pm 0.08‰$, $\Delta^{56}Fe_{mgt\text{-}melt} = 0.95 \pm 0.05‰$ and $\Delta^{56}Fe_{melt\text{-}fluid} = -0.2 \pm 0.07‰$. The melt-fluid fractionation factor showed that the heavy iron isotope partitioned into the fluid, as a result of tetrahedral coordination of Fe in the $FeCl_4^{2-}$ complex, compared to octahedral coordination in the melt. Bilenker's data also showed that magnetite is isotopically heavier than both the melt and fluid phases.

However, a second experiment which equilibrated a fluid of 10 wt% $NaCl_{equivalent}$ with magnetite yielded negligible fractionation factors between magnetite and fluid. Fractionation factors of $\Delta^{56}Fe_{mgt\text{-}fl} = 0.1 \pm 0.09‰$ and $\Delta^{57}Fe_{mgt\text{-}fl} = 0.14 \pm 0.13‰$ were calculated. Bilenker posited that the difference in $\Delta^{56}Fe_{mgt\text{-}fl}$ between the 2 experiments resulted from chlorinity.

Sossi and O'Neill (2016) investigated the effect of coordination number and oxidation state of Fe on the isotopic fractionation between minerals at 800 °C. A fractionation factor between magnetite and fluid was calculated, of $\Delta^{57}Fe_{mgt\text{-}fl} = 0.44‰$, a noticeably larger fractionation factor than that measured by Bilenker (2015) at the same temperature and similar salinities, perhaps owing to the difference in pressure at which the experiments were conducted (10kb, whereas Bilenker, 2015, worked at 1 and 1.5kb) Nevertheless, both experiments predict that the presence of magnetite results in an isotopically light fluid at magmatic temperatures.

3.5.4.2 Comparison of natural samples

In our previous paper (Wawryk and Foden, 2015) we hypothesized that magmatic-hydrothermal fluids equilibrated with a melt have iron isotope values that reflect the value of the source magma. The iron-bearing hydrothermal minerals precipitated from this fluid should in turn have $\delta^{57}Fe$ values that reflect the values of this fluid, modified by the temperature-dependent fractionation factors. We compare iron isotope ratios of igneous rocks, and sulfide/oxide mineral separates from different "end members" of the magma oxidation state spectrum. Iron isotope analyses of chalcopyrite separates from oxidized, porphyry deposits have been reported for

Grasberg (Graham et al., 2004) and Northparkes (Li et al., 2010). We have included isotope data from early biotite/potassic alteration zones in the deposits, so as to compare as far as possible sulfides deposited at similar temperatures. Minimum temperatures of magmatic-hydrothermal ore fluids are based on fluid inclusion studies, and are tabulated in Table 3.4.

Deposit	**Minerals analysed**	**Minimum fluid temperatures**	**References for temperatures**
Batu Hijau	mgt, bn, cpy	>500 to 330 °C	Garwin (2000), Armstrong (2012)
Grasberg	cpy, py	580-380 °C	Meinert et al. (2003;from Big Gossan)
Northparkes	cpy	~550-400 °C	Lickfold et al. (2003)

Table 3.4 Fluid temperatures, based on fluid inclusion studies, of porphyry Cu-Au deposits that have been sampled for iron isotope analysis in the literature, and this study. Mineral abbreviations as in Table 3.2.

Iron isotope data for granite and mineral separates from the Renison Sn-W deposit were reported by Wawryk and Foden (2015). The Renison deposit is a carbonate replacement Sn-W deposit whose ore fluids were derived from a reduced, ilmenite-bearing biotite granite (*sensu.stricto*). Magnetite and chalcopyrite were sampled from ore assemblages in proximity to the intrusion, where minimum temperatures of deposition range from >400 to 300 °C (Paterson, 1981; Kitto, 1994).

A comparison of $\delta^{57}Fe$ of intrusive rocks, magnetite and chalcopyrite from Batu Hijau and other porphyry Cu and the Renison Sn-W deposits is illustrated in Figures 3.8 and 3.9. Average isotopic values are 0.35‰ for Renison granite and 0.25‰ for the Batu Hijau intrusives, consistent with Foden et al's (2015) observation that differentiated S-type granites tend to heavier isotopic values compared to more oxidized I-type granite. These averages are plotted on Figure 3.9 for comparison, with data from analysis of mineral separates. It is clear that chalcopyrite from Batu Hijau has isotopic values identical to those from Northparkes and Grasberg.

However, chalcopyrite and magnetite from the Renison deposit are isotopically heavier that those from Batu Hijau.

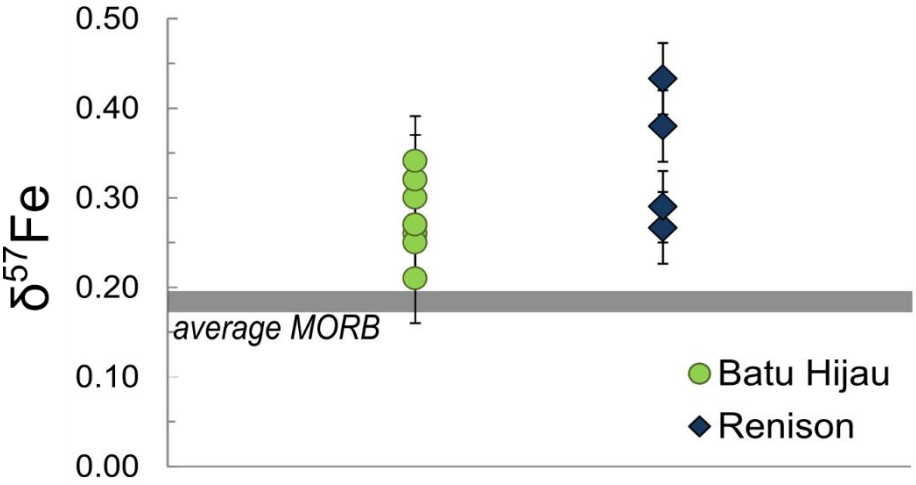

Figure 3.8 Iron isotope compositions of intrusions associated with magmatic-hydrothermal mineral deposits . Data from this study and Wawryk and Foden (2015)

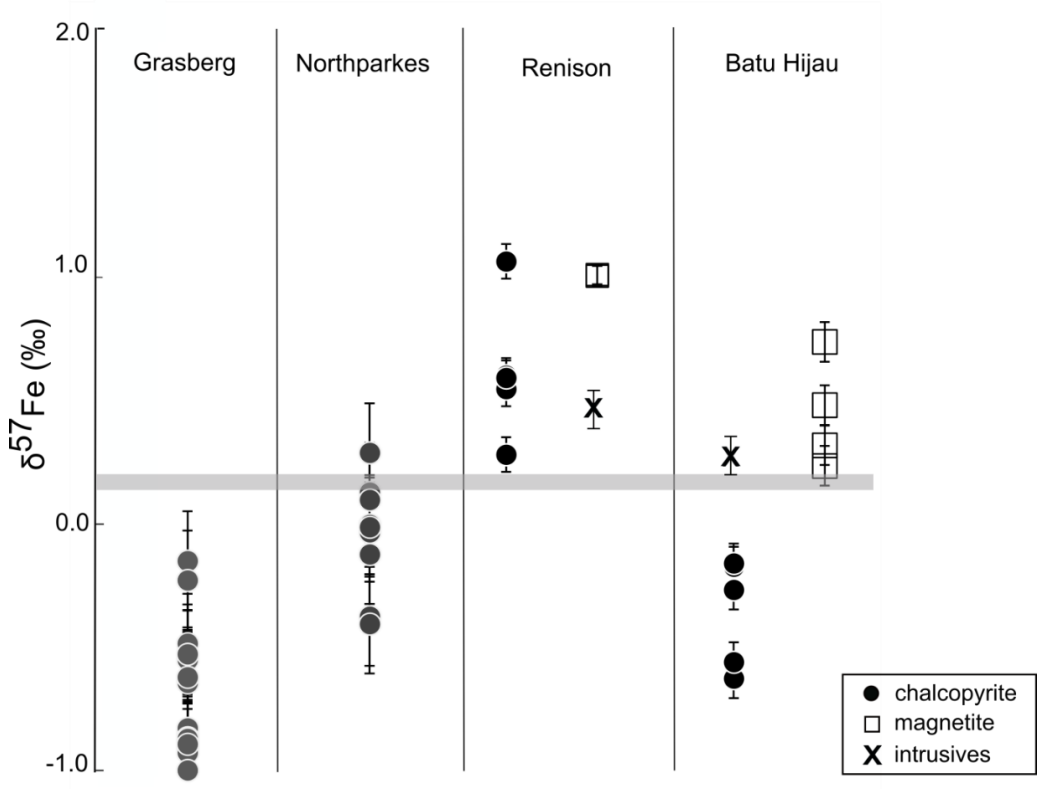

Figure 3.9 Fe isotope values of chalcopyrite, magnetite and average Fe isotope values of intrusive rocks from the Batu Hijau and Renison deposits. The shaded area is the average isotopic composition of MORB (Teng et al. 2013) for comparison. Northparkes data from Li et al. (2010). Grasberg data from Graham et al. (2004). Renison data from Wawryk and Foden (2015), Batu Hijau data from this study. No data from intrusive rocks or magnetite separates were reported from Grasberg and Northparkes deposits.

The prediction from theoretical fractionation factors is that ^{57}Fe isotopes would fractionate preferentially into pyrite>magnetite>chalcopyrite>siderite ~ pyrrhotite (Polyakov and Mineev, 2000; Polyakov et al., 2007, Polyakov and Soultanov, 2011). The sulfide-oxide mineral assemblages precipitated in ore deposits are a function of both fO_2 and fS_2 (Hemley et al., 1992 and many others), as well as temperature, pressure and presence or absence of ligands such as Cl^- (Reed and Palandri, 2006 and references therein). Mineral stability as a function of fO_2, fS_2 and temperature are shown in Figure 3.10, with the main mineral assemblages at both Renison and Batu Hijau indicated on the diagram. The diagram illustrates the inter-dependence of both sulfur and iron redox state in magmatic-hydrothermal fluids on the formation of minerals. In particular, wide variation in fS_2 at a given fO_2 can result in significant variation in mineral assemblages and thus significantly influence how iron isotopes are fractionated. The isotopic values of specific mineral types depends on which sulfide and oxide minerals are precipitated, in turn changing significantly as a function of fS_2 and fO_2. Qualitatively therefore, at Renison, widespread pyrrhotite preferentially incorporates the light isotope, so that chalcopyrite has values in between those of isotopically heavy magnetite and pyrite-arsenopyrite, and isotopically light pyrrhotite (Wawryk and Foden, 2015). However, at Batu Hijau, magnetite incorporates the heavy isotope, but pyrrhotite is absent, so that chalcopyrite-bornite incorporate the light iron isotope. The fluid history therefore may be more relevant to explain the large differences of Fe-isotope values between minerals, compared to the 0.1‰ difference between S type and I type intrusions. Clearly, more experimental work testing the effects of chlorinity and sulfur fugacity, with mass balance constraints are needed to elucidate the effects of fluid evolution on iron isotope signatures in metalliferous fluids.

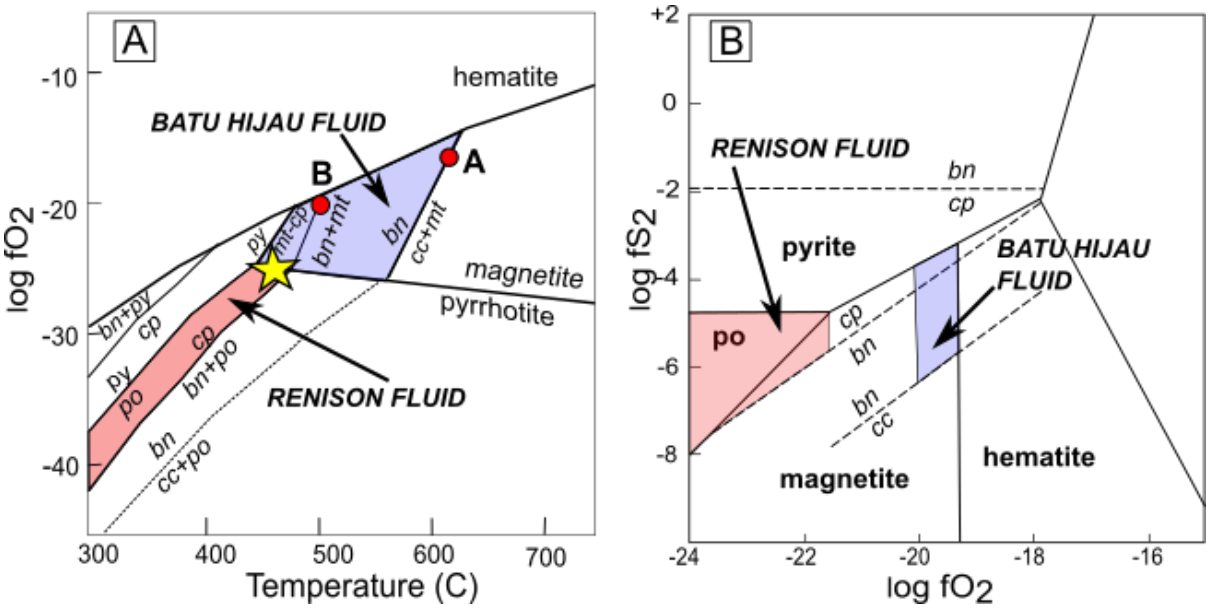

Figure 3.10 Temperature-Log fO_2 and Log fS_2-logfO_2 diagrams showing mineral assemblages deposited at Batu Hijau (shaded blue) and Renison (shaded red). A: Temperature-log fO_2 diagram after Garwin (2000). Stability fields of oxides in bold line, stability fields of sulfides shown in thin line. Red circles show interpreted formation conditions of magnetite-bornite-digenite±chalcopyrite bearing-A veins and bornite-chalcopyrite±magnetite bearing B veins at Batu Hijau. Yellow star shows interpreted formation of early magnetite alteration at Renison (Kitto, 1994), and stability fields of co-precipitated pyrrhotite-chalcopyrite in vein-hosted mineralisation. B: Log fO_2-fS_2 diagram at 500 °C and 1 kbar showing interpreted conditions of mineral formation at Batu Hijau and Renison, based on experimental work of Hemley et al. (1992). Buffers in the Fe-S-O system are shown in solid lines, and the Cu-Fe-S-O system shown in dashed lines. Abbreviations: bn=bornite, cc=chalcocite, cp=chalcopyrite, mt=magnetite, py=pyrite, po=pyrrhotite

3.5.5 Isotopic fractionation between minerals and fluid

3.5.5.1 Model parameters

If we consider that the fluid is an infinite reservoir compared to magnetite and sulfides deposited in quartz veins, then mineral deposition may be modelled by a Rayleigh process. We have chosen to model a Rayleigh process at 450 °C based on fluid inclusion homogenisation temperatures (see section 2.3) and the availability of published theoretical β-factors for ferrous chloro-aqueous species at this temperature (Hill et al., 2010; also see Saunier et al., 2011 for a compilation). At 450 °C aqueous species are dominated by $FeCl_2^0$ (e.g. Simon et al., 2004, Saunier et al., 2011). We note that in the hematite-saturated experiments of Saunier et al. (2011), spectroscopy and thermodynamic modelling at 450 °C demonstrated the presence of

Fe(III) aqueous species, but as hematite is absent in our samples, we have considered only the ferrous chloride species in our model.

XANES spectra used by Testemale et al. (2009) demonstrated that tetrahedral Fe-Cl species, such as $FeCl_4^{2-}$, are important for Fe(II) transport at high temperatures (>300 °C) and chloride molality (> 2M). We have therefore included this complex in our model for comparison. Throughout this section, for simplicity, we will refer to these ferro-aquo-chloride complexes as $Fe(II)_{aq}$.

To calculate a theoretical magnetite-$Fe(II)_{aq}$ fractionation factor, we use the β-factor for magnetite derived by Polyakov and Mineev (2007), which is 1.82‰ at 450 °C. The theoretical fractionation between magnetite and an aqueous complex, expressed as a β-factor, is given by

$$10^3 \ln\alpha_{mgt\text{-}Fe(II)aq} = 10^3 \ln\beta_{mgt} - 10^3 \ln\beta_{Fe(II)aq} \qquad \text{Eq (2)}$$

The β-factors derived by Hill et al. (2010) for both the $FeCl_2^0$ and the $FeCl_4^{2-}$ complexes are shown in Table 3.5. Note that Hill et al. (2010) computed four different β-factors for these complexes, using two different theoretical methods (UHF is the Unrestricted Hartree-Fock approach, and B3LYP is a Density Functional Theory approach) paired with three different basis sets.[2] By using Eq (2), we have calculated theoretical magnetite-$Fe(II)_{aq}$ fractionation factors, and these calculations are also shown in Table 3.5. For the $FeCl_2^0$ complex, the UHF/6-31G(d) and B3LYP/6-31G(d) combination return identical fractionation factors, and the B3LYP/6-311G(d) and B3LYP/VTZ combination also give identical fractionation factors, which are 0.33‰ lower.

Theoretical fractionation factors calculated using the β-factors for the $FeCl_4^{2-}$ complex predict overall larger magnetite-$Fe(II)_{aq}$ fractionation, but are less sensitive to the basis set used; the difference between the B3LYP/6-311G(d) and the B3LYP/VTZ basis sets is 0.19‰.

[2] In computational chemistry, a basis set is a group of mathematical equations (called basis functions) that describe the electron distribution in atomic orbitals. The 6-31G(d) and 6-311G(d) basis sets here include functions that distinguish between “core” and “valence” electrons and thus can account for orbital size variation during chemical bonding; the (d) shows that a function has been added to account for orbital shape (distortion from the effect of polarization during bonding). The VTZ basis set incorporates more polarization functions.

Aquo species	Method/Basis set	β-factor at 450°C	Calculated $10^3 ln\beta_{mgt\text{-}Fe(II)aq}$
$FeCl_2^0$	UHF/6-31G(d)	1.31	0.51
$FeCl_2^0$	B3LYP/6-31G(d)	1.26	0.51
$FeCl_2^0$	B3LYP/6-311G(d)	1.55	0.18
$FeCl_2^0$	B3LYP/VTZ	1.50	0.18
$FeCl_4^{2-}$	UHF/6-31G(d)	0.89	0.93
$FeCl_4^{2-}$	B3LYP/6-31G(d)	0.83	0.99
$FeCl_4^{2-}$	B3LYP/6-311G(d)	0.89	0.93
$FeCl_4^{2-}$	B3LYP/VTZ	0.92	0.90

Table 3.5 Calculated $10^3 ln\beta_{mgt\text{-}fl}$ for fractionation of iron isotopes between magnetite and ferrous aqueous species, at 450°C . β-factors for ferrous aqueous complexes are derived from different basis sets of Hill et. al. (2010). The β-factor for magnetite is derived from the polynomial expansion in Polyakov and Mineev (2007).

3.5.5.2 Fractionation Models

The equation describing the isotopic composition of minerals formed by a Rayleigh-type process is given by

$$\delta_P = \delta_R + \varepsilon_{P/R} \quad (3)$$

where δ_P is the is the isotopic composition of magnetite instantaneously deposited from the fluid, δ_R is the isotopic composition of the fluid and $\varepsilon_{P/R} = (\alpha_{P/R}-1)$, where $\alpha_{P/R}$ is the theoretical fractionation of iron isotopes between magnetite and Fe(II) aquo species in the fluid.

Furthermore, as magnetite is accumulated, the isotopic composition of the remaining fluid changes according to

$$\delta_R = \delta_{R,0} + \varepsilon_{P/R} * \ln f \quad (4)$$

where $\delta_{R,0}$ is the initial composition of the reactant, and *f* is the proportion of unused reactant (Mariotti, 1981).

Using equation (3) we calculated iron isotope values for instantaneously formed magnetite, using the $10^3 \ln\alpha_{mgt\text{-}Fe(II)aq}$ values in Table 3.5. Using Eq (4) we have modelled the corresponding change in isotopic composition of the fluid, as magnetite is precipitated. Typical results are shown in Figure 3.11, where it is clear that isotopic values of precipitated magnetite is dependent on both the $Fe(II)_{aq}$ species ($FeCl_2$ or $FeCl_4^{2-}$), and the basis set used for the calculation. We have also indicated in Figure 3.10 the range of $\delta^{57}Fe$ values of natural magnetite and sulfide samples measured by MC- ICPMS.

There is good agreement between modelled $\delta^{57}Fe$ values of magnetite and measured values, assuming a fluid composition of between -0.5 and -0.1 ‰, and using the UHF/6-31G(d) basis set for the $FeCl_2^0$ complex (Fig 3.11A). Interestingly, this model in which measured $\delta^{57}Fe$ values of sulfide minerals are the same as the modelled $\delta^{57}Fe$ values of remaining fluid (f), is consistent with the experiments of Syverson (2015) who concluded from time-series experiments at 350°C and 500 bars, that chalcopyrite deposited from a hydrothermal fluid records the isotopic value of the fluid, owing to rapid isotopic exchange between Fe-bearing fluid and chalcopyrite precipitates. In comparison, Fig 3.11B shows that the fractionation

factors calculated using the B3LYP/6-311G(d) basis set do not replicate the $\delta^{57}Fe$ values of natural magnetite, predicting magnetite which is isotopically heavy at ~+4‰.

Figures 3.11C and 3.11D illustrate the results of our models using $FeCl_4^{2-}$ as the main aqueous complex. Both figures illustrate that neither model is able to replicate $\delta^{57}Fe$ values of natural magnetite unless an isotopically heavy fluid of $\delta^{57}Fe$ = +0.5‰ is assumed. This also would require that most of the fluid would have to crystallise magnetite, before the isotopic composition becomes light enough to match our measured sulfide values, in which case any late precipitated magnetite would also be isotopically light; this could be tested by detailed sampling of veins.

We therefore conclude that the model which best fits our analytical data, is the model shown in Figure 3.11A, namely that the ore fluid had $\delta^{57}Fe$ values between -0.5 and -0.1 ‰, and was dominated by the neutral $FeCl_2$ complex.

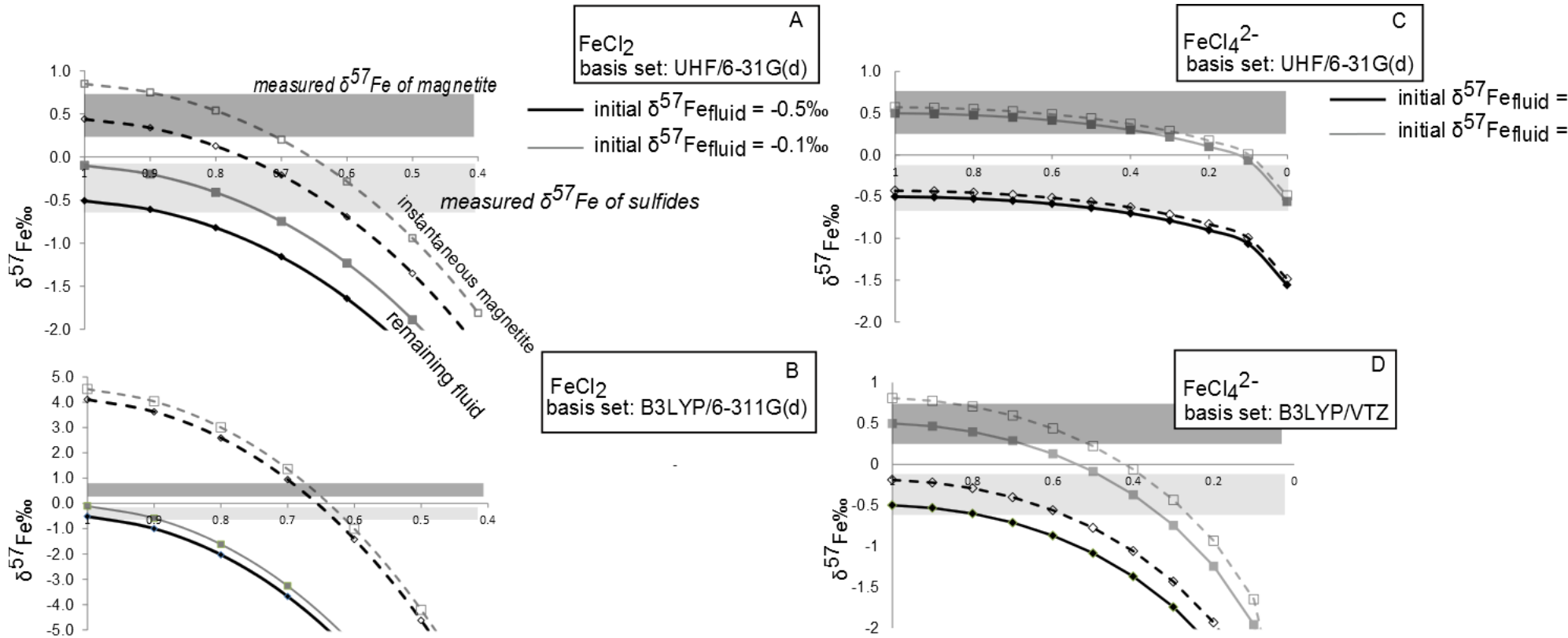

Figure 3.11 Predicted iron isotope values of magnetite deposited at 450 °C, modelled by a Rayleigh process using β-factors reported in the literature for magnetite (Polyakov et. al., 2007), $FeCl_2$ and $FeCl_4^{2-}$ complexes from Hill et al. (2010). Dashed lines represent magnetite $\delta^{57}Fe$ values assuming initial fluid $\delta^{57}Fe$ values -0.1 (square symbols) and -0.5 ‰ (diamond symbols). Solid lines are the calculated $\delta^{57}Fe$ of fluid remaining after deposition of magnetite. The horizontal shaded bars are the $\delta^{57}Fe$ values of magnetite (darker shading) and chalcopyrite/bornite (lighter shading) mineral separates measured by MC-ICP-MS. A and B show sensitivity of results using the $FeCl_2$ as the main aqueous complex, depending on the basis set used. C and D show results using $FeCl_4^{2-}$ as the main aqueous complex; the results are less sensitive to the basis set used, but would have to assume an isotopically heavy fluid to match measured $\delta^{57}Fe$ values of natural magnetite.

3.6. CONCLUSIONS

We have analysed magmatic-hydrothermal minerals and bulk intermediate plutonic rocks from the Batu Hijau porphyry Cu-Au deposit to characterise the Fe isotopic values of sulfide minerals and magnetite associated with an oxidized arc magma system. The systematic increase of $\delta^{57}Fe$ values of whole rocks as melt evolves from andesite to tonalite can be modelled by fractional crystallization of an initial mafic melt emplaced at 1.2 kbar, with an fO_2 of QFM+2 and starting H_2O of 2.5%. Although crystallization of magnetite would be expected to remove heavy iron isotopes from the melt, the greater proportion of Fe-Mg silicates (which incorporate light iron isotopes), in addition to up to 15% ulvospinel component in magnetite, results in an overall negative bulk-weighted fractionation factor; therefore there is overall removal of light Fe. This results in a melt which becomes isotopically heavier as fractionation proceeds.

Hydrothermal magnetite is isotopically heavier than bornite and chalcopyrite, consistent with theoretical fractionation factors. The chalcopyrite data from Batu Hijau is in agreement with results from other porphyry deposits, defining a range of $\delta^{57}Fe$ of -1.26 to 0.29‰. Our results are the first published results of $\delta^{57}Fe$ value of magmatic-hydrothermal bornite, co-precipitated with chalcopyrite, and show that bornite and chalcopyrite have similar isotopic values. This is unsurprising given that Fe in both minerals have the same valence state.

However, an empirical $\Delta^{57}Fe_{mgt\text{-}cpy}$ calculated from co-precipitating magnetite and chalcopyrite pairs yield temperatures of formation of ~210 °C, much lower than generally observed for hypogene mineral deposition in porphyry copper deposits, suggesting that kinetic processes between minerals and fluids may be the dominant effect which imparts isotopic values to mineral separates. Simple models of Rayleigh type fractionation, assuming an initial fluid $\delta^{57}Fe$ of between -0.5 and -0.1‰, result in modelled $\delta^{57}Fe$ values for minerals that match our analytical data. Furthermore, the modelled values are in agreement with experiments demonstrating that hypogene chalcopyrite has isotopic compositions reflecting the isotopic value of the hydrothermal fluid.

Comparison of the isotopic values of chalcopyrite and magnetite with those from the Renison deposit show a difference of ~1‰ in chalcopyrite values, an order of magnitude difference to the difference in isotope values between the bulk rock values

of associated intrusions. We propose that the interdependence of oxygen and sulfur redox state in ore fluids also affects the isotope signature of mineral assemblages, by controlling the presence or absence of pyrrhotite, although chlorinity, and coordination chemistry in aqueous species may also play a key role in determining the signature of metalliferous fluids. Experiments that examine the role of sulfidation and oxidation of Fe-bearing sulfides in Fe-isotope fractionation are a future research direction that would help to resolve the interpretation of isotope values observed in natural mineral assemblages.

ACKNOWLEDGEMENTS

This project was funded by a grant to JDF by the Institute for Mineral and Energy Resources at the University of Adelaide. The Centre for Tectonics, Research and Exploration at the University of Adelaide provided a Visiting Researcher Grant to CMW to collaborate with Steve Garwin. We thank Steve Garwin for providing samples of the Batu Hijau intrusions, and generously sharing his knowledge of the deposit. The geologists of the PT Newmont Nusa Tenggara Company at the Batu Hijau mine provided samples of mineralized veins and the authors gratefully acknowledge their assistance, and thank Newmont for permission to publish. Advice and assistance from P.Sossi and L. Kinsley whilst using the Neptune Plus at the Australian National University was much appreciated. Adam Simon and an anonymous reviewer are thanked for their comments which improved the manuscript. This paper is TRAX publication #329.

REFERENCES

Armstrong, J., 2012. Deciphering the evolution of ore fluids at the Batu Hijau Copper-Gold porphyry deposit, Sumbawa, Indonesia. M.S. thesis, University of Nevada.

Audétat, A., Pettke, T., 2003. The magmatic-hydrothermal evolution of two barren granites: A melt and fluid inclusion study of the Rito del Medio and Canada Pinabete plutons in northern New Mexico (USA). Geochim. Cosmochim. Acta. 67, 97-121.

Audétat, A., Pettke, T., Heinrich, C. A., Bodnar, R. J., 2008. The composition of magmatic-hydrothermal fluids in barren and mineralized intrusions. Econ Geol. 103, 877-908.

Barbieri, S., Bigioggero, B., Boriani, A., Cattaneo, M., Cavallin, A., Eva, C., Cioni, R., Gelmini, R., Giorgetti, F., Iaccarino, S., Innocenti, F., Marinelli, G., Slejko, D., Sudradjat, A., 1987. The island of Sumbawa; a major structural discontinuity in the Indonesian Arc. Bollettino della Societa Geologica Italiana 106, 547-620.

Bilenker, L.D., 2015. Elucidating igneous and ore-forming processes with iron isotopes by using experimental and field-based methods. Ph.D thesis, University of Michigan.

Blevin, P., 2004. Redox and compositional parameters for interpreting the granitoid metallogeny of Eastern Australia: implications for gold-rich ore systems. Resource Geol. 54, 241-252.

Burgisser, A., Scaillet, B. 2007. Redox evolution of a degassing magma rising to the surface. Nature, 445, 194-197.

Blundy, J., Mavrogenes, J., Tattitch, D., Sparks, S., Gilmer, A., 2015. Generation of porphyry copper deposits by gas-brine reaction in volcanic arcs. Nat. Geosci. 8, 235-240.

Candela, P.A. and Holland, H.D., 1984. The partitioning of copper and molybdenum between silicate melts and aqueous fluids. Geochim. Cosmochim. Acta 48, 373-380.

Chen L-M., Song, X-Y., Zhu, X-K., Zhang, X-Q., Yu S-Y., Yi, J-N., 2014. Iron isotope fractionation during crystallization and sub-solidus re-equilibration: Constraints from the Baima mafic layered intrusion, SW China. Chem. Geol. 380, 97-109.

Clode, C., Proffett, J., Mitchell, P., Munajat, I., 1999. Relationships of intrusion, wall-rock alteration and mineralisation in the Batu Hijau copper-gold porphyry deposit. In Proceedings PACRIM Congress, 485-498 (AusIMM Publication Series 4/99).

Craddock, P., Dauphas, N., 2009. Iron isotopic compositions of geological reference materials and chondrites. Geost. Geoanalytical Res. 35, 101-123.

Černý, P., Blevin, P. L, Cuney, M., London, D., 2005. Granite related ore deposits. Econ. Geol. 100, 337-370.

Dauphas, N., Roskosz, M., Alp, E., Neuville, D., Hu, M., Sio, C., Tissot, F., Zhao, J., Tissandier, L., Médard, E., Cordier,. C., 2014. Magma redox and structural controls on iron isotope variations in Earth's mantle and crust. Earth Planet. Sci. Lett. 398, 127-140.

Einaudi T., Hedenquist, J.W., Inan, E.E., 2003. Sulfidation state of fluids in active and extinct hydrothermal systems: Transitions from porphyry to epithermal environments. In Society of Economic Geologists Special Publication 10, 285-313.

Fiorentini, M., Garwin, S., 2009. Evidence of a mantle contribution in the genesis of magmatic rocks from the Neogene Batu Hijau district in the Sunda Arc, South Western Sumbawa, Indonesia. Contrib. Mineral. Petrol. 159, 819-837.

Fleet, M.E., 1981. The structure of magnetite. Acta Cryst. B37, 917-920.

Fleet, M.E., 2006. Phase equilibria at high temperatures. Rev. Min. Geochem. 61, 365-419.

Foden, J.D., Varne, R., 1980. The petrology and tectonic setting of Quaternary - Recent volcanic centres of Lombok and Sumbawa, Sunda Arc. Chem. Geol. 30, 201-226.

Foden, J., Sossi, P., Wawryk, C.M., 2015. Fe isotopes and the constrasting petrogenesis of A-, I- and S-type granite. Lithos. 212-215, 32-44.

Fudali, R.F., 1965. Oxygen fugacities of basaltic and andesitic magmas. Geochim. Cosmochim. Acta 29, 1063-1075.

Garwin, S. L., 2000. The setting, geometry and timing of intrusion-related hydrothermal systems in the vicinity of the Batu Hijau copper-gold deposit, Sumbawa, Indonesia. PhD thesis, University of Western Australia.

Garwin, S. L., 2002. The geologic setting of intrusion-related hydrothermal systems near the Batu Hijau porphyry copper-gold deposit, Sumbawa, Indonesia, in Society of Economic Geologists Special Publication 9, 333−366.

Goh, S. W., Buckley, A. N., Lamb, R. N., Rosenberg, R. A., Moran, D., 2006. The oxidation states of copper and iron in mineral sulfides, and the oxides formed on initial exposure of chalcopyrite and bornite to air. Geochim. Cosmochim. Acta 70, 2210-2228.

Graham, S., Pearson, N., Jackson, S., Griffin, W., O'Reilly,S.Y., 2004. Tracing Cu and Fe from source to porphyry: in situ determination of Cu and Fe isotope ratios in sulfides from the Grasberg Cu-Au deposit. Chem. Geol. 207,147-169.

Gualda, G.A.R., Ghiorso, M.S., Lemons, R.V., Carley, T.L. 2012. Rhyolite-MELTS: a modified calibration of MELTS optimized for silica-rich, fluid-bearing magmatic systems. J. Pet. 53, 875-890.

Gustafson, L. B., Hunt, J. P., 1975. The porphyry copper deposit at El Salvador, Chile: Econ Geol. 70, 857-912.

Heimann, A., Beard, B. L., Johnson, C.M., 2008. The role of volatile exsolution and sub-solidus fluid/rock interactions in producing high $^{56}Fe/^{54}Fe$ ratios in siliceous igneous rocks. Geochim. Cosmochim. Acta 72, 4379-4396.

Hemley, J. J., Cygan, G. L., Fein, J. B., Robinson, G. R., d'Angelo, W. M., 1992. Hydrothermal ore-forming processes in the light of studies in rock-buffered systems I: Iron-copper-zinc-lead sulfide solubility relations. Econ. Geol. 87, 1-22.

Hill, P. S., Schauble, E. A., Young, E. D., 2010. Effects of changing solution chemistry on Fe^{3+}/Fe^{2+} isotope fractionation in aqueous Fe–Cl solutions. Geochim. Cosmochim. Acta. 74, 6669-6689.

Idrus, A., Kolb, J., Meyer, F., 2007. Chemical composition of rock-forming minerals in copper-gold-bearing tonalite porphyries at the Batu Hijau deposit, Sumbawa Island, Indonesia: implications for crystallization conditions and fluorine-chlorine fugacity. Resource Geol. 57, 102-113.

Idrus, A., Kolb, J., Meyer, F. 2009. Mineralogy, lithogeochemistry and elemental mass balance of the hydrothermal alteration associated with the gold-rich Batu Hijau porphyry copper deposit, Sumbawa Island, Indonesia. Resource Geol. 59, 215-230.

Irianto, B., Clark, G H., 1995. The Batu Hijau porphyry copper-gold deposit, Sumbawa Island, Indonesia. In Proceedings PACRIM Congress 1995, 485-498 (AusIMM Publication Series 9/95).

Ishihara, S., 1977. The magnetite-series and ilmenite-series granitic rocks. Min.Geol. 27, 293–305.

Ishihara, S., 1998. Granitoid series and mineralization in the Circum-Pacific Phanerozoic granitic belts. Resource Geol. 48, 219-224.

Kitto, P. A., 1994. Structural and geochemical Controls on mineralisation at Renison, Tasmania. PhD thesis, University of Tasmania.

Li, W., Jackson, S.E., Pearson, N.J., Graham, S., 2010. Copper isotopic zonation in the Northparkes porphyry Cu-Au deposit, SE Australia. Geochim. Cosmochim. Acta 74, 4078-4096.

Li, Y., Liu, J., 2006. Calculation of sulfur isotope fractionation in sulfides. Geochim. Cosmochim. Acta 70, 1789-1795.

Lickfold, V., Cooke, D. R., Smith, S.G., Ulrich, T.D., 2003. Endeavour copper-gold porphyry deposits, Northparkes, New South Wales: intrusive history and fluid evolution. Econ. Geol. 98, 1607-1636.

Matjuschkin, V., Blundy, J. D., brooker, R. A., 2016. The effect of pressure on Sulphur speciation in mod- to deep-crustal arc magmas and implications for the formation of porphyry copper deposits. Contrib. Mineral. Petrol, 171:66. doi:10.1007/s00410-016-1274-4

Marrioti A., Germon J. C., Hubert P., Kaiser P., Leto Ile R., Tardieux A. and Tardieux P., 1981. Experimental determination of nitrogen kinetic isotope fractionation: some principles; illustration for the denitrification and nitrification processes. Pl. Soil 62, 413-430.

Meinert, L. D., Hedenquist, J. W., Satoh, H., Matsuhisa, Y., 2003. Formation of anhydrous and hydrous skarn in Cu-Au ore deposits by magmatic fluids. Econ Geol. 98, 147-156.

Meldrum, S. J., Aquino, R. S., Gonzales, R. I., Burke, R. J., Suyadi, A., Irianto, B., Clarke D. S., 1994. The Batu-Hijau porphyry copper-gold deposit, Sumbawa Island, Indonesia. J. Geochem. Expl. 50, 203-220.

Mikhlin, Y. L., Tomashevich, Y. V., Asanov, I. P., Okotrub, A. V., Varnek, V. A., Vyalikh, D. V,. 2004. Spectroscopic and electrochemical characterization of the surface layers of chalcopyrite ($CuFeS_2$) reacted in acidic solutions. Applied Surface Science 225, 395-409.

Mikhlin, Y. L., Tomashevich, Y. V., Tauson, V., Vyalikh, D. V., Molodtsov, S., Szargan, R., 2005. A comparative X-ray absorption near-edge structure study of bornite, Cu_5FeS_4, and chalcopyrite, $CuFeS_2$. Journal of Electron Spectroscopy and Related Phenomena. 83-88

Patterson, D. J., Ohmoto, H., Solomon, M. 1981. Geologic setting and genesis of cassiterite-sulfide mineralization at Renison Bell, Western Tasmania. Econ. Geol. 76, 393-438.

Poitrasson, F., Freydier, R., 2005. Heavy iron isotope composition of granites determined by high resolution MC-ICP-MS. Chem. Geol. 222, 132-147.

Polyakov, V. B., Mineev, S. D., 2000. The use of Mössbauer spectroscopy in stable isotope geochemistry. Geochim. Cosmochim. Acta 64, 849-865.

Polyakov, V. B., Clayton, R. N., Horita, J., Mineev, S. D., 2007. Equilibrium iron isotope fractionation factors of minerals: reevaluation from the data of nuclear inelastic resonant X-ray scattering and Mössbauer spectroscopy. Geochim. Cosmochim Acta 71, 3833-3846.

Polyakov, V. B., Soultanov, D. M., 2011. New data on equilibrium iron isotope fractionation among sulfides: constraints on mechanisms of sulfide formation in hydrothermal and igneous systems. Geochim. Cosmochim. Acta 75, 1957-1974.

Ramdohr, P, 1980. The ore minerals and their intergrowths, 2nd ed, Pergamon Press, Oxford

Ridolfi, F., Renzulli, A., Puerini, M., 2010. Stability and chemical equilibrium of amphibole in calc-alkaline magmas: an overview, new thermobarometric formulations and application to subduction-related volcanoes. Cont. Mineral. Pet. 1601, 45-66.

Reed, M.H., Palandri, J., 2006. Sulfide mineral precipitation from hydrothermal fluids. Rev. Mineral. Geochem. 61, 609-631.

Rustad, J. R., Casey, W. H, Yin, Q. Z., Bylaska, E. J., Felmy, A. R., Rogatko, S. A., Jackson, V. E., Dixon, D. A.,2010. Isotopic fractionation of Mg^{2+}(aq), Ca^{2+}(aq), and Fe^{2+}(aq) with carbonate minerals. Geochim. Cosmochim. Acta 74, 6301-6323.

Saunier, G., Pokrovski, G. S., Poitrasson, F., 2011. First experimental determination of iron isotope fractionation between hematite and aqueous solution at hydrothermal conditions. Geochim. Cosmochim. Acta. 75, 6629-6654.

Schauble, E. A., 2004. Applying stable isotope fractionation theory to new systems.Rev. Min. Geochem. 55, 65-111

Schuessler, J., Schoenberg, R., Sigmarsson, O., 2009. Iron and lithium isotope systematics of the Hekla volcano, Iceland-Evidence for Fe isotope fractionation during magma differentiation. Chem. Geol. 258, 78-91.

Seedorf, E., Dilles, J.H., Proffett, J.M., Einaudi, M.T., Zurcher, L., Stavast ,W.J.A., Johnson, D.A., Barton, M.D., 2005. Porphyry deposits: characteristcs and origin of hypogene features. Econ. Geol. 100, 251-298.

Shinohara, H., 2004. Exsolution of immiscible vapor and liquid phases from a crystallizing silicate melt: implications for chlorine and metal transport. Geochim. Cosmochim. Acta 58, 5215-5221.

Sillitoe, R. H., 2010. Porphyry Copper Systems. Econ. Geol. 105, 3-41.

Simon, G., Kesler, S. E., Essene, E.J., Chryssoulis, S. L. 2000. Gold in Porphyry Copper Deposits: experimental determination of the distribution of gold in the Cu-Fe-S system at 400° to 700°C. Econ. Geol. 95, 259-270.

Simon, A. C., Pettke, T., Candela, P.A., Piccoli, P. M.,Heinrich, C. A., 2004. Magnetite solubility and iron transport in magmatic-hydrothermal environments. Geochim. Cosmochim. Acta 68, 4905-4914.

Sossi, P. A., Foden, J. D., Halverson, G., 2012. Redox-controlled iron isotope fractionation during magmatic differentiation. Contrib. Mineral. Petrol. 164, 757-772.

Sossi, P. A., Nebel, O., and Foden, J. D., 2016 Iron isotope systematics in planetary reservoirs. Earth Planet. Sci. Lett. 452, 295-308.

Sossi, P.A and O'Neill, H., 2016. The effect of bonding environment on iron isotope fractionation between minerals at high temperature. Geochim. Cosmochim. Acta 196, 121-143.

Syverson, D. D., 2015. Fe and Cu isotope fractionation between chalcopyrite and dissolved metal species during hydrothermal recrystallization: An experimental study at 350C and 500 bars. Abstract OS43A-2012 presented at 2015 Fall Meeting, AGU, San Francisco, Calif., 14-18 Dec.

Teng, F-Z., Dauphas, N., Helz, R., 2008. Iron isotope fractionation during magmatic differentiation in Kilauea Iki Lava Lake. Science 320, 1620-1622.

Teng, F-Z., Dauphas, N., Huang, S., Marty, B., 2013. Iron isotopic systematics of oceanic basalts. Geochim. Cosmochim. Acta. 107, 12-26.

Testemale, D., Brugger, J., Liu, W., Etschmann, D., Hazemann J., 2009. In-situ X-ray absorption study of Iron(II) speciation in brines up to supercritical conditions. Chem. Geol. 264, 295-310.

Vasyukova, O. V., Kamenetsky, V. S., Goemann, K., Davidson, P., 2013. Diversity of primary CL textures in quartz from porphyry environments: implication for origin of quartz eyes. Contrib. Mineral. Petrol. 166:1253-1268.

Wang, Y., Zhu, X., Cheng, Y., 2015. Fe isotope behaviours during sulfide-dominated skarn-type mineralization. J. Asian Earth Sci. 103, 374–392.

Wawryk, C.M., Foden, J., 2015. Fe-isotope fractionation in magmatic-hydrothermal mineral deposits: a case study from Renison Sn-W deposit, Tasmania. Geochim. Cosmochim. Acta 150, 285-298.

Webster, J. D., 2004. The exsolution of magmatic hydrosaline chloride liquids. Chem. Geol. 210, 33-48.

Whitney, J.A., Hemley, J.J., Simon, F.O. 1985. The concentration of iron in chloride solutions equilibrated with synthetic granitic compositions; the sulfur-free system. Econ Geol. 80, 444-460.

Williams, H.M., Prytulak J., Plank, T.A.,Kelley, K.A. 2014. Iron stable isotopes, magmatic differentiation and the oxidation state of Mariana Arc magmas. AGU Fall Meeting Abstracts, A4864.

Yardley, B., 2005. Metal concentrations in crustal fluids and their relationship to ore formation. Econ Geol. 100**,** 613-632.

Young, E. D., Manning, C. E., Schauble, E. A., Shahar, A.,Macris, C. A., Lazar, C., Jordan, M., 2015. High-temperature equilibrium isotope fractionation of non-traditional stable isotopes: experiments, theory, and applications. Chem. Geol. 395, 176-195.

Zimmer, M., Plank, T., Hauri, E. H., Yogodzinski, G. M., Stelling, P., Larsen, J., Singer, B., Jicha, B., Mandeville, C., Nye, C. J., 2010. The role of water in generating the calc-alkaline trend: new volatile data for Aleutian magmas and a new Tholeiitic Index. J. Pet. 51, 2411-2444.

Zhao, J., Brugger, J., Ngothai, Y., Pring, A., 2014. The replacement of chalcopyrite by bornite under hydrothermal conditions Am. Mineral. 99, 2389-2397.

APPENDIX A. Method for separation of copper sulfides and magnetite from quartz veins at Batu Hijau

1. Veins were cut from each other and wallrock with GEMMASTA mini-rock saw
2. Samples were milled with a tungsten-carbide disk pulveriser to -1mm and +125µm size fraction.
3. A hand magnet was passed over the samples to remove magnetite.
4. Samples were run through a Frantz magnetic separator to separate quartz and other non-magnetic minerals from diamagnetic and paramagnetic minerals. The Frantz was cleaned with compressed air between samples. Configuration of the Franz separator followed Gaudin and Rush Spedden (1943).
5. Sulfides were separated from mica minerals by heavy liquid separation, using methylene iodide of density 3.32. Samples were cleaned with acetone.
6. The Frantz separator was used to separate bornite, chalcopyrite and pyrite, then checked using a binocular microscope.
7. Heavy magnetic minerals e.g. zircon, are resistant to aqua regia digestion, and were removed from Fe-solution via centrifuge before loading onto anion-exchange columns.

Reference

Gaudin, A.M., Rush Spedden, H. (1943) Magnetic separation of sulfide minerals. *Mining Technology, Technical Publication* 1549, American Institute of Mining and Metallurgical Engineers

Appendix B. Check of Fe-Elution chemistry

The aim was to ensure that the resin was not overloaded with Fe, and that elements which can interfere with Fe (Cu, Cr, Co, Ni, Zn) had been removed from the samples prior to MC-ICPMS.

Samples were dissolved at 140° C in reverse aqua regia (3 parts HNO_3 to 1 part HCl) to oxidise the Fe, and centrifuged to remove insoluble mineral inclusions prior to the column work.

The column chemistry is listed below. The eluent from steps 1-4, and washing steps 5 and 6 were collected from a sample each of magnetite, bornite and chalcopyrite mineral separates from Batu Hijau ore. The eluent from step 1 and 2 were collected together. The author had noted that after steps 1-3 a green-yellow band remained on the resin when working with Cu-bearing sulphides; so step 3 was repeated until the green band had been eluted. Thus a total of 6 to 9ml of 6M HCl was used to elute Cu.

Eluents were analysed by Optical Emission Spectroscopy at the CSIRO Analytical Chemistry department at Waite Campus. The concentration of Fe was measured on the Neptune multi collector ICPMS.

Column Procedure:

Sample Elution

1. Load the entire sample (½ ml) on to the top of the resin.
2. Rinse the beaker with 1ml of 6M HCl, and add to the column
3. Cu elution: **3 to 9 ml of 6M HCl**
4. Fe elution: **3ml of 0.05M HCl**
    a. Dry down beakers (**140°C**)
    b. Take the samples up in 5ml of 2%HNO_3 for mass spectrometry

Cleaning

5. 5ml of 6M HCl
6. ~7ml of 0.05M HCl
7. Equilibrate with 0.5ml of 6M HCl

Results

Fe elution: Results are shown in Table B1, and in the charts below. No Fe has eluted from the column prior to the Fe collection step, showing that the resin was not overloaded with Fe, with sample weights of 5-7 mg. The elution is quantitative, with 99% of the Fe recovered in the Fe elution step 4.

***Base metal elution**:* Table B1 show that 98% of the Cu from the chalcopyrite sample was eluted in steps 1 and 2, with the remaining 2% eluted in step 3. Further eluents were below the detection limit of 50ppb using OES. The charts below (Figure B.1) show the good separation of Cu and Fe using the current method.

Cr, Co and Ni all returned results less than the detection limit of 50 ppb. The signal intensity of ^{53}Cr on the Neptune consistently remains around 0.0008V showing effective separation of this element by the resin.

Sample ID	Elution Step	conc Fe (ppm)		%of total Fe	Cu (ppm)
cp1	6M HCl sample vial rinse	0.0004		0.0001%	**539**
cp2	6M HCl base metal elution	0.0021		0.0006%	**11.2**
sample collect	0.05M Fe elution	**336.0**		**99.46%**	<5
cp3	6M HCl wash	1.70		0.50%	<5
cp4	.05M HCL wash	0.13		0.04%	<5
			total [Fe] ppm	**337.83**	
mgt1a	6M HCl sample vial rinse	0.008		0.002%	<5
mgt1b	6M HCl base metal elution	0.004		0.001%	<5
sample collection	0.05M Fe elution	**517**		**99.16%**	<5
mgt2	6M HCl wash	3.89		0.75%	<5
mgt3	.05M HCL wash	0.47		0.09%	<5
			total [Fe] ppm	**521.37**	
bn1	6M HCl sample vial rinse	0.0002		0.0001%	**704**
bn2	6M HCl base metal elution	0.0003		0.0002%	<5
sample collection	0.05M Fe elution	**163.0**		**99.25%**	<5
bn3	6M HCl wash	1.1		0.69%	<5
bn4	.05M HCL wash	0.1		0.06%	<5
			total [Fe] ppm	**164.23**	<5

Table B1. Fe and Cu concentrations in eluent steps of ion exchange chromatography, used to separate Fe for mass spectrometry

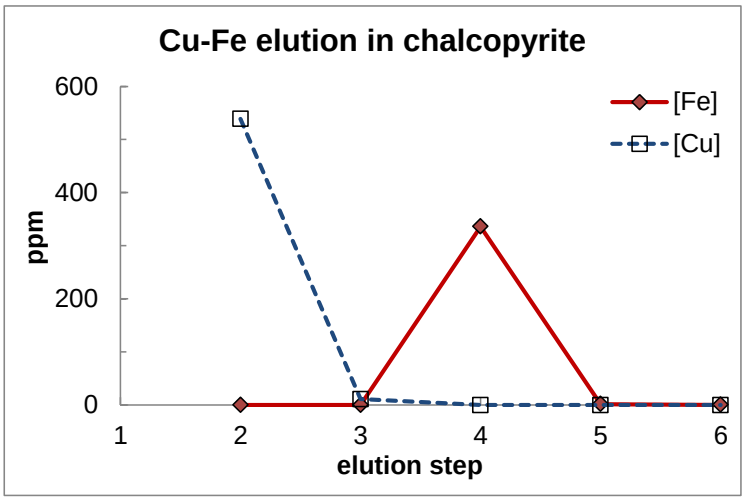

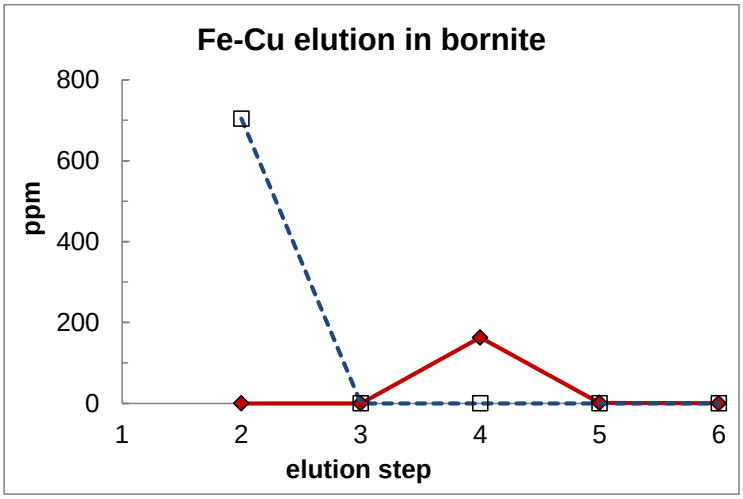

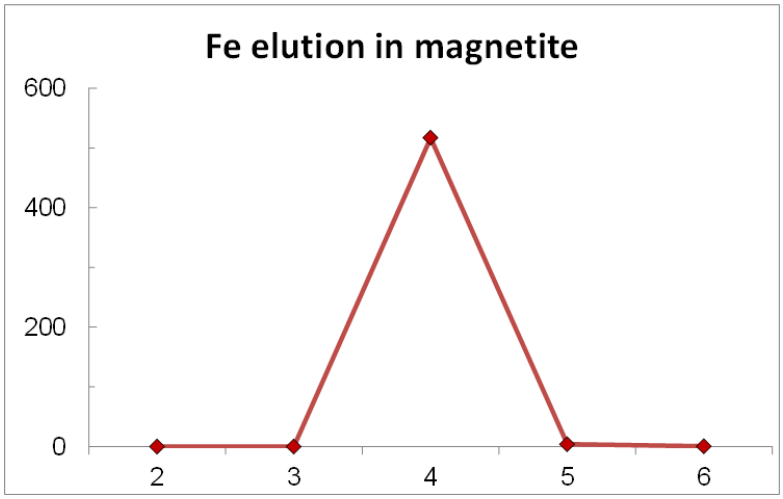

Figure B 1. Concentration of Fe in elution steps of the ion-exchange chromatographic method of separating Fe from other transition elements.

APPENDIX C. Estimation of Magmatic intensive variables

Geothermobarometry using the method of Ridolfi et al. (2010) was performed using amphibole and plagioclase phenocryst compositions measured by Garwin 2000. Results are shown in the table below. The hornblende-phyric andesites yield average crystallisation temperature of 1000°C at 6.4kb or 22km depth in the crust. Plagioclase dominated crystallisation within porphyritic felsic intrusions occurs in high-level magma chambers (4km to <2km). The porphyritic tonalities yield crystallisation ~800°C and ~5.4 wt% H_2O. The Young Tonalite yields crystallisation temperatures of ~780°C and pressures of 0.88kb, corresponding to ~3km depth, and ~4.5 wt% H_2O.

The temperature results are in agreement with Garwin's 2000 estimates of P and T conditions using the amphibole-plagioclase geothermometer of Holland and Blundy (1994), although the pressure results using the Ridolfi calculations are somewhat less by 30-50% than those calculated by Garwin 2000 using the Al-in-hornblende barometer of Anderson and Smith (1995).

Table A 1 Comparison of crystallisation pressure (P) and temperature (Temp) estimates from Batu Hijau, calculated using amphibole-plagioclase geothermometry. R=Ridolfi et al. (2010), H&B=Holland and Blundy. Oxygen fugacity, crustal depth and H_2O content were estimated using the Ridolfi et al. (2010) Geothermobarometry.

Rock Type	Age	P (Kb; A&S)	Temp C (H&B)	P(Kb;R)	Temp C;(R)	depth (oceanic crust)	ΔNNO	log *fO2*	H2O wt%
early andesite	7	-	-	6.36	1016	22	1	-8.8	8.5
QD1	5.9	**0.3**	**699**	0.56	755	2	2.4	-12.5	3.1
QD3	4.4	**1.1**	**672**	0.69	770	2.4	2.4	-12.2	3.4
QD3	4.4-3.8	**0.9**	**709**	0.67	788	2.4	2.1	-12	3.5
po tonalite	5	**1.8**	**739**	1	795	3.5	2.0	-12	5.4
po tonalite	4.7	**2.3**	**718**	1.08	807	3.8	2.0	-12	5.4
tonalite	3.7	**1.4**	**783**	0.88	783	3.1	2.2	-12.1	4.7
late andesite	<3.7	**0.8**	**792**	0.73	772	1.9	1.9	-12.7	4.4

Application of the plagioclase-melt hygrometer of Lange et al. (2009), using average anorthite content of plagioclase phenocryst cores, and whole-rock compositions in lieu of glass, plus a temperature of 800° yields broadly similar H_2O contents for the porphyritic tonalite and Young Tonalite, given the errors of estimation (± 0.4 for Ridolfi, and ±0.3 for Lange). This, in conjunction with amphibole geothermooxybarometry described above, provides a useful constraint for water contents generated by thermodynamic modelling in section 5.3 of the main paper.

Table A 2 Estimates of H_2O content of Batu Hijau melts using the hygrometer of Lange et al. (2009)

Rock Type	An content	P (kb)	T (C)	H_2O wt%
QD3	0.7	1	800	7.2
Po tonalite	0.55	1	800	6.1
Young Tonalite	0.55	1	800	6.7
Late andesite	0.65	1	800	6.4

References

Lange R., Frey H., Hector H. (2009) A thermodynamic model for the plagioclase-liquid hygrometer/thermometer. *Am. Miner.* **94**, 494-506.

Ridolfi F., Renzulli A., Puerini M. (2010) Stability and chemical equilibrium of amphibole in calc-alkaline magmas: an overview, new thermobarometric formulations and application to subduction-related volcanoes. *Cont. Mineral. Pet.* **160**(1), 45-66.

Sample	Rock type	Author	SiO_2	$Al2O_3$	TiO_2	FeO total	MgO	CaO	Na_2O	K_2O	V	LOI	Total
98100301	micro-gabbro	Garwin 2000	49.9	19.2	0.8	8.6	6.0	10.3	2.6	0.5	249.0	1.35	100.32
97092601	phyric hornblende andesite	Garwin 2000	55.2	17.2	0.7	7.6	4.8	7.4	3.6	0.1	193.0	1.74	99.64
SGD 01 383.8	phyric hornblende andesite	Garwin 2000	52.9	17.9	0.8	9.0	4.6	8.7	3.1	0.0	221.0	1.40	99.77
SAD 04 232.1	quartz diorite (QD1)	Garwin 2000	63.8	15.7	0.6	5.4	2.7	5.0	3.2	0.8	109.0	1.79	99.81
SKD 01 276.0	porphyritic tonalite	Garwin 2000	62.3	19.0	0.5	5.4	2.6	2.3	4.9	1.5	93.0	1.63	100.98
97101144	porphyritic tonalite	Garwin 2000	62.1	18.0	0.5	5.4	2.4	5.4	3.8	0.7	106.0	1.40	100.49
SRD 02 366.3	porphyritic tonalite	Garwin 2000	64.2	16.4	0.5	4.8	2.5	5.3	3.7	0.8	100.0	1.12	100.30
97101143	porphyritic tonalite	Garwin 2000	65.9	16.0	0.4	4.4	2.4	5.4	3.6	0.7	83.0	0.91	100.40
SRD 02 304.7	porphyritic tonalite	Garwin 2000	65.9	16.0	0.4	4.0	2.3	5.5	3.9	1.0	91.0	1.11	101.10
SRD 02 319-320	porphyritic tonalite	Garwin 2000	65.3	15.5	0.5	4.0	2.7	5.5	3.5	1.0	71.0	1.04	99.60
SBD 031 430	quartz diorite (QD3)	Garwin 2000	61.2	17.0	0.5	7.2	2.9	2.5	5.7	1.2	103.0	1.75	100.88
99050502	quartz diorite (QD3)	Garwin 2000	57.2	18.2	0.6	7.0	3.2	7.1	3.4	0.8	134.0	2.32	99.97
98062708	quartz diorite (QD3)	Garwin 2000	61.0	17.1	0.5	6.1	2.9	5.6	4.0	0.5	117.0	1.91	100.83
97101030	quartz diorite (QD3)	Garwin 2000	58.9	18.4	0.6	5.4	2.7	6.5	3.9	0.8	109.0	1.01	99.13
99050902	quartz diorite (QD3)	Garwin 2000	62.8	17.1	0.4	5.1	1.8	4.9	4.1	1.3	81.0	1.94	100.20
SKD 02 110-111	quartz diorite (QD3)	Garwin 2000	62.0	17.3	0.6	5.0	2.9	5.0	3.8	1.0	93.0	1.32	99.89
SBD 091 416	Old Tonalite	Garwin 2000	68.1	14.2	0.3	6.6	1.4	2.0	5.0	0.7	67.0	0.93	100.01
SBD 048 308	Intermediate Tonalite	Garwin 2000	66.9	15.4	0.3	5.9	1.6	2.1	5.3	0.9	57.0	1.12	100.24
SBD 014 612	Intermediate Tonalite	Garwin 2000	67.4	14.7	0.3	5.6	1.4	3.6	4.6	0.3	50.0	1.45	100.07
SBD 120 404	porphyritic dacite	Garwin 2000	64.5	17.7	0.4	5.5	1.6	3.8	4.8	0.6	73.0	2.31	100.30
BH7	Young Tonalite	Foden, unpublished	69.5	15.1	0.3	4.9	1.2	3.7	4.6	0.5	53.0	1.13	98.96
BH13	Old Tonalite	Foden, unpublished	68.6	15.8	0.3	4.7	1.4	3.9	4.7	0.3	51.0	0.88	99.70
BH6	Old Tonalite	Foden, unpublished	66.3	17.1	0.4	4.5	1.6	4.1	5.3	0.4	53.0	0.86	99.22

Sample	Rock type	Author	SiO_2	$Al2O_3$	TiO_2	FeO total	MgO	CaO	Na_2O	K_2O	V	LOI	Total
SBD 021 545	Young Tonalite	Garwin 2000	67.7	16.0	0.3	4.0	1.2	3.4	5.1	0.5	40.0	1.75	100.53
BH12	Young Tonalite	Foden, unpublished	66.6	17.4	0.4	3.7	1.6	4.3	5.1	0.7	52.0	0.58	99.30
SBD 14 585.1	Young Tonalite	Garwin 2000	66.0	16.5	0.3	3.4	1.3	4.2	4.9	0.5	38.0	0.91	98.65
SBD 41 405.0	Young Tonalite	Garwin 2000	67.8	16.1	0.3	3.2	1.4	3.6	5.0	0.8	37.0	0.70	99.34
BH4	Old Tonalite	Foden, unpublished	68.2	16.9	0.3	2.9	1.3	4.4	4.8	0.8	45.0	0.41	99.60
SBD04-157	Intermediate Tonalite	Garwin 2000	66.4	16.0	0.3	2.9	1.5	2.5	5.0	0.9	59.0	2.10	99.93
98070736	porphyritic andesite	Garwin 2000	54.5	15.8	0.7	7.0	5.3	7.1	3.4	0.4	178.0	4.79	100.06

Table EA1 Geochemical data for Batu Hijau intrusive rocks

Statement of Authorship

Title of Paper	IRON ISOTOPE FRACTIONATION IN MAGMATIC-HYDROTHERMAL MINERALS: A CASE STUDY FROM THE SUR SUR BRECCIA COMPLEX
Publication Status	☐ Published ☐ Accepted for Publication ☐ Submitted for Publication ☑ Unpublished and Unsubmitted work written in manuscript style
Publication Details	

Principal Author

Name of Principal Author (Candidate)	Christine Wawryk
Contribution to the Paper	Collected the samples, and performed all sample preparation, analyses and interpretation.
Overall percentage (%)	100
Certification:	This paper reports on original research I conducted during the period of my Higher Degree by Research candidature and is not subject to any obligations or contractual agreements with a third party that would constrain its inclusion in this thesis. I am the primary author of this paper.
Signature	Date 31/3/2017

Co-Author Contributions

By signing the Statement of Authorship, each author certifies that:

i. the candidate's stated contribution to the publication is accurate (as detailed above);

ii. permission is granted for the candidate in include the publication in the thesis; and

iii. the sum of all co-author contributions is equal to 100% less the candidate's stated contribution.

Name of Co-Author			
Contribution to the Paper			
Signature		Date	

Name of Co-Author			
Signature		Date	

Please cut and paste additional co-author panels here as required.

CHAPTER 4. IRON ISOTOPE FRACTIONATION IN MAGMATIC-HYDROTHERMAL MINERALS: A CASE STUDY FROM THE SUR SUR BRECCIA COMPLEX

4.1. INTRODUCTION

This chapter describes the results of Fe isotope analyses of intrusive rocks and Fe oxides and sulfides from the Sur Sur breccia complex, which is one of several porphyry centres that comprise the giant Río Blanco-Los Bronces porphyry copper deposit in Chile. The deposit is intimately associated with arc magmatism in an Andean margin tectonic setting, distinct from the island-arc setting of the Batu Hijau deposit, thus enabling a comparison of Fe-isotope values between the two deposits.

Batu Hijau differs from the Río Blanco-Los Bronces area in that Batu Hijau exhibits a relatively simple concentric zoning of alteration assemblages, vein density and sulfide mineral assemblages around a central porphyry stock (Garwin, 2000), and it is possible to sample rock types representative of crystal fractionation that resulted in differentiation from andesite to tonalite (see Chapter 3). However, the multiplicity of breccia pipes intruding host rock lithologies at Río Blanco-Los Bronces renders it difficult to find any unaltered host rock (Mike Baker and David Cooke, pers comm). Hence, no thermodynamic modelling has been performed for this deposit.

Notwithstanding the lack of samples from igneous suites associated with Río Blanco-Los Bronces, the relatively simple sulfide paragenesis and lack of re-brecciated mineralisation with multiple vein opening and sealing suggest that the Sur breccia and ore mineral formation formed during only one hydrothermal event (Frikken et al., 2005; D. Cooke, pers comm.) Thus, this breccia complex is ideal to examine Fe isotopes over a considerable vertical column of rock.

4.2. GEOLOGICAL SETTING

4.2.1 Regional Geology

There is a significant body of literature about the Río-Blanco-Los Bronces district, reporting discovery history and early deposit descriptions (Warnaars, 1985), igneous petrology and geochronology (e.g. Deckart et al., 2005, 2010, 2013; Davidson et al., 2005; Garrido et al., 2002; Skewes et al., 2003), review papers (e.g. Toro et al., 2012), and recent detailed structural mapping (Piquer et al., 2015).

The Río Blanco-Los Bronces porphyry copper deposit is situated in the Chilean Miocene magmatic arc. It is one of 3 giant porphyry copper deposits, including El Teniente to the south and Los Pelambres to the north, that are located between 31 ºS and 34 ºS in the southern part of the Chilean flat slab segment (Figure 4.1).

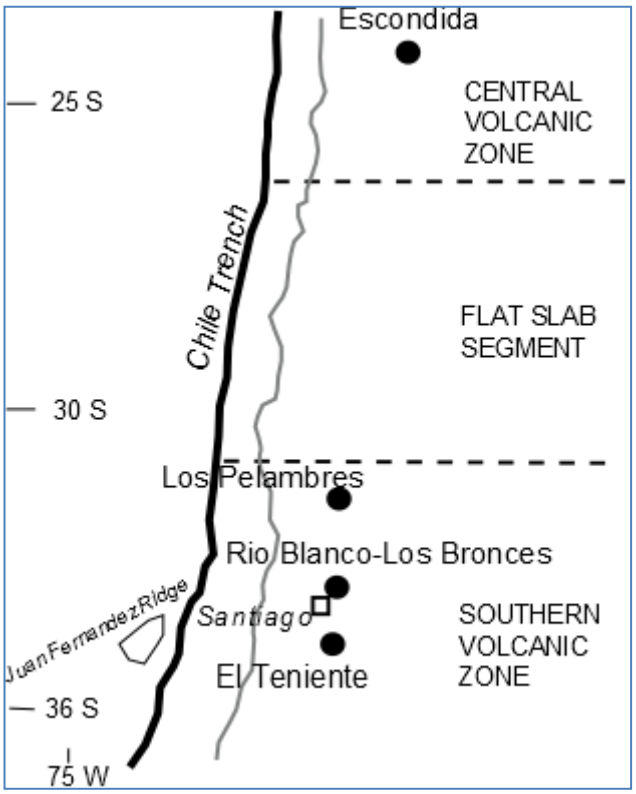

Figure 4.1 Location of Río-Blanco-Los Bronces, Los Pelambres and El Teniente porphyry Cu deposits. Modified after Garrido et al. (2002).

Geology of the Río Blanco-Los Bronces area is shown in Figure 4.2. The oldest rocks of the Río Blanco-Los Bronces district are late Eocene to early Miocene (34-25 Ma) andesites and basaltic-andesite lavas, intercalated with pyroclastic and sedimentary deposits termed the Abanico Formation. These rocks are interpreted to have formed in an extensional intra-arc basin (Piquer et al., 2015).

Tectonic basin inversion commenced at 23 Ma, when the tectonic regime changed from extension to east-west compression (Piquer et al., 2015). Basin inversion was coeval with the onset of both volcanism (the Farollenes Formation) and plutonism. The largest intrusive complex in the area is the San Francisco batholith, some 30 km long (north-south) by 20 km wide (east-west; Piquer et al., 2015). Lithological, petrographic and geochronological (K-Ar and U-Pb) studies (e.g. Waarners et al.,

1985, Deckart et al., 2005) report a wide variety of compositional types from gabbro to granodiorite, syenogranites and monzonite, monzodiorites and tonalites recording several cycles of magmatic differentiation of melts between 23 Ma and 8 Ma (see Piquer et al., 2015, their Table 2), which precede the main mineralising event.

In the late Miocene to early Pliocene, subvolcanic porphyries and hydrothermal breccias intruded the Farollenes and San Francisco batholith. The age range for emplacement has been constrained by U-Pb dating to have occurred between 7.12 ± 0.19 and 4.69 ± 0.23 Ma (Deckart et al., 2013). The porphyries range from quartz monzonite and monzonite to dacite and rhyolite in composition. Garrido et al. (2002) report total Fe_2O_3/ FeO of between 1 and 3 in magmatic rocks demonstrating that oxidation state of magmas had increased sharply just príor to onset of the mineralization event.

The breccias are characterized by large volumes of fragmentation, high hypogene copper grades (>0.8% Cu), Cu-Mo mineralization and absence of by-product gold (Garrido et al., 2002). Hydrothermal activity lasted ~4my and ceased shortly after the La Copa Rhyolite subvolcanic complex was emplaced at 4.31 Ma (Frikken et al., 2005).

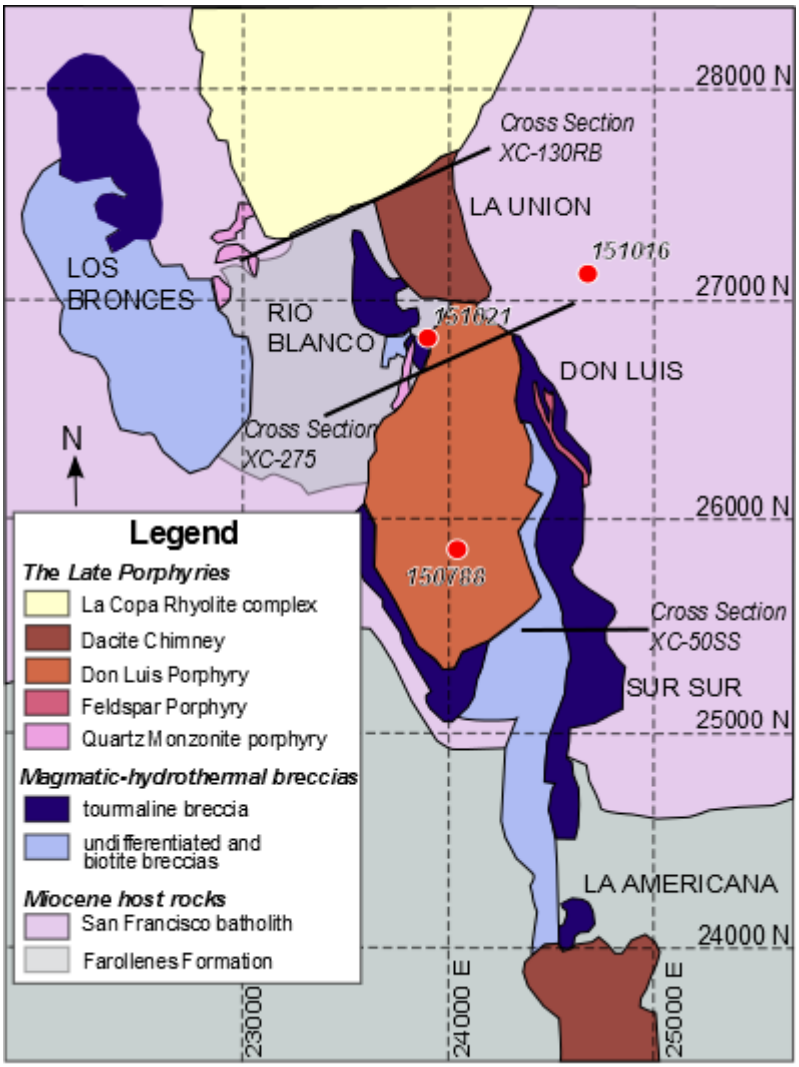

Figure 4.2 Deposit Geology of the Río Blanco-Los Bronces breccia cluster. Sample locations (red circles) mapped where possible, from Frikken (2003). Principal cross sections shown, but drill holes location data such as collar coordinates, azimuth direction and dip angle are not detailed, nor is each drill hole trace annotated with the hole identification number in Frikken (2003).

4.2.2 Geology of the Sur Sur breccia complex.

The Sur Sur breccia complex was studied in detail by Frikken (2003) and Frikken et al. (2005), and the summary that follows is taken from these works.

The Sur Sur breccia occurs in the south east part of the Río Blanco-Los Bronces area (Figure 4.2). It is >3 km long and 300m wide, and is mineralised to at least 1.3km depth (Figure 4.3) It is hosted within, and contains clasts of the San Francisco batholith. The breccia is cemented by tourmaline, sulfides, Fe oxides, biotite, quartz and anhydrite (Frikken et al., 2005).

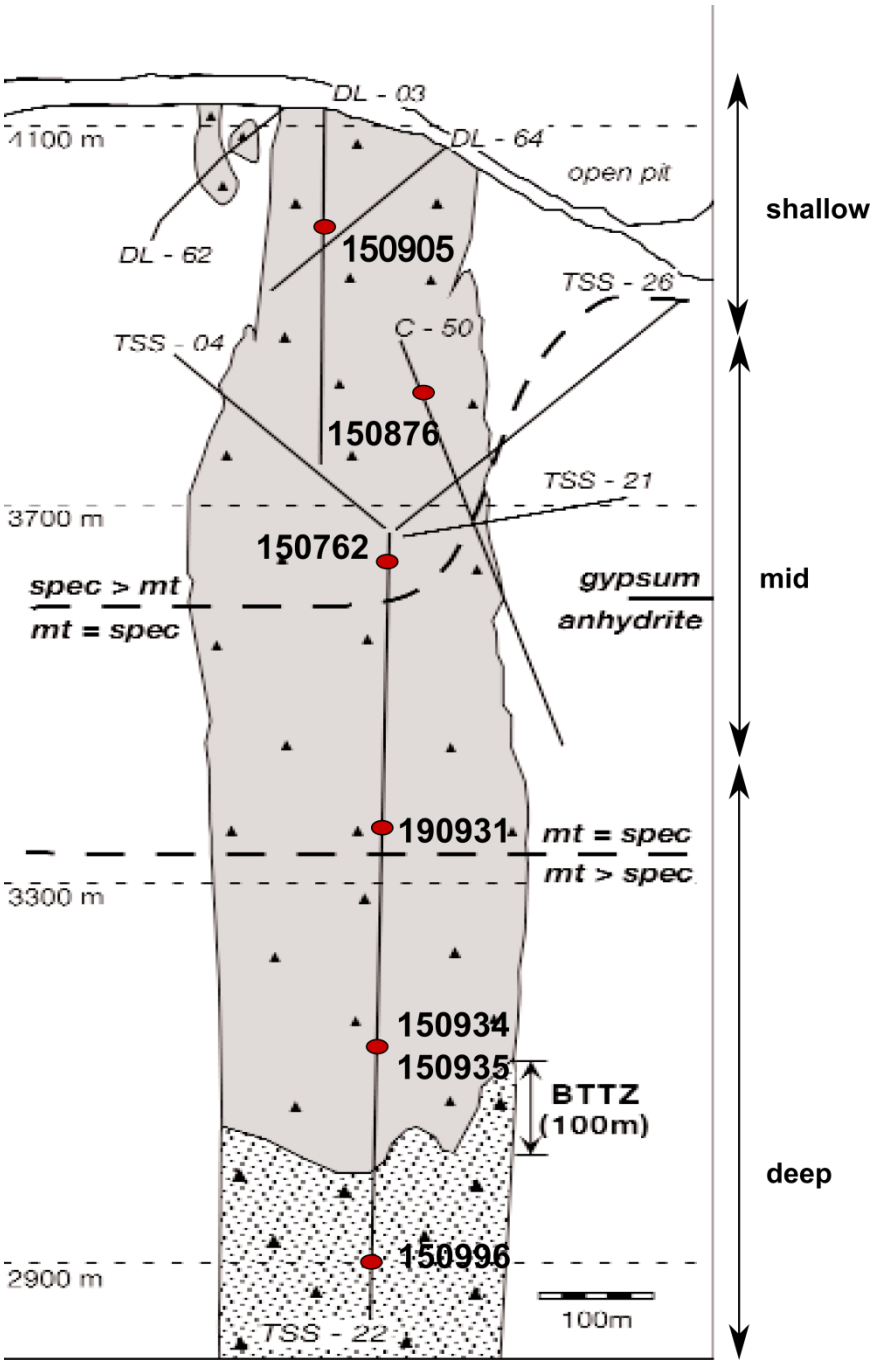

Figure 4.3 East-west cross section through the Sur tourmaline breccia. The bottom stippled zone indicates biotite rich breccia matrix, and solid grey shading indicates tourmaline dominant breccia matrix. Thin solid grey lines are drill hole traces. Abbreviations: BTTZ-biotite-tourmaline transition zone, mt = magnetite, spec = specularite. Sample locations are indicated with red circles. After Frikken et al. (2005)

4.2.3 Breccia Infill paragenesis

Infill mineralogy is divided into the oxide and mineralisation stages. The oxide stage resulted in precipitaiton of biotite-anhydrite at deep levels (<3,400m above sea level)

and tourmaline-specularite at higher levels (>3000m). Tourmaline needles radiate outwards from breccia clast margins (Fig 4.4A). Specularite partly fills vugs and may be up to 3mm long (Fig 4.4B). The deposit thus shows a zoning in Fe-oxides from magnetite-dominated at depth to specular hematite dominated at upper levels of the deposit, concomitant with biotite –anhydrite (-Kspar) breccia cement at depth grading to tourmaline-sericite-quartz breccia matrix near surface (Fig 4.3).

The mineralisation stage deposited chalcopyrite-magnetite-quartz and pyrite. Sulfides show zonation from chalcopyrite-bornite- rich at depth, to pyrite rich at upper levels and lateral extremeties of the deposit.

Microthermometry performed on fluid inclusions in quartz cement yielded mineralisation stage temperatures of formation of 450 to 300 °C, based on homogenisation temperatures. Stable oxygen and sulfur isotope work are interpreted to show that a temperature gradient of 150 °C existed between early specularite-pyrite assemblages near surface and magnetite-chalcopyrite assemblages at depth. The temperatures obtained by Frikken (2003) are similar to those from Río Blanco reported by Kusakabe et al. (1990), who used S isotope geothermometry, fluid inclusion microthermometry and Mg^{2+}-Fe^{2+}-Fe^{3+} partitioning in biotite to estimate mineralisation and alteration temperatures at Río Blanco and El Teniente. Kusakabe et al. (1990) reported alteration temperatures of about 460 °C for potassic alteration with biotite forming at 430° to 440 °C. Those authors also noted that temperatures measured from microthermometry were 50° to 60 °C lower than those obtained from isotope and biotite geothermometry.

Frikken (2005) proposes a two stage model for mineralization; first, an early, catastrophic phreatomagmatic explosion exceeded lithostatic load, causing fracturing of the overlying rock mass, and depositing the early biotite-magnetite-anhydrite cement. This was followed by upwelling of magmatic brine that resulted in chalcopyrite precipitation.

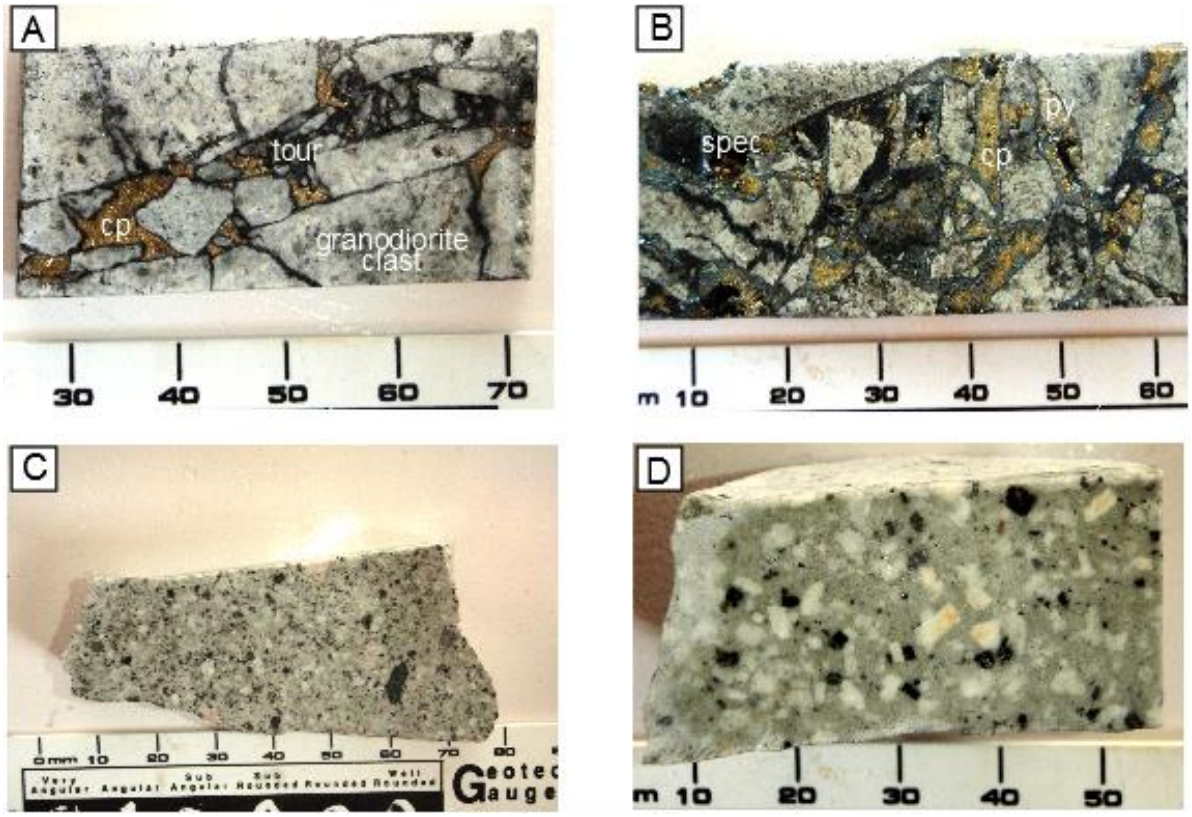

Figure 4.4 Examples of rock types from Sur and Río Blanco. A: Sample 150772-typical tourmaline breccia with sericite altered clasts of San Francisco batholith rimmed by tourmaline (black) ± magnetite and infill of chalcopyrite (yellow). B: Sample 150849-tourmaline breccia. Coarse-grained, bladed specularite (shiny grey) grows into vugs, Chalcopyrite (dark yellow) and tourmaline (black) infill space between clasts of granodiorite. Pyrite (paler yellow) appears to be paragenetically earlier than chalcopyrite. C: Don Luis Porphyry. D: Quartz Monzonite Porphyry

4.3. METHODS

4.3.1 Sample Selection

Core samples were collected from the rock library at the University of Tasmania. Samples were chosen from Río Blanco where drill core has intersected the earliest, highest-temperature magnetite-biotite-chalcopyrite assemblages,and from the Sur Sur breccia to cover a depth of ~1000m through the breccia pipe (Fig 4.3). A list of sample descriptions is contained within Table 4.1.

Table 4.1. Sample descriptions and Fe isotope analyses from Sur and Río Blanco

Sample Number	Deposit	Cross Section	Drill Hole	Depth (m)	Description	Mineral analysed	$\delta^{57}Fe$	2SD	$\delta^{56}Fe$	2SD
149064	Río Blanco		unknown		Dacite Chimney	whole rock	-0.64	0.09	-0.42	0.09
150866	Río Blanco	XC-155	DDH-555	250	Dacite Chimney	whole rock	-0.45	0.10	-0.30	0.03
150788	Río Blanco		surface		Don Luis Porphyry	whole rock	0.21	0.17	0.15	0.10
151016	Don Luis	XC-245	DDH-738	276.5	Felsic Porphyry	whole rock	0.33	0.06	0.21	0.02
151021	Río Blanco	XC-235	DDH-576		Felsic Porphyry	whole rock	0.21	0.09	0.14	0.03
150865	Río Blanco	XC-035	DDH-513	134	La Copa Rhyolite	whole rock	0.29	0.15	0.17	0.06
153209	Río Blanco		not recorded		La Copa Rhyolite	whole rock	0.20	0.08	0.13	0.06
150896	Río Blanco	XC-125	DDH--344	210	Quartz Monzonite Porphyry	whole rock	0.06	0.05	0.04	0.07
150762cp	Sur Sur	XC-50	TSS-22	37	chalcopyrite-pyrite ore	cp	-0.16	0.14	-0.12	0.10
150762py	Sur Sur					py	0.50	0.14	0.34	0.06
150773cp	Río Blanco	XC-130	DL-139.1	170	specularite-chalco ore	cp	-0.47	0.20	-0.32	0.16
150773hem	Río Blanco					spec	0.44	0.11	0.29	0.04
150773py	Río Blanco					py	-0.13	0.11	-0.10	0.08
150795cp	Río Blanco	XC-275	DDH-734	328.8	chalco-mgt ore	cp	0.07	0.12	0.04	0.07
150795mgt	Río Blanco					mgt	0.54	0.15	0.37	0.09
150805cp	Río Blanco	XC-275	DDH-734	386	chalco-mgt ore	cp	0.12	0.08	0.11	0.03
150805mgt	Río Blanco					mgt	0.76	0.09	0.51	0.05
150849cp	Sur Sur	XC-40	DL 57	86	specularite-chalco ore	cp	-0.24	0.07	-0.16	0.03
150849hem	Sur Sur					spec	0.30	0.02	0.17	0.01

Sample Number	Deposit	Cross Section	Drill Hole	Depth (m)	Description	Mineral analysed	$\delta^{57}Fe$	2SD	$\delta^{56}Fe$	2SD
150849py	Sur Sur					py	0.17	0.09	0.10	0.08
150851cp	Sur Sur	XC-90	TSS 12	118	chalco-mgt ore	cp	0.02	0.06	0.01	0.05
150851mt	Sur Sur					mgt	0.78	0.08	0.52	0.06
150856cp	Sur Sur	XC-70	DL-71	98	chalco-mgt ore	cp	-0.24	0.11	-0.17	0.09
150856mgt	Sur Sur					mgt	0.70	0.18	0.47	0.11
150876cp	Sur Sur	XC-50	C 50	60	chalco-mgt ore	cp	-0.41	0.12	-0.27	0.09
150876mgt	Sur Sur					mgt	0.24	0.14	0.15	0.11
150876py	Sur Sur					py	0.52	0.13	0.33	0.08
150905cp	Sur Sur	XC-50	DL 03	132	chalcopyrite-pyrite ore	cp	-0.46	0.11	-0.31	0.04
150905py	Sur Sur					py	0.57	0.01	0.39	0.01
151012py	Río Blanco	XC-130	DL 139.1	295.1	high grade ore	py	0.53	0.09	0.34	0.02
150923cp	Sur Sur	XC-50	TSS22	802	chalcopyrite ore	cp	-0.09	0.08	-0.07	0.08
150931cp	Sur Sur		TSS22	305	chalcopyrite ore	cp	-0.342	0.08	-0.25	0.08
150934cp	Sur Sur		TSS22	500.0	chalcopyrite ore	cp	-0.13	0.07	-0.18	0.07
150935py	Sur Sur		TSS22	501.0	chalcopyrite ore	py	0.68	0.04	0.44	0.12
150996cp	Sur Sur		TSS22	736.0	chalcopyrite ore	cp	0.30	0.04	0.18	0.09
151004cp	Río Blanco	XC-130	DL 139.1	300	high grade ore	cp	-0.35	0.16	-0.28	0.09

py=pyrite
mgt=magnetite
hem=specularite
cp=chalcopyrite

4.3.2 Mineral Separation:

Minerals were separated by either drilling with a tungsten-carbide tipped hand tool, or by cutting a wafer from drill core, which was then crushed in an agate mortar and pestle, and minerals hand-picked in ethanol under a binocular microscope. Magnetite was separated by a hand magnet.

4.3.3 Iron separation and Mass Spectrometry

Iron purification by ion-exchange chromatography, and mass spectrometry using the Neptune multi-collector housed at the Waite Campus followed methods described in Chapters 2 and 3, and are not described in detail here.

A 3-isotope plot, shown in Figure 4.5 illustrates the close fit of analyses to the mass dependent fractionation line of 0.667, showing that medium resolution is sufficient to resolve interferences from argon oxide and nitride species in the spectrometer.

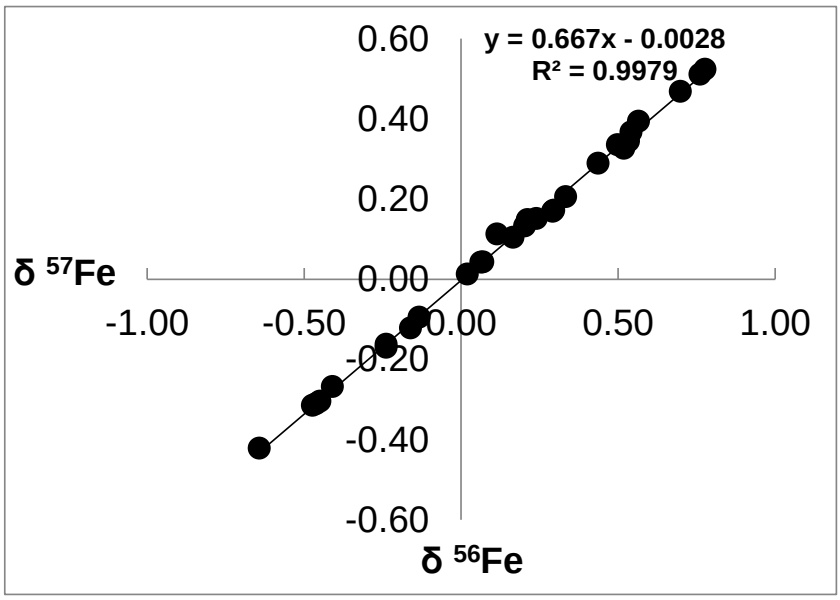

Figure 4.5 Three isotope plot of $\delta^{56}Fe$ v $\delta^{57}Fe$. The slope of the line at 0.667 matches the theoretical mass-dependent fractionation, showing that spectral interferences have been effectively eliminated in medium resolution mode.

4.4. RESULTS

Results are reported in delta notation, as for isotope values reported in Chapters 2 and 3. Uncertainties are reported as 2 times the standard deviation of replicate

analyses of the same sample. Samples were analysed a minimum of 3 times. Results are tabulated in Table 4.1, and illustrated in Figure 4.6.

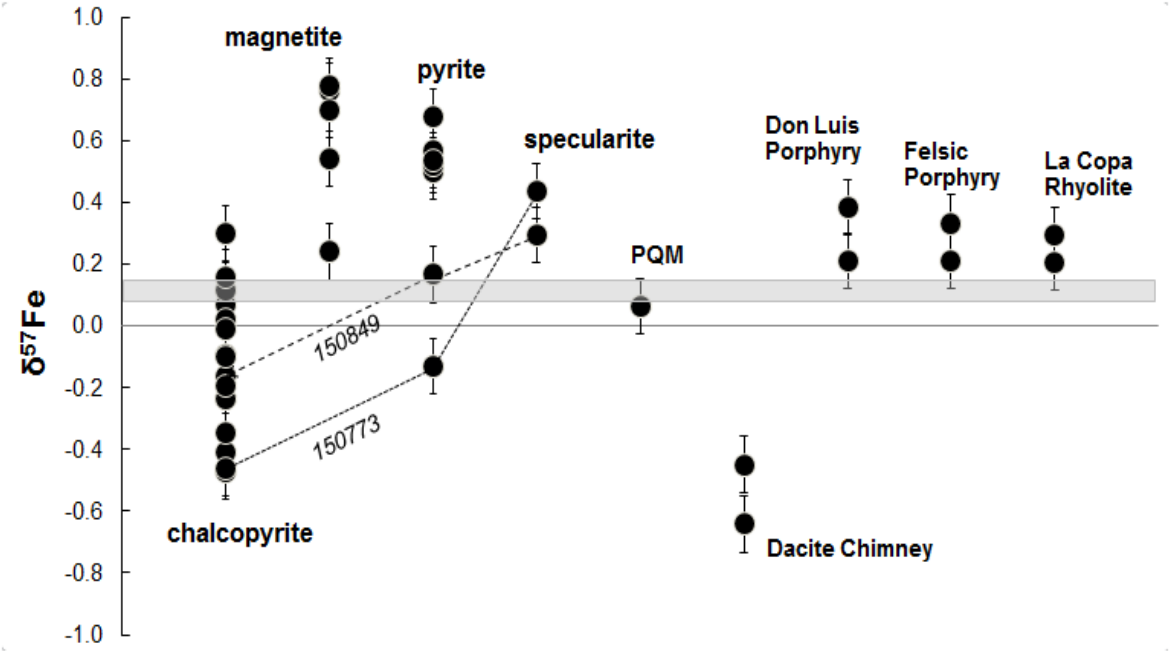

Figure 4.6 Iron isotope results of mineral separates and intrusions sampled from and around the Sur Sur tourmaline breccia. Tie lines join minerals sampled from the same piece of core, and are included to highlight the isotopically light values of pyrite replacing specularite. The horizontal shaded line is the $\delta^{57}Fe$ of MORB (+0.105‰; (Teng, 2013), shown for reference. PQM= Quartz Monzonite Porphyry

4.4.1 Iron isotopic composition of intrusions

The Quartz Monzonite Porphyry returned a $\delta^{57}Fe$ of 0.06 ± 0.05‰ and is thus isotopically lighter than the Don Luis Porphyry (0.21 ± 0.17 ‰), the Felsic Porphyry (+0.21 ± 0.09‰ and +0.33 ± 0.06‰) and La Copa Rhyolite (+0.29 ± 0.15 ‰ and +0.20 ± 0.08‰).

The two samples of the Dacite Chimney are isotopically light compared to the other intrusives (-0.45 ± 0.10‰ and -0.64 ± 0.09‰), which was unexpected; this could be a result of argillic alteration in the sample, but thin section petrography is required to confirm which minerals are present.

4.4.2 Iron isotopic composition of mineral separates

Results for mineral separates are shown in Figure 4.6 and detailed in Table 4.1. Chalcopyrite (n=15) results range from –0.47 ± 0.2‰ to 0.3 ± 0.04‰. Pyrite (n= 7) shows a cluster around +0.5‰, and two noticeably isotopically lighter values less than +0.1‰. Magnetite (n=5) varies from +0.24‰ to +0.78‰, and, with the exception of one sample, is heavier than specularite (n=2).

4.5. DISCUSSION

4.5.1 Fe isotope zonation

The well documented alteration zonation from biotite dominant at depth, to tourmaline dominant at shallow levels, and the change of Fe oxide mineralogy from magnetite to specularite allows a categorisation of samples into broad groups termed “deep”, “mid” and “shallow” (Figure 4.3). The Fe-isotope data grouped according to elevation are shown in Figure 4.7. The sample sets for Fe-oxides and pyrite are small, 7 samples in each, but clusters at values of around 4‰ (magnetite) and 5 ‰ (pyrite) suggest that isotope values are independent of depth. However, many more samples are needed to confirm this observation.

Chalcopyrite data display an intriguing suggestion that isotopic values are lighter at higher elevation, in tourmaline alteration zones, and heavier at depth in the biotite alteration zones. This distribution is examined with respect to temperature gradients as explored by Frikken (2003) and Frikken et al. (2005).

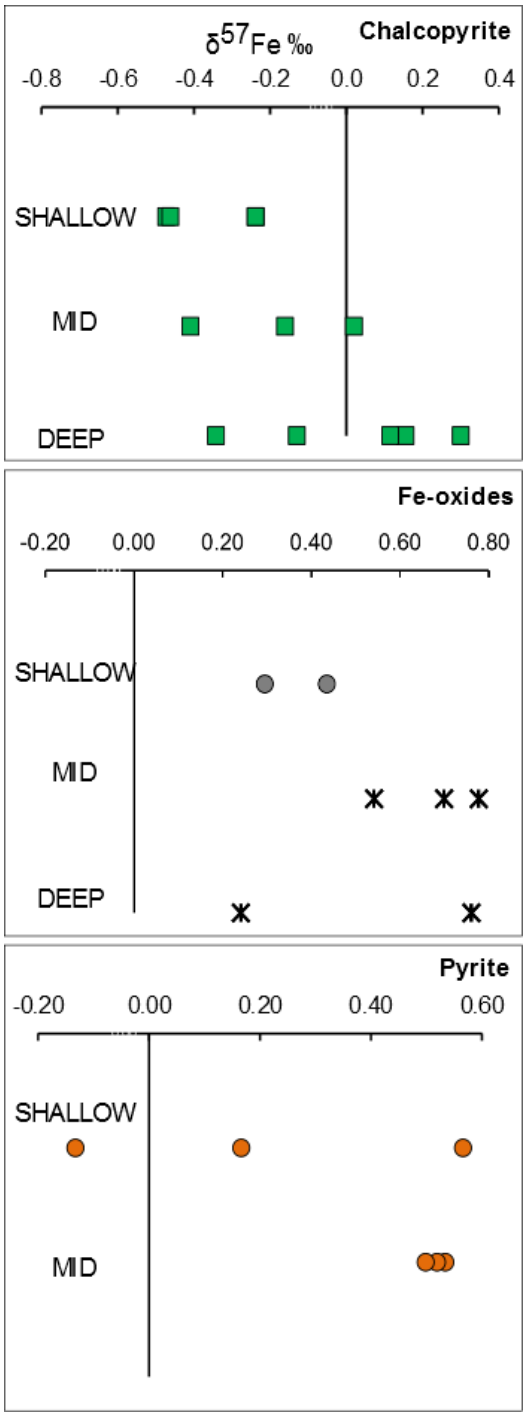

Figure 4.7 Variation of Fe isotope values of mineral separates with depth.

Frikken et al. (2005) report a zonation of $\delta^{34}S$ values in sulfide minerals from near-zero at depth to -4‰ in chalcopyrite at high levels in the breccia (>3,700m) in drill holes DL 03 and DL 64. These light $\delta^{34}S$ are coincident with enriched Cu grades (>2%; see Frikken et al., 2005 Figure 10). The models used by the authors required a temperature gradient of 150 °C to account for the $\delta^{34}S$ zonation.

If the Fe isotope fractionation between chalcopyrite-magnetite is mostly temperature controlled, then the fractionation observed should change with depth. Fractionation is inversely proportional to temperature (Schauble, 2004), so we would expect smaller fractionation in samples from the deeper part of the breccia, and larger fractionation in samples from higher levels.

The theoretical fractionation between magnetite and chalcopyrite has been calculated by spectroscopic means (Polyakov et al., 2007; Polyakov and Soultanov, 2011), and the theoretical fractionation is shown as a function of temperature in Figure 4.8 as a smooth curve which approaches zero as temperature increases.

An apparent fractionation, $\Delta^{57}Fe_{mgt\text{-}cp}$ is calculated from the measured delta values of the magnetite and chalcopyrite mineral separates by simple subtraction:

$$\Delta^{57}Fe_{mgt\text{-}cp} = \delta^{57}Fe_{mgt} - \delta^{57}Fe_{cp}$$

The results for 5 magnetite-chalcopyrite mineral pairs are shown in Table 4.2 and Figure 4.8. Note that the allocation of “deep” and “mid” levels is based on geological logging codes reported by Frikken (2003) which are based on presence of either biotite or tourmaline cementing the breccia.

Sample number	Depth	Apparent fractionation	Formation Temperature
150795	deep	0.47	400 ºC
150805	deep	0.65	290 ºC
150851	mid	0.76	250 ºC
150856	mid	0.94	190 ºC
150876	mid	0.65	290 ºC

Table 4.2 Apparent fractionation between magnetite and chalcopyrite mineral pairs

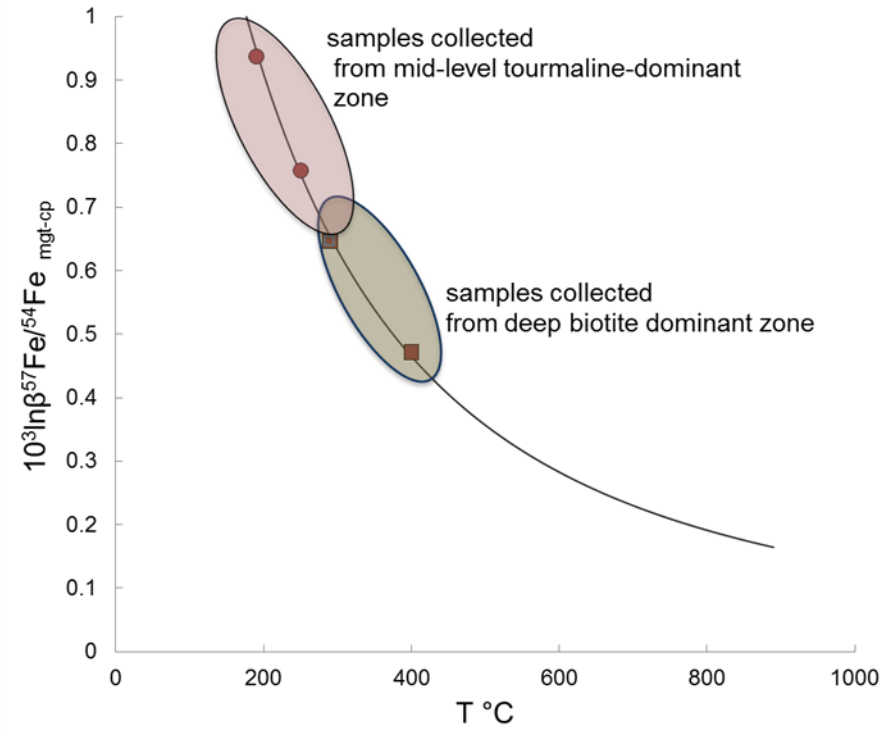

Figure 4.8 Apparent fractionation of Fe isotopes between magnetite and chalcopyrite pairs as function of temperature

The apparent fractionation between magnetite and chalcopyrite is consistent with larger fractionations at higher level, which would explain the distribution of chalcopyrite $\delta^{57}Fe$ values with depth. The smallest apparent fractionation, 0.47‰ (sample 150795) yields a formation temperature of 400 °C which is consistent with temperatures calculated by Frikken (2003) from fluid inclusion microthermometry. The difference between the hottest and coolest formation temperatures indicated by the fractionation curve (190 and 400 °C) is 210 °C, a similar result to the temperature gradient modelled by Frikken et al. (2005) to explain sulfur isotope zonation. These results are encouraging for the use of ore minerals as geothermometers, however the present sample set is rather small and more data is required to explore this trend fully.

However, the results have an overall displacement towards cooler temperatures, as observed in the Batu Hijau data (Chapter 3), again suggesting that isotope fractionation between magnetite and chalcopyrite is controlled by other factors than just temperature, for example, a kinetic overprint (e.g. Dziony et al., 2013).

A Rayleigh-type process of magnetite-chalcopyrite formation was modelled for Batu Hijau (Chapter 3). A comparison of the Batu Hijau model and $\delta^{57}Fe$ values for Río Blanco magnetite-chalcopyrite pairs is shown in Figure 4.9, which clearly demonstrates the similarity of results between the two deposits, and that an isotopically light fluid of around -0.1‰ can produce magnetite and chalcopyrite of the $\delta^{57}Fe$ values measured in this study.

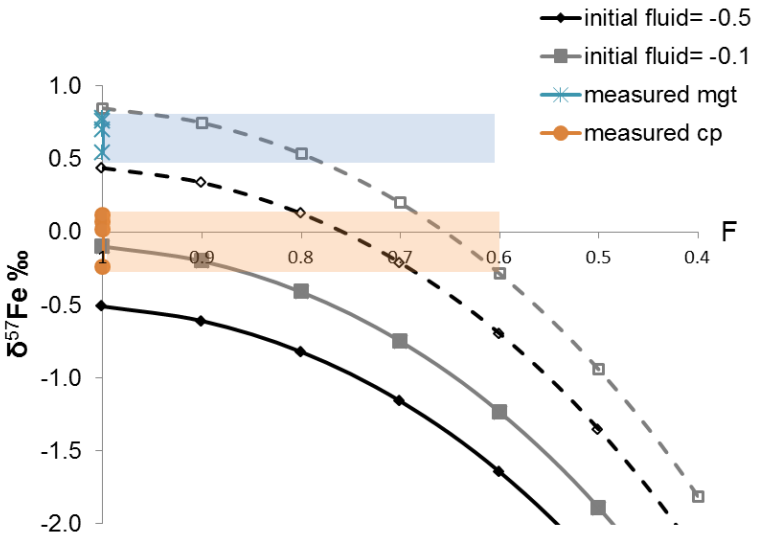

Figure 4.9 Rayleigh model of magnetite-chalcopyrite formation. The solid curves represent the starting $\delta^{57}Fe$ of a hydrothermal fluid from which magnetite and chalcopyrite are co-precipitated. The dashed lines are the $\delta^{57}Fe$ of the instantaneous magnetite product.

4.5.2 Fe isotopes integrated with copper grade and sulfur isotope data

Several samples in this study were selected where fluid inclusion and stable sulfur isotope analyses had been performed by Frikken (2003). Cu grade is also known for most samples. The relationship between $\delta^{57}Fe$ and $\delta^{34}S$ and Cu grade is shown in Figure 4.10.

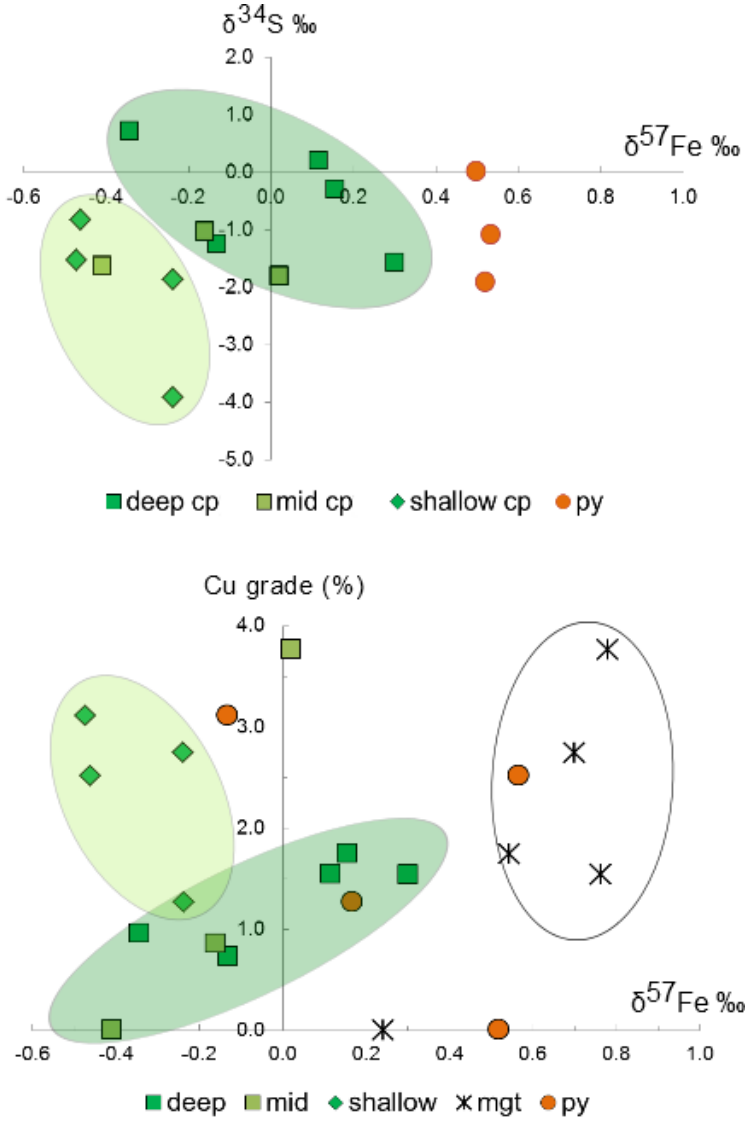

Figure 4.10 Fe isotope values of mineral separates compared to S isotope values and Cu grade. Chalcopyrite mineral separates are categorised according to the alteration zone from which they were sampled, viz., the “deep” biotite magnetite zone (dark green squares), the “mid” level of tourmaline-mgt>specularite zone (light green squares) and the “shallow” tourmaline-specularite zone (green diamonds).

There are few samples of magnetite and pyrite with corresponding Cu grade and S isotope data. No conclusions can be drawn at this stage from such few data points. However, the chalcopyrite analyses suggest some trends. In the upper figure, the chalcopyrite samples from the shallow level in the deposit appear to form a cluster of samples with light values of both δ^{57}Fe and δ^{34}S. The samples from deeper levels have δ^{34}S isotope values between -2 and +1 ‰ and the group covers almost all the range of measured δ^{57}Fe values. In the lower figure, the chalcopyrite samples from

the shallow level in the deposit cluster at higher copper grades, interpreted by Frikken (2003) to have formed from remobilisation of an earlier generation of copper minerals. There is also an apparent positive correlation between $\delta^{57}Fe$ and Cu grade in samples from deeper in the deposit.

The grouping of isotopically light $\delta^{57}Fe$ and $\delta^{34}S$ values is intriguing, because it implies that coupled studies may be able to distinguish generations of chalcopyrite that have formed from different processes. For example, experimental studies by Zhao et al. (2014a, 2014b) at hydrothermal temperature (200 to 320 °C) demonstrate that Fe^{2+} is released into solution during the replacement of chalcopyrite by bornite, and the replacement of hematite by chalcopyrite. Qian et al. (2010) demonstrated that sulfidation of magnetite to pyrite also releases Fe^{2+} into solution. The release of Fe^{2+} incorporates the light isotope (e.g. Dziony et al., 2013), thus Cu-Fe sulfides formed by replacement reactions could be expected to be isotopically light. This is one explanation for the isotopically light pyrite in samples 150849 and 150773, and the isotopically lightest chalcopyrite samples from shallow levels in the deposit (samples 150773 and 150905).

4.5.3 Comparison with Batu Hijau

Results from both porphyry deposits are illustrated in Figure 4.11. With the exception of the Quartz Monzonite Porphyry, the felsic intrusions from Río Blanco have an identical range to the quartz diorites and tonalites from Batu Hijau, consistent with thermodynamic modelling in Chapter 3 demonstrating that I-type magmas evolve to isotopic values generally 0.2-0.3 ‰.

The Fe-oxide mineral separates also cover an identical range. Bornite and chalcopyrite from Batu Hijau have a more restricted range of values than the chalcopyrite separates from Sur Sur. However, with the exception of the two isotopically light pyrite samples, mineral separates show the groupings predicted by theory; magnetite and pyrite are expected to have heavier values compared to chalcopyrite owing to the presence of Fe^{3+} in the mineral lattice and covalent Fe-S bonding respectively.

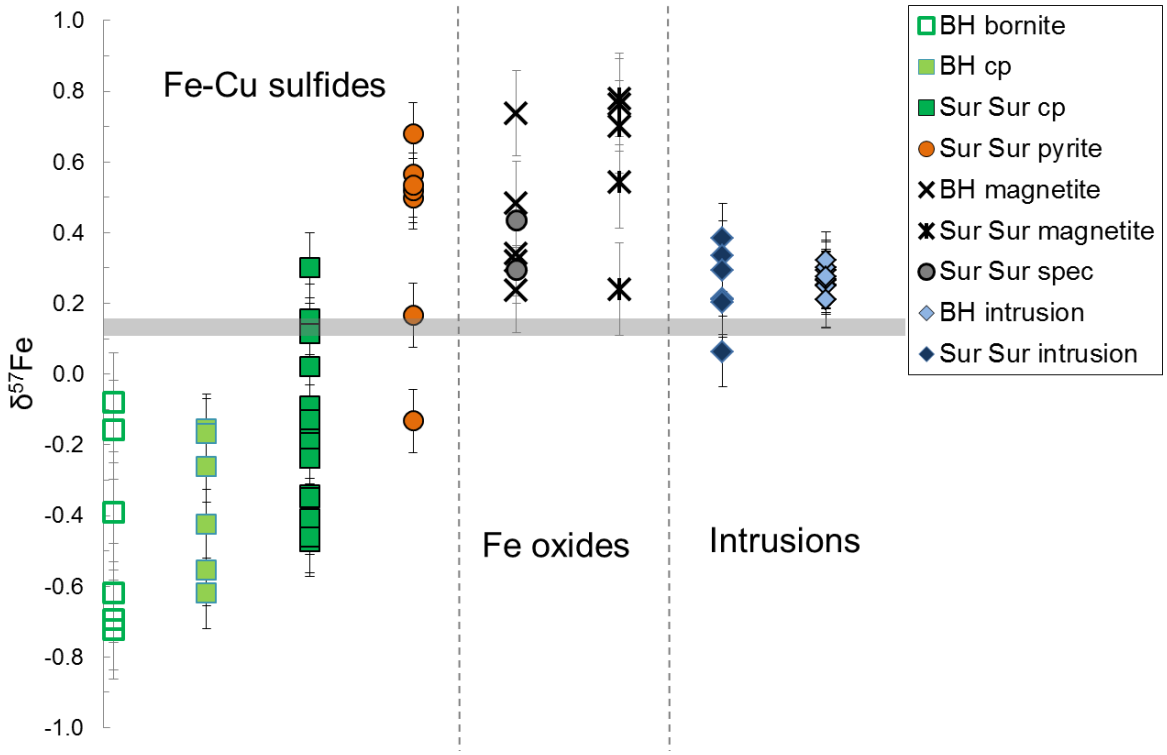

Figure 4.11 Fe-isotope values for intrusions and mineral separates from Batu Hijau and Sur Sur. The grey shaded bar is the average δ^{57}Fe of MORB for comparison. Pyrite is atypical at Batu Hijau (Garwin, 2000) and is not present in the samples included in this study. Error is 2 times standard deviation of replicate analyses of the same sample. Abbreviations: BH = Batu Hijau, cp = chalcopyrite, spec = specularite.

4.6. CONCLUSION

This study analysed the δ^{57}Fe values of magmatic intrusions and separates of magnetite, specularite, chalcopyrite and pyrite from the giant Río Blanco-Los Bronces porphyry copper-molybdenum deposit, and compared the results to those obtained from Batu Hijau, a porphyry copper-gold deposit. Despite the differences in tectonic setting (Andean margin and island arc, respectively), the results are strikingly similar, pointing to the local influence of fluid and mineral formation processes in determining the δ^{57}Fe values of minerals.

The δ^{57}Fe values of chalcopyrite, when coupled with δ^{34}S values result in grouping of minerals that highlight the potential of integrated studies to track metal formation processes. The use of multiple isotope systems helps to resolve fluid sources and processes, given that isotopically light δ^{57}Fe values in sulfides can result from a variety of processes, and the interpretation of data is therefore non-unique. Both inter-mineral fractionation and remobilisation of Fe^{2+} during coupled dissolution-

reprecipitation reactions can produce sulfides with isotopically light $\delta^{57}Fe$ values, highlighting the necessity of establishing clear paragenetic history of minerals to be sampled.

ACKNOWLEDGMENTS

This work forms part of the author's PhD research. This study was funded by a grant from the Institute for Mineral and Energy Resources at the University of Adelaide to Professor John D. Foden, the author's principle supervisor. Collection of samples from the University of Tasmania was funded by the award of an Eric Rudd Scholarship to the author. The author gratefully acknowledges the assistance of Professor David Cooke, Dr. Mike Baker, Dr. Nathan Fox, Dr Jose Piquer and Ms Isabel von Lichtan at UTAS for discussion and logistical support.

References

Davidson, P. (2004). A new methodology for the study of magmatic-hydrothermal transition in felsic magmas: application to barren and mineralised systems. PhD thesis, University of Tasmania.

Davidson, P., Kamenetsky, V., Cooke, D. R., Frikken, P., Hollings, P., Ryan, C., Van Achterbergh, E., Mernagh, T., Skarmeta, J., Serrano, L., Vargas, R. (2005). Magmatic precursors of hydrothermal fluids at the Río Blanco Cu-Mo deposit, Chile: Links to silicate magmas and metal transport. Economic Geology 100, 963-978.

Deckart, K., Clark, A. H., Aguilar, C., Vargas, R., Bertens, A., Mortensen, J. K., Fanning, M. (2005). Magmatic and hydrothermal chronology of the giant Río Blanco porphyry copper deposit, central Chile: Implications of an integrated U-Pb and Ar-40/Ar-39 database. Economic Geology 100, 905-934.

Deckart, K., Godoy, E., Bertens, A., Jerez, D., Saeed, A. (2010). Barren Miocene granitoids in the Central Andean metallogenic belt, Chile: Geochemistry and Nd-Hf and U-Pb isotope systematics. Andean Geol 37, 1-31.

Deckart, K., Clark, A. H., Cuadra, P., Fanning, M. (2013). Refinement of the time-space evolution of the giant Mio-Pliocene Río Blanco-Los Bronces porphyry Cu-Mo cluster, Central Chile: new U-Pb (SHRIMP II) and Re-Os geochronology and Ar-40/Ar-39 thermochronology data. Miner Deposita 48, 57-79.

Dziony, W., Horn, I., Lattard, D., Koepke, J., Steinhoefel, G., Schuessler, J. A., Holtz, F. (2014). In-situ Fe isotope ratio determination in Fe-Ti oxides and sulfides from drilled gabbros and basalt from the IODP Hole 1256D in the eastern equatorial Pacific Chem. Geol., 363, 101-113.

Frikken, P.H. (2003). Breccia-hosted copper-molybdenum mineralisation at Río Blanco, Chile. Ph.D thesis, University of Tasmania.

Frikken, P.H., Cooke, D. R., Walshe, J. L., Archibald, D., Skarmeta, J., Serrano, L., Vargas, R. (2005). Mineralogical and isotopic zonation in the Sur-Sur tourmaline breccia, Río Blanco-Los Bronces Cu-Mo deposit, Chile: Implications for ore genesis. Economic Geology 100, 935-961.

Garrido, I., Cembrano, J., Sina, A., Stedman, P., Yanez, G. (2002). High magma oxidation state and bulk crustal shortening: key factors in the genesis of Andean porphyry copper deposits, central Chile (31-34 degrees S). Rev Geol Chile 29, 43-54.

Garwin, S. L. (2000). The setting, geometry and timing of intrusion-related hydrothermal systems in the vicinity of the Batu Hijau copper-gold deposit, Sumbawa, Indonesia. PhD thesis, University of Western Australia.

Kusakabe, M., Hori, H., and Matsuhisa, Y. (1990). Primary mineralization-alteration of the El Teniente and Río Blanco porphyry copper deposits, Chile. Stable isotopes, fluid inclusions and Mg2+/Fe2+/Fe3+ ratios of hydrothermal biotite.

Piquer, J. H., Skarmeta, J. and Cooke, D. R. (2015). Structural Evolution of the Río Blanco-Los Bronces District, Andes of Central Chile: Controls on Stratigraphy, Magmatism, and Mineralization. Econ Geol 110, 1995-2023.

Polyakov, V. B., Clayton, R. N., Horita, J., Mineev, S. D. (2007). Equilibrium iron isotope fractionation factors of minerals: reevaluation from the data of nuclear inelastic resonant X-ray scattering and Mössbauer spectroscopy. Geochim. Cosmochim Acta 71, 3833-3846.

Polyakov, V. B., Soultanov, D. M. (2011). New data on equilibrium iron isotope fractionation among sulfides: constraints on mechanisms of sulfide formation in hydrothermal and igneous systems. Geochim. Cosmochim. Acta 75, 1957-1974.

Schauble, E. A. (2004). Applying stable isotope fractionation theory to new systems. Rev. Min. Geochem. 55, 65-111.

Schauble, E. A. (2004). Applying stable isotope fractionation theory to new systems. Rev. Min. Geochem. 55, 65-111.

Skewes, M.A., Holmgren, C., Stern, C. R. (2003). The Donoso copper-rich, tourmaline-bearing breccia pipe in central Chile: petrologic, fluid inclusion and stable isotope evidence for an origin from magmatic fluids. Miner Deposita 38, 2-21.

Teng, F.-Z., Dauphas, N., Huang, S., Marty, B. (2013). Iron isotopic systematics of oceanic basalts. Geochim. Cosmochim. Acta 107, 12-26.

Warnaars, F.W., Holmgren, C., Barassi, S. (1985). Porphyry Copper and Tourmaline Breccias at Los-Bronces-Río-Blanco, Chile. Economic Geology 80, 1544-1565.

Toro, J., Ortúzar, J., Zamorano, J., Cuadra, P., Hermosilla, J., Spröhnle, C. (2012). Protracted magmatic-hydrothermal history of the Río Blanco-Los Bronces District, Central Chile: Development of the World's greatest known concentration of copper. In Hedenquist, J. W., Harris, M. and Camus, F. (Eds), Geology and Genesis of Major Copper Deposits and Districts of the World: A Tribute to Richard H. Sillitoe. Society of Economic Geologists Special Publication 16.

Qian, G., Brugger, J., Skinner, W. M., Chen, G., Pring, A. (2010). An experimental study of the mechanism of the replacement of magnetite by pyrite up to 300 °C. Geochim. et Cosmochim. Acta 74, 5610-5630.

Zhao, J., Brugger, J., Chen, G., Ngothai, Y., Pring, A. (2014a). Experimental study of the formation of chalcopyrite and bornite via the sulfidation of hematite: Mineral replacements with a large volume. Am. Mineral. 99, 343-354.

Zhao, J., Brugger, J., Ngothai, Y., Pring, A. (2014b). The replacement of chalcopyrite by bornite under hydrothermal conditions. Am. Mineral. 99, 2389-2397.

Statement of Authorship

Title of Paper	Fe-isotope fractionation in magmatic-hydrothermal mineral deposits: A Case studies from the Olympic Iron Oxide-Copper-Gold Domain, South Australia
Publication Status	☐ Published ☐ Accepted for Publication ☐ Submitted for Publication ☑ Unpublished and Unsubmitted work written in manuscript style
Publication Details	

Principal Author

Name of Principal Author (Candidate)	Christine Wawryk
Contribution to the Paper	Collected samples from the field and mine sites. Performed all sample preparation, analyses and interpretation. Wrote the manuscript and acted as corresponding author.
Overall percentage (%)	100
Certification:	This paper reports on original research I conducted during the period of my Higher Degree by Research candidature and is not subject to any obligations or contractual agreements with a third party that would constrain its inclusion in this thesis. I am the primary author of this paper.
Signature	Date 4/4/2017

Co-Author Contributions

By signing the Statement of Authorship, each author certifies that:

i. the candidate's stated contribution to the publication is accurate (as detailed above);

ii. permission is granted for the candidate in include the publication in the thesis; and

iii. the sum of all co-author contributions is equal to 100% less the candidate's stated contribution.

Name of Co-Author			
Contribution to the Paper			
Signature		Date	

Name of Co-Author			
Contribution to the Paper			
Signature		Date	

Please cut and paste additional co-author panels here as required.

CHAPTER 5. FE ISOTOPE FRACTIONATION IN MAGMATIC-HYDROTHERMAL MINERAL DEPOSITS: CASE STUDIES FROM THE OLYMPIC IRON OXIDE COPPER GOLD DOMAIN, SOUTH AUSTRALIA

Christine M. Wawryk*,[a] ,John D. Foden[a] and K. Ehrig[b]

[a]Centre for Tectonics, Research and Exploration, University of Adelaide, North Tce, South Australia, 5005, Australia

[b]BHP Billiton, Adelaide South Australia, 5000, Australia

[*]corresponding author. Tel: +61 8 8313 1717. E-mail address: christine.wawryk@adelaide.edu.au

ABSTRACT

The giant Olympic Dam breccia and Hillside skarn are Iron Oxide Copper Gold (IOCG) deposits located on the Gawler Craton, South Australia. Deposit formation is spatially and temporally associated with the 1.59 Ga voluminous, bimodal Gawler Range Large Igneous Province. Iron isotope analyses of bulk whole rock A-type granites of Hiltaba Suite intrusions, and magnetite, siderite, pyrite, chalcopyrite, bornite and hematite were measured to investigate the $\delta^{57}Fe$ values of mineral separates from the IOCG deposit style. A total of 92 samples were prepared for analysis from Olympic Dam and surrounding prospects, and 35 samples were collected from the Hillside deposit. Iron isotope measurements were performed at the University of Adelaide on a Thermo Finnigan Neptune Multi-Collector ICP-MS.

Hiltaba Suite intrusions are relatively isotopically heavy ($\delta^{57}Fe$ up to 1.03‰), consistent with published results from the literature for evolved high silica magmatic rocks. Mineral separates such as siderite, magnetite, hematite, chalcopyrite and pyrite have isotopic values that are consistent with theoretical mineral-mineral fractionation factors. Siderite from Olympic Dam and bornite from Hillside are the minerals with the lightest $\delta^{57}Fe$ values (siderite ranges from -2.20 to -1.59 ±0.04‰; bornite values are -1.44±0.21‰ and -1.53±0.05‰). Pyrite and magnetite returned ranges that are similar between the deposits, however the opposing signs of $\Delta^{57}Fe_{py\text{-}mgt}$ are enigmatic and may be a result of preservation of isotopically light precursor minerals or quantitative dissolution of isotopically heavy precursor minerals. Hematite

from Olympic Dam returned $\delta^{57}Fe$ values ranging from -0.43±0.05‰ to 1.38±0.15‰. The data suggest that the area of the deposit sampled by drill hole RD1988 has different fluid characteristics, as hematites are isotopically relatively heavy (>0.5‰) from this area, paired with higher levels of Mo-As-W-Sn-Sb. Isotope values of hematite and magnetite, sampled where clear overprinting relationships are evident at Olympic Dam, are isotopically indistinguishable within analytical error. This contrasts with previously published oxygen isotope results, suggesting that Fe isotopes alone are unable to discriminate fluid mixing events at hydrothermal temperatures.

Bladed hydrothermal hematite crystals intergrown with chalcopyrite yield temperatures of formation between 210-390°C, calculated using theoretical fractionation factors. These temperatures are consistent with fluid inclusion microthermometric homogenisation temperatures of between 130 °C and 360°C. This highlights the applicability of Fe isotopes as a geothermometer in opaque minerals.

5.1. INTRODUCTION

The use of stable Fe isotopes to investigate magmatic processes has been facilitated by the advent of sensitive analytical equipment that can resolve the small fractionations arising from high temperature processes, and/or small relative mass differences (Johnson et al., 2004). Over the last decade, the number of stable Fe isotope analyses of igneous rocks has illustrated that the “bulk terrestrial igneous rock” ratio of $\delta^{56}Fe$ 0.0±0.05‰ (Beard et al., 2003) can be refined into a much wider range of isotopic compositions, particularly for granite rocks which may be as heavy as 0.89‰ ($\delta^{57}Fe$, Wang et al., 2015). Magmatic processes that result in isotopically heavy granites include anatexis (Foden et al., 2015; Telus et al., 2012), crystal fractionation (e.g. Teng et al., 2008; Schuessler et al., 2007; Dauphas et al., 2014), mass diffusion (Huang et al., 2009; Gajos, 2014; Zambardi et al., 2014) and fluid exsolution (Poitrasson and Freydier, 2005; Heimann et al., 2008). Telus et al. (2012) analysed pegmatites from the Black Hills in Dakota, where the reaction between exsolved fluids and reacted country rock were well documented. The authors used thermodynamic modelling to show that fractional crystallisation alone cannot account for the large dispersion of Zn/Fe ratios observed in the samples, and concluded that fluid exsolution does control iron isotope fractionation to some extent in magmatic processes.

Fluid exsolution from cooling and crystallising magmas may produce chloride-rich, metal-bearing fluids that form economic ore deposits (e.g. Candela and Holland 1984; Eugster 1985). Furthermore, properties of magmas such as composition, oxidation state, degree of evolution and degree of differentiation are important parameters that control the ore element associations in mineralised igneous terrains (Ishihara 1981; Blevin and Chappell 1992; Blevin 2003). Tin-tungsten deposits are commonly associated with strongly evolved and fractionated, reduced (fO_2<FMQ) S-type granites. Porphyry style Cu-Au-Mo deposits are usually associated with oxidised (fO_2≥FMQ+2), hydrous, I-type arc magmas which are generally less fractionated and have intermediate SiO_2 contents. The A-type granites are generally potassic, Fe-rich and metaluminous (Frost et al., 2001), and show evidence for protracted fractional crystallisation histories (e.g. Foden et al., 2015). However, the metallogeny of A-type granites, especially with respect to Iron Oxide Copper Gold (IOCG) deposits remains controversial, with evidence for both magmatic and magmatic-hydrothermal (e.g. Pollard, 2006) and non-magmatic fluids (e.g. Barton and Johnson,1996) reported in the extensive literature.

The effect of variables such as oxidation state and mode of buffering on the Fe isotope evolution of S, I and A-type magmas was examined by Foden et al. (2015). Whilst relatively reduced magmas may fractionate to yield isotopically heavy Fe in the most evolved felsic end-members, oxidised systems tended to show less fractionation towards heavy Fe or may even evolve towards isotopically slightly lighter end members. The other key influence was the mode of buffering of the magma; closed (unbuffered) systems tend to evolve to isotopically heavy final fractionates, while buffered “open-system” behaviour can dampen trends towards final relative enrichment in ^{57}Fe and ^{56}Fe.

Although granite type (S, I or A), oxidation state and degree of fractionation influence both Fe isotope composition of crystallising igneous rocks, and metal associations in related ore deposits, it is poorly understood whether the Fe-isotopes of commonly found ore minerals such as magnetite, pyrite and chalcopyrite also reflect key variables such as oxidation state. We have previously measured magnetite and chalcopyrite from the Renison Sn deposit which is associated with a reduced, highly fractionated S-type granite (Wawryk and Foden, 2015), and the Batu Hijau Cu-Au deposit, which is associated with oxidised, intermediate juvenile arc magmas (Wawryk et al., 2017, submitted). Our results clearly show that magnetite and

chalcopyrite from the Renison deposit (magnetite $\delta^{57}Fe$=1.0±0.06‰, chalcopyrite $\delta^{57}Fe$= 0.28 to 1.32±0.07‰) are isotopically heavier than magnetite and chalcopyrite from the porphyry copper deposit (magnetite $\delta^{57}Fe$= 0.24 to 0.74±0.1‰, chalcopyrite $\delta^{57}Fe$= -0.62 ‰ to -0.16 ± 0.05‰). Comparison with magmatic-hydrothermal chalcopyrite analyses from the literature also shows chalcopyrite to be isotopically light (0 to -3‰ at Grasberg, Graham et al., 2004; ~0 ‰ at Northparkes, Li et al., 2010).

To date, no Fe-isotope analyses of minerals from IOCG deposits have been published. The iron oxide copper gold (IOCG) deposits of the Gawler Craton, South Australia, which include the supergiant Olympic Dam deposit (e.g. Reeve et al., 1990), were formed during a tectonothermal event coincident with extensive extrusive and intrusive magmatic activity (e.g. Skirrow et al., 2007; Hayward and Skirrow, 2010). The magmatic intrusions comprise the well-studied A-type Hiltaba suite granitoids (e.g. Creaser, 1995, 1996; Stewart, 1994; Stewart and Foden, 2003). In this paper we present results of iron isotope analyses of Hiltaba Suite granites (s.l) and Fe-bearing sulfides, oxides and siderite mineral separates from the Olympic Dam Cu-U-Au-Ag deposit and peripheral IOCG systems, and the Hillside Cu-Au deposit. Fluid inclusion, stable isotope and mineral chemistry provide independent data with regard to fluid temperatures in both deposits (e.g. Oreskes and Einaudi, 1992; Ismail et al., 2014a) enabling an evaluation of the use of iron isotopes as a geothermometer. We also investigate whether the magnetite-hematite replacement seen at Olympic Dam are characterised by Fe-isotope fractionation.

5.2. REGIONAL SETTING

The geodynamic and structural framework of the Gawler Craton has been recently reviewed by Hayward and Skirrow (2010). These authors review the findings of multidisciplinary studies of basement geology conducted by Primary Industries and Resources South Australia, Geoscience Australia, the University of Tasmania, the University of Adelaide and industry partners. The Geoscience Australia studies were published in 2007, in a Special Issue of Economic Geology, Volume 102, number 8. The summary below draws on contributions to the 2007 Economic Geology Special Issue and Hayward and Skirrow's (2010) review paper, and considers mainly the crystalline basement comprising the eastern part of the Gawler Craton, defined by Skirrow et al. (2002) as the "Olympic Cu-Au Domain".

A generalised geological map of the Gawler Craton is illustrated in Fig 5.1. The development of Paleo- to Mesoproterozoic basement between ca. 2000 and 1690 Ma was dominated by rift basin development (Hand et al., 2007). The largest basin sequence is the Hutchinson Group, a sequence of shallow marine clastic and chemical sedimentary rocks with felsic volcanics and volcaniclastics in the upper parts. The Hutchinson group was intruded along much of the eastern craton margin by granodiorite, and lesser granite, quartz monzonite and mafic rocks of the Donington Suite at ca.1850, during the Cornian orogeny (Hand et al., ibid).

From ca. 1790 to 1760 Ma, bimodal volcanics and sediments of the Wallaroo Group were deposited in syn-rift basins (Hand et al, 2007). The Wallaroo Group is an important host rock for IOCG systems studied by Skirrow et al. (2007). It consists of sequences of diverse volcanosedimentary rocks including siltstones, graphitic sediments, quartzites, iron-rich sediments, and possibly evaporates, based on sodium-rich lithologies and metamorphic scapolite (Conor et al., 2010). The Wallaroo Group and equivalents were deformed and metamorphosed during the Kimban orogeny (1730 to 1690 Ma), with regional metamorphic facies ranging from upper greenschist to mid-amphibolite grade (Ferris et al., 2002; Conor et al, ibid).

Development of the Olympic Cu-Au domain between ca.1600 and 1575 Ma coincides with the emplacement of voluminous bimodal lavas and felsic ignimbrites and pryoclastics of the Gawler Range Volcanics (e.g. Giles, 1988; Creaser and White, 1991, Stewart and Foden, 2003). Co-magmatic with the extrusive rocks were plutons and batholiths of the Hiltaba Suite, a series of A-type, oxidised and evolved granitoids, at least some of which were synchronous with regional deformation in the Moonta subdomain (Conor et al., 2010). The characteristics of the Hiltaba Suite are described in more detail in the following section.

Archaean and early Mesoproterozoic rocks in the Olympic Dam area are overlain by Mesoproterozoic, Neoproterozoic and Cambrian sedimentary successions of the Stuart Shelf (Skirrow et al., 2007).

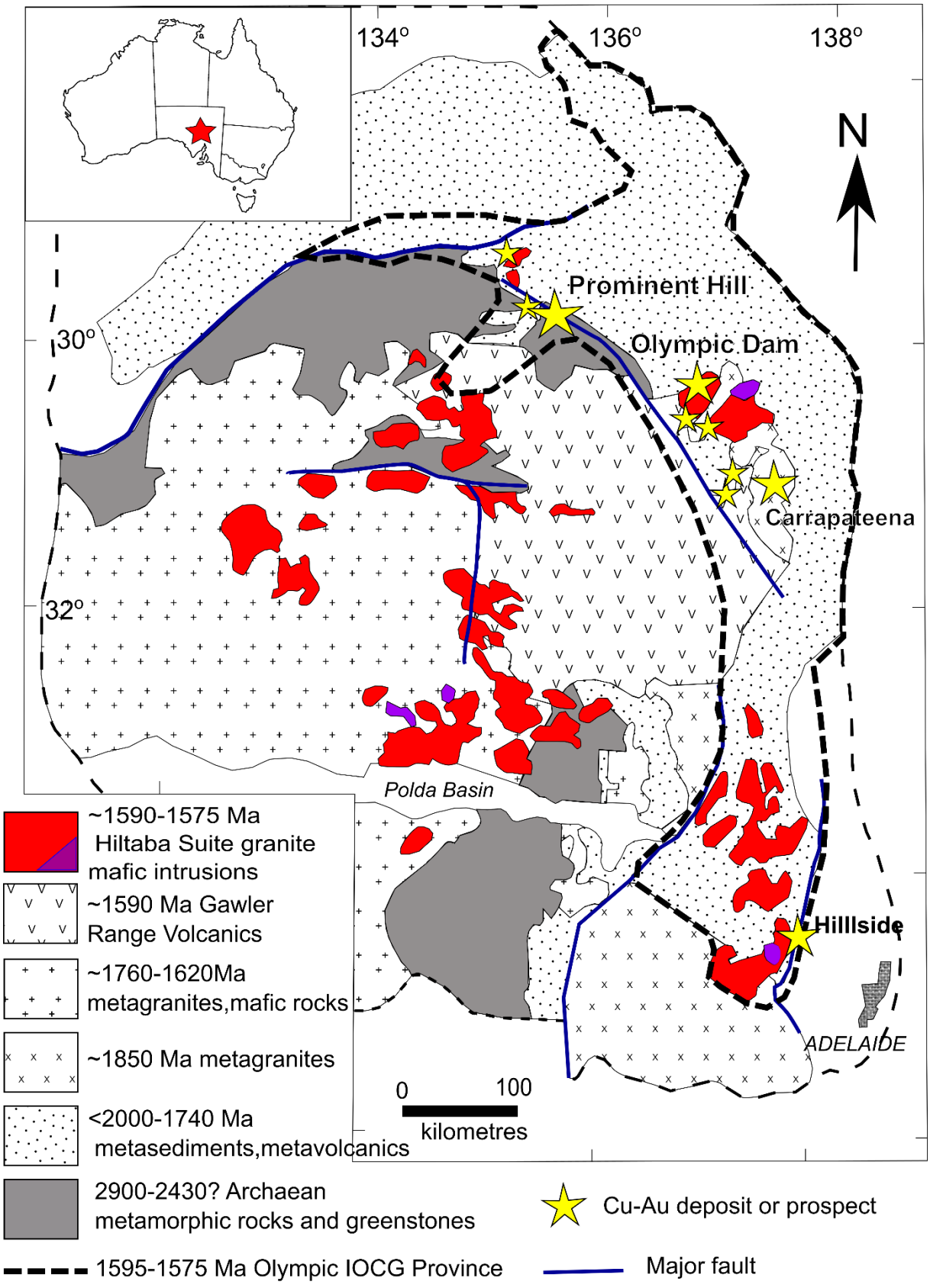

Figure 5.1 Geology of the Gawler Craton. Simplified basement geology showing the Olympic Cu-Au province, and location of IOCG deposits and prospects. (after Skirrow and Davidson, 2007).

5.3. THE HILTABA SUITE

The Hiltaba Suite, together with the voluminous ~1590 Gawler Range Volcanics (GRV), forms a volcano-plutonic complex which covers an estimated 25,000km3 of the Gawler Craton in South Australia (Blisset et al, 1993; Creaser and Cooper, 1993). The Hiltaba Suite is bimodal; quartz monzodiorites and tonalites, granites, granodiorites and syenogranites are dominant, however, ultramafic and mafic rocks, whilst apparently volumetrically minor, are widespread (Creaser and Cooper 1993 and references therein; Johnson and McCulloch, 1995; Creaser 1996; Stewart and Foden, 2003; Zhang et al, 2007). The Hiltaba Suite has been dated by precise U-Pb in zircon geochronology. Ages range from ~1600 to ~1585 Ma (Fanning et al, 1988; Creaser and Cooper, 1993; Johnson and Cross, 1995; Conor et al., 2010).

5.3.1 General Mineralogy and Geochemical Characteristics

Geochemical analyses reported by Wurst (1994), Creaser (1993,1996); Stewart (1994), Stewart and Foden (2003), Zhang et al. (2007) and Kirk (2012), demonstrate that Hiltaba Suite granites (s.l) can be classified as A-types , with the following general characteristics: abundant large ion lithophile elements and enrichment in Nb, Y and REE; trends from metaluminous to peraluminous with increasing silica; depletion of Sr, Eu, Ba, P and Ti with increasing silica indicating fractionation of feldspar, apatite and Fe-Ti oxides. Iron enrichment and tholeiitic character are illustrated by sample data spanning the ferroan to magnesian boundary of Frost et al. (2001); samples range from calc-alkalic to alkalic in composition on the modified alkali-lime index (MALI) diagram of Frost et al. (2001).

Hiltaba Suite intrusions of are divided by Stewart and Foden (2003), on a textural basis, into coarse grained- megacrystic, coarse grained- equigranular, and sub-volcanic fine grained to porphyritic types. Mineralogy is dominated by quartz, feldspar (potassium feldspar, with subordinate plagioclase), biotite and magnetite. Potassium feldspar is often perthitic, may exhibit granophyric intergrowth with quartz, and may be mantled by plagioclase, forming rapakivi texture. Hematite “dusting” of feldspar gives the granites a characteristic pink to red colour. Zircon, apatite, allanite, fluorite, titanite are common accessory minerals (Creaser, 1996; Stewart and Foden, ibid).

The Roxby Downs Granite, which hosts the Olympic Dam deposit is composed of quartz monzodiorites and quartz monzonites (Creaser 1996). Mineralogy is

dominated by plagioclase, alkali feldspar, quartz, augite, and biotite. Accessory minerals include magnetite, ilmenite, titanite, apatite, zircon, allanite and uranothorite. Augite is partly replaced by magnesio-hornblende. Both amphibole and biotite are partly replaced by hastingsite (Creaser, ibid).

Hiltaba Suite felsic intrusions found on the Yorke Peninsula are termed the Tickera and Arthurton granites (Jack et al., 1917). A detailed study by Wurst (1994) defined chemical variation and compositions of the intrusions, and documented the variations in texture including porphyritic, fine grained microgranites through to coarse grained and pegmatitic variations. The Tickera granite comprises a pink, oxidised monzonite and a white, more reduced leuco-tonalite. These units are locally foliated, suggesting syn-tectonic emplacement at depth. The Arthurton Granite is pink-red, dominantly coarse grained and varies from monzonite to granite and adamellite in composition (Wurst, ibid).

Geochronological dates are similar for the Tickera (1575±7 Ma, 1586±5 Ma, 1600±16 Ma: all U-Pb in zircon; Fanning in Conor et al., 2010) and Arthurton Granites (1582±7 Ma; U-Pb; Creaser and Cooper, 1993). The Curramulka Gabbro has been dated by Zhang et al. (2007) at 1588±4.8 Ma (SHRIMP U-Pb).

5.3.2 Intensive variables of magmas

Intensive variables of the magmatic systems that produced the Hiltaba Suite intrusions have been estimated using the chemistry of well-preserved minerals and melt inclusions within units of the Gawler Range Volcanics. Creaser (1996) used mineral chemistry of feldspars, biotite and amphiboles in a quartz latite to estimate intensive variables of the magmatic system that produced the granitoids of the Roxby Downs Area. Two-feldspar geothermometry yielded a minimum temperature before eruption of 910°C. Application of Al-in hornblende geobarometry yielded a pressure estimate of 200 MPa, corresponding to a final crystallisation depth of 6-8km.The fO_2 conditions were estimated to be about between the FMQ and the NNO buffers, based on the intersection of ilmenite isopleths and the Fe^{2+}/Fe^{3+} ratios of biotite in fO_2-T space (Creaser's Fig 5), given that magnetite compositions were not measured.

Stewart and Foden (2003) used data from the Eucarro Dacite and the Yardea Dacite to estimate intensive magmatic variables using 2-pyroxene geothermometry. They estimated temperatures of 950° and 1075°C, and oxygen fugacity of about FMQ-1,

based on the observation that higher fO_2 would result in early crystallisation of magnetite which would prevent Fe-enrichment in the melt and thence the observed tholeiitic trend.

Creaser and White (1991), Stewart (1994) and Creaser (1996) conducted estimates of H_2O content of magma sources to the GRV, using mineral paragenesis and comparison of mineralogy with experimental and theoretical phase diagrams published at the time. Water contents were estimated to be generally ≤2%. More recently, Agangi et al. (2012) estimated water contents (H_2O*, calculated by the "water by difference" method) of melt inclusions to be1.6±1.3%.

The presence of magmatic fluorite, fluoro-apatite and high concentrations of fluorine in amphibole and biotite all attest to the high concentrations of fluorine in melts (Creaser, 1996, McPhie et al., 2011; Ehrig et al., 2012). Fluorine in melt inclusions has been estimated at up to 1.3% (Agangi et al., 2012).

5.3.3 Models of petrogenesis

Creaser (1996) favoured a model of partial melting of Paleoproterozoic and Archaean orthogneiss as a source of the primary quartz latite melt, based on similar εNd1590 values, enrichment of incompatible elements and K_2O, and REE concentrations indicating residual plagioclase in the source rocks. A model wherein magmas fractionated at depth before emplacement at mid-crustal levels (~ 10km) was rejected owing to the very high levels of fractionation needed (80%) to reproduce incompatible element (Nd, Th) chemistry of the rocks studied.

However, field studies and Sm-Nd systematics in Hiltaba Suite samples demonstrate a mantle component to some granitoids. Field evidence for mantle involvement includes high temperature basalt (1100-1200°C) units erupted within the GRV (Stewart 1994), co-magmatic ultramafic and mafic rocks at Olympic Dam (Reeve et al., 1990; Johnson and McCulloch, 1995), and Hiltaba aged gabbros identified on Yorke Peninsula (Zhang et al., 2007, Conor et al., 2010).

Fresh Roxby Downs Granite was analysed by Wawryk, (1989), and Johnson and McCulloch (1995), who reported εNd1585 of -3.2 and -4.8, respectively. Creaser (1996) reported an average εNd1590 of -5.1 for granite and quartz latites from the Roxby Downs area, and -3.7 for a quartz monzodiorite. Stewart and Foden (2003 and references therein), Skirrow et al. (2007), Wurst (1994) and Kirk (2012) report εNd1590 values from other Hiltaba Suite plutons ranging from +2.8 to -6, generally

more juvenile than Paleoproterozic basement, which has εNd1590 as low as -12 to -16 (Creaser, 1995 and references therein).

In summary, the mantle component of Sm-Nd isotope systematics in the granites, high magma temperatures, and field evidence of bimodal magmatism, has led to a model of granite formation resulting from partial melting of Archaean and Paleoproterozoic basement induced by underplating of mantle-derived magmas. A complex interplay of crystal fractionation, magma chamber convection and assimilation and mixing processes were involved (e.g. Giles, 1988; Stewart, 1994; Creaser, 1995; 1996; Stewart and Foden, 2003, Agangi et al., 2012).

5.4. DEPOSIT GEOLOGY: OLYMPIC DAM

A deposit scale summary of lithology, geochemistry and mineralogy of the deposit was reported by Ehrig et al. (2012). Their new observations and interpretations were based on a data set of 10,000 drill hole samples (15m long 14-core composites) which were analysed for whole rock and trace elements (65 elements+CO_2) and modal mineralogy measured by Mineral Liberation Analysis. A subset of 6,000 samples was analysed by XRD to obtain quantitative mineralogical composition. These detailed analyses were used to further refine definitions of types and extent of hydrothermal alteration, mineralisation associations and zoning, first described in seminal papers such as Roberts and Hudson (1983), Reeve et al. (1990), Oreskes and Einaudi (1990, 1992), Haynes et al. (1995), Johnson and Cross (1995), and Johnson and McCulloch (1995). Throughout this paper, we use the terminology of Ehrig et al. (2012). We restrict our descriptions and discussion to those aspects of deposit geology relevant to the distribution and deposition of chalcopyrite and pyrite, magnetite, hematite and siderite.

The deposit is hosted entirely within the Olympic Dam Breccia Complex (ODBC; Reeve et al. 1990), which is composed primarily of brecciated and hydrothermally altered Roxby Downs Granite (RDG) and, in the northwest of the deposits, mafic dykes which are pre- and syn-brecciation (Ehrig et al., 2012). A previously unknown mineralisation host, a quartz-phyric felsic dyke, has been intersected by drill hole RD2773 (Ehrig et al., ibid; Fig 5. 2).

5.4.1 Roxby Downs Granite

The RDG is a pink-red, medium to coarse grained granite composed of K-feldspar (45%), plagioclase (20%), quartz (30%), minor biotite and amphibole, accessory

magnetite, titanite, apatite and zircon and trace fluorite, allanite, siderite and a variety of U-REE±Ca bearing phosphates and carbonate minerals (Reeve et al., 1990; Ehrig et al., 2012). Geochronological studies have dated the RDG at 1588±4 Ma (U-Pb; Creaser and Cooper, 1993), and 1592±8ma and 1584±20Ma (SHRIMP U-Pb data on felsic dykes; Johnson and Cross, 1995).

Unaltered granite is defined by the presence of magmatic biotite and K_2O/Na_2O ratios of 5.5:3.5 (Ehrig et al., 2012). Although labelled 'unaltered', hematite dusting of feldspars gives a characteristic pink to red colour to the granite (Fig 5.3A), and some fracturing and cross-cutting by carbonate veinlets is common.

5.4.2 Olympic Dam Breccia Complex and Hydrothermal Alteration

The ODBC is composed mostly of clasts of the Roxby Downs granite, with some components of Gawler Range Volcanics, mafic and felsic intrusions, and clastic sedimentary rocks (Reeve et al., 1990; Ehrig et al., 2012). Breccia types are described in detail by Reeve et al. (ibid) and Oreskes and Einaudi (1990), and are defined as hematite rich breccias, heterolithic breccias and granite rich breccias. The authors stress that within each type there is a wide range of textures; furthermore, the divisions between each type are gradational. Breccia types span a continuum from hematite-quartz breccias at the centre of the deposit, with no primary rock features remaining, through to only incipiently altered Roxby Downs Granite (Fig.5.3).

More recently, Ehrig et al. (2012) used systematic differences in whole rock geochemistry at the deposit scale to refine the definitions of brecciation and alteration zones. The classification and rock nomenclature used by those authors is summarised in Table 5.1, and shown at the deposit scale in Figure 5.2. Three iron-oxide alteration zones are defined; the alteration of magmatic biotite to chlorite (termed the "biotite-out" contour) and magmatic magnetite to hematite defines an outer margin of hydrothermal alteration and the ODBC. "Granite-rich breccias" are defined by whole rock Fe content of 5 wt%, to 20 wt% Fe. The transition from granite-rich to hematite rich breccia occurs at ~20 wt%Fe.

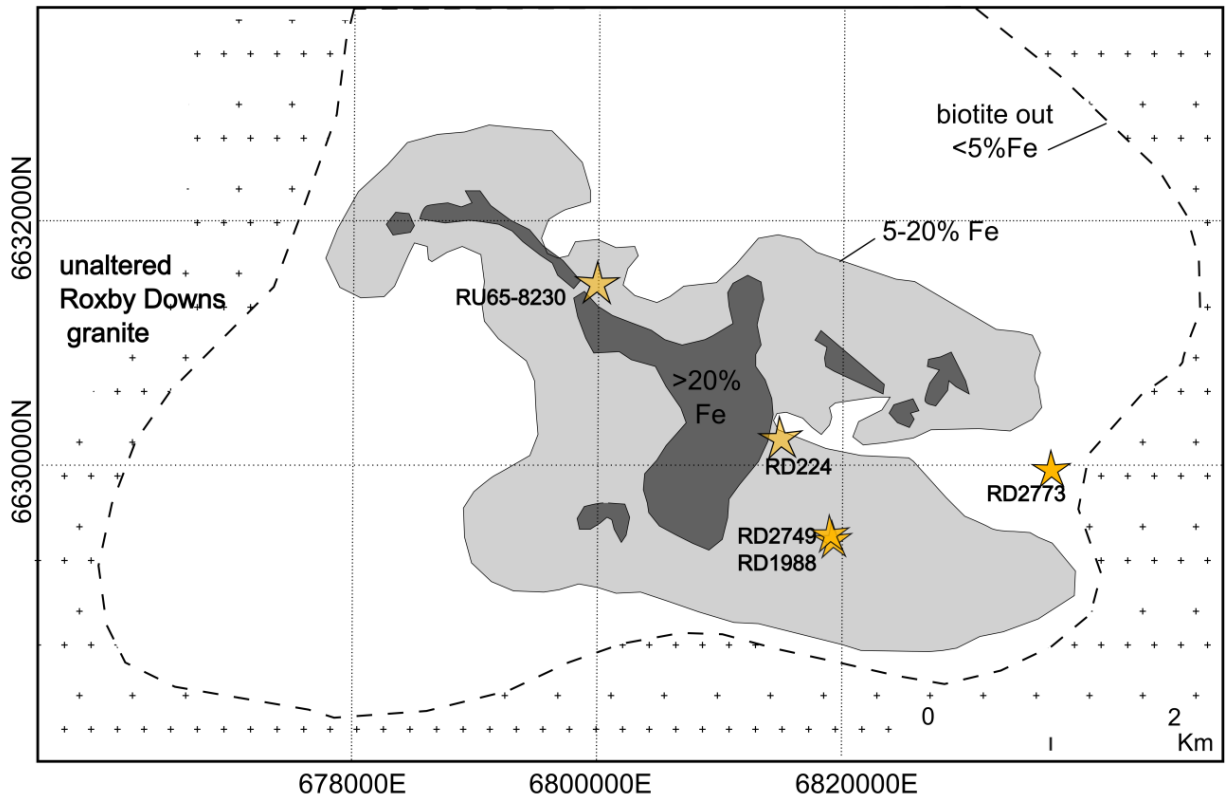

Figure 5.2 Distribution of Fe oxide alteration at Olympic Dam. The locations of drill holes sampled in this study are also shown (after Ehrig et al., 2012).

Both the degree of brecciation and intensity of Fe metasomatism increase towards the centre of the deposit. This hematite-quartz assemblage is characterised by lack of sulfide and aluminosilicate minerals, and is composed of granite-derived relict quartz and hematite clasts within a hematite-clear hydrothermal quartz matrix (Fig. 5.3G). The breccias can be dense and hard, to porous and vuggy (Reeve et al., 1990, Ehrig et al., ibid). An overprint of monomineralic white barite veins is common.

Figure 5.3 Hand specimens of fresh and altered Roxby Downs Granite. A: Fresh Roxby Downs Granite, with salmon-pink K-feldspar and magmatic magnetite and biotite present. B: The “biotite-out” granite of Ehrig et al. (2012). Magmatic biotite is replaced by green chlorite, and magmatic magnetite is replaced by hematite. C: Chlorite-altered Roxby Downs Granite. D and E: Granite dominated breccia. F: Black hematite matrix dominated breccia, with red granite clasts preserved. G: Hematite-quartz-barite breccia from the barren core. White mineral is barite. Black/white bars on the scale represent 1cm.

Mineralogical changes in the RDG that resulted from alteration and brecciation can be visualised in a variation diagram of whole rock K_2O v Na_2O wt%, shown in Figure 5.4. The trend of decreasing Na_2O with increasing K_2O reflects replacement of plagioclase by sericite. The transition between granite-rich breccia to hematite-rich breccia involves Fe metasomatism via replacement of K-feldspar by sericite and hematite, then replacement of sericite by hematite (Ehrig et al., ibid).

The degree of Fe-metasomatism is shown in a variation diagram of K_2O vs Fe_2O_3 (Fig 5.5). Fresh A type granites cluster at ~ 3-6 wt% K_2O and generally ≤5 wt% Fe_2O_3. The onset of alteration is clear in the BTOUT group of samples, which have K_2O content between 6 and 9 wt%. The K_2O content decreases with increasing Fe-metasomatism. Samples selected for Fe-isotope analyses were selected to cover the range of total Fe-content from silica-rich leucogranites and fresh RDG to the hematite-quartz-barite breccias at the centre of the deposit.

Table 5.1. Summary of hematite breccia classification based on Fe content and petrographic observations. (Ehrig et al., 2012).

Rock type	Fe-content	Nomenclature
Fresh Roxby Downs Granite, magmatic magnetite and biotite present	<5%	RDG
Outer limit of alteration; magnetite altered to hematite and biotite altered to chlorite (“biotite out”). Feldspars altering to sericite	<5%	BTOUT
Granite rich breccia	5-20%	GRNB
Hematite rich breccia	>20%	HEMH
Hematite-quartz±barite breccia in the deposit centre	>60%	HEMQ

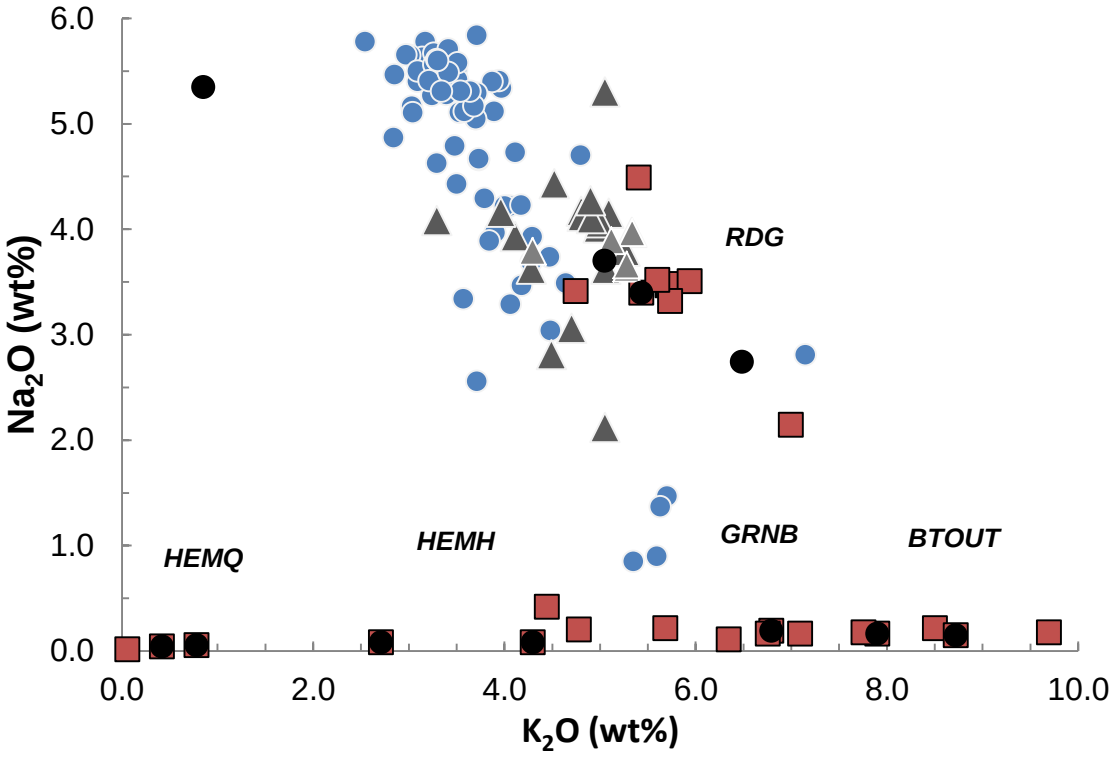

Figure 5.4 Variation diagram of whole rock Na_2O (wt%) vs K_2O (wt%). Samples from this study, shown in red squares, are fresh Roxby Downs granite (RDG), hematite/sericite-altered granite-rich breccias (GRNB), hematite-rich breccias (HEMH) and the barren Hematite-Quartz core (HEMQ). Samples selected for Fe isotope analyses are shown in closed dark circles. Shown for comparison are major element data for samples of the Hiltaba igneous suite (blue circles, data from Wurst, 1994; Creaser, 1996; Foden and Stewart, 2003; Kirk, 2012) and A-type granites from the literature (grey triangles, data from Poitrasson and Freydier, 2005; Schoenberg and von Blanckenburg, 2006; Heimann et al., 2008; Craddock and Dauphas, 2011; Telus et al., 2012; Zambardi et al., 2014; Foden et al., 2015).

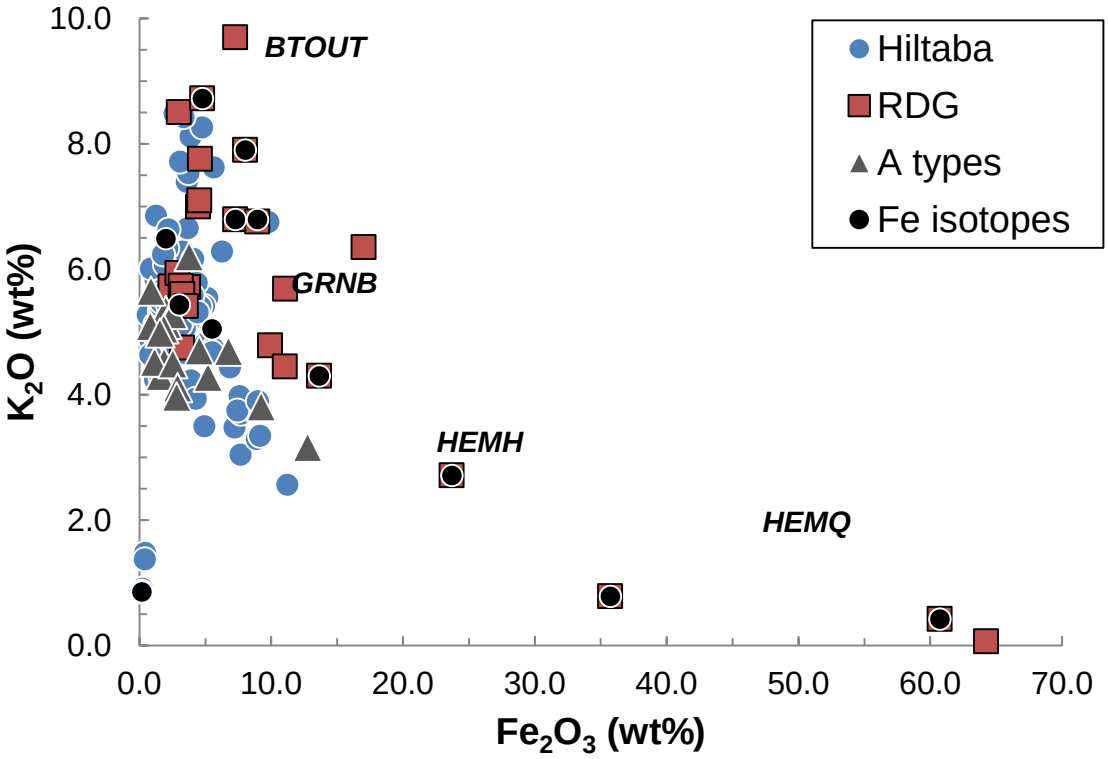

Figure 5.5 Variation diagram of whole rock K2O (wt%) vs Fe2O3 (wt%) , showing the degree of Fe-metasomatism moving from RDG to the Barren Core. Abbreviations and sources of data for Hiltaba and A-type granites as in Figure 5.4.

5.4.2.1 Alteration

Two broad stages of iron oxide-sulfide alteration have been documented (Oreskes and Einaudi, 1992. Haynes et al., 1995; Ehrig et al., 2012), and are classified according to the redox state of Fe. The reduced Fe assemblage is magnetite-pyrite-apatite-siderite-chlorite-quartz. This assemblage is found in the east of the deposit (Oreskes and Einaudi, 1992) and in the deeper parts of the deposit (Ehrig et al., 2012).

The oxidised Fe assemblage consists of hematite-sericite-fluorite-barite (Ehrig et al., 2012), and overprints and replaces the reduced Fe stage. Copper sulfides were deposited during this stage. As previously mentioned, hematite abundance increases toward the deposit centre, and has been interpreted to be deposited in multiple hydrothermal events (Reeve et al., 1990, Oreskes and Einaudi, 1992). Hematite has a variety of colours and textures and is described in more detail below.

5.4.2.2 Cu-Fe sulfide mineralisation

Copper mineralisation is intimately associated with hematite alteration, evidenced by 3 decades of detailed drill core logging, underground mapping and geochemical analyses (Reeve et al., 1990; Oreskes and Einaudi, 1990; Ehrig et al., 2012, their Fig 7). Copper mineralisation is also found in granite-rich breccias and, in the northwest of the deposit, along the margins of and within fine-grained hematite veins, which may have originally been mafic dykes (Ehrig et al., ibid). Photographs of mineralisation from different parts of the deposit are illustrated in Figure 5.6.

The main sulfide minerals (98% of total, Ehrig et al., ibid) are chalcopyrite, bornite, chalcocite (and its variations djurleite and digenite) and pyrite. The distribution of bornite-chalcocite, chalcopyrite-bornite and pyrite-chalcopyrite pairs are illustrated in Ehrig et al. (2012 their Fig 14), and highlight the following relative abundance of sulfide pairs; pyrite-chalcopyrite>bornite-chalcocite>chalcopyrite-bornite. Pyrite-chalcopyrite is more abundant at depth and at the margins of the deposit. The transitions from chalcopyrite-pyrite to more sulfide rich species are termed the “bornite-chalcopyrite” and the “bornite-chalcocite” interfaces (Reeve et al., 1990). These interfaces occur towards the centre and upper parts of the deposit.

Photomicrographs illustrating sulfide textures are illustrated in Fig 5.7. Sulfides occur mostly as disseminated grains with an average size of ~100μm, although individual grain sizes can vary from <20μm to millimetres in scale (Oreskes and Eianudi, 1990; Reeve et al., 1990; Ehrig et al., 2012).

Two types of pyrite are present: (1) fine to coarse-grained, sub-to euhdral disseminated pyrite as individual grains and agglomerates (Fig .57A), and (2) anhedral to subhedral grains that are replaced by chalcopyrite. Pyrite crystals may occur as islands within a chalcopyrite matrix, or be brecciated and infilled by chalcopyrite-hematite±gangue (Fig. 5.7B-D).

Chalcopyrite occurs as anhedral disseminated grains (Fig 5.7A, C), or may be interstital to bladed black hematite grains. Inclusions of bladed hematite within chalcopyrite suggest synchronous deposition

Gangue mineralogy intergrown with Cu-Fe sulfides and hematite is variable and includes siderite, fluorite, barite, sericite, quartz and chlorite (Reeve et al., 1990; Ehrig et al., 2012).

5.4.2.3 Hematite morphology

Hematite is variable in morphology and paragenesis, owing to an extended history of hydrothermal alteration and brecciation. Detailed descriptions have been published in Roberts and Hudson (1983), Reeve et al. (1990), Oreskes and Einaudi (1990); and Ciobanu et al. (2014). We describe the morphology of hematite types in our samples, based on hand specimens and reflected light thin section petrography.

Samples OD1405_55 and 57 (Fig 5.6E-F) provide an illustration of the different hematite types. Red “earthy hematite” clasts (c.f.“microbreccia clast” in the terminology of Oreskes and Einaudi, 1990 Fig 9b) and layers of “wispy” textured red-brown hematite (c.f. terminology of Reeve et al., 1990, Plate 2f) are overprinted by disseminated chalcopyrite in a black hematite matrix. In thin section, the red microbreccia hematite clasts are composed of randomly oriented net-textured hematite with poorly sorted, angular quartz fragments (Fig 5.7C).The red-brown wispy hematite and are composed of aggregates of fine grained (~50-100μm), randomly oriented net-textured hematite.

The black hematite associated with chalcopyrite (also termed “black hematite” by Oreskes and Einaudi, ibid and Reeve et al., ibid) is larger in grain size (1-10mm) and varies in crystal shape from euhdral laths and blades (Fig 5.7B, C) or tabular, to massive. Hematite commonly exhibits twinning and oscillatory zoning.

5.4.2.4 Siderite, base metal and tin-tungsten zoning

It is now known that a siderite halo surrounds the deposit laterally and at depth (Ehrig et al., 2012), and is paragenetically early, being associated with magnetite and pyrite. Siderite is white when fresh (Fig 5.6G), and weathers to a characteristic tan colour on exposed surfaces. It occurs as sub-millimetre anhedral crystals intergrown with magnetite and sulphides, as breccia infill, or as masses of tabular sub- to euhedral crystals of ~2-3mm in veins.

A deposit wide Cu-Pb-Zn zonation is now known, since drilling in the southeast of the deposit has intersected Pb-Zn sulphides which were previously reported from the north west area (Ehrig et al., ibid). In drill hole RD2773, in the south east of the deposit, sphalerite is co-precipitated with chalcopyrite, either as infill in fractured pyrite or interstitial to bladed hematite (Figure 5.7D).

The deepest drill intersections of copper sulphide mineralisation occur in drill hole RD1988, which ends at -1789m RL. Samples from this drill hole have elevated

concentrations of Mo-As-W-Sn-Sb, which are not known elsewhere in the deposit. This “granitophile” signature occurs in only weakly mineralised rocks (Cu grade ≤ 0.1%), and its paragenetic significance remains unclear (Ehrig et al. ibid).

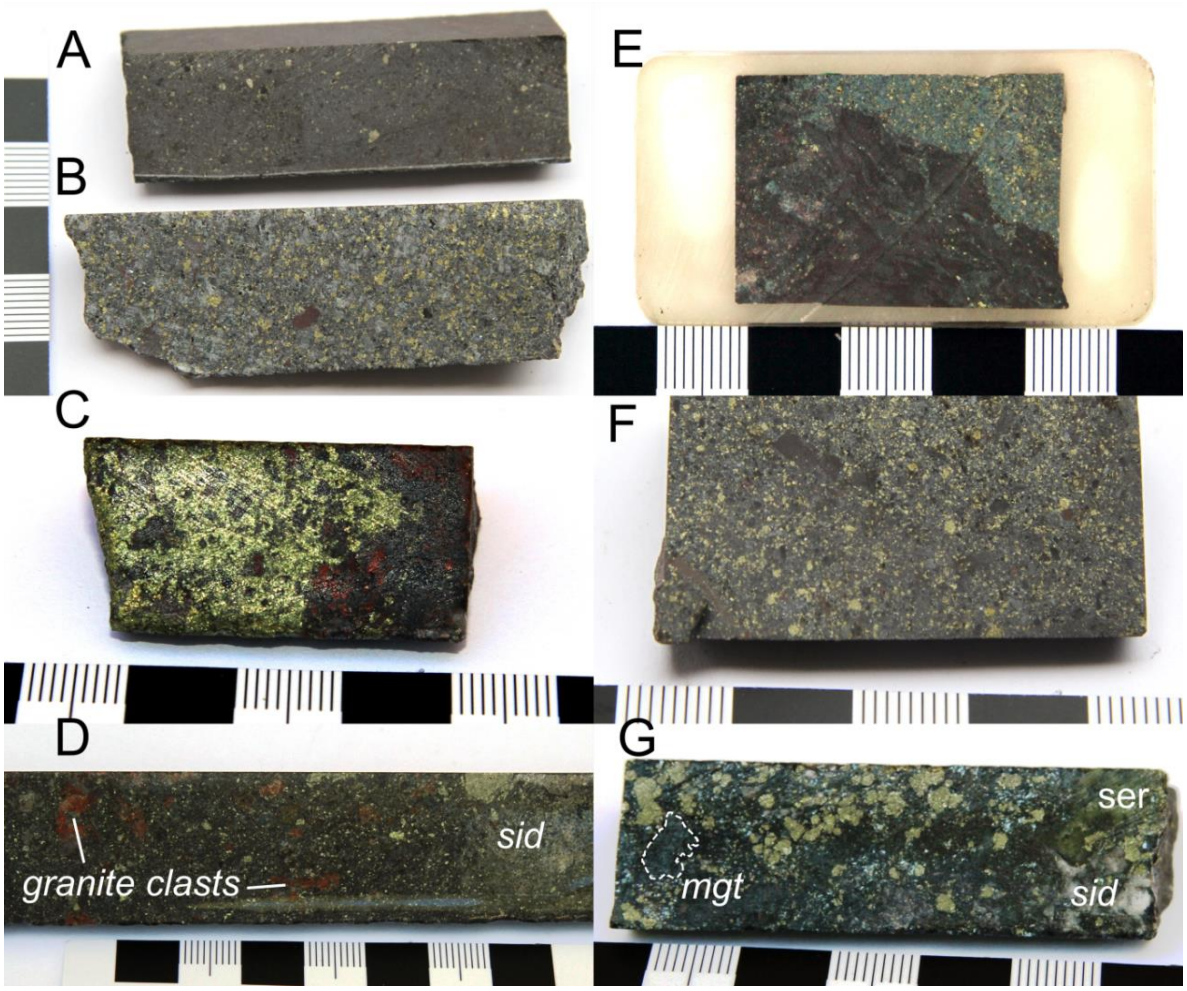

Figure 5.6 Examples of Cu mineralisation at Olympic Dam. Samples A-C were sampled from drill hole RU65-8230 in the north western part of the deposit. E-F sampled from RD1988 in the south of the deposit. G sampled from RD2773 in the south east of the deposit. A: fine grained disseminated chalcopyrite-pyrite ore in black hematite matrix, sample 1405-73. B: Disseminated chalcopyrite-hematite replaces magnetite-chlorite-altered granite breccia, sample 1405-68. C: Rare, almost massive chalcopyrite ore, sample 1405-73. D: Disseminated chalcopyrite ore in matrix dominated breccia, with clasts of disaggregated granite and siderite. E: Dark red-brown clasts of 'wispy" earthy hematite (centre), infilled by chalcopyrite-bladed hematite (top right), sample 1405-57. F: Disseminated chalcopyrite-hematite ore, sample 1405-55. G: Coarse grained pyrite-magnetite overprinted by bladed hydrothermal hematite (silver grey). Chalcopyrite is not visible at this scale, but pyrite occurs as single, rounded grains and hematite replaces fine grained magnetite. Chalcopyrite infills cracks in pyrite and is interstitial to hematite. White siderite infills matrix around a sericitised granite clast (top right), sample 1405_15. Abbreviations: sid=siderite, mgt=magnetite, ser=sericite. Scale bar divisions are 1 cm.

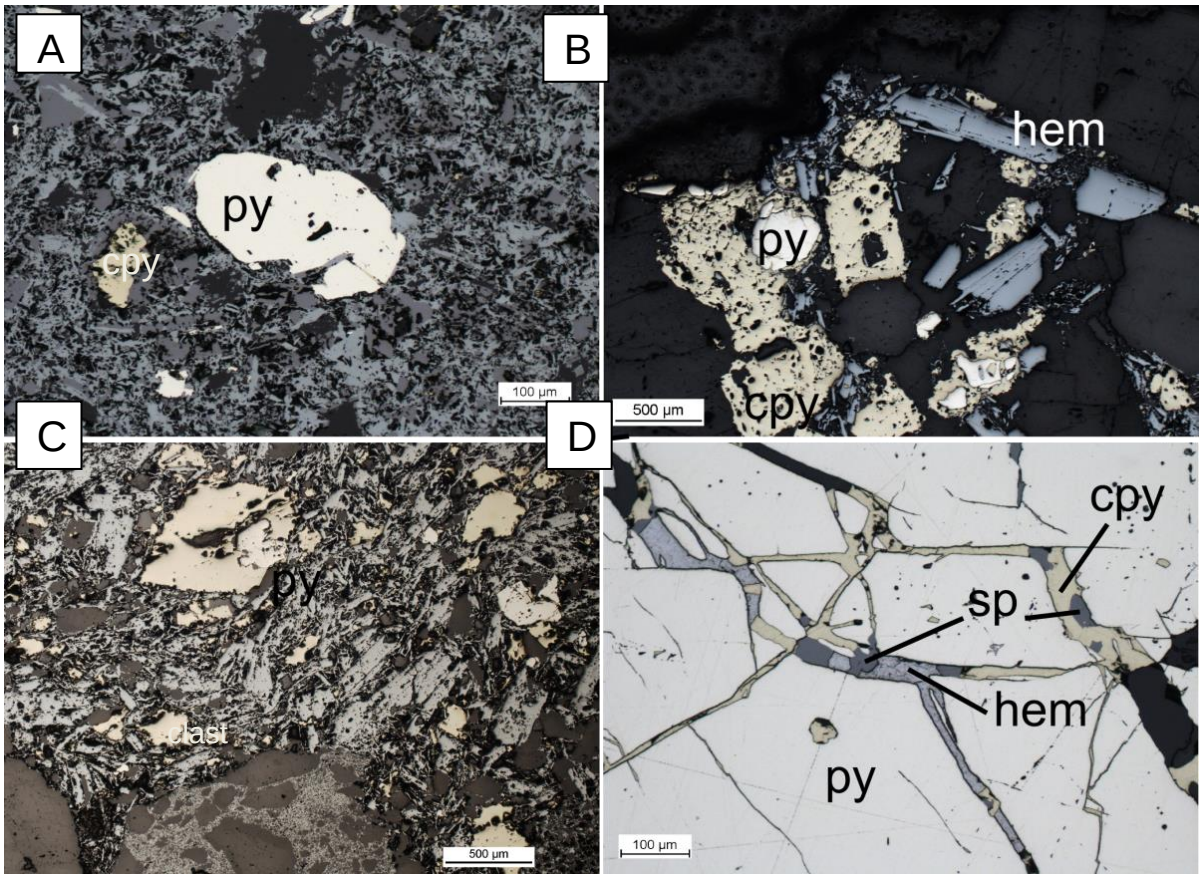

Figure 5.7 Photomicrographs of mineral textures at Olympic Dam. All photomicrographs are reflected light. A: Fine grained disseminated ore from drill hole RU65-8230, similar to specimen from Figure 5.2A. Pyrite occurs as single, rounded grains or aggregates and hematite replaces fine grained magnetite. B: Sample 1405-85 from drill hole RD2749. Chalcopyrite replaces pyrite and is co precipitated with bladed hematite. C: Photomicrograph of sample 1405-57. A clast of earthy hematite and quartz (bottom centre) located within a matrix of bladed hematite and chalcopyrite. Islands of early pyrite occur within chalcopyrite grains. D: Typical brittle cracking of early pyrite, which is infilled by co-precipitating chalcopyrite-sphalerite-bladed hematite (sample 1405-15). Abbreviations: cpy=chalcopyrite, hem=hematite, mgt=magnetite, py=pyrite, sp=sphalerite

5.4.3 Stuart Shelf Iron Oxide Occurrences

The locations of other prospects in the Olympic Domain that we have sampled are shown in Figure 5.8 and examples of the rock types are shown in Figure 5.9. These prospects are sub economic in Cu±Au±U, but share some similarities in terms of alteration, mineralisation style and gangue mineralogy. Useful compilations of the characteristics of sub-economic prospects of the Olympic Cu-Au province can be found in Skirrow et al. (2002) and Skirrow et al. (2007). The prospects are briefly described in this section, reporting the salient features that guided our sampling.

A key feature of the prospects described below is the zones of massive ironstones immediately below the cover sequence. These may represent basement highs, and a paleo-regolith profile has been interpreted at Oak Dam (Davidson et al., 2007).The massive iron oxides are like the “steely grey” hematite of Reeve et al. (1990; Plate 1h, and our Fig 5.9A,J). In thin section the hematite is geometric, interlocking and fine grained, a noticeably different texture to the random orientation of bladed hematite associated with copper-sulfides at Olympic Dam. The massive ironstones are commonly cut by late stage veins and vugs containing specular hematite intergrown with barite±quartz (Fig 5.9A,G).

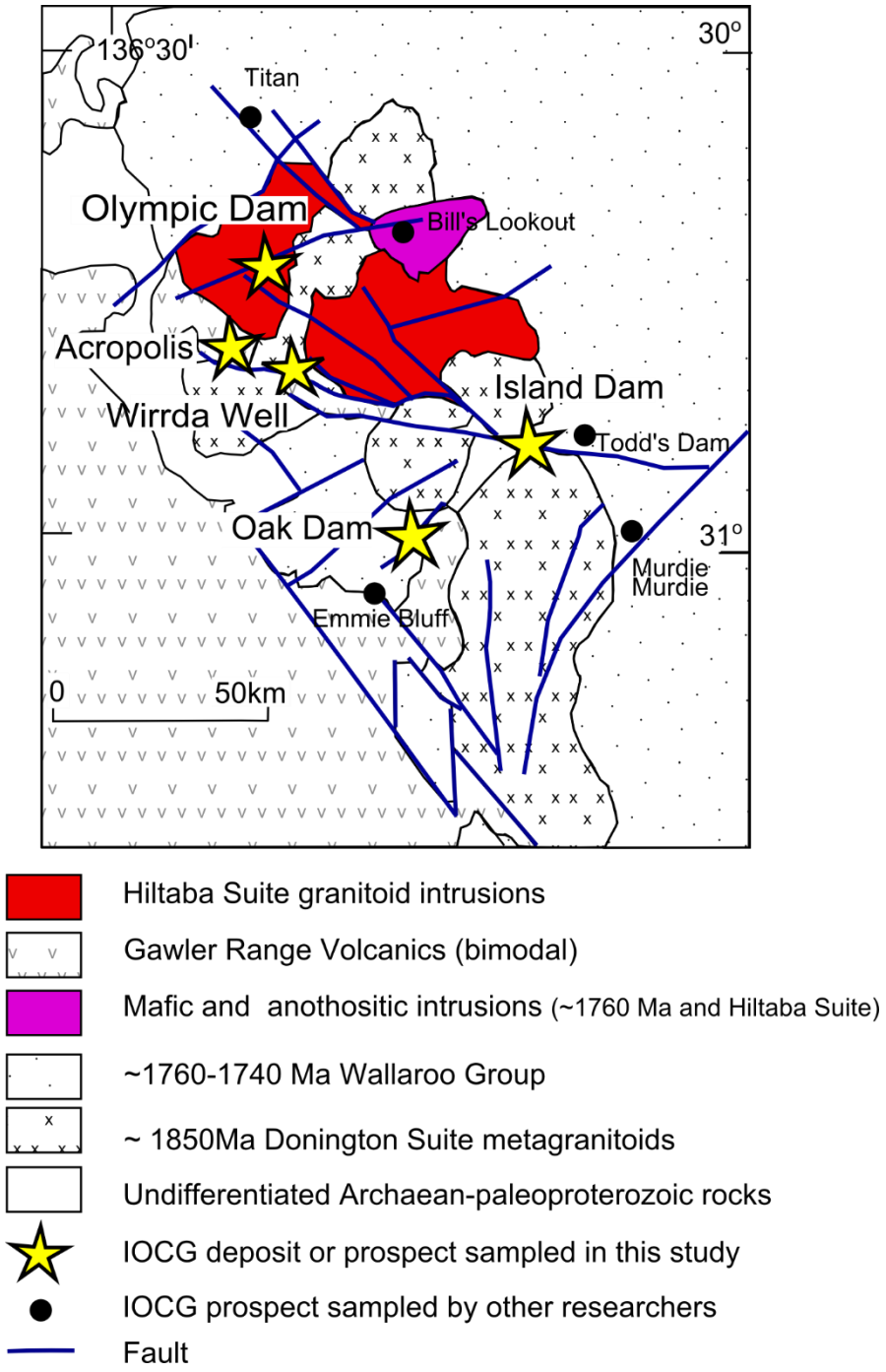

Figure 5.8 Locations of IOCG prospects in the Olympic Dam area. The closed black circles show IOCG prospects studied by Bastrakov et al. (2007) and Skirrow et al. (2007).

5.4.3.1 Wirrda Well

Wirrda Well is located approximately 20km south-south- east of Olympic Dam within a zone of widespread magnetite alteration (Skirrow et al., 2007). Copper mineralisation is hosted in hydrothermal hematite-rich breccias and vein networks within deformed metagranite of the Donnington Suite (Skirrow et al., ibid). Alteration styles are similar to Olympic Dam, with an early magnetite-chlorite-pyrite-siderite

assemblage overprinted by hematite-sericite-chalcopyrite assemblage, illustrated in Figure 5.9C.

Two types of pyrite are seen at Wirrda Well. In Figure 5.10A, inclusion-rich sub- to euhedral pyrite clearly predates coarse-grained lath-shaped hematite. In Figure 5.10B, subhedral pyrite is co-precipitated with euhedral magnetite, with interstitial siderite. Chalcopyrite forms disseminated grains, infills fractures in pyrite and may be interstitial to bladed hematite. Gangue minerals include fluorite, barite, siderite, uraninite and chlorite (Skirrow et al., 2002)

5.4.3.2 Acropolis

The Acropolis prospect is located ~20km south-south-west of Olympic Dam, and is hosted entirely within porphyritic dacite rocks of the Gawler Range Volcanics. Widespread magnetite alteration has also been interpreted (Skirrow et al., 2007). Phenocrysts within the dacite are altered to sericite, and copper mineralisation is hosted in magnetite-hematite-K-feldspar-apatite-quartz veins and massive replacement zones (Hayward and Skirrow, 2010). Gangue minerals include fluorite, pyrite, barite, siderite, uraninite and chlorite (Skirrow et al., 2002), similar to the Wirrda Well prospect.

In the drill hole we sampled (ACD1), magnetite is distributed as veinlets and matrix infill in a weakly brecciated porphyritic dacite (Fig 5.9F), and is thus interpreted to represent early hydrothermal fluids (Oreskes and Einaudi, 1992). Magnetite is more massive further up the drill hole (Fig 5.9E). The hole is poorly mineralised, and sulfides were not separated for analysis.

In thin section (Fig 5.10E), magnetite is euhedral, and may be inclusion rich. The association between chalcopyrite deposition and hematite alteration is clear in Figure 5.10E. In the near surface ironstone, cockade textured supergene iron oxy-hydroxides show a fracture control, and chalcopyrite has altered to idaite (Figure 5.11C)

5.4.3.3 Oak Dam East

The Oak Dam East prospect is a Cu-Au-U prospect hosted in hematite rich breccias. Its geology is reported in detail by Davidson et al. (2007). The host rocks are interpreted as Donnington Suite meta-granites and Paeoproterozoic meta-sediments, cross cut by granite, diorite and mafic dykes interpreted to be Hiltaba Suite. Oak Dam

East varies from Olympic Dam in having no fluorite, much less barite and more quartz veins (Davidson et al., ibid).

The geology is divided into an upper “sulfide-absent” massive ironstone, and a lower “sulfide-present” zone, which overlies a magnetite core (Skirrow et al., 2002; Davidson et al., ibid). Chalcopyrite, pyrite, sphalerite and carrolite comprise the sulfide-present zone, and the sulphide association changes downwards into a zone dominated by disseminated pyrite.

The alteration and mineralisation paragenesis described by Davidson et al. (ibid) is more complex than that described for Acropolis and Wirrda Well. These authors interpret an early high temperature (360° to ~500°C) skarn-like amphibole-albite-magnetite assemblage, overprinted by colloform hematite (Hematite I), then a magnetite-apatite-quartz-chlorite-pyrite stage (Magnetite I) probably equivalent to the reduced Fe assemblage at Olympic Dam. The Hematite II stage consists of martitisation, vein infill by specular hematite and widespread, pervasive replacement of rock textures by fine grained steely massive hematite±pyrite, and infill of pore spaces with quartz-pyrite-chalcopyrite-sericite-chlorite-illite-apatite-monazite-carbonate minerals and tourmaline. Hematite stage II is broadly synchronous with copper sulphide-uranium-REE mineralisation; this stage of alteration may be equivalent to the oxidised Fe assemblage at Olympic Dam.

The drill hole we sampled (AD6) is located 500m north of the thickest part of the mineralisation. The sulfide zone is poorly mineralised and consists of pyrite veinlets and some massive pyrite within massive hematite (Fig 5.9K, L). In thin section, pyrite contains inclusions of magnetite. Pyrite crystals and aggregates are corroded, and are replaced by hematite and a clear gangue mineral which rims and eventually cements relict pyrite grains (Fig 5.10D). Hematite is fine grained and geometric. Near the top of the ironstone (601m downhole), steely hematite appears in thin section as fine grained and geometric. Ghost textures of phenocrysts and an early magnetite are preserved (Fig 5.11A).

We were unable to separate any chalcopyrite for analysis. The drill hole did not intersect the magnetite core.

5.4.3.4 Island Dam

The Island Dam prospect is located approximately 60km southeast of Olympic Dam. Host rocks consist of Donnington Suite meta-granites and a metasedimentary and

metavolcanic rocks interpreted to be the ~1760 to1740 Wallaroo Group. The prospect is only known from a few vertical drill holes, so is at present poorly understood.

Drill hole IDD7 was selected for sampling to investigate whether hydrothermal hematite alteration, from fluids which have circulated through metasedimentary basement, have a different iron isotope signature from hematite sampled from Cu-Au prospects hosted in Hiltaba Suite intrusive rocks.

Relatively unaltered metasediment is pink, fine grained and foliated, with black hematite forming clots, or a wispy “layer replacement” look (Fig 5.9H). Hematite alteration gets progressively more pervasive, until the metasediment is pervasively replaced by bands of hematite-pyrite (Fig 5.9I). Near the top of the hole, hematite is steely grey and vuggy, with vugs infilled by specular hematite-barite± coarse grained euhedral pyrite.

In thin section the pink metasediment is granoblastic with rounded feldspar grains, some broken, in a quartz matrix. Fine grained, polygranular hematite with small magnetite inclusions surrounds quartz and feldspar grains and fragments. Fine grained hematite aggregates also replace an earlier bladed mineral.

A photomicrograph of the massive hematite-pyrite association is illustrated in Figure 5.10C.Bladed hematite has co-crystallised with a large, idioblastic pyrite grain. The clear gangue mineral that appears to overprint both the pyrite and hematite may be a silica overprint, but further work is required to confirm this interpretation.

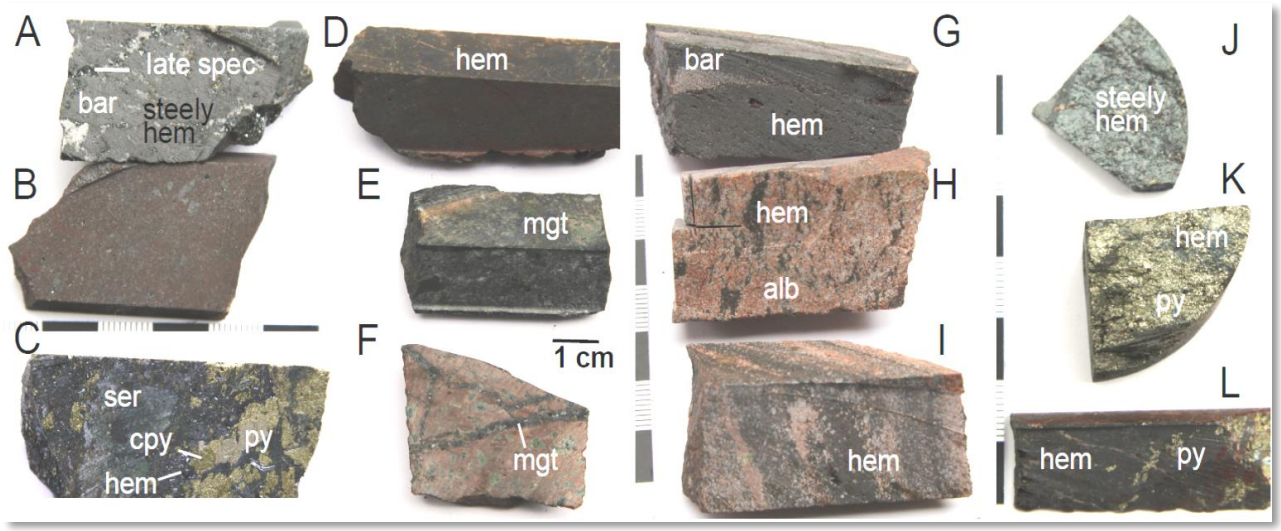

Figure 5.9 Hand specimens of samples from IOCG prospects. A-C from Wirrda Well, D-F from Acropolis, G-I from Island Dam and J-L from Oak Dam. A: Sample 1405-25; massive steely grey hematite crosscut by barite-specular hematite veins. B: Sample 1405-2; mixture of red earthy and grey steely hematite. C: Sample1405-34; coarse grained intergrown pyrite-magnetite overprinted by chalcopyrite-hematite. Matrix hematite surrounds a sericitised (ser) clast of Donnington Suite metagranite. D: Sample 1405-61; massive earthy hematite pale orange veinlets contain idaite and hematite with supergene textures. E: Sample 1405-60; massive magnetite altered rock. F: sample 1405-58; porphyritic volcanic rock, with magnetite veins, and magnetite infilling incipient breccia textures. Green spots are phenocrysts altered to sericite. G: sample 1405-39; massive steely hematite, cross cut by barite-specular hematite veins. H: Sample 1405-36; red albitised metasediment showing the onset of hematite alteration. I: 1405-43; hematite becoming more massive and overprinting granoblastic albite. J: Sample 1405-51; massive steely grey hematite. K: Sample 1405-52; massive pyrite. L: sample 1405_50; massive hematite with pyrite stringers and blebs. Abbreviations as in Figure 5.3, bar=barite, spec=specular hematite. Scale bar divisions are 1cm.

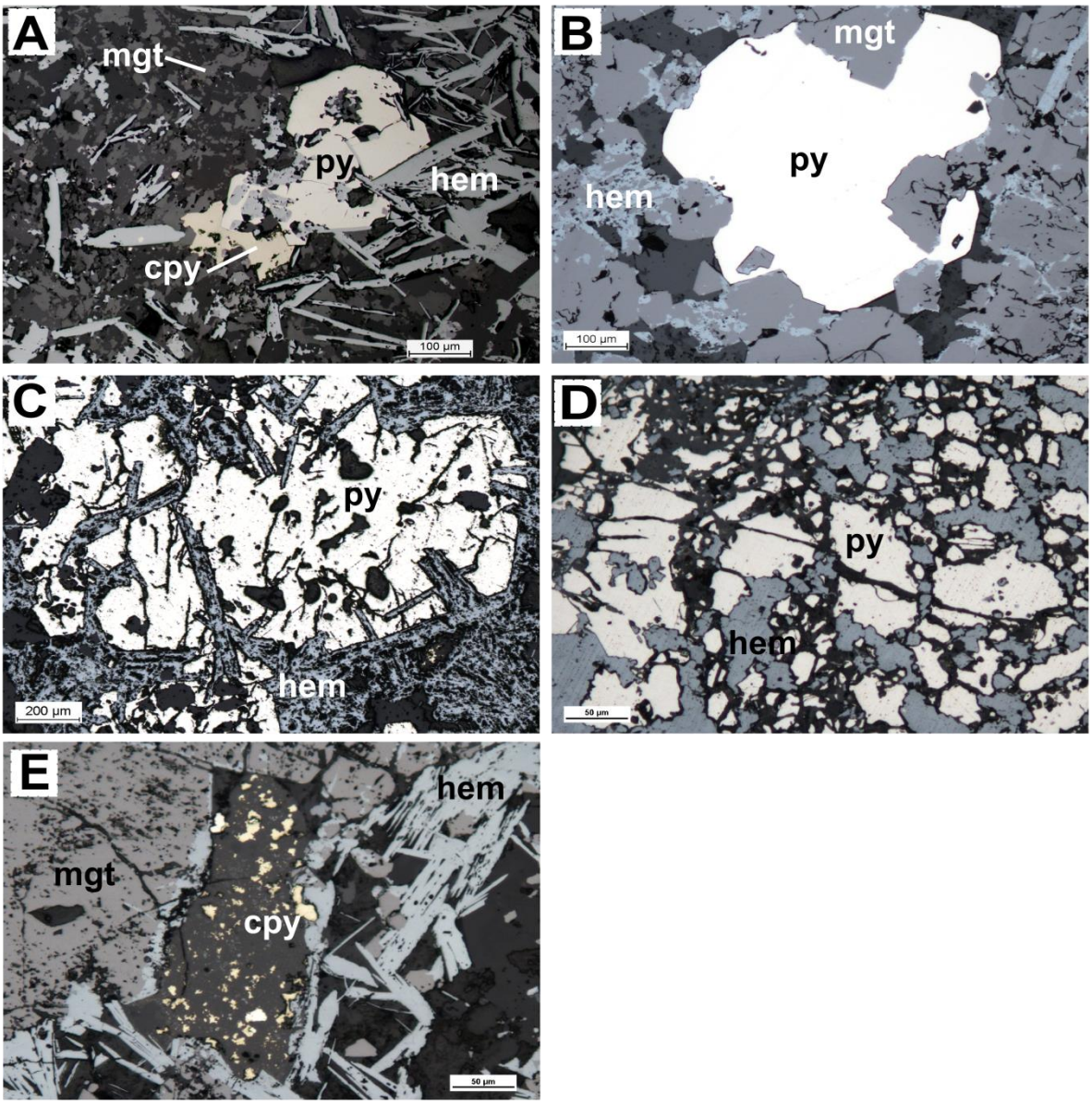

Figure 5.10 Photomicrographs of Fe-bearing sulfides and oxides from IOCG prospects. All photomicrographs are reflected light. A: Sample 1405_28 from Wirrda Well. Pyrite occurs as single, often inclusion-rich, rounded, subhedral grains. Hematite replaces fine grained magnetite, as well as forming blades. B: Sample 1405_30 from Wirrda Well. Subhedral pyrite is intergrown with sub to euhedral magnetite, with interstitial siderite (darker grey) Martitisation of magnetite occurs along grain edges. C: Sample 1405-41 from Island Dam. Net texture of coarse grained idioblastic pyrite intergrown with bladed hematite. D: Sample 1405_50 from Oak Dam. Sieve texture resulting from aggregates of pyrite being replaced by hematite. Pyrite grains are corroded and rimmed by an unidentified clear gangue mineral. E: Sample 1405-59 from Acropolis. Early magnetite alters to hematite along the edge of a cavity filled with chalcopyrite, clear gangue minerals and coarse-grained bladed hematite. Abbreviations as in Figures 5.6, 5.7

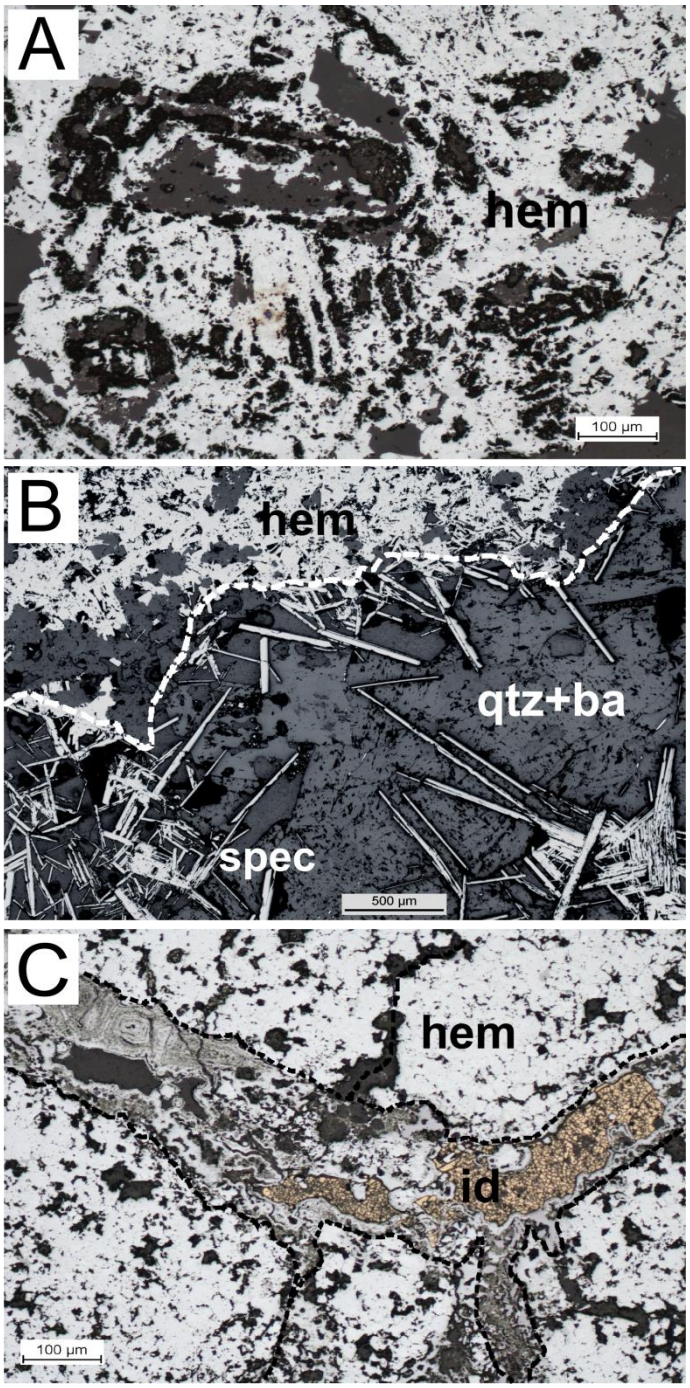

Figure 5.11 Photomicrographs of massive ironstones from Oak Dam, Island Dam and Acropolis. All photomicrographs are reflected light. A: Sample 1405-51 from Oak Dam. Hematite is fine grained and geometric. Ghost textures of probable feldspar, centre left of field of view and magnetite(?) bottom left of field of view. B: Sample 1405- 25 from Island Dam. Fine grained geometric hematite is cross cut by quartz-barite-specular hematite vein. C: Sample 1405-61

5.4.4 Constraints on Fluid temperatures and composition

5.4.4.1 Olympic Dam

Previous research used both fluid inclusion microthermometry and stable isotope geothermometry ($\delta^{18}O$, $\delta^{13}C$) to investigate fluid temperatures at Olympic Dam. Oreskes and Einaudi (1992) calculated temperatures ranging from ~420 °C to 540 °C for a magnetite-quartz assemblage from the east area of the Olympic Dam mine, and concluded that magnetite at Acropolis probably formed from similar fluids. Geothermometry using ^{13}C isotopes in siderite associated with magnetite in the eastern side of the orebody resulted in temperatures consistent with formation of magnetite at ~400°C. That early fluids had relatively high temperatures (>300°C) is also supported by chlorite geothermometry. Conan-Davies (1987) studied both Mg-rich and Fe-rich chlorite from the northwest area of the deposit and reported formation temperatures of 200 °C to 280 °C (Mg-rich chlorite) and 360 °C to 390 °C (Fe-rich chlorite).

Oreskes and Einaudi (ibid) also sampled quartz fragments from the barren core of the Olympic Dam deposit. Samples showed a spread of temperatures and salinities. Fluids were generally lower temperature than the magnetite stage, with homogenisation temperatures (T_h) spread around a well-defined mode of 180 °C to 190 °C although a range of temperatures between 150 °C and 290 °C was reported. Salinities between 7 and 42 wt% equivalent NaCl (Oreskes and Einaudi, ibid) were measured. Hematite crystals were observed in inclusions with Th of 190°C, although it is not clear whether these were trapped or daughter crystals.

Samples from purple fluorite veins at the margin of the deposit returned T_h values similar to those of the hematite rich breccias, and a late low temperature event (<120°C) was interpreted from secondary inclusion in late stage green fluorite.

The most detailed study of fluid inclusion from the Olympic Dam deposit to date was conducted by Bodnar (2000). Samples were selected from the main rock types observed in the deposit from pristine Roxby Downs Granite through sericite and hematite altered granite breccias, to the barren core. Fluid inclusions from barite-fluorite±chalcopyrite veins that cross-cut the deposit, and late carbonate veins that cross cut both the deposit and fresh granite distal to the ore zones, were also analysed.

Bodnar identified five sets of inclusions related to fluid exsolution from a granitic magma crystallising at depth. These fluid inclusions are described below:

CO_2-NaCl-Fe-rich magmatic fluids ("salt melt") formed at T>600°C. This type evolves with time to:

- saline, vapour+liquid inclusions with probable hematite±chalcopyrite daughter crystals, and
- moderate salinity NaCl-vapour+liquid inclusions with homogenisation temperatures of 160 °C to 190°.

The 2 other inclusion types comprise:

- Liquid-CO_2 ± aqueous liquid which grades into
- 2 phase CO_2 rich inclusions.

The close spatial association of types I and IV, in some inclusions, along with the observation that type IV is found only in early quartz, led Bodnar (2000) to conclude that the CO_2-rich inclusions result from volatile saturation and liquid immiscibility in a crystallising granitic magma. The presence of hematite and chalcopyrite daughter crystals, and semi-quantitative analysis of decrepitated salt melt inclusions demonstrate that Fe, and some Cu and S were provided by fluids from a deep magmatic source. The characteristics of the fluid inclusions, paragenetic relationships and homogenisation behaviour show that pressures must have been greater than at least 1.3kb, or 4-5km depth in the crust, during crystallisation of the Roxby Downs granite.

The most common type of fluid inclusions occur as secondary inclusions in early quartz but as a primary set in later quartz, fluorite, calcite, barite and siderite. The inclusions consist of both liquid+vapour and liquid-rich types; Bodnar suggests that this assemblage is the same set studied by Oreskes and Einaudi (1992), and notes that these inclusions are never seen in association with the CO_2 rich inclusions. Bodnar reports a range of T_h of 100 °C to 360°C, somewhat higher temperatures than those reported by Oreskes and Einaudi (1992), and the inclusions have salinities of a few weight percent to 25-30 wt%. These fluids could represent either the onset of magmatic-hydrothermal activity, or non-magmatic fluids; however, this distinction was not possible petrographically, and no microanalytical fluid inclusion

composition data was available at the time of Bodnar's study. Involvement of non-magmatic fluids is evidenced by ^{18}O isotopes (Oreskes and Einaudi, 1992), but analysis of fluid inclusions would be informative, given that halogen ratios of fluid inclusions from IOCG deposits worldwide clearly demonstrate that non magmatic brines are commonly involved in the mineralisation process (e.g. Bastrakov et al., 2007, Baker et al., 2008; Williams et al., 2010; Rusk et al., 2015, Xavier et al., 2015).

Homogenisation temperatures of inclusions in clear quartz associated with hematite-breccias in the barren core range from 150 °C to 250°C, identical to the results reported by Oreskes and Einaudi (1992).

Liquid-rich inclusions are common in late barite-fluorite veins that cross cut the deposit (T_h=100° to 200°C), and barite deposited in the barren core. Inclusions in barite indicated trapping temperatures of below about 150°C. Similar results were reported by the purple and green fluorite samples studied by Oreskes and Einaudi (1992).

5.4.4.2 Oak Dam

Davidson et al. (2007) reported average T_h in fluid inclusions from a pre-mineralising Magnetite Stage at Oak Dam of 133°C, 141 °C and 305°C, with moderate to high salinities of 49, 22 and 24 wt% NaCl equivalent, respectively. The sulfide-bearing Hematite Stage II at Oak Dam returned similar temperatures to the Magnetite stage, between 100 °C and 312°C, with data clustering into two populations; one around 180 °C and the other at ≥250°C. Salinities of Hematite Stage II inclusions are distinctly lower than Magnetite Stage fluids, between ~1 to 10 wt% NaCl equivalent.

5.4.4.3 Regional prospects

The study by Bastrakov et al. (2007) of fluid properties of IOCG prospects in the Olympic Domain further demonstrates that magnetite-stage assemblages were associated with high temperature (~450 °C to 500 °C), Cu rich (~500ppm), hypersaline brines. Those authors interpreted a magmatic, or leached igneous rock origin for S, and showed that $\delta^{18}O$ in magnetite could have resulted from either cooling of a magmatic fluid, or equilibration with country rock heavier than a hypothetical GRV dacite. The authors also did not exclude isotope exchange reactions with basement metasedimentary rocks as an alternative explanation for the range of isotopic compositions, and this interpretation is supported by Br/Cl ratios in fluid inclusions which are clearly non magmatic in composition. Homogenisation

temperatures between 150° and 250 °C for hematite stage fluids and a diverse range of ^{34}S and ^{18}O isotope values (their Fig 15, p1437) were reported. These results, and Nd isotope studies by (Skirrow et al., 2007), demonstrate that metals and sulphur were derived locally from crustal rocks.

5.5. DEPOSIT GEOLOGY: HILLSIDE

The Hillside deposit is situated in the Moonta subdomain of the Olympic Cu-Au province (Fig 5.12), and is hosted by the metasediments of the Wallaroo Group and intrusive rocks of the Hiltaba event (Conor et al., 2010). The deposit is located in the Pine Point Fault Zone (PPFZ), a zone of deformation some 20m to 100m wide (Fig 5.13). Within the PPFZ, three north-south striking, anastomosing faults control the bulk of the mineralisation, with ore zones developed as discrete north-south striking, steeply dipping skarns (Conor et al., 2010), associated with intrusions of Hiltaba Suite gabbros and granites (s.l). The deposit is covered by Tertiary sediments up to 30m in thickness, so that descriptions and interpretations of deposit geology are known only from drill core.

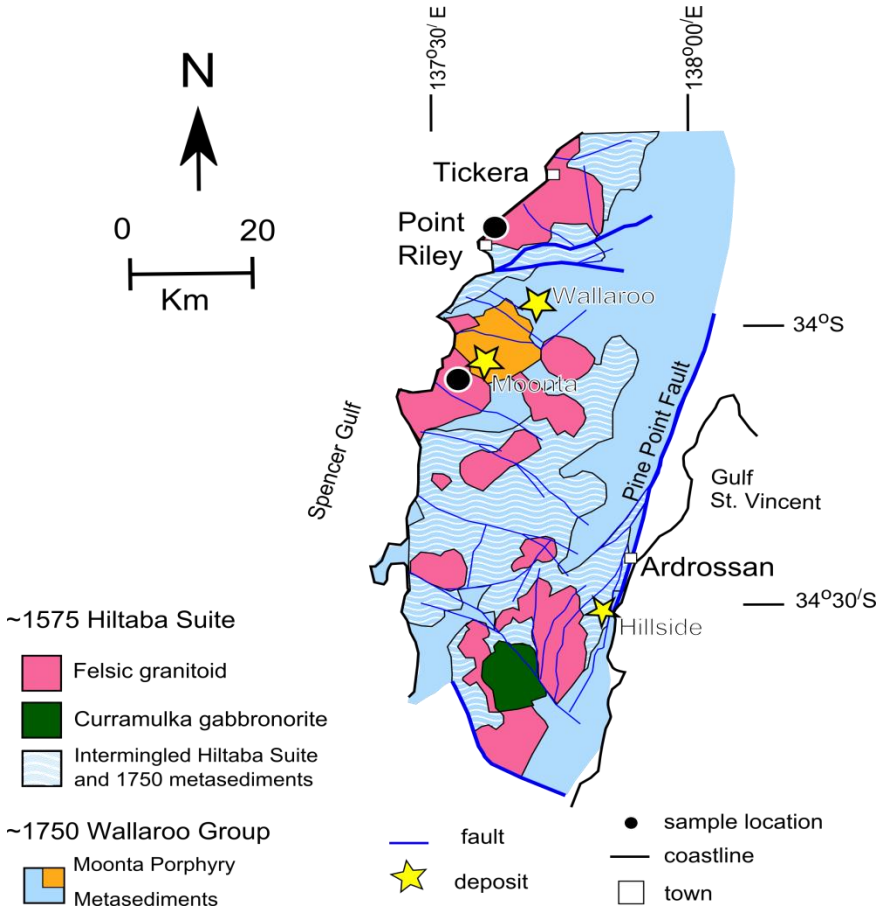

Figure 5.12 Simplified basement geology map of the Moonta Sub-domain . Modified from Conor et al. (2010).

5.5.1 Host Rocks

Within the PPFZ, metasediments are steeply dipping, altered to chlorite and clay minerals, with milled breccia and mylonite fabrics observed. The intrusions are bimodal in composition, including syenite, granite (ss), micro-gabbro, porphyritic gabbro and gabbro-diorite (Conor et al., 2010). Kirk (2012) used Sm-Nd geochronology to date the syenite and gabbro at 1585 Ma, and U-Pb dating of titanite from alteration zones yielded a date of 1570±8 Ma (Reid, 2010 in Conor, ibid), demonstrating that alteration is co-eval with emplacement of intrusions.

Two types of felsic intrusive have been identified, and are termed the “Hillside Syenite” and “Eastern Granite” by project geologists. The Hillside Syenite (60-65 wt% SiO_2) is coarse grained and equigranular. Mineralogy is dominated by K-feldspar (orthoclase and microcline), lesser plagioclase, quartz, biotite and accessory zircon and titanite. The Eastern Granite has similar mineralogy but has very little titanite or zircon (G. Teale, pers comm, 2012). Both felsic units are fractured, and have an intense red colour owing to hematite dusting of feldspar and/or albitisation (Fig 5.14A). Ismail et al. (2014a) report relict biotite and preservation of magmatic apatite. Both biotite and titanite are altered to chlorite. Only the Hillside Syenite is brecciated and mineralised; the Eastern Granite is not mineralised. Discovery of the Hillside Syenite expands the range of Hiltaba Suite felsic rocks known from the Moonta subdomain, and is illustrated in Figure 5.14 along with fresh examples of leuco-tonalite and monzonite from Port Riley mapped by Wurst (1994; Fig 5.12).

Two mafic intrusions have been identified on the basis of texture. One intrusion is porphyritic, the other is equigranular and fine to medium grained. No fresh gabbro remains in the deposit; gabbros commonly show alteration to magnetite-biotite-K feldspar±bornite (Conor et al., ibid), or may be regressed to chlorite (Ismail et al., 2014)

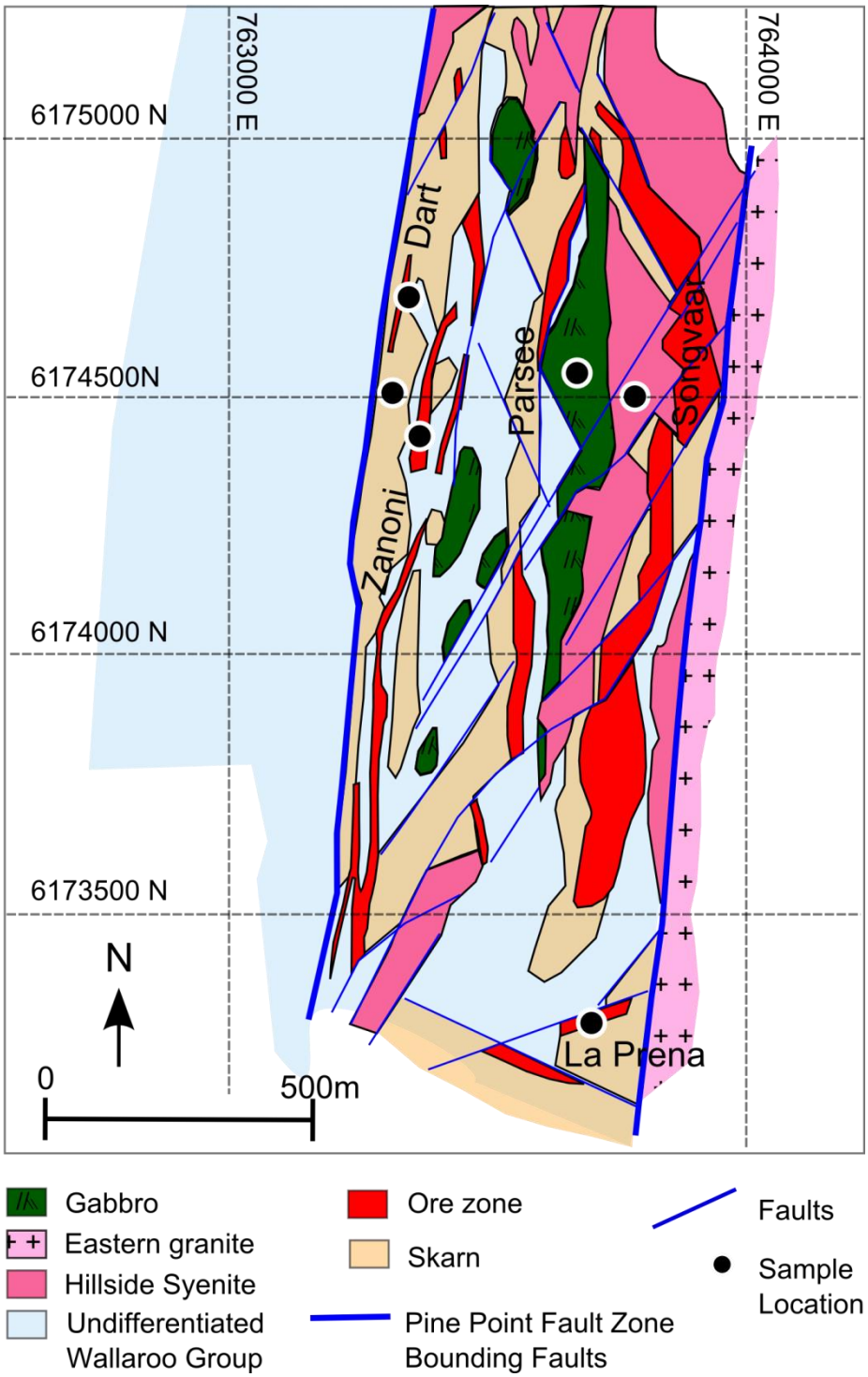

Figure 5.13. Geology map of the Hillside deposit. (Courtesy of Rex Minerals)

5.5.2 Hydrothermal alteration

Both endo- and exoskarn mineralogy is complex, with both low and high temperature mineral assemblages reported. Conor et al., (2010) summarise the skarn mineralogy in general, and more recently Ismail et al. (2014a) report their results of element

mapping, particularly REE distribution, within individual skarn minerals, accompanied by detailed petrography.

Prograde skarn mineralogy varies according to protolith, but can be generalised as magnetite±quartz±garnet±pyrite (Fig 5.14E, G), or a monomineralic garnet skarn (Fig 5.14F). A retrograde association of clinopyroxene, K feldspar, epidote, actinolite, allanite, biotite, albite, chlorite and hematite replaces earlier prograde skarn (Fig 5.14E). The latest alteration stage is a carbonate-silica phase, associate with chlorite±chalcopyrite replacement of clinopyroxene, actinolite and garnet. Thin calcite-quartz veins cross-cuts all host rocks, skarns and mineralisation (Fig 5.14E).

5.5.3 Copper mineralisation

Copper mineralisation is associated with oxidising, retrograde fluids (Conor et al., 2010) with early magnetite-pyrite replaced by hematite and copper sulphides. The principle copper mineral is chalcopyrite with lesser bornite and chalcocite.

Chalcopyrite typically occurs as disseminated grains in skarn (Fig 5.15E, F), as blebs or lenses and as bands of massive sulphide (Fig 5.15D). Chalcopyrite replaces pyrite during skarn retrogression and infills cracks and fractures in brecciated pyrite (Fig 5.15C, D)

5.5.4 Fluid temperatures and composition

There are few published studies of temperature constraints from the Hillside deposit. Ismail et al. (2014a) used Zr in titanite geothermometry to estimate the onset of magmatic-hydrothermal activity at ~660°C, and sulphide deposition at ~550°C.

A fluid inclusion study in garnet and quartz reported by Ismail et al. (2014b) was hampered by the lack of clearly identifiable primary fluid inclusions, coloured host minerals, and ubiquitous cracks in host minerals. Nevertheless, the study reports high temperatures of fluids forming garnet, with homogenisation temperatures of ≥500°C. Temperatures of formation of late stage calcite-quartz veins vary from 100 °C to 350 °C with a cluster at 200-250°C.Salinites of garnet hosted fluid inclusions were estimated at 25 wt% NaCl equivalent. In comparison, calcite-quartz hosted fluid inclusions form two populations; the first has low salinity (<5wt% NaCl equivalent) and the second shows overall moderate salinity (~7 to 20 wt% NaCl equivalent). The authors suggest their results indicating mixing between magmatic-hydrothermal fluid and meteoric waters.

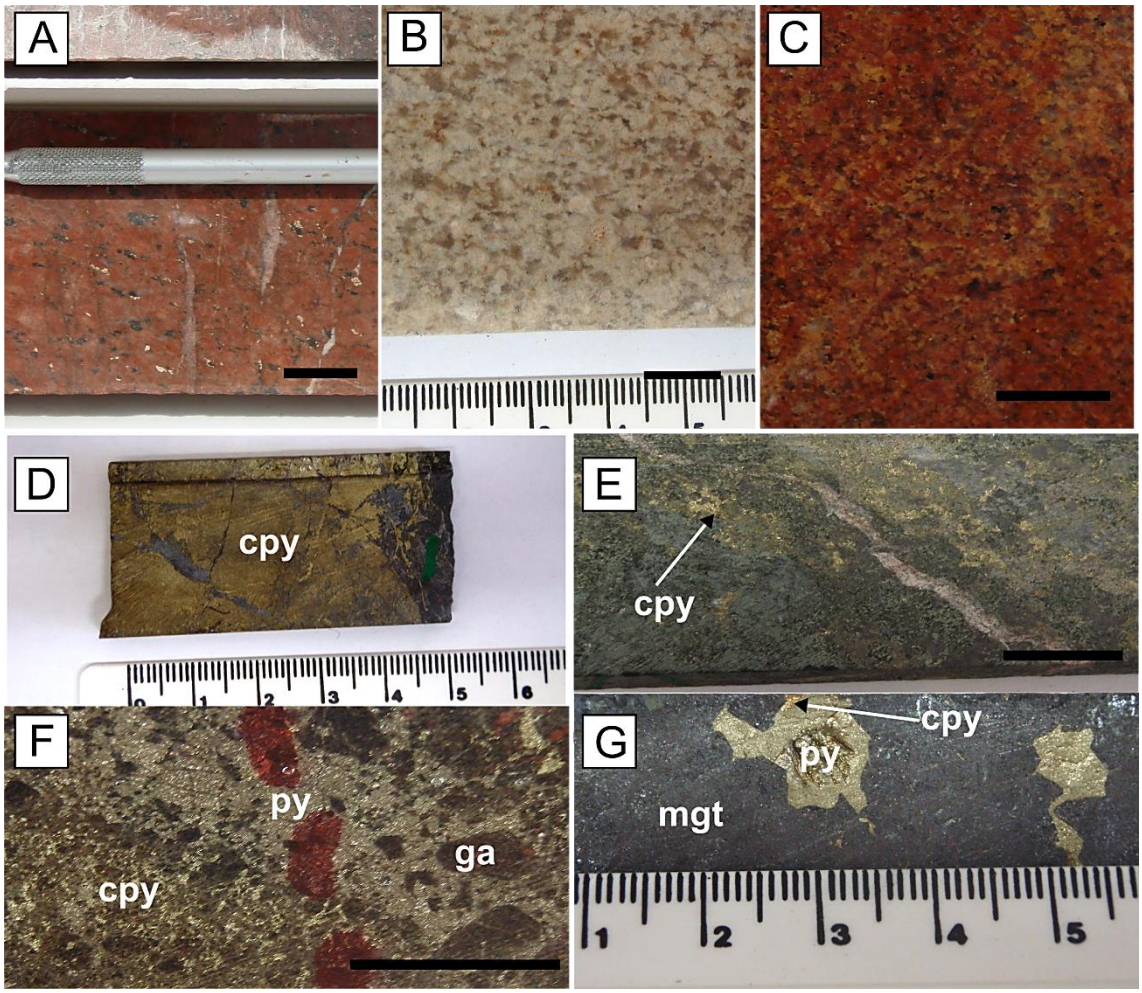

Figure 5.14 Hand specimens from the Hillside deposit. Photomicrographs of skarn mineralisation at the Hillside deposit. A: Hillside Syenite (sample HS018). B: Port Riley leuco-tonalite (sample JK005). C: Port Riley monzonite (sample JK005). D: Massive chalcopyrite overprints prograde pyrite-magnetite-garnet skarn (sample HS01). E: wispy chalcopyrite pyroxene-magnetite skarn (HS015). F::disseminated chalcopyrite overprints pyrite-garnet skarn (HS005). G: Early pyrite-magnetite skarn overprinted by fracture controlled chalcopyrite-hematite (sample HS008). Black scale bars are 1cm. Mineral abbreviations as in Figure 5.6 and 5.7, ga=garnet

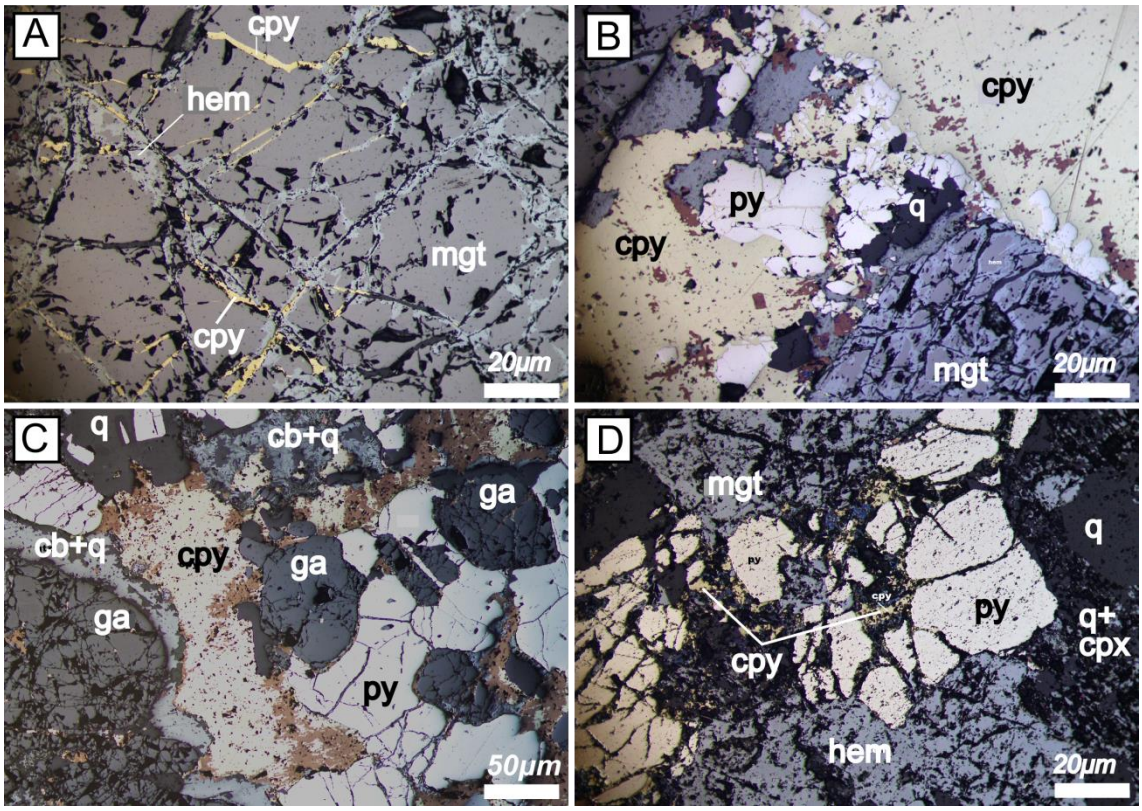

Figure 5.15 Ore mineral textures at Hillside. A. chalcopyrite-hematite infill fractures in massive magnetite skarn (sample HS008); B. Clots of chalcopyrite replacing pyrite-magnetite skarn (sample HS008). C. disseminated py replaces garnet skarn, and is in turn overprinted by disseminated chalcopyrite. Note reaction rim of quartz and an unidentified carbonate mineral surrounding a large garnet crystal on the lower left (sample HS005). D. Chalcopyrite-hematite replacing magnetite-pyrite skarn (sample HS014). Red-brown staining on edges of chalcopyrite grains is carbon coating from SEM work by Kirk (2012).

5.6. SAMPLE SELECTION AND ANALYTICAL METHODS

A total of 92 samples were prepared for analysis from Olympic Dam and surrounding prospect. Sample descriptions and locations are tabulated in Table 5.2. Drill holes to be sampled were selected from the following broad mineralogical zones:

- “Fresh” Roxby Downs Granite (‘RDG’), where magmatic biotite and magnetite are preserved (drill hole RD2495).
- Altered Roxby Downs Granite from the “biotite-out” zone to the Hematite-Quartz (HMQ) barren core zone, at different stages of increasing total iron (RD2678, RD2749 and RB224).
- Early magnetite-siderite-pyrite mineralisation (RD2773, RU65-8230)

- Chalcopyrite-hematite mineralisation (RD1988, RD2749, RD2773 and RU65-8230)
- Massive hematite, both red-brown earthy and grey steely types. Massive hematite, possibly representing relict sub aerial weathered ironstones (Davidson et al., 2007), were sampled from Oak Dam, Acropolis and Wirrda Well.
- Late, coarse-grained specular hematite, occurring as veinlets and coarse grained blades infilling vugs with barite (WRD33 and IDD7).

A total of 35 samples were analysed from the Hillside Deposit, and these are described in Table 5.4.

Table 5.2 Samples selected for iron isotope analysis from Olympic Dam

Prospect	sample number (prefix 1405)	Location	HoleID	Depth From	Host Rock	Cu (%)	Description
		Olympic Dam					
OD Mine	1	Fresh granite	RD2495	442.3	RDG	0.00	Fresh Granite. magmatic magnetite present
	9		RD2495	793.4	RDG	0.00	Fresh Granite. magmatic magnetite present
	11	SE side of Deposit	RD2773	2098.1	unnamed felsic	0.08	top of ore zone, Increasing frequency of hem veinlets and siderite approaching ore
deeper, early mgt-py	12		RD2773	2181.5	unnamed felsic	0.12	pervasively silicified felsic. Early sid-mgt-py, overprinted by hem- cp
	15		RD2773	2208.2	unnamed felsic	0.17	as above
	17		RD2773	2234.7	unnamed felsic	0.35	as above
	18		RD2773	2262.5	unnamed felsic	0.19	as above
	20		RD2773	2326.6	unnamed felsic	0.22	as above
	66	Barren Core	RB224	820.6	RDG	0.06	earthy hem
	67		RB224	808	RDG	0.16	massive hem

Prospect	sample number (prefix 1405)	Location	HoleID	Depth From	Host Rock	Cu (%)	Description
OD Mine	44	Marginal granite	RD2678	427.2	RDG	0.08	altered granite, hematite <20%
	48a		RD2678	765.4	RDG	0.71	hem-ser altered RDG
	68	A-block: drilled from ore zone to margin of deposit	RU65-8230	6	RDG	0.87	fg mgt-hem, fg disseminated py-cpy
	73		RU65-8230	196.3	RDG	5.06	brecciated RDG, almost massive cpy
	79		RU65-8230	646.1	RDG	0.05	mgt-chl altered RDG
	80		RU65-8230	667.2	RDG	0.03	thin ~2-3mm siderite veins in chl-mgt altered RDG
	82		RU65-8230	398.3	RDG	0.17	hem-ser altered "bt-out" granite
OD Mine	84	variably hem-altered from barren core	RD2749	899.3	RDG	0.73	massive hematite

Prospect	sample number (prefix 1405)	Location	HoleID	Depth From	Host Rock	Cu (%)	Description
from barren core to granite	85		RD2749	953.7	RDG	5.98	disseminated cpy-hem ore
varying amounts of hematite altn	86		RD2749	915.2	RDG	0.44	granite breccia, 30-50% hem clasts
	87		RD2749	960.2	RDG	0.17	granite breccia,10-20% hem clasts.
	55	South side of deposit with anomalous granite signature"	RD1988	1773.3	RDG	2.63	fg dissem sulfides (>1%), in hematite breccia
	56		RD1988	1815.3	RDG	2.64	fg dissem sulfides (>1%), in hematite breccia
	57		RD1988	1891.4	RDG	1.07	fg dissem suls in hematite as matrix around earthy hematite clasts
	57_clast		RD1989	1892.4	RDG		earthy hematite clast
		Wirrda Well					
Wirrda Well	22		WRD33	404.9	Donnington metagranite	0.05	massive earthy hem

Prospect	sample number (prefix 1405)	Location	HoleID	Depth From	Host Rock	Cu (%)	Description
	25		WRD33	714.2	Donnington metagranite	0.02	massive steely hem, cross cut by specular hematite vein
	26		WRD33	843.4	Donnington metagranite	0.24	mgt altered to specular hem
	28		WRD33	1087.5	Donnington metagranite	0.05	cpy-hem overprints early mgt
	30		WRD33	1404.6	Donnington metagranite	0.35	as above
	31		WRD33	1604	Donnington metagranite	0.96	as above
	32		WRD33	1819.8	Donnington metagranite	0.07	siderite-mgt vein
	34		WRD33	1948.8	Donnington metagranite	1.03	euhedral mgt-py overprinted by cpy
		Island Dam					
metasediment host	36		IDD7	469.2	Wallaroo Gp metasediment	0.00	hematite alteration in metasediment
	41		IDD7	420.5	Wallaroo Gp metasediment	0.05	banded hem-py layers

Prospect	sample number (prefix 1405)	Location	HoleID	Depth From	Host Rock	Cu (%)	Description
	43		IDD7	395.8	Wallaroo Gp metasediment	0.02	massive hematite, vugs filled with specular hem+barite
		Oak Dam					
top part of system?	50		AD6	650	Donnington metagranite	0.06	massive hem with pyrite stringers
	51		AD6	601	Donnington metagranite	0.00	massive hem
	52		AD6	694.9	Donnington metagranite	0.04	py blebs in hem
		Acropolis					
	58		ACD1	1095.5	Gawler Range volcanics	0.10	magnetite forms veins and breccia infill
GRV hosted	59		ACD1	1039	Gawler Range volcanics	0.01	as above
	60		ACD1	968.4	Gawler Range volcanics	1.37	as above
	61		ACD1	928	Gawler Range volcanics	1.18	massive hematite

Abbreviations: py=pyrite; mgt=magnetite; hem=hematite; spec=specularite; sid=siderite; cpy=chalcopyrite

5.6.1 Sample preparation

Samples of fresh and altered granites and granite-rich breccias were crushed and milled in their entirety. Samples from Olympic Dam were analysed by ICP-MS for 50 elements by Intertek-Genalysis. Samples from Hillside were analysed by XRF and ICP-MS by Kirk (2012). Mineral separates were prepared by the following method:

Wafers were cut from drill core, and pulverised with an agate mill to -125 µm. Mineral grains were then cleaned using acetone. A hand magnet was passed over the samples to remove magnetite. Samples were run through a Frantz magnetic separator to separate hematite, chalcopyrite and pyrite, according to a method outlined by Gaudin and Rush Spedden (1943). Siderite occurs in veins, and is coarse grained, easily sampled by a tungsten-carbide tipped hand tool. Sulfide minerals in drill hole RU65-8230 are fine grained, and were difficult to separate. Only 2 mineral pairs were able to be separated.

Samples were inspected under a binocular microscope for purity. Total separation of hematite and magnetite was not achieved owing to at least incipient martitisation present in magnetite, and inclusions of magnetite in hematite. We noted that chalcopyrite at Olympic Dam separates contained ~10% clear gangue minerals, probably quartz and barite. Quartz and barite are relatively insoluble in aqua regia, so we assume that most of the Fe in the sample will come from dissolution of chalcopyrite. Pyrite separates also included ~5% of the same clear gangue minerals generally.

Hematite from Hillside is very fine grained, and was unable to be separated.

5.6.2 Dissolution of sulfides and siderite

Between 1-5 mg of sample was weighed into a teflon beaker

Samples were dissolved in reverse aqua regia (1.5ml conc HNO_3 and 0.5 ml conc HCL) overnight at 140°C.

Samples were evaporated and converted to chloride form in 2ml of 6M HCl.

Samples were evaporated and taken up in 1ml of 6M HCl and centrifuged prior to anion exchange chromatography.

5.6.3 Dissolution of iron oxides

Between 1-5 mg of sample was weighed into a teflon beaker.

Samples dissolved in reverse aqua regia (1.5ml conc HNO_3 and 0.5 ml conc HCL) and HF overnight at 140°C.

Samples were evaporated, with periodic additions of HNO_3 to prevent precipitation of fluorides. Samples were converted to chloride form in 2ml of 6M HCl.

Samples were evaporated and taken up in 1ml of 6M HCl and centrifuged prior to anion exchange chromatography.

Iron in the samples was purified using Bio-Rad AG 1X4 200-400 mesh anion exchange resin, and eluted with HCl, following the method of Poitrasson and Freydier (2005).

5.6.4 Mass spectrometry

Iron isotope measurements were performed at the University of Adelaide on a Thermo Finnigan Neptune Multi-Collector ICP-MS. Measurements were performed in medium resolution mode, with H-geometry sample cones. Sample introduction was via a glass spray chamber and Scott double pass assembly, together with a low flow, self-aspirating PFA nebulizer (between 50-70 µl/min). Samples were analysed in a 2% HNO_3 solution. Iron was set to concentration of ~3.5 ppm to give a sensitivity of ~0.95V on ^{57}Fe. Ni spiking was set to a concentration of ~8 ppm, to give a signal of ~1V on ^{61}Ni.

Sample take-up time to achieve a stable signal was set at 120s. A measurement consisted of 35 cycles of 8s integration time in static mode, with 30s idle time between each measurement. A baseline measurement was done before each sample measurement. Each sample was run a minimum of 3 times.

Data are corrected for mass bias using the Ni-spiking method of Poitrasson and Freydier (2005). All data are reported using delta notation, in units of per mil (‰) relative to the international isotopic reference standard IRMM-014:

$$\delta^{57}Fe = [(^{57}Fe/^{54}Fe_{sample}) / (^{57}Fe/^{54}Fe_{IRMM14}) - 1] \times 10^3$$

Uncertainties are reported as 2 times standard deviation (2SD) of replicate analyses of the same sample. The long-term reproducibility is monitored by preparation and analysis of geostandard GSP2 with each batch of samples. Our average $\delta^{57}Fe$ for GSP2 was +0.274‰ ± 0.05‰ (95% confidence interval), close to the published $\delta^{57}Fe$ value of +0.23‰ reported by Craddock and Dauphas (2011).

A pyrite sample from Olympic Dam was repeated from the dissolution step, to check the method. The two samples returned 0.58±0.14‰ and 0.59±0.09‰.

5.7. RESULTS

5.7.1 Olympic Dam

5.7.1.1 Granite whole rocks

Fe isotope ratios of fresh RDG and Hiltaba Suite intrusive rocks are reported in Table 5.3 and plotted against SiO_2 as an index of differentiation in Figure 5.16. The data show an increase in $\delta^{57}Fe$ at SiO_2 of greater than about 72%, consistent with the growing number of studies in the literature that differentiated silicic rocks are isotopically heavy (Poitrasson and Freydier, 2005; Heimann et al., 2008; Schuessler et al., 2008; Gajos, 2014; Zambardi et al., 2014; Foden et al., 2015).

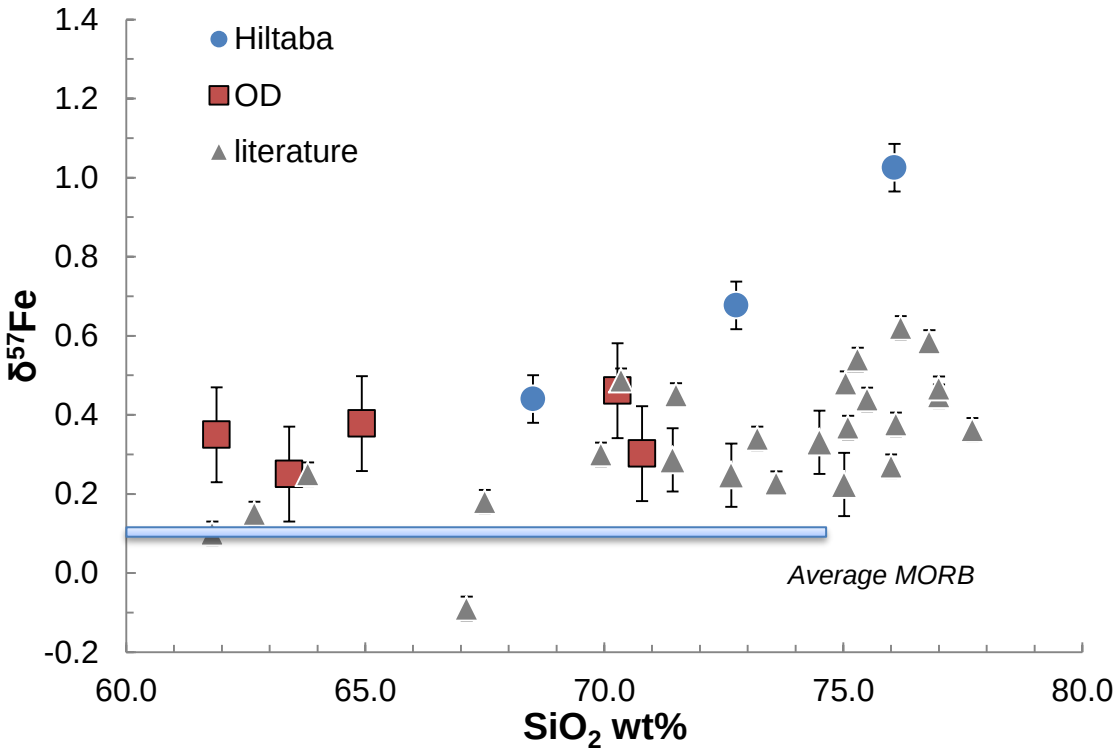

Figure 5.16 Variation diagram of SiO_2 vs $\delta^{57}Fe$ isotope ratio of Roxby Downs Granite (squares) and Hiltaba Suite Intrusions (circles). Data from the literature (grey triangles) are from Poitrasson and Freydier (2005), Schoenberg and von Blanckenburg (2006), Heimann et al. (2008), Craddock and Dauphas (2011), Telus et al. (2012), Zambardi et al. (2014), Foden et al. (2015). The average $\delta^{57}Fe$ for MORB (Teng et al., 2008) is shown for comparison.

Table 5.3 Sample descriptions and Fe isotope results for whole rocks and mineral separates from Olympic Dam and surrounding prospects

sample number (prefix 1405)	Description	$\delta^{57}Fe$ whole rock	2SD	$\delta^{57}Fe$ mgt	2SD	$\delta^{57}Fe$ py	2SD	$\delta^{57}Fe$ hem	2SD	$\delta^{57}Fe$ cpy	2SD	$\delta^{57}Fe$ sid	2SD
1	Fresh Granite. magmatic magnetite present	0.30	0.49	1.13	0.09								
9	Fresh Granite. magmatic magnetite present			1.06	0.06								
11	top of ore zone, Increasing frequency of hem veinlets and siderite approaching ore			0.41	0.13	0.19	0.31	0.47	0.09				
12	pervasively silicified felsic. Early sid-mgt-py, overprinted by hem- cp					0.60	0.07	0.24	0.02	0.25	0.06	-1.77	0.02
15	as above			1.42	0.03	0.58	0.14						
17	as above			0.71	0.07	0.01	0.06			0.11	0.06	-1.90	0.10
18	as above					0.61	0.10	-0.26	0.05	0.39	0.09	-2.20	0.04
20	as above			0.37	0.12			0.24	0.06				
66	earthy hem	1.22	0.01										
67	massive hem	0.37	0.10										

sample number (prefix 1405)	Description	$\delta^{57}Fe$ whole rock	2SD	$\delta^{57}Fe$ mgt	2SD	$\delta^{57}Fe$ py	2SD	$\delta^{57}Fe$ hem	2SD	$\delta^{57}Fe$ cpy	2SD	$\delta^{57}Fe$ sid	2SD
44	altered granite, hematite <20%	0.38	0.36										
48a	hem-ser altered RDG	0.35	0.02										
68	fg mgt-hem, fg disseminated py-cpy			0.52	0.02	0.54	0.07			0.35	0.08		
73	brecciated RDG, almost massive cpy							0.40	0.06	-0.14	0.07		
79	mgt-chl altered RDG	0.25	0.12	0.45	0.16								
80	thin ~2-3mm siderite veins in chl-mgt altered RDG											-1.59	0.06
82	hem-ser altered "bt-out" granite	0.46	0.06										
84	massive hematite	1.14	0.01										
85	disseminated cpy-hem ore			0.40	0.08			0.67	0.14	0.45	0.05		
86	granite breccia, 30-50% hem clasts	1.36	0.01										
87	granite breccia,10-20% hem clasts.	1.44	0.02										
55	fg dissem sulfides (>1%), in hematite breccia							0.72	0.02	-0.32	0.03		

sample number (prefix 1405)	Description	$\delta^{57}Fe$ whole rock	2SD	$\delta^{57}Fe$ mgt	2SD	$\delta^{57}Fe$ py	2SD	$\delta^{57}Fe$ hem	2SD	$\delta^{57}Fe$ cpy	2SD	$\delta^{57}Fe$ sid	2SD
56	fg dissem sulfides (>1%), in hematite breccia			0.68	0.11			0.58	0.07	-0.03	0.16		
57	fg dissem suls in hematite as matrix around earthy hematite clasts					1.28	0.04	1.38	0.15	0.52	0.02		
57_clast	earthy hematite clast							1.06	0.16				
22	massive earthy hem							0.67	0.14				
25	massive steely hem, cross cut by specular hematite vein							0.66					
26	mgt altered to specular hem			0.73	0.20								
28	cpy-hem overprints early mgt			0.47	0.13	1.46	0.09	0.47	0.12	0.51	0.04		
30	as above			0.65	0.06	0.57	0.06			0.21	0.04		
31	as above					0.54	0.13	0.39	0.05	-0.36	0.04		
32	siderite-mgt vein			1.29	0.08							-1.79	0.19
34	euhedral mgt-py overprinted by cpy			1.27	0.13	0.75	0.03			0.63	0.13		

sample number (prefix 1405)	Description	$\delta^{57}Fe$ whole rock	2SD	$\delta^{57}Fe$ mgt	2SD	$\delta^{57}Fe$ py	2SD	$\delta^{57}Fe$ hem	2SD	$\delta^{57}Fe$ cpy	2SD	$\delta^{57}Fe$ sid	2SD
36	hematite alteration in metasediment							0.85	0.02				
41	banded hem-py layers					0.61	0.01	0.50	0.07				
43	massive hematite, vugs filled with specular hem+barite					0.52	0.07	0.56	0.04				
50	massive hem with pyrite stringers					0.65	0.06	0.46	0.01				
51	massive hem							0.30	0.07				
52	py blebs in hem					0.60	0.10	0.40	0.10				
58	magnetite forms veins and breccia infill			0.39	0.14								
59	as above			0.96	0.05								
60	as above			0.38	0.15								
61	massive hematite							0.82	0.03				

The change in Fe-isotope composition of granite and granite breccias with total Fe is shown in Figure 5.17. There is no difference within analytical error between fresh Roxby Downs Granite and granite-rich breccias. However, hematite dominated (>20% Fe_2O_3) breccias, with the exception of one sample, are clearly isotopically heavier than fresh granite, suggesting that one (or more) of the hematite alteration events has a unique isotope signature. There could be potential for distinguishing hematite alteration that has occurred with the onset of mineralisation from deuteric fluid circulation that has resulted in the characteristic red colouring of hematite dusted feldspars found in Hiltaba Suite intrusions (Kontonikas-Charos et al., 2016; Putnis et al., 2007). In a detailed study of feldspar chemistry and textures, Kontonikas-Charos et al. (2016) posit that a relative increase in FeO content of red feldspars results from incorporation of Fe released from magmatic amphiboles during alteration to biotite; in an analysis of a bulk sample of "least altered granite" and "granite-rich breccias", therefore, the magmatic Fe has simply been shifted to a different mineral phase so that the overall $\delta^{57}Fe$ remains the same.

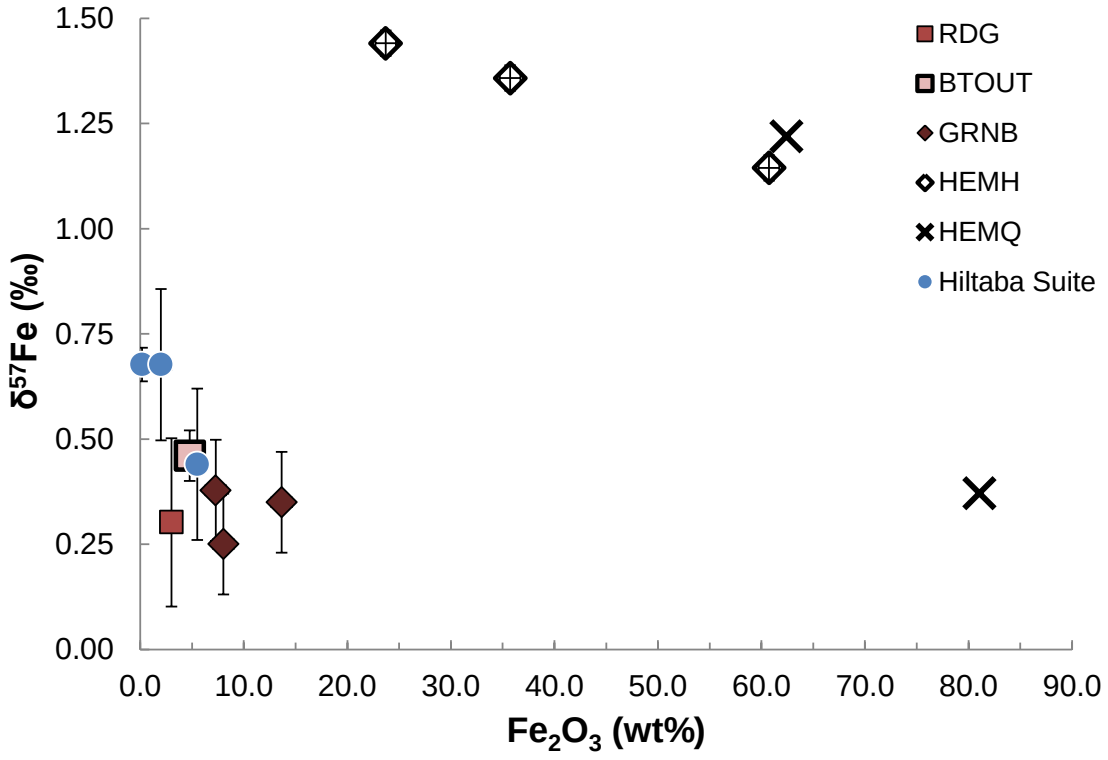

Figure 5.17 Scatterplot of Fe isotope ratio with total Fe content, categorised by breccia type (see text for details). Error bars for HEMH and HEMQ samples are smaller than the symbols used.

5.7.1.2 Mineral Separates

Fe isotope ratios for chalcopyrite (n=13), hematite (n=21), hydrothermal magnetite (n=16), magmatic magnetite (n=2), pyrite (n=15) and siderite (n=5) mineral separates are illustrated in Figure 5.18 and listed in Table 5.3. Iron isotope ratios of fresh Hiltaba Suite granites (including the RDG; n=5) and granitic and hematite-rich breccias (n=5) are also shown in Figure 5.18, but for clarity, are not subdivided into all the different breccia categories.

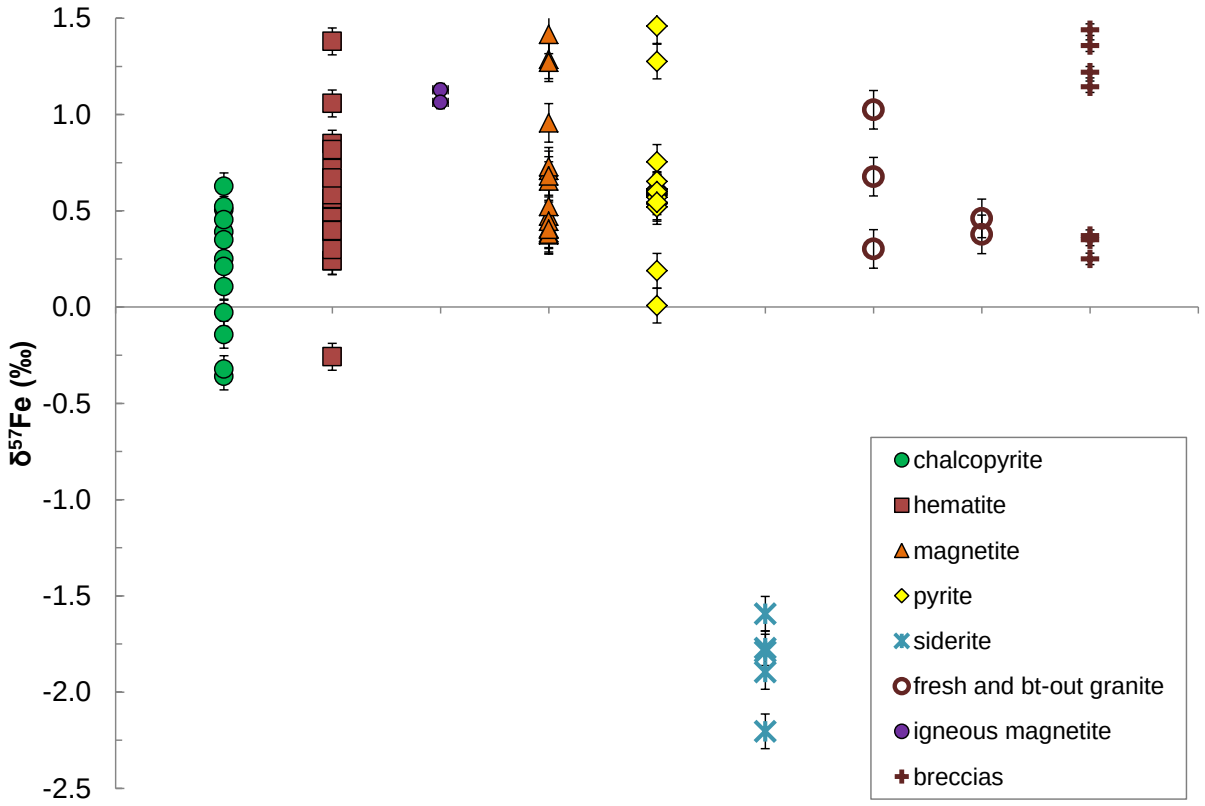

Figure 5.18 Fe isotope ratios of granites, granite-rich and hematite-rich breccias, and mineral separates from the Olympic Dam deposit.

Chalcopyrite δ^{57}Fe ranges from -0.36±0.04‰ to 0.63±0.13‰. Hydrothermal magnetite δ^{57}Fe ranges from 0.37±0.12‰ to 1.42±0.03‰. Magmatic magnetite returned two δ^{57}Fe values of 1.13±0.09‰ and 1.06±0.06‰ which are identical within analytical error, and appear on the whole to be heavier than hydrothermal magnetite. Pyrite δ^{57}Fe ranges from 0.01±0.06‰ to 1.46±0.08‰. Siderite is isotopically light; δ^{57}Fe ranges from -2.20±.04‰ to -1.59‰.

Hematite δ^{57}Fe ranges from -0.43±0.05‰ to 1.38±0.15‰. Whilst appearing to cover a range greater than all the other sulfide and oxide minerals, there are groupings within the hematite samples, and these will be discussed in a separate section.

5.7.2 Hillside Deposit

The results of Fe isotope analyses of granite and mineral separates are shown in Table 5.4 and Figure 5.19. The two samples of Hillside granites have a δ^{57}Fe of 0.36±0.05‰ and 0.38±0.1‰. Magnetite mineral separates (n=8) range from 0.21±0.01‰ to 0.84±0.08‰. Pyrite mineral separates (n=6) range from 0.38±0.03‰ to 1.09±0.04‰. Chalcopyrite results (n=13) have a wide range from -0.88±0.05‰ to 0.67±0.05‰. Bornite (n=2) is the most isotopically light mineral, with δ^{57}Fe of -1.44±0.21‰ and -1.53±0.05‰.

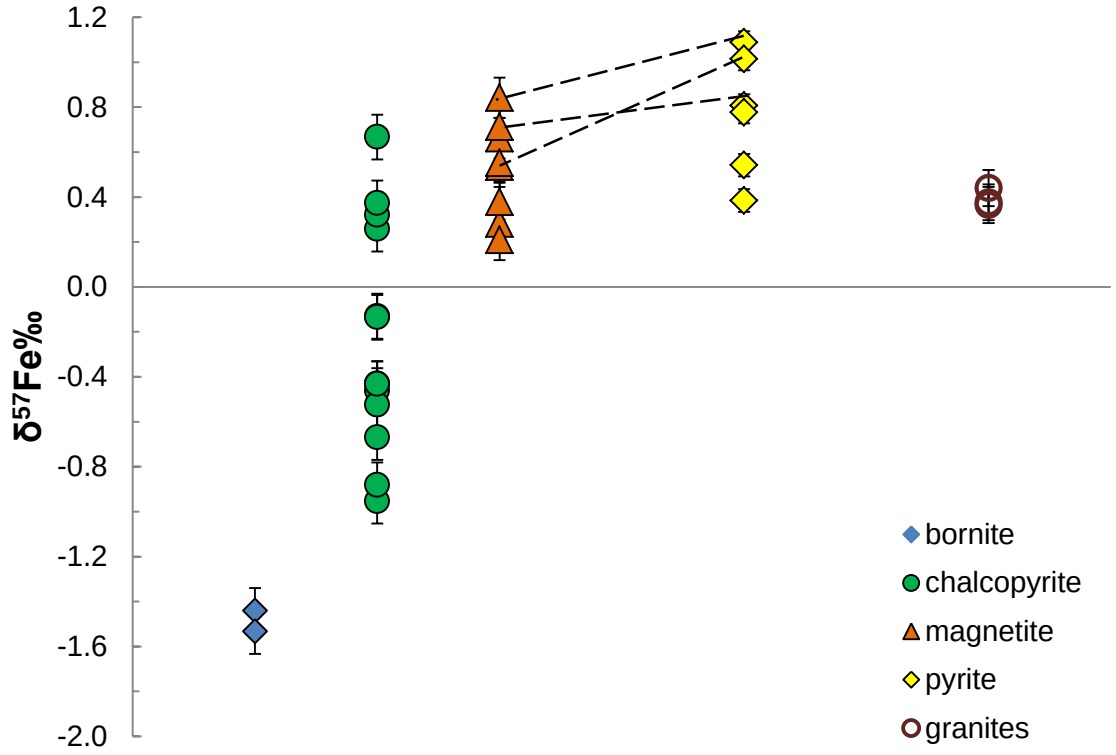

Figure 5.19 Fe-isotope ratios in granites and mineral separates from the Hillside deposit. Dashed lines are tie lines connecting magnetite and pyrite from the same sample.

Table 5.4 Sample descriptions and Fe isotope analyses from the Hillside deposit

Sample Number	Location	HoleID	Depth From	Description	mineral	$\delta^{57}Fe$	2SD	$\delta^{56}Fe$	2SD
HS391bn		HDD406	391.5	brecciated Hillside Syenite	bn	-1.44	0.21	-0.96	0.08
HS629bn				brecciated Hillside Syenite	bn	-1.53	0.05	-0.98	0.07
HS001cpy2	Zanoni	HDD277	100	massive cpy mineralisation	cpy	0.67	0.05	0.38	0.00
HS002cpy2		HDD277	178.72	massive cpy mineralisation	cpy	-0.67	0.05	-0.49	0.03
HS003cp2		HDD018W1	263.14	massive cpy replacing py-mgt skarn	cpy	0.26	0.06	0.17	0.01
HS003mgt					mgt	0.66	0.01	0.44	0.09
HS003py1					py	0.81	0.07	0.54	0.05
HS004mgt		HDD018W1	265.66	cpy-hematite replacing early mgt skarn	mgt	0.84	0.08	0.57	0.05
HS004py1					py	1.09	0.04	0.74	0.02
HS005cpy2		HDD018W1	416.4	cpy ore replaces py in garnet skarn	cpy	-0.13	0.04	-0.09	0.08
HS005py					py	0.78	0.04	0.54	0.02
HS006cpy2		HDD018W1	423.6	cpy ore replaces py in garnet skarn	cpy	-0.46	0.02	-0.32	0.03
HS007cpy2		HDD018W1	431.26	cpy ore replaces py in garnet skarn	cpy	-0.95	0.01	-0.67	0.03
HS007py		HDD018W1	431.26	cpy ore replaces py in garnet skarn	py	0.54	0.06	0.36	0.07

Sample Number	Location	HoleID	Depth From	Description	mineral	$\delta^{57}Fe$	2SD	$\delta^{56}Fe$	2SD
HS008cpy1		HDD018W1	440.7	wispy cpy-hem replaces mgt skarn	cpy	-0.88	0.09	-0.62	0.06
HS008mgt					mgt	0.71	0.08	0.46	0.01
HS009mgt	La Prena?	HDD346	381.45	hematite-magnetite-epidote skarn	mgt	0.28	0.12	0.20	0.07
HS010cpy1		HDD346	383.82	py-cpy-hem vein cross-cuts garnet skarn	cpy	0.32	0.01	0.24	0.06
HS010cpy2					cpy	-0.43	0.04	-0.29	0.06
HS010mgt					mgt	0.54	0.14	0.35	0.02
HS011cpy2		HDD346	408.08	cpy-hem overprints py-mgt	cpy	-0.52	0.06	-0.35	0.05
HS011mgt					mgt	0.55	0.12	0.36	0.03
HS011py					py	1.01	0.08	0.68	0.08
HS014cpy1	Le Prena	HDD280	195.04	wispy cpy in magnetite skarn	cpy	-0.43	0.12	-0.29	0.06
HS014mgt					mgt	0.21	0.01	0.12	0.08
HS015cpy2	Dart	HDD381	292.63	wispy cpy in magnetite skarn	cpy	0.37	0.03	0.22	0.06
HS016cpy1		HDD381	300.7	cpy ore replaces py in garnet skarn	cpy	-0.14	0.11	-0.07	0.11
HS016py1					py	0.38	0.03	0.28	0.02

Sample Number	Location	HoleID	Depth From	Description	mineral	$\delta^{57}Fe$	2SD	$\delta^{56}Fe$	2SD
HS017mg		HDD381	312.71	mgt-cpx-amph skarn	mgt	0.38	0.13	0.25	0.03
HS018		HDD016	502.5	red-rock altered granite	whole rock	0.36	0.05	0.26	0.00
HS020		HDD016	570.09	red-rock altered granite	whole rock	0.38	0.10	0.25	0.02
HS021		HDD023		relatively unaltered fine grained gabbro	whole rock	0.22	0.01	0.18	0.07
194030	Moonta	DD33		Arthurton granite	whole rock	0.44	0.03	0.31	0.11
JK001	Port Riley			Tickera granite	whole rock	0.68	0.17	0.45	0.14
JK005	Port Riley			Tickera granite	whole rock	1.03	0.04	0.68	0.05

Abbreviations: mgt=magnetite; hem=hematite; sid=siderite; cpy=chalcopyrite; py=pyrite; chl=chlorite; cpx=clinopyroxene; amph=amphibole; bn=bornite

5.8. DISCUSSION

5.8.1 Mineral-mineral fractionation and geothermometry at Olympic Dam

In this section we report $\delta^{57}Fe$ results for mineral separates based upon the sample location within the Olympic Dam deposit, to ascertain whether mineral separates sampled from different areas of the deposit have different $\delta^{57}Fe$ signatures. We also compare the theoretical mineral formation temperatures from Fe isotopes to fluid inclusion data using magnetite-siderite, pyrite-siderite and hematite-chalcopyrite pairs.

5.8.1.1 Theoretical mineral-mineral Fe isotope fractionation

A large body of research has reported temperature-dependent theoretical equilibrium Fe isotope fractionation between mineral pairs. It is beyond the scope of this paper to discuss the many parametric and spectroscopic derivations of theoretical fractionation factors (termed β-factors) for different minerals, and the interested reader is referred to Schauble (2004) for a review. The theoretical Fe isotope fractionation between 2 minerals precipitating in equilibrium from an isotopic reservoir (in this case a hydrothermal fluid) is shown in Figure 5.20. There are 2 key concepts to note; first, fractionation is inversely related to temperature, i.e. minerals deposited from cooler temperatures (e.g. 100°C) will show larger Fe isotope fractionations between them, than minerals deposited at magmatic-hydrothermal temperatures (~400°C). Second, there are predictions that can be made about the preference of the heavy isotope, ^{57}Fe, for partitioning into different minerals; magnetite and hematite are predicted to have similar $\delta^{57}Fe$ at a given temperature, pyrite will be somewhat isotopically heavier, and chalcopyrite and siderite will be the isotopically lightest.

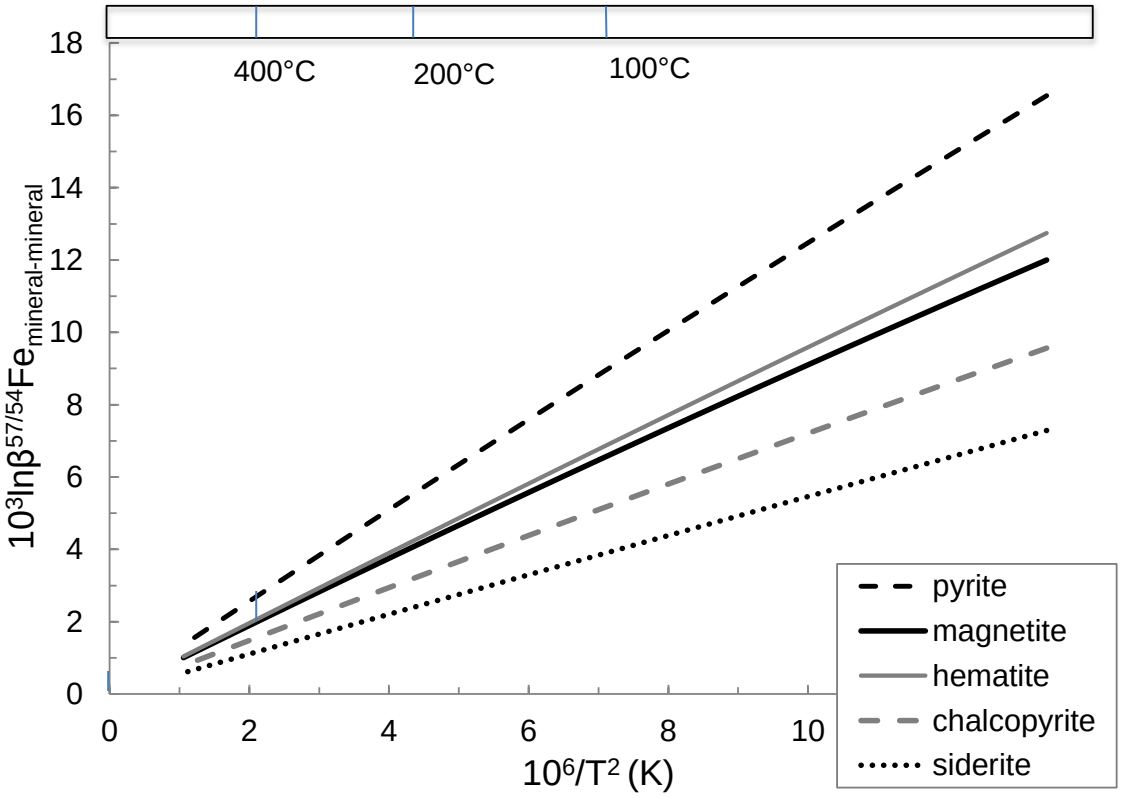

Figure 5.20. Theoretical mineral-mineral fractionation curve calculated from $10^3 \ln\beta$ factors for different minerals from the following sources: siderite sourced from Polyakov and Mineev (2000); hematite and magnetite from Polyakov et al. (2007); chalcopyrite from Polyakov and Soultanov (2011); pyrite from Blanchard et al. (2009). Each unit on the y-axis corresponds to 1‰ isotopic fractionation. The vertical distance between the curves for two minerals at a given temperature corresponds to the predicted isotopic fractionation between those two minerals.

The potential of magnetite-siderite and pyrite-siderite mineral pairs for geothermometry was highlighted by Polyakov and Mineev (2000). The heavy isotope, ^{57}Fe, is predicted to preferentially partition into Fe^{3+} bearing minerals, such as magnetite, or minerals with strongly covalent Fe-S bonds, such as pyrite. In contrast, ^{54}Fe is predicted to preferentially partition into Fe^{2+} bearing minerals such as pyrrhotite and carbonate minerals, such as siderite or ankerite. We therefore expect that (assuming equilibrium) there will be large fractionations between magnetite or pyrite and siderite, at hydrothermal temperatures documented at Olympic Dam and surrounding prospects.

The next few paragraphs describe in detail the results of mineral separates in each drill hole, each of which represents a different mine area. The hematite results

reported in this section refer to black, coarse-grained, bladed hydrothermal hematite that is co-precipitated with chalcopyrite.

5.8.1.2 RD2773

Results for mineral separates from drill hole RD2773 are shown in Figure 5.21. One magnetite-siderite pair (sample 1405_17) and three pyrite-siderite pairs (1405_12, 17 and 18) were analysed. Two magnetite-pyrite pairs were separated and analysed (samples 1405_15 and 17). Pyrite is isotopically lighter than the magnetite contrary to theoretical predictions; consequently, our negative $\Delta^{57}Fe/^{54}Fe_{pyrite\text{-}magnetite}$ results are unable to be plotted on a fractionation curve. Siderite is isotopically lighter than the oxide and sulphide minerals, consistent with theoretical predictions (refer Fig 5.20). There are 2 hematite-chalcopyrite pairs (1405_12 and 17) and these show contrasting results; one pair has identical $\delta^{57}Fe$, and the other pair has hematite which is isotopically lighter than chalcopyrite, opposite to theoretical predictions.

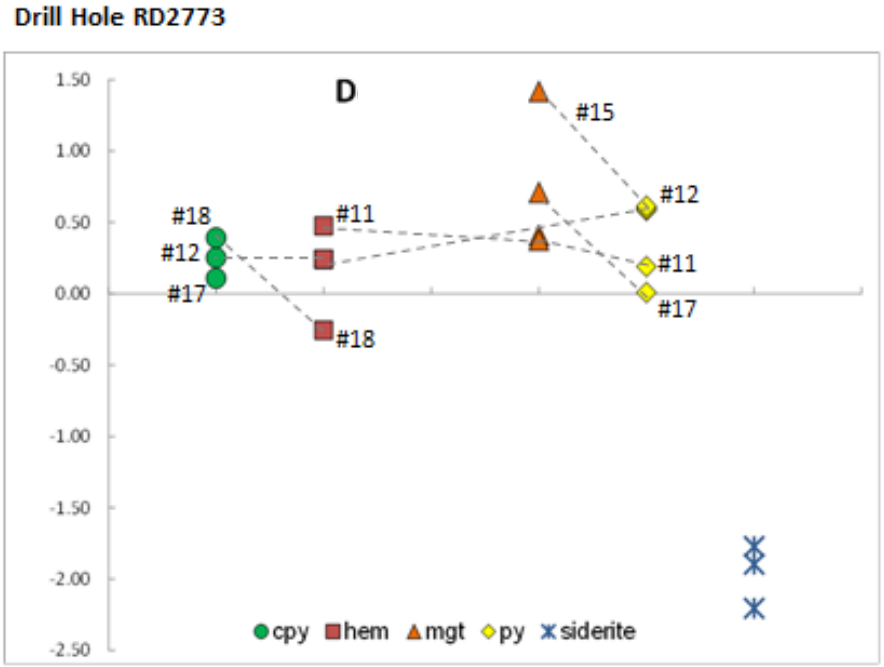

Figure 5.21 Iron isotope ratios for mineral separates from the Deep SE part of the Olympic Dam deposit. Mineral pairs are indicated using tie-lines, except for magnetite-siderite pairs which are omitted for clarity. Abbreviations cpy=chalcopyrite, hem=hematite, mgt=magnetite, py=pyrite.

The observed fractionation, $\Delta^{57}Fe/^{54}Fe_{A/B}$, between minerals A and B is equal to $\delta^{57}Fe_A$-$\delta^{57}Fe_B$. We have calculated an observed fractionation for magnetite-siderite

and pyrite-siderite pairs. These are shown in Table 5.5, and plotted on the theoretical fractionation curves in Figure 5.22. Pyrite-siderite pairs, assuming equilibrium, yield temperatures between 230° and 350°C; these temperatures are lower than those calculated by Oreskes and Einaudi (1992) for early magnetite formation. However the magnetite-siderite pairs give a much lower temperature of 110°C.

Our zero and negative values for $\Delta^{57}Fe/^{54}Fe_{hematite\text{-}chalcopyrite}$ cannot be plotted on the theoretical fractionation curve.

Table 5.5. Observed mineral-mineral fractionation ($\Delta^{57}Fe/^{54}Fe_{A/B}$) between mineral pairs. The observed fractionation between mineral A and B = $\delta^{57}Fe_A$-$\delta^{57}Fe_B$

sample number	**Δmgt-sid**	**Δpy-sid**
1405_12		2.37
1405_17	2.60	1.90
1405_18		2.82

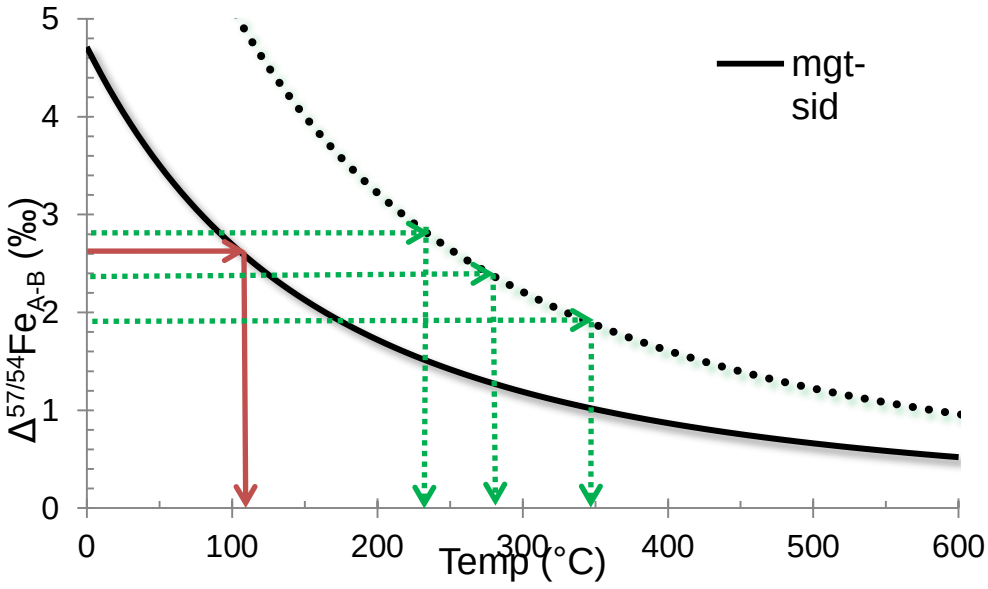

Figure 5.22 Theoretical fractionation curves for magnetite-pyrite, magnetite-siderite and pyrite-siderite curves, calculated using the same β-factors referred to in Figure 5.20. Dotted arrows indicate observed pyrite-siderite pairs. Solid arrows indicate the single observed magnetite-siderite pair. Thin dashed arrows indicate observed magnetite-pyrite pairs. Abbreviations as in Figure 5.21, sid=siderite

5.8.1.3 RD1988

Results for mineral separated samples from drill hole RD1988 are shown in Figure 5.23. We have included analyses from sample 1405_85, from drill hole RD2749 in this section because the two drill holes are relatively close to each other (Fig. 5.2). Chalcopyrite is uniformly isotopically lighter than hematite, consistent with theoretical predictions illustrated in Figure 5.20. We also analysed a granitic clast composed of fine-grained earthy hematite, and surrounding bladed black hydrothermal hematite in sample 1405_57. The hydrothermal hematite is relatively heavier than the earthy hematite clast (1.38±0.15‰ compared to 1.06±0.15‰).

There are 2 differences between minerals sampled from RD1988 and drill hole RD2773. First, the single pyrite sample here is relatively isotopically heavy at 1.28±0.04‰ (Fig 5.5), compared to the pyrite samples in the Deep SE mine area (0.0±0.06‰ to 0.61±0.1‰; Fig 5.3), well outside analytical uncertainty. Second, the hydrothermal hematites sampled from RD1988 cluster around $\delta^{57}Fe$ >0.5‰, whereas the hydrothermal hematites sampled from RD2773 cluster around $\delta^{57}Fe$ values less than 0.5‰.

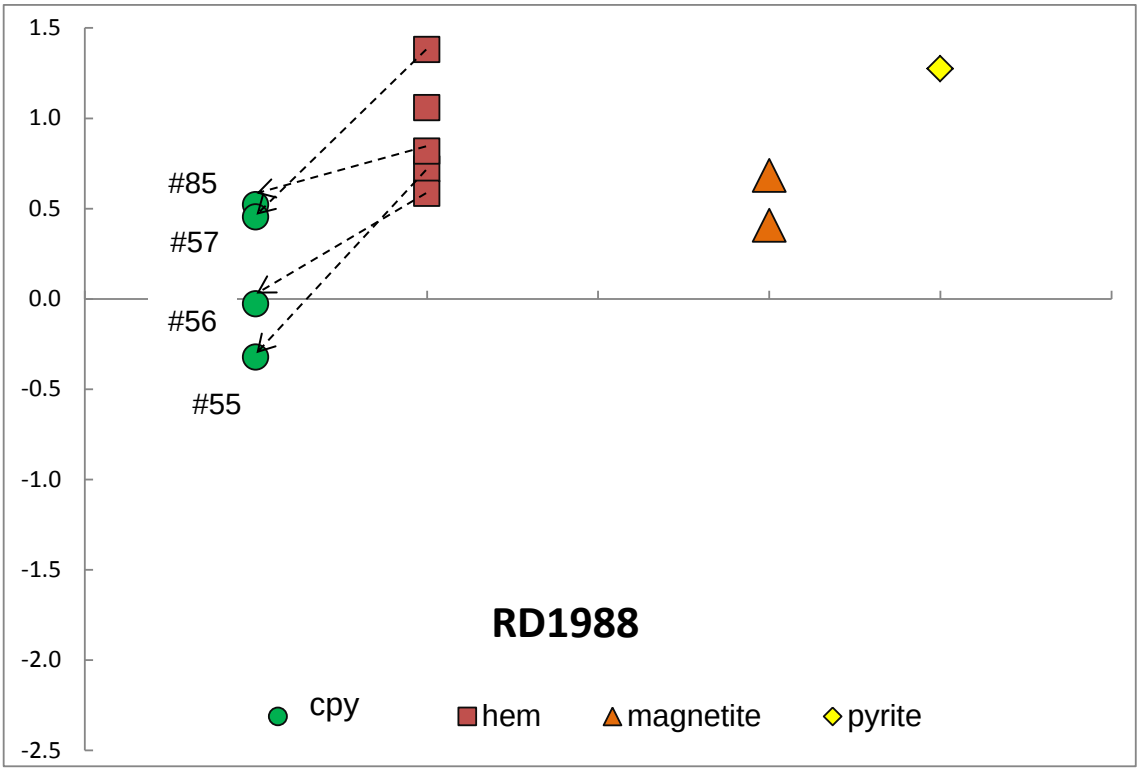

Figure 5.23 Iron isotope ratios for mineral separates from drill hole RD1988 from the Olympic Dam deposit. Mineral pairs are indicated using tie-lines. Abbreviations as in Figure 5.21

Four chalcopyrite-hematite pairs were analysed. These pairs yield similar values of $\Delta^{57}Fe/^{54}Fe_{hematite\text{-}chalcopyrite}$, of 1.06‰, 0.86‰ and 0.6‰, which yield temperatures of formation (refer to Figure 5.24) between 210° and 355 °C (Fig 5.24), consistent with the range of temperatures reported by Oreskes and Einaudi (1992) and Bodnar (2000). However 1405_85 has a $\Delta^{57}Fe/^{54}Fe_{hematite\text{-}chalcopyrite}$ of 0.22‰, which gives an unrealistically high formation temperature of over 700°C.

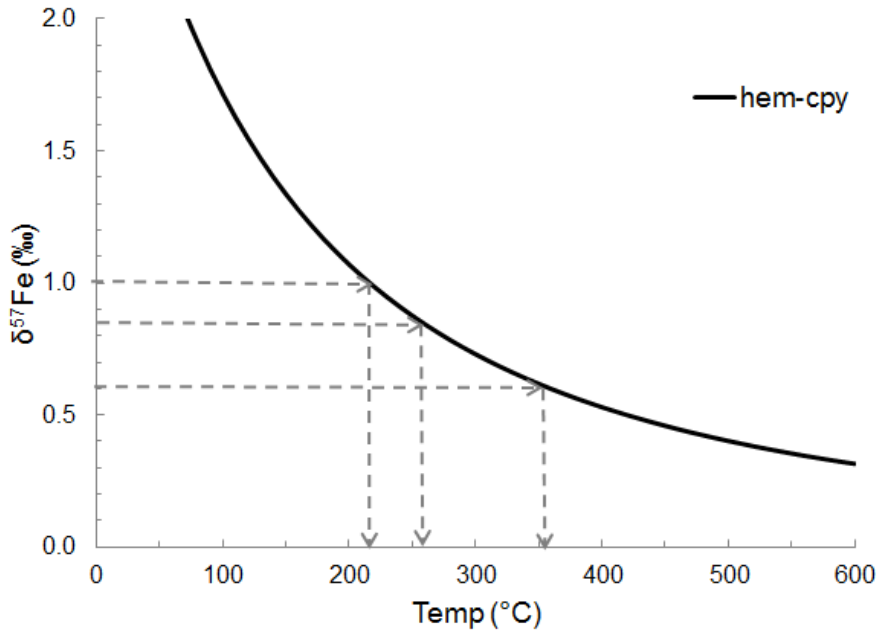

Figure 5.24 Theoretical fractionation curves for hematite-chalcopyrite pairs, calculated using the same β-factors referred to in Figure 5.20. Dashed arrows indicate empirical Fe-isotope fractionation between hematite-chalcopyrite pairs.

5.8.1.4 RU65-8230

Results for mineral separates from drill holes RU65-8230 are shown in Figure 5.25. The minerals in this drill hole are fine grained, and were difficult to separate, hence, only one single hematite-chalcopyrite pair (1405_73) was analysed. Sample 1405_73 is a sample of rare, massive chalcopyrite. Sample pair 1405_73 has a $\Delta^{57}Fe/^{54}Fe_{hematite\text{-}chalcopyrite}$ of 0.54‰ which equates to a temperature of formation of 395 °C (refer to Figure 5.24), entirely consistent with temperatures calculated by Conan-Davies (1987) for the formation of Fe-rich chlorites.

Although not obtained from the same sample, if we assume that the magnetite, pyrite and siderite precipitated at the same time from the same fluid, we can calculate $\Delta^{57}Fe/^{54}Fe_{pyrite\text{-}siderite}$ =2.14‰, which yields a temperature of formation of 310°C,

within the range of temperatures calculated using samples from RD2773. Calculated $\Delta^{57}fe/^{54}Fe_{magnetite\text{-}siderite}$=2.04‰, which yields a temperature of formation of 160°C, much lower than the ~400 °C calculated by Oreskes and Einaudi (1992).

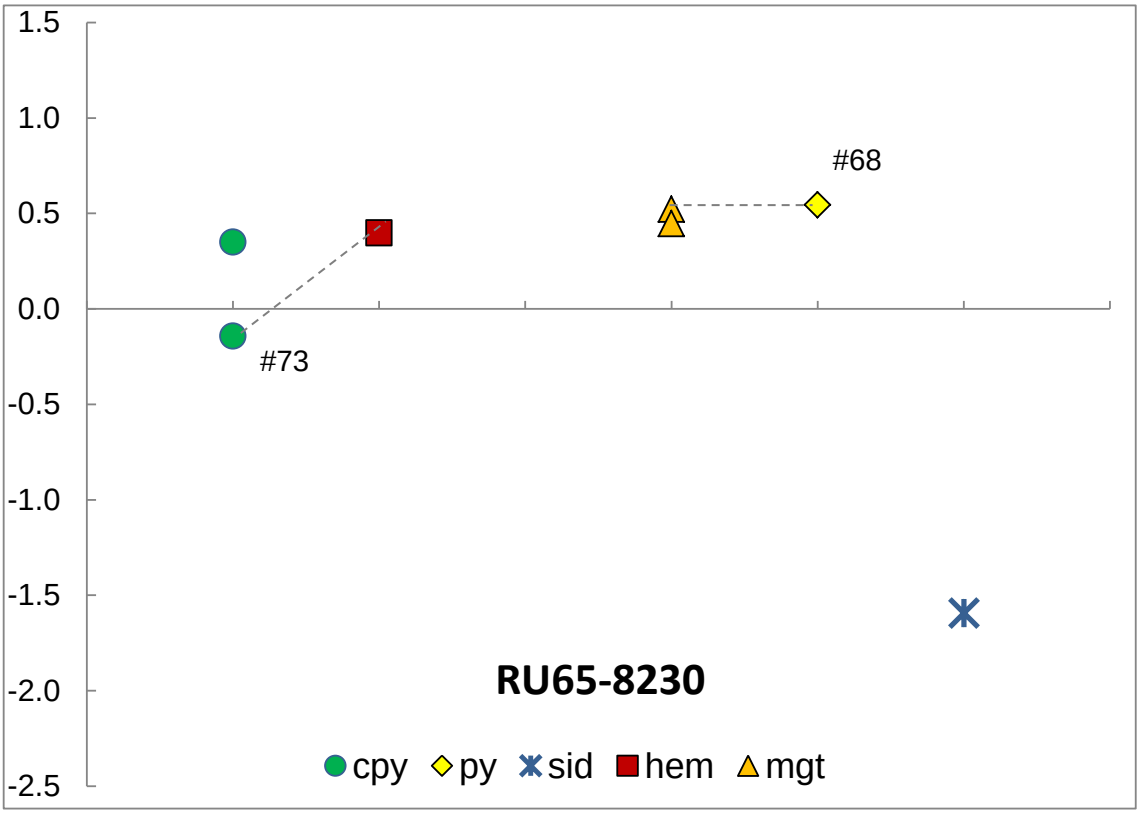

Figure 5.25 Iron isotope ratios for mineral separates from drill hole RU65-8230 from the northwest of the Olympic Dam deposit. Mineral pairs are indicated using tie-lines. Abbreviations as in Figure 5.21.

5.8.2 Wirrda Well

Iron isotope compositions of mineral separates from Wirrda Well are shown in Figure 5.26. Tie lines linking sample pairs show no consistency. In sample 1405_28, pyrite grains are rounded and inclusion rich (Fig 5.10A), and may occur as inclusions in chalcopyrite and coarse-grained magnetite. We have therefore excluded this sample from a temperature calculation. We note that similar to Olympic Dam, euhedral pyrite co-precipitated with magnetite (e.g. sample 1405_34, Fig 5.10B) is isotopically lighter, in contradiction to theoretical predictions.

We calculated an observed mineral-mineral fractionation and thence formation temperature for magnetite-siderite pair 1405_32, and hematite-chalcopyrite pair 1405_31 (Table 5.6) to compare to other datasets described previously.

Table 5.6. Empirical mineral-mineral fractionation ($\Delta^{57}Fe/^{5}Fe_{A/B}$) between mineral pairs at Wirrda Well.

sample number	Δmgt-sid	Δhem-cpy
1405_31		0.75
1405_32	3.08	

Sample 1405_32 yields a $\Delta^{57}Fe/^{54}Fe_{magnetite\text{-}siderite}$ of 3.08‰, which gives a formation temperature of ~70-80° a significantly lower temperature than those indicated by pyrite-siderite pairs from RD2773. Although not obtained from the same sample, if we assume that the pyrite from samples 1405_30, 31 and 34 and siderite from sample 1405_32 were precipitated at the same time from the same fluid, we can calculate $\Delta^{57}Fe/^{54}Fe_{pyrite\text{-}siderite}$ of 2.36, 2.33 and 2.54‰ respectively; these yield temperatures of formation of 280-260°C, consistent with the range of temperatures calculated using samples from RD2773 and RU65-8230.

Sample 1405_31 yields a $\Delta^{57}Fe/^{54}Fe_{hematite\text{-}chalcopyrite}$ of 0.75‰, which gives a formation temperature of ~300 °C (refer Figure 5.24). This result is consistent with the temperatures obtained from other hematite-chalcopyrite pairs described above, which range from 210 °C to 355 °C (RD1988) and 390 °C (RU65-8230).

Although this deposit is some 20km away from Olympic Dam, the isotopic compositions of mineral separates are identical in range to samples from the Olympic Dam drill holes, pointing to the similarity of mineralisation processes between the two deposits. We note that hydrothermal bladed hematite clusters around 0.5‰, which suggests that the different clusters observed between hematite samples from RD1988 and RD2773 may be artefacts of sampling density, rather than differences in fluid composition or geochemical processes.

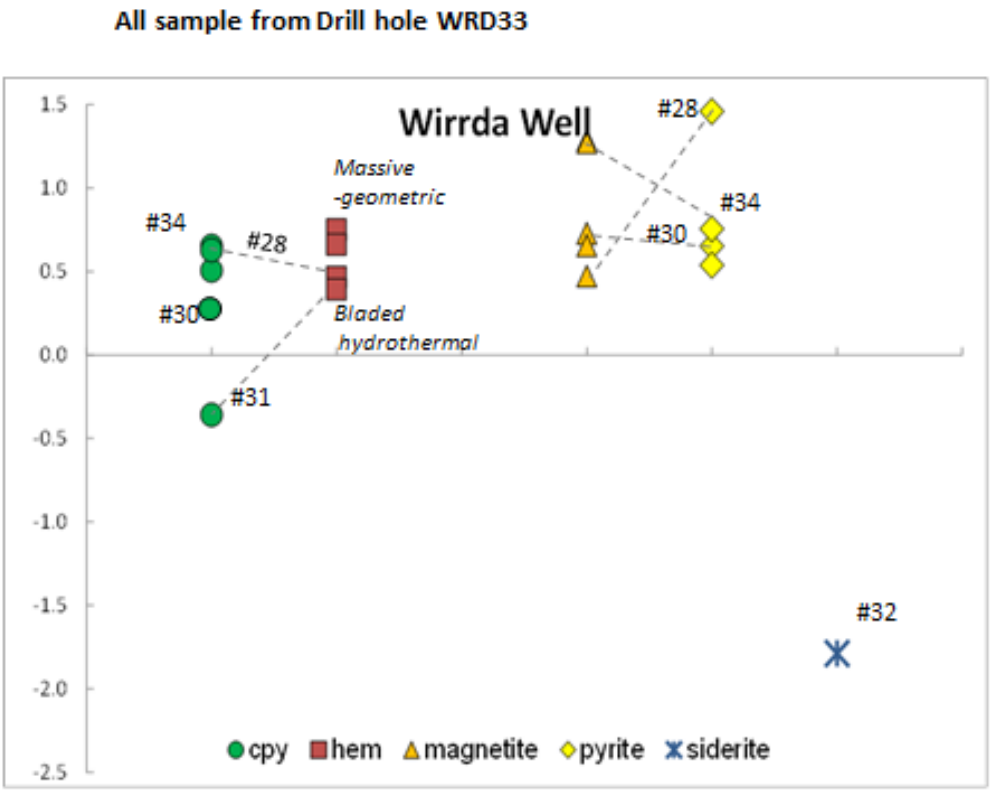

Figure 5.26. Iron isotope composition of mineral separates from the Wirrda Well prospect. Abbreviations as in Figure 5.21.

In summary, six out of the nine hematite-chalcopyrite pairs we analysed yield temperatures of formation between 210-390°C, which are consistent with the fluid inclusion temperatures of 130 °C and 280 °C (Oreskes and Einaudi, 1992) and 100 °C to 360 °C (Bodnar, 2000).

However, the empirical $\Delta^{57}Fe_{mgt\text{-}sid}$ return large values which yield formation temperatures which are much lower than microthermometry, or oxygen isotope geothermometry. The simplest explanation is that the 2 minerals were not precipitated at equilibrium conditions. Alternatively, several generations of siderite have been described from the deposit (e.g. Reeve et. al., 1990) so that in some samples we may have sampled a later generation of siderite. Yet a third alternative is that the fractionation factor we used for magnetite is incorrect, perhaps owing to mineral chemistry; Polyakov and Mineev (2000) showed that element substitution such as Co in magnetite can shift the theoretical fractionation factor by as much as 1‰ at 700K (430°C). Likewise the fractionation factors for siderite may have been affected by the substitution for Fe by Mn, Mg and Ca (Ehrig et al., 2012).

5.8.3 Magnetite replacement by hematite

One aspect of this study is to compare the iron isotope values of hematite which has replaced paragenetically early magnetite. We have 5 samples where we were able to sample across a reaction zone. These are samples 1405-11, 20 28 56 and 85 (Table 5.7 and Figure 5.27). We note that sample 1405_85 is different to the other 4 pairs. This sample is a fine grained breccia, and in thin section there are micro-breccia clasts composed of fine grained aggregates of hematite (similar to the isotopically heavy red earthy clast of 1405_57) of similar size to the bladed black hematite grains; thus sample 1405_85 may be isotopically heavier owing to mixing of different hematites in the sample. If we discount this sample, the other 4 pairs show that within analytical error, the two minerals have identical values.

Conversion of magnetite to hematite has been proposed as the key mechanism for copper sulfide deposition at Olympic Dam (e.g. Haynes et al., 1995), as magnetite acts as a source of electrons to reduce sulphur from the 6+ oxidation state (as sulphate) to the 2- oxidation state (sulfide). The oxidation of magnetite occurs in the following reaction (Haynes et al., 1995):

$$2Fe_3O_4 + SO_4^{2-} + 2H^+ \rightarrow 3Fe_2O_3 + H_2S + 1.5O_2$$

This reaction results in pseudomorphic replacement of magnetite by hematite (martitisation; Mücke and Cabral, 2005), which is widespread in the deposit (e.g. Fig5.10B). If Fe is conserved, and not mobilised, then no fractionation would be expected.

Table 5.7 Comparison of Fe isotope ratios between magnetite and overprinting hematite

Sample Number	**Mineral**	**δ^{57}Fe**	**2SD**
11hem	hematite	0.47	0.09
11mgt	magnetite	0.41	0.13
20hem	hematite	0.24	0.06
20mgt	magnetite	0.37	0.12
28hem	hematite	0.47	0.12
28mgt	magnetite	0.47	0.13

Sample Number	Mineral	$\delta^{57}Fe$	2SD
56hem	hematite	0.58	0.07
56mgt	magnetite	0.68	0.11
85hem	hematite	0.67	0.14
85mgt	magnetite	0.40	0.08

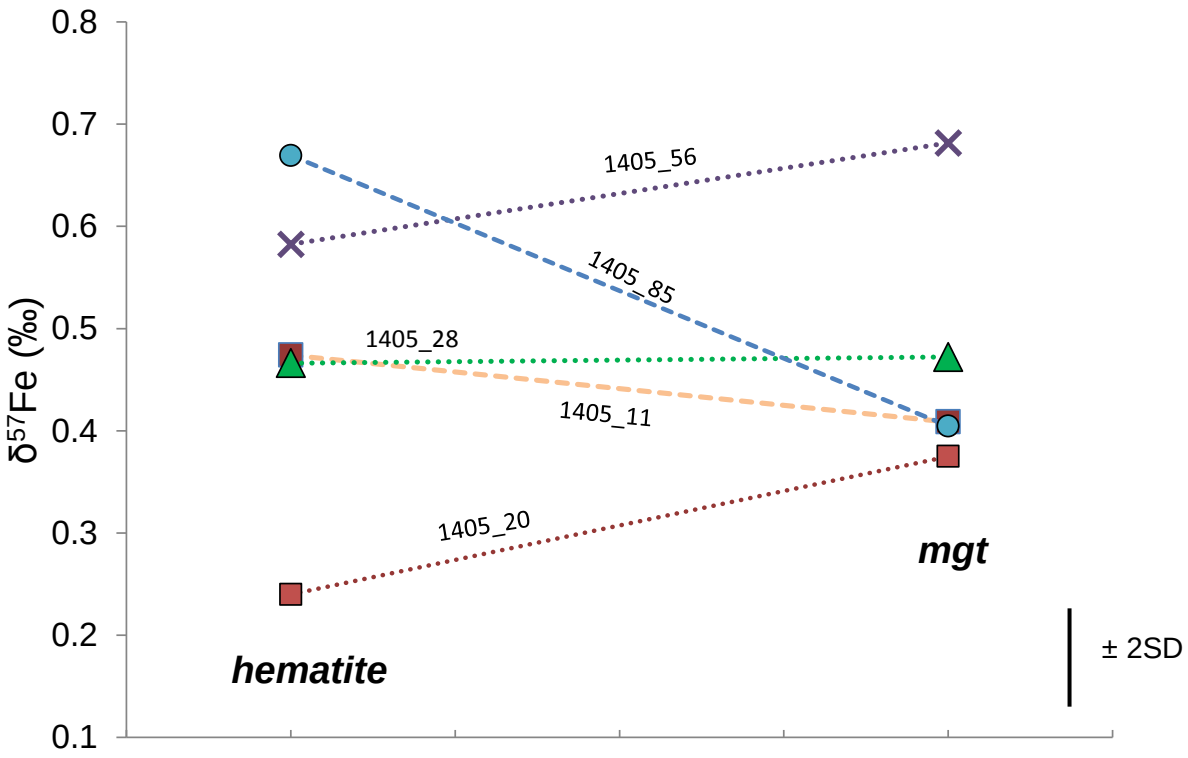

Figure 5.27 Fe isotope values of magnetite overprinted by hydrothermal hematite. Olympic Dam samples are from RD2773 (red squares), RD12749 (blue circle), RD1988 (purple cross). Wirrda Well sample 1405_28 is from WRD33, shown in the green triangle.

5.8.4 On the Fe-isotope composition of massive geometric and specular hematite

Samples of massive, steely hematite, examined in thin section (Figure 5.11), are fine grained and geometric, clearly different in morphology from the bladed hydrothermal hematite associated with sulfide deposition (Fig 5.7B,C). However, these steely

hematites have isotopic compositions similar to those of bladed hydrothermal hematites (Figure 5.28). At Wirrda Well, the steely hematite from sample 1405_25 higher up the hole (714m) is ~0.2‰ isotopically heavier than the bladed hematite from samples 1405_28 and 31 at depth (1087 and 1605m respectively). At Island Dam the composition of both bladed and steely hematite, are within analytical error. Davidson et al. (2007) posited that weathering during the Proterozoic caused the formation of a large inselberg with supergene leaching of sulfides and metals, prior to the deposition of sedimentary successions during the Mesoproterozoic (1424±51 Ma; Fanning et al., 1983). The similar petrography of hematite from Island Dam and Wirrda Well (bluish steely grey; Fig 5.9), as well as supergene texture development (e.g. cockade textures in Fig 5.11C), suggests that these areas were also exposed to weathering and leaching processes.

Insights into the behaviour of Fe iron isotopes in during weathering processes, characterised by near surface temperatures and oxygenated waters, can be gained by studying modern day ferruginous soil and laterite profiles. Poitrasson et al. (2008), studied a modern day laterite profile in the Cameroon, developed over a granodiorite bedrock, and demonstrated that there was only ~0.2‰ range in the $\delta^{57}Fe$ of hematite and goethite-rich nodules and clays ($\delta^{57}Fe$ range from 0.059‰ to 0.268‰). Mössbauer spectroscopy confirmed >96% of Fe was exclusively in the ferric state. Wiederhold et al. (2007) studied a cambisol (a soil in which chemical weathering has occurred, but no mobilisation of iron), in which crystalline iron oxides form the bulk of the Fe pool, and found negligible variation in $\delta^{57}Fe$ throughout the profile ($\delta^{57}Fe$ ~0.3‰).

The effect of oxidative weathering of sulphide minerals was tested by Fernandez and Borrok (2009). These researchers discovered that a thin coating of Fe(III)-bearing minerals developed on the sulphide mineral surfaces when samples were left in air for up to 7 months before leaching. These iron oxides resulted in the first leachate being isotopically heavier by up to 1‰ compared to the bulk rock. Similar results have been reported by Cheng et al. (2015), who reported isotopically heavy gossans ($\delta^{57}Fe$ range from 0.11‰ to 0.3‰) compared to primary sulphide ore ($\delta^{57}Fe$ range from -0.49‰ to -0.04‰) from the Gaosong Sn-Pb-Zn deposit. Therefore, our results can be explained by a model in which weathering of hematite breccias occurred with little overall Fe isotope fractionation, owing to the oxidising conditions in which Fe

remains in the ferric state, combined with an acid rock leaching process whereby Fe oxy-hydroxides developed on sulphide surfaces provided a reservoir of heavy iron.

In contrast, the isotopic composition of specular hematite infill from vugs which cross cut massive hematite, is clearly isotopically lighter than the massive hematite (Fig 5.28), by 0.99‰ in the case of sample 1405_43 (0.56‰ for steely hematite, -0.43‰ for specular hematite). The vugs also contain barite and quartz, determined from thin section petrography. The isotopically light specular hematite is consistent with the experiments of Wu et al. (2010) who found that Si-bearing, near neutral (pH ~7-8) solutions in contact with hematite resulted in enrichment of light isotopes in the solution. However, Skulan et al. (2002), found that Fe (III)-bearing solutions in contact with hematite produce a strongly time dependent fractionation. Initially, an isotopically light hematite is rapidly precipitated, leaving an isotopically heavy solution. Over time, the fractionation between $Fe(III)_{aqueous}$ and hematite decreased to -0.1±0.2‰. It is possible, therefore, that the isotopically light specular hematite is dominated by an early kinetic fractionation process. A further alternative is that the Fe in the specular hematite was sourced from a separate Fe reservoir, not from the ironstone. Further isotope studies (e.g. ^{18}O) and dating would be needed to confirm this interpretation.

Thus, the Fe isotope signature of weathering products records a complex interplay of variables such as composition of the source materials and fluids, redox processes and pH. This is notwithstanding the significant fractionation effects of biogenic processes such as dissimilatory iron reduction and organic ligands (e.g. Beard et al., 2003), a detailed discussion of which is beyond the scope of this chapter.

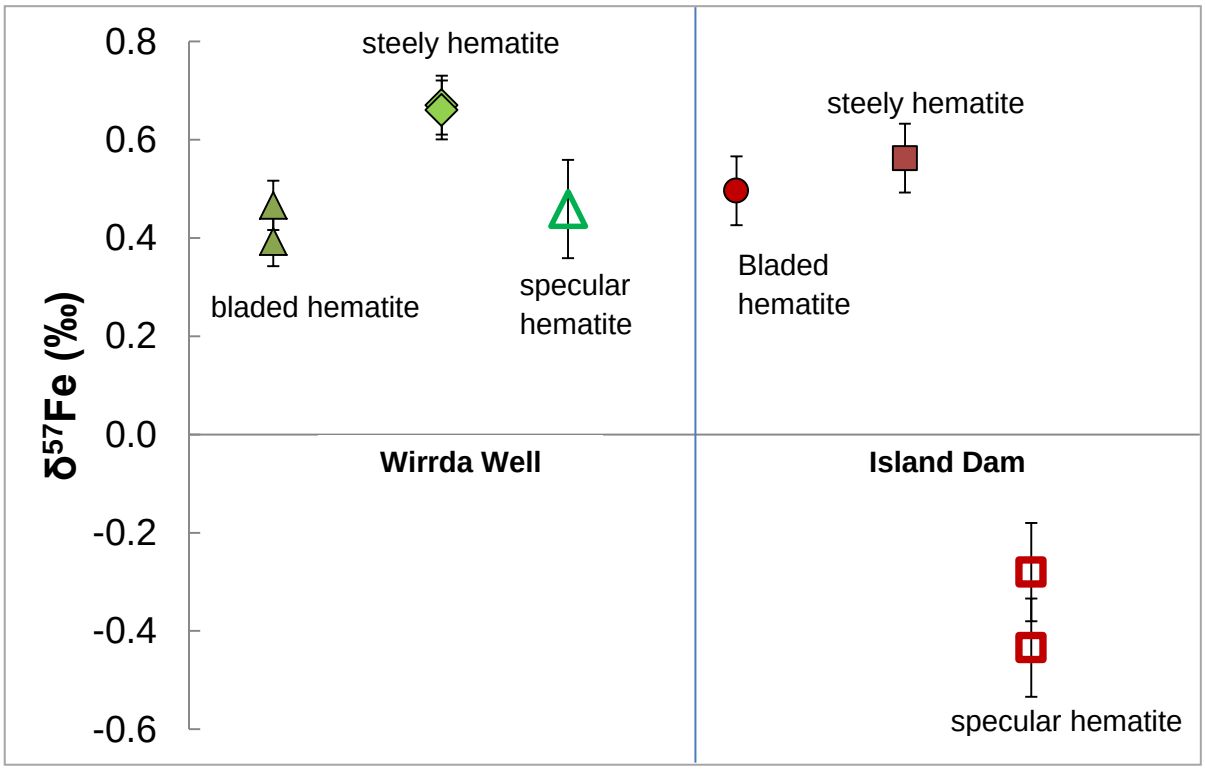

Figure 5.28. The different Fe isotope compositions of different generations of hematite from Wirrda Well (green triangles/diamond) and Island Dam (red circle/squares). Bladed hematite is hydrothermal and associated with chalcopyrite deposition. Massive hematite is classified as “ironstone” (Davidson et al., 2007), and specular hematite is coarse grained and fills vugs that cross cut massive hematite (Fig 5.11C).

5.8.5 On the Fe-isotope composition of siderite

There are few studies of siderite reported in the literature. Weisli et al. (2004) reported results of experiments at 20 °C which investigated Fe-isotope fractionation between Fe(II)-bearing aqueous fluids and siderite. They demonstrated that siderite is expected to be isotopically lighter than a fluid, a result later confirmed by theoretical studies (Blanchard et al., 2009; Rustad et al., 2010). Markl et al. (2006) reported δ^{56}Fe results of natural hydrothermal and supergene siderite from the iron and base metal deposits of the Schwarzwald district in Germany. Dideriksen et al. (2006) reported δ^{56}Fe results of natural calcium carbonate materials from a range of geological environments, including pegmatite, skarn, marble, limestone and hydrothermal deposits. Wawryk and Foden (2015) reported hydrothermal siderite analyses from the Renison Sn-W deposit in Tasmania.

Our siderite results are shown in comparison with published results in Figure 5.29. The compositions from different localities (Dideriksen et al., 2006) span a large range of isotopic compositions, from 0.05‰ to -2.20‰.

Isotopic compositions of siderite from the Schwarzwald and Olympic Dan are identical in composition. The Schwarzwald hydrothermal hematite-base metal veins are interpreted to have formed from mixing of a basinal brine with oxidised meteoric waters at temperatures between 120° and 150 °C (Markl et al., 2006). However, thermodynamic modelling by those authors demonstrates that siderite must have precipitated from a separate, more reduced fluid, containing CO_2. The modelling presented by Markl et al. (2006) predicts that a reduced fluid would precipitate magnetite then siderite; this is observed at Olympic Dam, with CO_2 provided by magmatic fluids exsolved from a magma crystallising at 4-5km depth (Bodnar, 2000). Fluid inclusions and stable isotope geothermometry (Oreskes et al., 1992) suggest that magnetite-siderite at Olympic Dam formed at temperatures ~400°C.

The Renison siderites formed at similar temperatures of ~350 °C (Kitto, 1994). The Renison siderites, however, are isotopically heavier than both Schwarzwald and Olympic Dam siderites. Siderite at both Renison and Olympic Dam form an outer halo to the deposits (Kitto, 1994; Ehrig et al., 2012)., An explanation for the differences in siderite composition may lie in a consideration of coprecipitating mineral assemblages; at Renison, siderite is formed as an outer halo to pyrrhotite replacement of carbonate. Pyrrhotite is isotopically lighter than siderite (Wawryk and Foden, 2015), so if light iron was preferentially sequestered into pyrrhotite, then the siderite would include the heavier isotopes. In comparison, siderite at Olympic Dam is co-precipitated with magnetite and pyrite, both of which preferentially incorporate the heavy iron isotopes (see Fig 5.20); thus, siderite preferentially incorporates the lighter isotope.

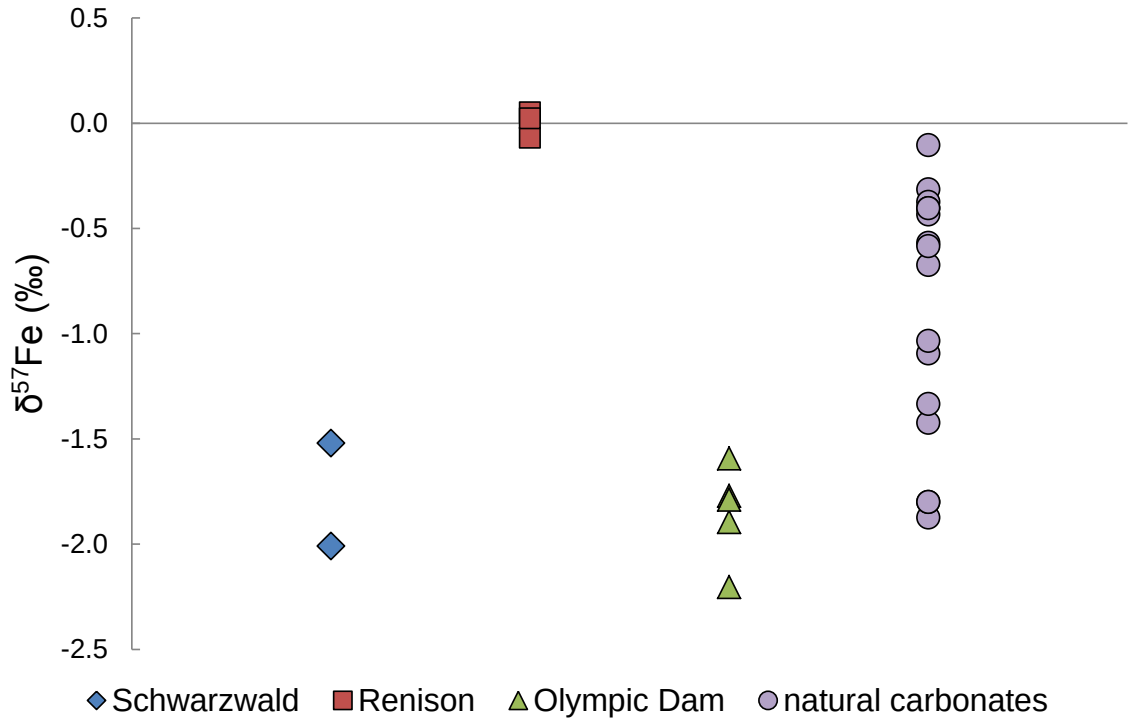

Figure 5.29. Iron isotope results for siderites mineral separates from Olympic Dam. Results from other published sources shown for comparison. Schwarzwald data from Markl et al. (2006), only primary siderite data shown. Renison data from Wawryk and Foden (2015). Natural carbonate data from Dideriksen et al. (2006) shown for comparison.

5.8.6 Magnetite-pyrite geothermometry at Hillside

Previous temperature estimates report that sulphide deposition at Hillside may have initiated at ~550 °C (Ismail et al., 2014). There are fewer examples of co-precipitated minerals in our sample suite to use as potential geothermometers. However, our pyrite samples are usually isotopically heavier than the magnetite samples, so we have calculated $\Delta^{57}Fe/^{54}Fe_{pyrite\text{-}magnetite}$ for 3 mineral pairs (HS003, HS004 and HS011), tabulated below in Table 5.8.

Table 5.8 Calculated Fe isotope fractionation factors for pyrite-magnetite pairs at Hillside.

Sample Number	calculated $\Delta^{57}Fe/^{54}Fe_{py\text{-}mgt}$	Temperature
HS003	0.145	>900
HS004	0.246	>900
HS011	0.462	580°C

Two of the mineral pairs yield unrealistically high temperatures for magmatic hydrothermal fluids, however, sample HS011 yields a temperature of formation of 580°C, identical to the estimate of Ismail et al. (2014).

5.8.7 Olympic Dam and Hillside Compared

When compared to each other, the overall spread of isotope values of minerals appears to be similar (Fig 5.30). Bornite was not sampled from Olympic Dam, so only results from bornite samples at Hillside are presented.

Bornite in the Hillside samples occurs in brecciated Hillside Syenite and is unaccompanied by magnetite or other sulfides in our samples. The bornite has relatively light isotopic values compared to chalcopyrite, and is lighter than values from hypogene bornite sampled from the Batu Hijau porphyry Cu-Au deposit ($\delta^{57}Fe$ values range from -0.72 to -0.08‰; Wawryk and Foden, submitted).

The ranges of isotopic values for each group of mineral separates from both Olympic Dam and Hillside overlap, suggesting similar fractionation processes operated during mineral formation, despite the differences in host rocks and estimated temperatures of deposition. However, the $\Delta 57^{Fe}_{py\text{-}mgt}$, calculated by $\delta^{57}Fe_{py} - \delta^{57}Fe_{mgt}$ have opposing signs. The calculated $\Delta 57^{Fe}_{py\text{-}mgt}$ at Hillside (average of 0.28‰) give temperatures at ~800°C (Figure 5.31), which is unreasonably high, given that pyrite is stable at a maximum temperature of 740 °C in the presence of liquid sulfur (J. Walshe, pers comm).

That magnetite and pyrite most likely formed in disequilibrium conditions is illustrated in Figure 5.32. The graph shows the values of $\delta^{57}Fe$ that would be exhibited by magnetite-pyrite pairs formed at equilibrium, at different temperatures. Because magnetite is predicted to be isotopically lighter than pyrite, the trends would have a positive slope, which is clearly not the case here; the Olympic Dam samples (blue triangles) are scattered with no obvious trend, and the Hillside samples (orange squares) form close to a line predicting a temperature of formation of >700 °C. Two samples fall on the equilibrium contours for around 450-500°C, which illustrates that there is potential for geothermometry, but a careful interpretation of mineral textures would be required to choose the most appropriate samples.

The opposing signs of $\Delta 57^{Fe}_{py\text{-}mgt}$ between the two deposits is enigmatic. Pyrrhotite has been observed at Olympic Dam (Ehrig et al., 2012), so one possibility is that pyrite at Olympic Dam formed from an isotopically light FeS precursor (c.f. Rouxel et

al., 2008), which has retained an isotopically lighter kinetic fractionation signature. This is supported by the experiments of Syverson et al. (2013), who demonstrated that at 300°C, pyrite has an isotopically light value which gets heavier over time. This was attributed to the formation of an FeS precursor which is isotopically light owing to kinetic fractionation.

Alternatively, paragenetically early pyrite (see Figures 5.8A and 5.10A), or earthy amorphous hematite (see Figure 5.8C) have isotopically heavy values. For example sample 1405_28 from Wirrda Well contains rounded early pyrite grains with a $\delta^{57}Fe$=1.28‰. Earthy hematite clast from sample1405-57 has a -1.44±0.21‰ and -1.53±0.05‰.Magmatic magnetite in the Roxby Downs granite is also relatively heavy (1.13±0.09‰ and 1.06±0.06‰). Dissolution of these minerals and quantitative precipitation as hydrothermal magnetite would thus retain the initially isotopically heavy values (c.f. Horn et al., 2006).

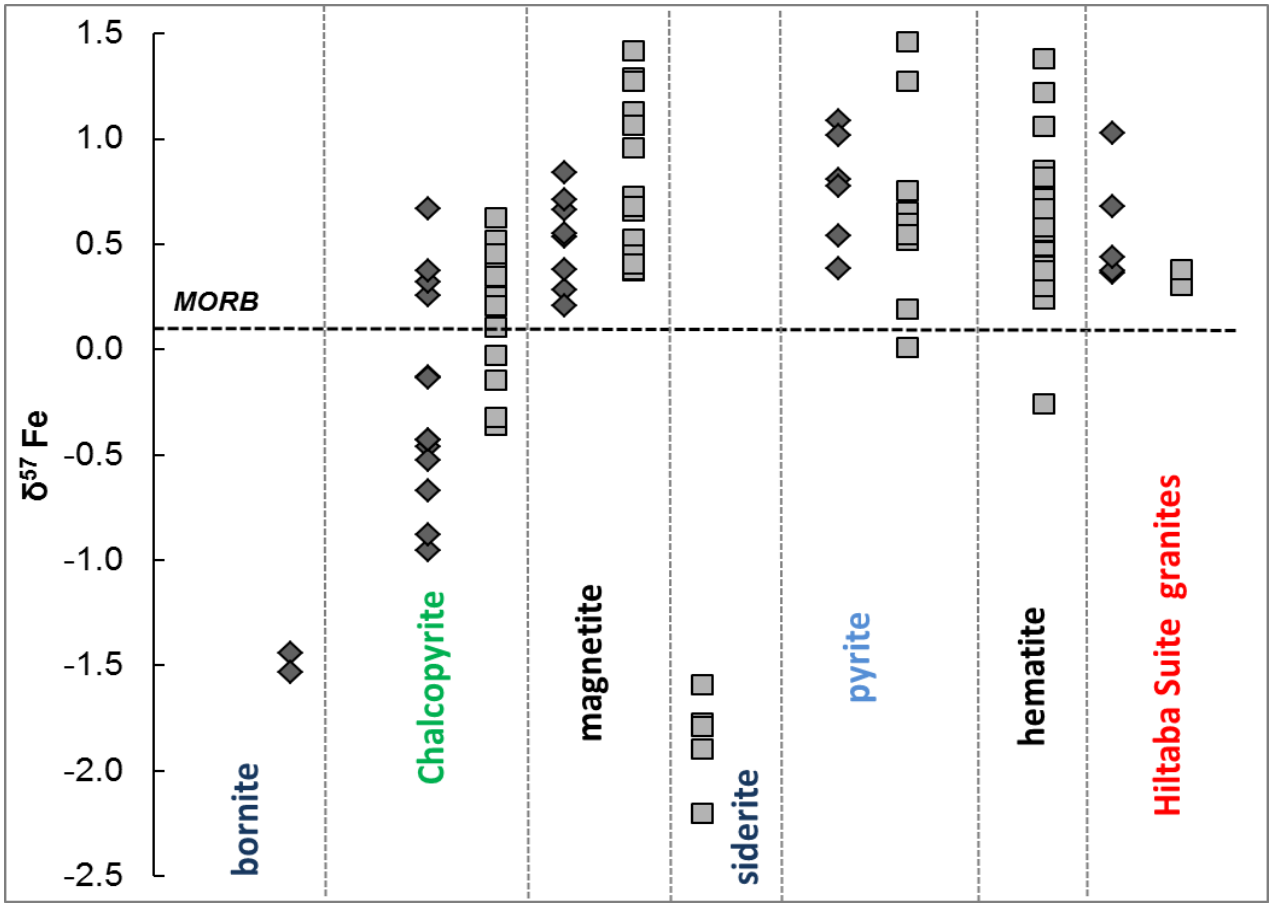

Figure 5.30 Comparison of Fe isotope values in samples from Olympic Dam (squares) and Hillside (diamonds)

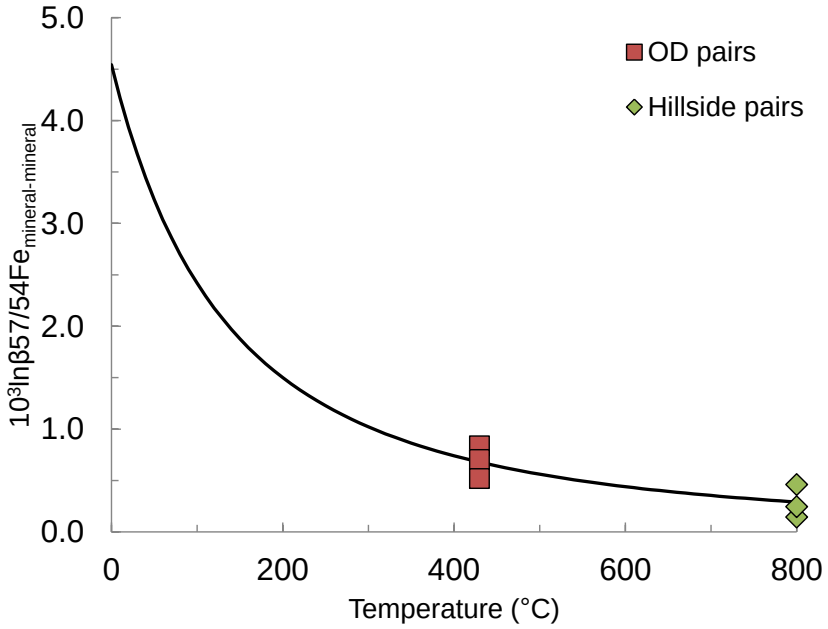

Figure 5.31 Apparent iron isotope fractionation between magnetite and pyrite pairs at Olympic Dam and Hillside. The solid curve is theoretical iron isotope fractionation between magnetite and pyrite as a function of temperature. The curve has been calculated using the beta factor for magnetite from Polyakov et al. (2007) and the pyrite beta factor derived by Blanchard et al. (2009)

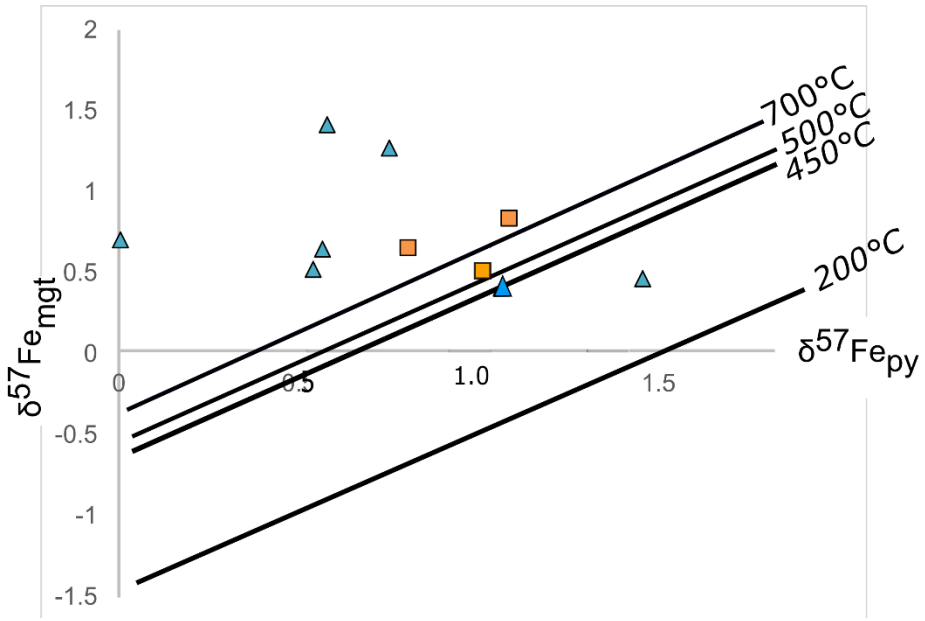

Figure 5.32 Scatterplot of iron isotopes ratios of magnetite and pyrite shown with predicted equilibrium temperature contours**.** Magnetite-pyrite pairs from Olympic Dam are shown in blue triangles and pairs from Hillside are shown in orange squares.

5.8.8 On the Fe isotope composition of magnetite from IOCG and IOA deposits

The use of stable Fe isotopes to investigate the origin of Fe in Iron Oxide Apatite (IOA) deposits has been investigated by Weis (2013), Knipping et al. (2015) and Bilenker et al. (2016). These authors have analysed magnetite separates from IOA deposits from Kiruna (Sweden), the Chilean Iron Belt, China and the USA, as well as magmatic magnetite from volcanic lavas that range from basalt to dacite in composition. Knipping et al. (2015) propose a 3 step model of massive magnetite deposition. First, magnetite crystals are preferentially wetted compared to other minerals in a silicate melt; second, magnetite crystals become suspended in bubbles within an exsolving magmatic-hydrothermal fluid, and aggregates of magnetite-bubble pairs form a magnetite suspension during fluid ascent; and third, massive magnetite precipitates from the magnetite suspension in faults during tectonic activity.

Our Fe isotope analyses of magnetite separates from Olympic Dam and Hillside compared to the published data are illustrated in Figure 5.33, along with isotope ratios from magmatic magnetite separated from Hiltaba Suite granite. All groups overlap. Magnetite separates from the Hillside skarn deposit are isotopically heavy relative to the Fe-skarn samples from the Dannemora district in Sweden.

These authors also measured ^{18}O isotopes in the magnetite samples, and concluded that magmatic-hydrothermal magnetite can be distinguished from magnetite formed by secondary alteration or lower temperature hydrothermal processes by comparing the coupled Fe and O isotope signatures. The authors have defined a ‘box’ of orthomagmatic isotope compositions (orange area), for temperatures>600°C, which is distinct from the isotopic values of samples interpreted to precipitate from lower temperature hydrothermal processes, i.e., <400 °C (green and grey shaded areas in Figure 5.34).

Although we have not analysed ^{18}O isotopes in our magnetite separates, values for magnetite were reported by Oreskes and Einaudi (1992), for magnetite sampled from the east side of Olympic Dam, and Acropolis. We have added the range of Fe and O isotope values of Olympic Dam and Acropolis magnetite separates to the data reported by Bilenker et al. (2016), in Figure 5.34. The Olympic Dam and Acropolis data lie within the high temperature ‘box’, consistent with ^{18}O geothermometry of Oreskes and Einaudi (1992), who calculated temperatures up to 540°C, and

Bodnar's (2000) interpretation that an early Fe-rich "salt-melt" liquid existed at >600 °C which would have produced iron oxide mineralisation similar to IOA deposits.

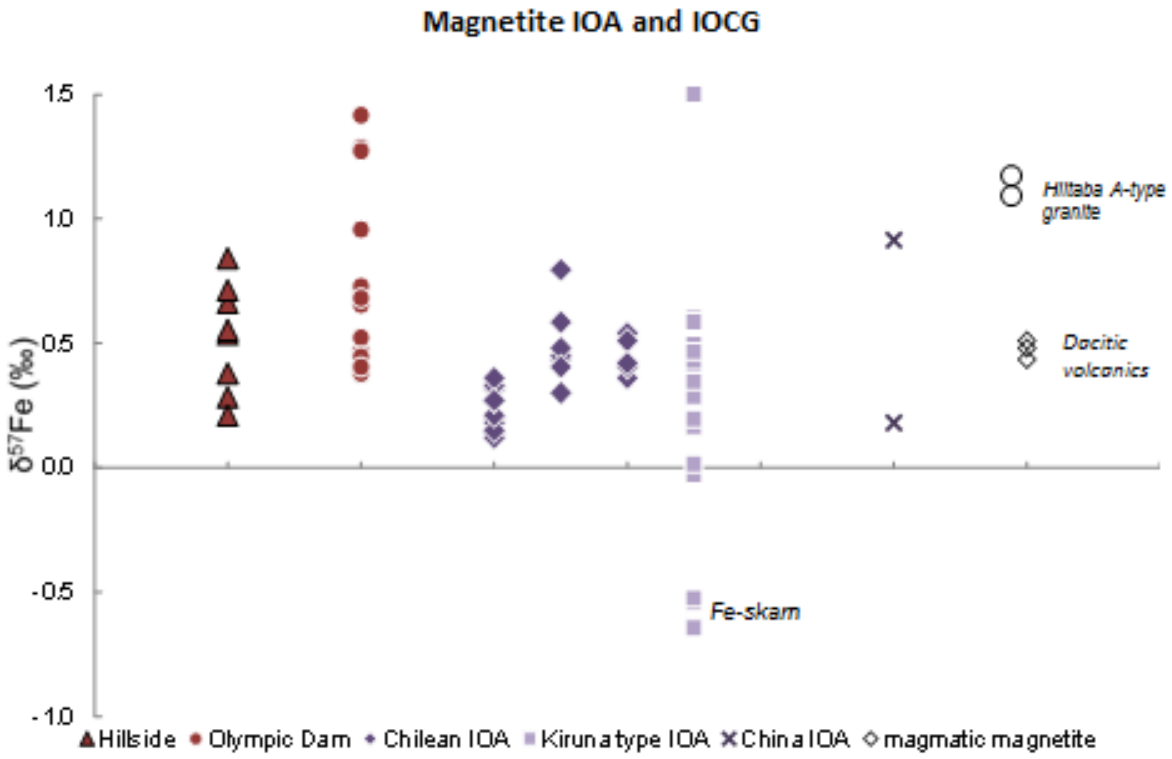

Figure 5.33 Fe isotope values of mineral separates (red symbols) from Olympic Dam and Hillside compared to data from IOA deposits (purple symbols). IOA and magmatic magnetite data in dacite lavas from Weis (2013) and Bilenker (2016). Magmatic magnetite from Hiltaba Suite granites from this study.

Oreskes and Einaudi also reported ^{18}O analyses of hematite mineral separates, and the values range from +1.1‰ (relative to SMOW) to -12.9‰, which covers the entire range of data reported by Bilenker et al. (2016), including the orthomagmatic classification. However, numerous studies (e.g. Haynes et al., 1995, Baker et al., 2008, Bastrakov et al., 2007) demonstrate that fluid mixing is a key process for formation of IOCG deposits, and hematite and copper sulfides are precipitated at a range of temperatures less than 600 °C as demonstrated by fluid inclusion microthermometry (Oreskes and Einaudi, 1992, Bodnar, 2000). The figure clearly demonstrates that Fe isotopes alone are insufficient to resolve fluid sources.

However, the combined use of Fe-O isotopes with careful petrographic analysis has potential to delineate different Fe-mobilising events within a single deposit.

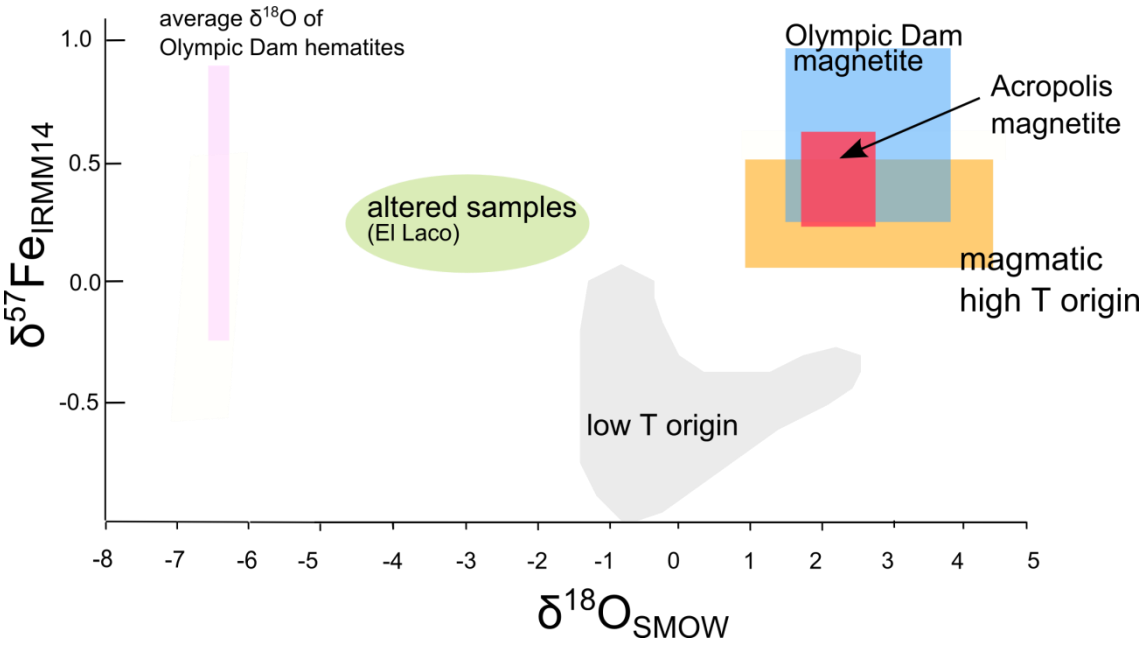

Figure 5.34 $\delta^{57}Fe$ v $\delta^{18}O$ values for magnetite and hematite from Olympic Dam and Acropolis compared to published data from Bilenker et al. (2016), with $\delta^{56}Fe$ recalculated to $\delta^{57}Fe$ using the mass dependent fractionation of $\delta^{57}Fe = \delta^{56}Fe*1.5$ The $\delta^{18}O$ data from Olympic Dam and Acropolis from Oreskes and Einaudi (1992). For clarity, we have plotted the average $\delta^{18}O$ of -6.5‰ (pink shaded bar).

5.9. CONCLUSION

In this case study we have used multi-collector mass spectrometry to measure the Fe isotope ratios of granitoid rocks of the Hiltaba Suite, and mineral separates from two IOCG deposits on the Gawler Craton, South Australia. Least altered Hiltaba Suite granitoids have $\delta^{57}Fe$ isotope values similar to those reported in the literature for other A-type intrusions. Hematite altered granite-rich breccias within the Olympic Dam Breccia Complex have isotope signatures that are different to granites with hematite occurring as dusting of feldspars, which suggests Fe isotopes have potential to help distinguish regional fluid flow events from the onset of mineralisation. Analysis of different generations of hematite is needed to explore this idea.

Mineral separates such as siderite, magnetite, hematite, chalcopyrite and pyrite have isotopic values that are consistent with theoretical mineral-mineral fractionation factors. The range of values for mineral separates sampled from the Olympic Dam, Acropolis, Wirrda Well and Hillside deposits is almost identical, pointing to similar mineral formation conditions in each deposit. An intriguing exception to theoretical prediction is magnetite-pyrite pairs at Olympic Dam. The opposing sign of $\Delta^{57}Fe_{py\text{-}mgt}$ between Olympic Dam and Hillside is enigmatic, and could result from a number of possible processes at Olympic Dam including kinetic fractionation or quantitative dissolution of paragenetically early pyrite and reprecipitation as magnetite. In situ isotope analysis of minerals with clear overprinting and replacement textures, and growth zones would be useful to help distinguish isotope fractionation associated with different fluid events, which is difficult with the average values generated at the scale of handpicked or milled samples. We also cannot discount that element substitution in magnetite and siderite means that theoretical fractionation factors, based on pure mineral compositions, cannot be applied to this case. Microanalyses of mineral phases are needed to confirm this interpretation.

There is widespread fluid inclusion microanalysis, and oxygen and sulphur isotope evidence that fluid mixing is a key process in the deposition of Cu-Au ore in IOCG deposits. Our data show that magnetite and overprinting hematite pairs have identical Fe isotope values, within analytical error, demonstrating that Fe isotopes alone are likely to be unable to distinguish between fluid mixing events. However, the isotope values for bladed hydrothermal hematite at Olympic Dam suggests a location-specific control on isotope values, with $\delta^{57}Fe$ in hematite from RD1988 clearly isotopically heavier (>0.5‰) than hematite from other drill holes (<5‰); hole RD1988 occurs in an area where As-W-Mo-Sb are enriched, suggesting that the Fe-isotope value of hematite may be reflecting a difference in fluid chemistry. However, further sampling and analyses is required to confirm that the isotope data distribution is not an artefact of low sampling density.

Six out of the nine hematite-chalcopyrite pairs we analysed at Olympic Dam yield temperatures of formation between 210-390°C, calculated using published theoretical fractionation factors. These temperatures are consistent with fluid inclusion microthermometry, highlighting the potential for Fe isotopes as a geothermometer in opaque minerals.

ACKNOWLEDGEMENTS

This study would not have been possible without the financial and logistical support of BHP Billiton. C. Wawryk thanks the geologists and Core Farm staff at the Olympic Dam minesite for discussion about the deposit, and assistance with sample collection. Christiana Ciobanu is thanked for her generous assistance with reflected light microscopy.

References

Agangi A., Kamenetsky, V. S. and McPhie, J. (2012). Evolution and emplacement of high fluorine rhyolites in the Mesoproterozoic Gawler silicic large igneous province, South Australia. Precambrian Research, 208-211 124-144.

Baker, T., Mustard, R., Fu, B., Williams, P.J., Dong, G., Fisher, L., Mark, G. and Ryan, C.G. (2008). Mixed messages in iron oxide-copper-gold systems of the Cloncurry district, Australia: insights from PIXE analysis of halogens and copper in fluid inclusion, Mineralium Deposita, 43, 599-608.

Barton, M. D and Johnson, D. A. (1996). Evaporitic source model for igneous-related Fe-oxide-(REE-Cu-Au-U) mineralisation. Geology, 24, 259-262.

Bastrakov, E. N., Skirrow, R. G. and Davidson, G. J. (2007). Fluid Evolution and Origins of iron oxide Cu-Au prospects in the Olympic Dam District, Gawler Craton, South Australia. Economic Geology, 102, 1415-1440.

Beard, B. L., Johnson, C. M., Skulan, J. L., Nealson, K. H., Cox, L. and Sun, H. (2003). Application of Fe isotopes to tracing the geochemical and biological cycling of Fe. Chem. Geology, 195, 87-117.

Blanchard, M., Poitrasson, F., Meheut, M., Lazzeri, M., Mauri, F., Balan, E. (2009). Iron isotope fractionation between pyrite (FeS_2), hematite (Fe_2O_3) and siderite ($FeCO_3$): A first-principles density functional theory study. Geochim. Cosmochim. Acta 73, 6565-6578.

Bilenker, L. D., Simon, A. C., Reich, M., Lundstrom, C. C., Gajos, N., Bindeman, I., Barra, F., Munizaga, R. (2016). Fe–O stable isotope pairs elucidate a high-temperature origin of Chilean iron oxide-apatite deposits. Geochim. Cosmochim. Acta 177, 94-104.

Blevin, P. (2003). Metallogeny of Granitic Rocks, in Blevin P., Jones, M. and Chappell, B. (Eds), Magmas to Mineralisation: the Ishihara Symposium. Geoscience Australia Record 2003/14.

Blevin, P. L., Chappell, B. W. (1992). The Role of Magma Sources, Oxidation-States and Fractionation in Determining the Granite Metallogeny of Eastern Australia. Transactions of the Royal Society of Edinburgh-Earth Sciences 83, 305-316.

Blisset, A. H., Creaser, R. A., Daly, S. J., Flint, R. B., Parker, A. J. (1993). In Drexel, J.F., Preiss, W.V and Parker, A.J., (Eds), The geology of South Australia. Vol I, the Precambrian: Geological Survey of South Australia, Bulletin 54, 107-124.

Bodnar, R. (2000). Unpublished report to WMC Resources Ltd.

Candela P. A., Holland H. D. (1984). The partitioning of copper and molybdenum between silicate melts and aqueous fluids. Geochim. Cosmochim. Acta 48, 373-380.

Cheng, Y., Mao, J., Zhu, X., Wang, Y. (2015). Iron isotope fractionation during supergene weathering process and its application to constrain ore genesis in Gaosong deposit, Gejiu district, SW China, Gondwana Research, 27, 1283-1291.

Ciobanu C. L., Wade, B. P., Cook, N. J., Schmidt-Mumm, A. and Giles, D. (2013). Uranium-bearing hematite from the Olympic Dam Cu–U–Au deposit, South Australia: A geochemical tracer and reconnaissance Pb–Pb geochronometer Precambrian Research, 238, 129-147.

Conan-Davies, M.S.M. (1987). A sheet silicate and fluid inclusion study of the mine area DNW, Olympic Dam, South Australia. Honours thesis, The Australian National University.

Conor, C., Raymond, O. Baker, T., Teale, G., Say, P. and Lowe G. (2010). Alteration and mineralisation in the Moonta-wallaroo copper-gold mining field regions, Olympic Domain, South Australia, in Porter T.M., (ed). Hydrothermal Ion Oxide Copper-gold and related Deposits: A Global perspective, v.3-Advances in the understanding of IOCG deposits; PGC Publishing, Adelaide, 147-170.

Craddock, P., Dauphas, N. (2011). Iron isotopic compositions of geological reference materials and chondrites. Geostandards and Geoanalytical Research, 35, 101-123.

Creaser, R. A. (1995). Neodymium isotopic constraints for the origin of Mesoproterozoic felsic magmatism, Gawler Craton, South Australia,Canadian Journal of Earth Sciences 1995), 32(4):460-471.

Creaser, R. A. (1996). Petrogenesis of a Mesoproterozoic quartz latite-granitoid suite from the Roxby Downs area, South Australia. Precambrian Research, 79(3-4):371-394.

Creaser, R. A., Cooper, J. A. (1993). U-Pb geochronology of middle Proterozoic felsic magmatism surrounding the Olympic Dam Cu-U-Au-Ag and Moonta Cu-Au-Ag deposits, South Australia. Econ Geol, 88, 186-197.

Creaser, R. A., White, A. J. R. (1991). Yardea Dacite—Large-volume, high-temperature felsic volcanism from the Middle Proterozoic of South Australia. Geology, 19, 48-51.

Davidson, G. J., Paterson, H., Meffre S., Berry R. F. (2007). Characteristics and origins of the oak Dam east breccia-hosted iron oxide Cu-U-(Au) deposit: Olympic Dam region, Gawler Craton, South Australia. Economic Geology, 102, 1471-1498.

Dauphas, N., Roskosz, M., Alp, E. E., Neuville, D. R., Hu, M. Y., Sio, C. K., Tissot, F. L. H., Zhao, J., Tissandier, L., Médard, E. and Cordier, C. (2014). Magma redox and structural controls on iron isotope variations in Earth's mantle and crust. Earth and Planetary Science Letters, 398, 127-140.

Ehrig, K., McPhie, J., Kamenestsky, V. (2012). Geology and mineralogical zonation of the Olympic Dam iron oxide-Cu-U-Au-Ag deposit, South Australia, in Hedenquist, J. W, Harris, M. and Camus, F. (Eds), Geology and genesis of major copper deposits and districts of the World: A tribute to Richard Sillitoe. Society of Economic Geologists Special publication 16, 237-268.

Eugster, H. P. (1985). Granites and Hydrothermal Ore-Deposits - a Geochemical Framework. Mineralogical Magazine, 49, 7-23.

Fanning, M., Flint, R. B., Parker, A. J., Ludwig, K. R., Blissett, A. H. (1988). Refined Proterozoic evolution of the Gawler Craton, South Australia, through U-Pb zircon geochronology. Precambrian Research, 40-41, 363-386.

Ferris, G. M., Schwarz. M. P., Heithersay, P. (2002). The geological framework, distribution and controls of Fe-oxide Cu-Au mineralisation in the Gawler Craton,

South Australia: Part I: Geological and Tectonic Framework, in Porter T.M., (Ed). Hydrothermal Ion Oxide Copper-Gold and Related Deposits: A Global Perspective, v.2 PGC Publishing, Adelaide, 9-31.

Fernandez, A., Borrok, D. (2009). Fractionation of Cu, Fe, and Zn isotopes during the oxidative weathering of sulfide-rich rocks. Geochim. Cosmochim. Acta, 122, 170-183.

Foden J., Sossi P., Wawryk C.M. (2015). Fe isotopes and the contrasting petrogenesis of A-, I- and S-type granite. Lithos. 212-215, 32-44.

Frost, B. R., Barnes, C. G., Collins, W. J., Arculus, R. J., Ellis, D. J., Frost, C. D. (2001). A geochemical classification for granitic rocks. J. Petrol. 42, 2033–2048.

Gajos, N. (2014). Spatially controlled Fe isotope variations at Torres Del Paine. Masters of Science dissertation, University of Illinois, Urbana-Champaign.

Gaudin A. M and Rush Spedden H. (1943). Magnetic separation of sulphide minerals. Mining Technology, Technical Publication 1549, American Institute of Mining and Metallurgical Engineers.

Giles, C.W. (1988). Petrogenesis of the Proterozoic Gawler Range Volcanics, South Australia Precambrian Research, 40-41, 407-427.

Hand, M., Reid, A., Jagodzinsky, E.A. (2007). Tectonic framework and evolution of the Gawler Craton, Southern Australia. Economic Geology, 102, 1377-1395.

Haynes D. W, Cross, K. C., Bills, R. T., Reed, M. H. (1995). Olympic Dam ore genesis; a fluid-mixing model. Economic Geology 90, 281-307.

Hayward, N., Skirrow, R.G. (2010). Geodynamic setting and controls on iron oxide Cu-Au-(±U) ore in the Gawler Craton, South Australia; in Porter T.M., (Ed). Hydrothermal Ion Oxide Copper-gold and related Deposits: A Global Perspective, v.3-Advances in the understanding of IOCG deposits; PGC Publishing, Adelaide, 119-146.

Heimann, A., Beard, B. L., Johnson C.M. (2008). The role of volatile exsolution and sub-solidus fluid/rock interactions in producing high $^{56}Fe/^{54}Fe$ ratios in siliceous igneous rocks. Geochim. Cosmochim. Acta 72, 4379-4396.

Huang, F., Lundstrom, C. C., Glessner, J., Ianno, A., Boudreau, A., Li, J., Ferré, E. C., Marshak, S., DeFrates, J. (2009). Chemical and isotopic fractionation of wet

andesite in a temperature gradient: Experiments and models suggesting a new mechanism of magma differentiation. Geochim. Cosmochim. Acta 73, 729-749.

Ishihara, S. (1981). The granitoid series and mineralisation, Econ. Geol, 75th Anniv volume, 458-484.

Ismail R., Ciobanu, C.L., Cook, N. J.,Teale, G. S.,Giles, D., Schmidt-Mumm, A., Wade, B. (2014a). Rare earths and other trace elements in minerals from skarn assemblages, Hillside iron oxide–copper–gold deposit, Yorke Peninsula, South Australia, Lithos, 184-187, 456-477.

Ismail, R., Lin, Y., Ciobanu, C. L., Cook, N.J. (2014b). The Hillside Cu-Au Deposit, South Australia: A Preliminary Fluid Inclusion Study Acta Geologica Sinica - English Edition, 88, 1454-1456.

Jack, R.L (1917). The geology of the Moonta and Wallaroo mining district; South Australian Geological Survey, Bulletin 6.

Johnson, C. M., Beard, B L., Albarede, F. (2004). Overview and General Concepts. Reviews in Mineralogy and Geochemistry, 55, 1-24.

Johnson, D. (2009.) The Geology of Australia, 2nd Ed. Cambridge University Press, port Melbourne, Victoria.

Johnson, J. P., Cross, K.C. (1995). U-Pb geochronological constraints on the genesis of the Olympic Dam Cu-U-Au-Ag deposit, South Australia Economic Geology, 5, 1046-1063.

Johnson, J. P., McCulloch, M. T. (1995). Sources of mineralising fluids for the Olympic Dam deposit (South Australia): Sm-Nd isotopic constraints. Chemical Geology, 121, 177-199.

Kirk, J. T. (2012.) Controls on iron isotope variation in granites and associated hydrothermal ore systems: The Hillside example. Honours thesis, University of Adelaide.

Knipping J. L., Bilenker, L.D., Simon, A. C., Reich, M., Barra, F., Deditius, A. P., Lundstrom, C., Bindeman, I., Munizaga, R. (2015). Giant Kiruna-type deposits form by efficient flotation of magmatic magnetite suspensions. Geology, 43, 591-594.

Kontonikas-Charos, A., Ciobanu, C. L., Cook N. J., Ehrig, K., Krneta, S., Kamenetsky, V. D. (2017). Feldspar evolution in the Roxby Downs Granite, host to Fe-oxide Cu-Au-(U) mineralisation at Olympic Dam, South Australia Ore Geology reviews 80, 838-859.

McPhie, J., Kamenetsky, V., Allen S., Ehrig, K., Agangi, A., Bath, A. (2011) The fluorine link between a supergiant ore deposit and a silicic large igneous province. Geology, 39, 1003-1006.

McQueen, K. G, Pillans, J. B., Smith. M. L. (2005). Doing the time warp with element dispersion. In Roach I.C. (Ed) 2005 Regolith 2005-10 years of CRC LEME, CRC LEME, p 2290234.

Mucke A., Cabral A. R. (2005). Redox and non-redox reactions of magnetite and hematite in rocks. Chemie de Erde, 65, 271-278.

Oreskes, N., Einaudi, M. T. (1990). Origin of rare earth element-enriched hematite breccias at the Olympic Dam Cu-U-Au-Ag deposit, Roxby Downs, South Australia Economic Geology, 85, 1-28.

Oreskes, N., Einaudi, M. T. (1992). Origin of hydrothermal fluids at Olympic Dam: preliminary results from fluid inclusions and stable isotopes Economic Geology, 87, 64-90.

Poitrasson, F., Freydier, R. (2005), Heavy iron isotope composition of granites determined by high resolution MC-ICP-MS. Chem. Geol. 222, 132-147.

Poitrasson, F., Viers, J., Martin, F., Braun, J. (2008). Limited iron isotope variations in recent lateritic soils from Nsimi, Cameroon: Implications for the global Fe geochemical cycle. Chem. Geol. 253, 54-63.

Pollard, P. (2006). An intrusion-related origin for Cu–Au mineralization in iron oxide–copper–gold (IOCG) provinces. Mineralium Deposita, 41, 179-187.

Polyakov, V. B., Mineev, S. D., 2000. The use of Mössbauer spectroscopy in stable isotope geochemistry. Geochim. Cosmochim. Acta 64, 849-865.

Polyakov, V. B., Clayton, R. N., Horita, J., Mineev, S. D., 2007. Equilibrium iron isotope fractionation factors of minerals: reevaluation from the data of nuclear

inelastic resonant X-ray scattering and Mössbauer spectroscopy. Geochim. Cosmochim Acta 71, 3833-3846.

Polyakov, V. B., Soultanov, D. M., 2011. New data on equilibrium iron isotope fractionation among sulfides: constraints on Putnis, A., Hinrichs, R., Putnis, C. V., Golla-Schindler, U., Collins, L. G. (2007). Hematite in porous red-clouded feldspars: Evidence of large-scale crustal fluid–rock interaction. Lithos, 95, 10-18.

Reeve, J. S., Cross, K. C., Smith, R. N., Oreskes, N. (1990). Olympic Dam copper-uranium-gold-silver deposit, in Hughes, F.E. (Eds) Geology of the Mineral Deposits of Australia and Papua New Guinea, 1009-1035, AusIMM. Melbourne.

Roberts, D. E., Hudson, G. R. T. (1983). The Olympic Dam copper-uranium-gold deposit, Roxby Downs, South Australia. Economic Geology, 78, 799-822.

Rouxel, O., Shanks, W. C., Bach, W., Edwards, K. J. (2008). Integrated Fe- and S-isotope study of seafloor hydrothermal vents at East Pacific rise 9-10°N. Chem. Geol. 252, 214-227.

Rusk, B., Emsbo, P., Xavier, R.P., Corriveau, L., Oliver, N., Zhang, D. (2015). A comparison of fluid origins and compositions in iron oxide-copper-gold and porphyry Cu-(Mo-Au) deposits. In Proceedings of PACRIM 2015 Congress, AUSIMM Publication Series 2/2015 271-279.

Schuessler J., Schoenberg R., Sigmarsson O. (2008). Iron and lithium isotope systematics of the Hekla volcano, Iceland-Evidence for Fe isotope fractionation during magma differentiation. Chem. Geol. 258, 78-91.

Schoenberg, R., von Blanckenburg, F. (2006). Modes of planetary-scale Fe isotope fractionation. Earth Planet. Sci. Lett. 252, 342–359.

Skirrow, R.G., Bastrakov, E., Davidson, G., Raymond O.L. and Heithersay, P (2002). The geological framework, distribution and controls of Fe-oxide Cu-Au mineralisation in the Gawler Craton, South Australia: Part II: Alteration and Mineralisation, in Porter T.M., (Ed). Hydrothermal Ion Oxide Copper-Gold and Related Deposits: A Global Perspective, v.2 PGC Publishing, Adelaide, 33-47.

Skirrow, R. G., Bastrakov, E. N., Barovich, K., Fraser, G. L, Creaser, R. A. Fanning, C. M., Raymond, O. L., Davidson, G.J. (2007). Timing of iron oxide Cu-Au-(U)

hydrothermal activity and Nd isotope constraints on metal sources in the Gawler Craton, South Australia. Economic Geology, 102, 1441-1470.

Skulan, J., Beard, B., Johnson, C. (2002). Kinetic and equilibrium Fe isotope fractionation between aqueous Fe(III) and hematite, GCA,66, 2995-3015.

Stewart K. (1994). High temperature silicic volcanism and the role of mantle magmas in Proterozoic crustal growth: the Gawler Range Volcanic Province. Ph D thesis, University of Adelaide.

Stewart, K., Foden, J. D. (2003). Mesoproterozoic granites of South Australia: South Australia Department of Primary Industries and Resources, Report Book, 2003/15.

Syverson, D. D., Borrok, D. M., Seyfried, W. E. (2013). Experimental determination of equilibrium Fe isotopic fractionation between pyrite and dissolved Fe under hydrothermal conditions. Geochim. Cosmochim. Acta 122,170-183.

Telus, M., Dauphas, D., Moynier, F., Tissot, F., Teng, F., Nabelek, P., Craddock, P., Groat, L. (2012). Iron, zinc, magnesium and uranium isotopic fractionation during continental crust differentiation: The tale from migmatites, granitoids and pegmatites. Geochim. Cosmochim. Acta 97, 247-265.

Teng F-Z., Dauphas, N., Helz R. (2008). Iron isotope fractionation during magmatic differentiation in Kilauea Iki lava lake. Science, 320, 1620-1622.

Wang, Y., Zhu, X., Cheng, Y. (2015). Fe isotope behaviours during sulfide-dominated skarn-type mineralisation Journal of Asian Earth Sciences 103, 374-392.

Wawryk, C .M. (1989). Strontium and rare earth element geochemistry of barite-fluorite mineralisation at Olympic Dam, South Australia. Honours thesis, University of Adelaide.

Wawryk. C. M., Foden, J. D. (2015). Fe-isotope fractionation in magmatic-hydrothermal mineral deposits: A case study from Renison Sn-W deposit, Tasmania. Geochim. Cosmochim. Acta. 150, 285-298.

Wawryk, C. M., Foden J. D. Iron Isotope systematics at the Batu Hijau Cu-Au deposit Sumbawa, Indonesia (submitted).

Wiederhold, J. G. Teutsch, N., Kraemer, S. M., Halliday, A. N., Kretzschmar, R. (2007). Iron isotope fractionation in oxic soils by mineral weathering and podsolization. Geochim. Cosmochim. Acta, 71, 5821-5833.

Weis, F. (2013). Oxygen and Iron Isotope Systematics of the Grängesberg Mining District (GMD), Central Sweden. M.Sc thesis, Uppsala University, Sweden.

Williams P. J, Kendrick M. A and Xavier, R .P. (2010). Sources of ore fluid components in IOCG deposits. In Porter T.M., (Ed). Hydrothermal Ion Oxide Copper-gold and related Deposits: A Global Perspective, v.3-Advances in the understanding of IOCG deposits; PGC Publishing, Adelaide, 107-116.

Wu, L., Beard, B. L.., Roden, E. E., Kennedy, C. B., Johnson, C. (2010). Stable Fe isotope fractionations produced by aqueous Fe(II)-hematite surface interactions Geochimica et Cosmochimica Acta, 74, 4249-4265.

Wurst, A.T. (1994). Analyses of late stage, Mesoproterozoic, syn and post tectonic magmatic events in the Moonta Subdomain: Implication for Cu-Au mineralisation in the “Copper Triangle” of South Australia. Honours thesis, University of Adelaide.

Xavier, R. P., Monteiro, L. V. S., Moreto, C. P. N., Melo, G. H. C., Santiago, E. S. B. (2015). Non-magmatic versus magmatic fluids in the genesis of Archaean and Palaeoproterozoic iron oxide-copper-gold systems of the Carajás mineral province (Brazil). in Proceedings of PACRIM 2015 Congress, AUSIMM Publication Series 2/2015, 281-287.

Zambardi, T., Lundstrom, C. C., Li, X., McCurry, M. (2014). Fe and Si isotope variations at Cedar Butte volcano; insight into magmatic differentiation Earth and Planetary Science Letters 405, 169-179.

Zhang, W. L., Fanning, C. M., Purvis, A. C., Raymond, O .L., Both, R. A. (2007). Early Mesoproterozoic bimodal plutonism in the southeastern Gawler Craton, South Australia Australian Journal of Earth Sciences: an International Geoscience Journal of the Geological Society of Australia, 54 661-674.

CHAPTER 6. DO IGNEOUS PROCESSES CONTROLLING METALLOGENY AFFECT IRON ISOTOPE VALUES OF HYDROTHERMAL MINERALS?

One of the hypotheses that this research aims to address is "Do the $\delta^{57}Fe$ values of sulfide and oxide minerals reflect the oxidation state of the source magma?" The approach used was to sample intrusive rocks and oxide, sulfide and carbonate minerals from 3 world class deposit styles, each one associated with a different magmatic style. The deposits sampled are: 1) the Sn-W deposit associated with the peraluminous S-type, reduced (fO_2~FMQ-1) Renison Granite; 2) the Batu Hijau porphyry-style Cu-Au deposit associated with oxidised (fO_2~NNO+1) calc-alkaline arc magmatism (I-type) and 3) the Olympic Dam and Hillside iron-oxide-copper-gold (IOCG) deposits of the Gawler Graton, where mineralisation is associated with A-type magmatism (fO_2~FMQ). The number of igneous rock samples (n=33) from each deposit category is shown in Table 6.1. In this chapter, the results of all the granitoid and mineral sample analyses are compared and contrasted on the basis of metallogeny.

Table 6.1 Summary of igneous rock types sampled for Fe isotope analysis

Deposit	Deposit Style	Rock type	Samples
Renison	Sn-W	S-type biotite granite	4
Batu Hijau	Porphyry Cu-Au	andesite to tonalite	11
Sur Sur	Porphyry Cu-Mo	monzonite-dacite-rhyolite	9
Olympic Dam	IOCG	A type Hiltaba granite	4
Hillside	IOCG	A type Hiltaba granite	5

6.1. INTRUSIVE ROCKS

In Chapter 2, samples of the biotite-rich, ilmenite-series Renison Granite were analysed, and returned isotopic values of 0.27 ± 0.09‰ to 0.43 ± 0.01‰ (Fig 2.7). The Renison Granite is part of a batholith interpreted to have formed by crustal anatexis generated from heat input during post-collisional lithospheric underplating

(Black et al., 2010). The Renison Granite has compositions at the haplogranite minimum, thus trace element geochemistry was used to argue that the Renison Granite results from crystal fractionation (Bajwah et al., 1995). Although a thermodynamic model of fractionation is not presented in this work, qualitative interpretations can be made considering the results of Telus et al. (2012), who explored the fractionation of Fe isotopes during anatexis in their analyses of leucosomes and melanosomes within migmatites. They showed that partial melting results in isotopically heavy melts, relative to the residue, which they attributed to the incompatible nature of Fe^{3+} in the melt.

In addition, measurement of the force constants of Fe bonds in silicate glasses using synchrotron Nuclear Resonant Inelastic X-ray Scattering (NRIXS; Dauphas et al., 2014) demonstrates that in rhyolite composition glasses, Fe^{3+} has a stronger force constant than in basalt to dacite composition glasses. The greater force constant leads to larger equilibrium fractionation between melt and minerals ($\Delta^{57}Fe_{melt\text{-}min}$), with the most silicic melts trending to heavy isotope compositions. Those authors attribute the greater force constants to be a function of coordination geometry in the melt, in which Fe^{3+} is stabilised in tetrahedral coordination. Dauphas et al's (2014) modelling of a hypothetical andesite fractionating to rhyolite, using measured force constants to model Fe isotope fractionation, shows a close match between predicted delta values, and actual measured values from natural rock samples. Those authors also concluded that magmatic differentiation is likely the main process leading to isotopically heavy silicic melts. In summary, therefore, the Renison granite can be expected to be isotopically heavy on two counts; anatexis, and magmatic differentiation to high silica values thereafter.

Chapter 3 explores the evolution of the Batu Hijau magmatic suite, a hydrous, calc-alkaline suite of andesite, quartz diorites, dacites and tonalites formed in the Sunda-Banda Arc. It has been demonstrated by Foden et al. (2015) that I-type arc magmas generally evolve to isotopic values of ~0.2 to 0.3‰, somewhat lighter than S-types generally, owing to co-crystallisation of magnetite with silicate minerals throughout the fractional crystallisation process, effectively removing the heavy isotope from the melt, thus suppressing an evolution to heavy isotopic values. The samples from Batu Hijau are consistent with these observations (Fig 3.3), showing a slight increase in $\delta^{57}Fe$ values with crystallisation, from 0.24 ± 0.08‰ in pre-mineralisation quartz diorite to 0.32 ± 0.05‰ in the Young Tonalite intrusion, which is co-eval with waning

of the hydrothermal system. Upon return to andesitic composition, lavas have lighter isotope values of 0.17 ± 0.02‰. Thermodynamic modelling presented in Chapter 3, using published fractionation factors for magnetite and ferromagnesian silicate minerals showed that crystal fractionation can explain the isotopic evolution trend seen in this suite of magmatic rocks.

Chapter 5, a case study from two IOCG deposits on the Gawler Craton, sampled A-type granitoids of the Hiltaba Suite. Samples of the Roxby Downs Granite and Tickera Granite returned results ranging from 0.30 to 1.03 ± 0.04‰, consistent with Foden et al. (2015) who demonstrated that A-type granites, derived from protracted fractional crystallisation in closed (i.e. no oxygen exchange) magma chambers, can evolve to the heaviest Fe isotope values. Changes in $\delta^{57}Fe$ values are accentuated in rocks with low Fe content.

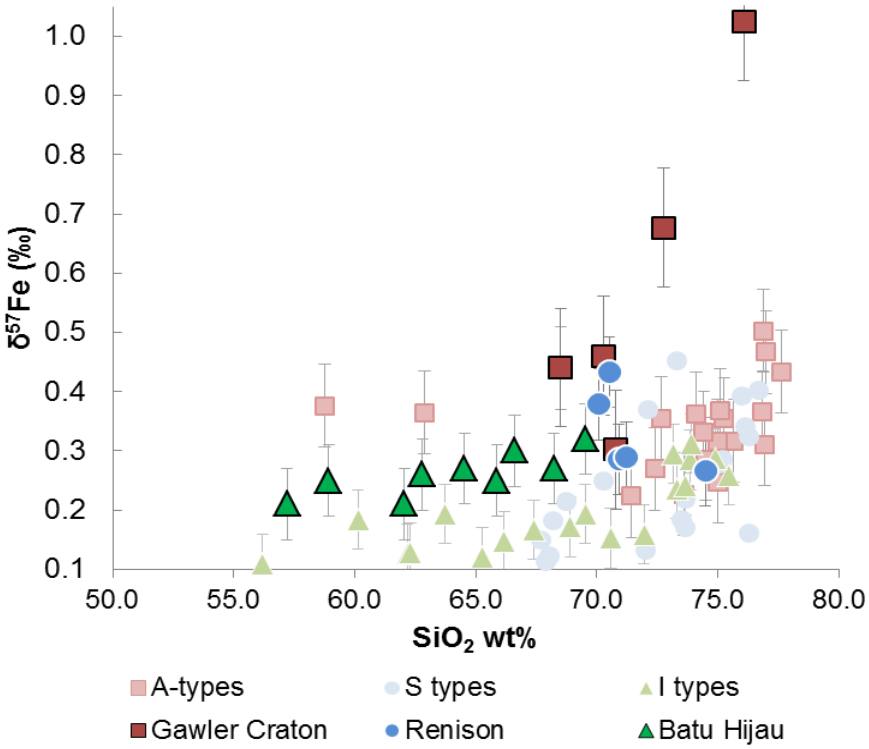

Figure 6.1 Variation diagram of $\delta^{57}Fe$ vs SiO_2 for A, S and I type igneous rocks. Solid colours are samples from this study, and paler colours are published data from Foden et al. (2015)

Apparent from Fig 6.1 is that the intrusive rocks sampled from Renison and Batu Hijau differ by ~0.1‰; if the $\delta^{57}Fe$ value of an exsolved magmatic fluid has the same isotopic values of a cooling melt, then there would be a similarly small difference in exsolved fluids from the intrusions at Renison and Batu Hijau.

Fresh Roxby Downs Granite spans a range of $\delta^{57}Fe$ values from 0.30 to 0.46‰ which overlaps the values of samples from the Renison Granite. The samples that have $\delta^{57}Fe$ values of ~0.46‰ are 0.2‰ heavier than then the Batu Hijau tonalites. So despite the differences in geodynamic setting of each suite of intrusions, these results show that the intrusions have a relatively restricted range of isotopic values.

6.2. MINERAL SEPARATES

Common hydrothermal Fe bearing sulfides, oxides and carbonate minerals were separated from each deposit as shown in Table 6.2. Not all minerals are found in every deposit. Some minerals are very fine grained and were not able to be separated, for example, hematite at Hillside.

Table 6.2 Summary count of all minerals separates collected for Fe isotope analysis

Deposit	magnetite	hematite*	siderite	pyrite	chalcopyrite	bornite	pyrrhotite	arseno-pyrite
Renison	2		3	7	5		16	7
Batu Hijau	5				6	6		
Sur Sur	5	2		7	15			
Olympic Dam	16	13	5	16	13			
Hillside	8			6	12	2		
totals	**36**	**15**	**8**	**36**	**51**	**8**	**16**	**7**

*only hydrothermal specularite and bladed hematite from OD included. Massive “ironstone” samples are excluded.

Fe isotope values for pyrite mineral separates are shown in Figure 6.2. The pyrite separates from Renison are clearly heavier than pyrite samples from the Sur Sur breccia. Pyrite from the Hillside and Olympic Dam deposit span a range of values between the two, with samples from Olympic Dam showing greatest range of 1.4‰.

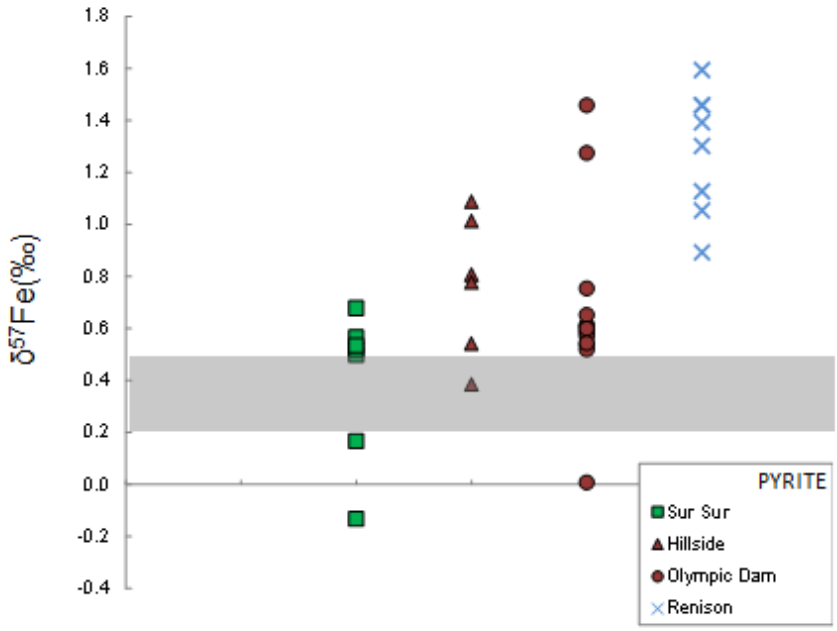

Figure 6.2 Fe isotope values of all pyrite separates categorised by deposit type. The range of all Fe-isotope values for intrusions listed in Table 1 is shown by the grey bar.

Magnetite values for samples from both porphyry copper deposits and the Hillside IOCG deposit span an identical range of values (Fig 6.3). Magnetite separates from Olympic Dam area extend to relatively heavy values between 0.9‰ and 1.42‰ and, like the pyrite separates, shows the largest variability in a mineral group. Only two magnetite separates were analysed from Renison, as most early magnetite has been replaced by sulfide minerals (J. Harvey, pers. Comm.). Although isotopically heavier than magnetite separates from the porphyry copper deposits, this may be an artefact of sampling and no firm conclusion should be drawn from only 2 data points.

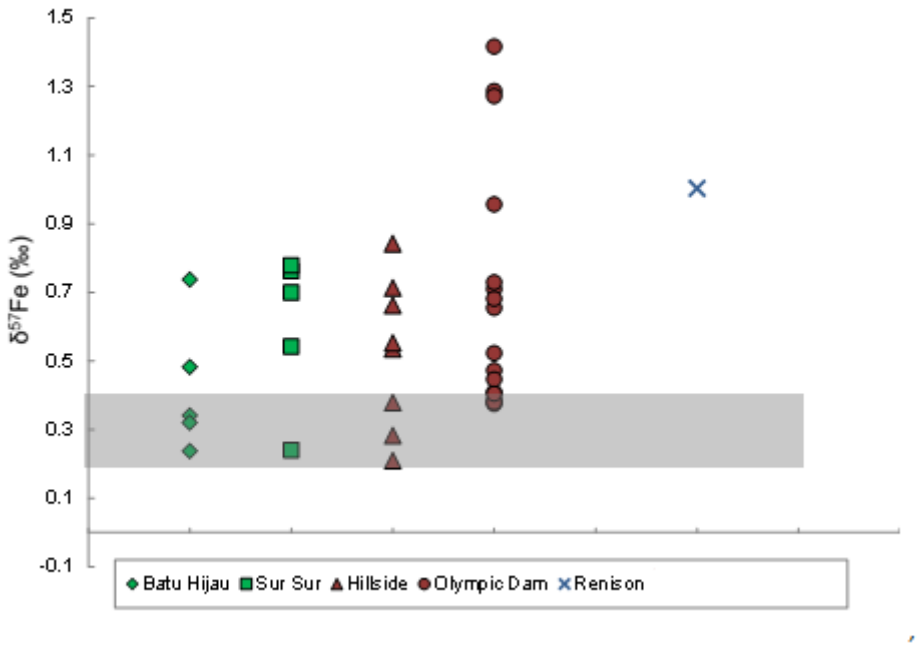

Figure 6.3 Fe isotope values for magnetite mineral separates categorised by deposit type. Grey shaded area is the range of Fe isotope values from igneous rocks associated with the deposits.

The isotope values of chalcopyrite separates are shown in Figure 6.4. The values follow a similar distribution to that of pyrite, with pyrite from Renison generally clustering at isotopically heavier values than that of the porphyry copper deposit ('PCD') samples. The chalcopyrite separates from the IOCG deposits again span a range of values that overlap both PCD and Renison samples.

Generally, chalcopyrite values are relatively light compared to the bulk magmatic rock values, in contrast to isotope values for pyrite, which are mostly heavier than bulk magmatic rock values. These results are in agreement with Syverson (2015), who argued that chalcopyrite equilibrates rapidly with hydrothermal solution, and thus may represent the isotopic values of the fluid. Our Rayleigh modelling of fractionation between magnetite and chalcopyrite at Batu Hijau and Rio Blanco-Sur Sur (see Chapters 3 and 4) reproduces the measured δ^{57}Fe values of the minerals if a fluid with δ^{57}Fe values between -0.5 and -0.1‰ is assumed; this would also explain the light δ^{57}Fe values of hypogene bornite from Batu Hijau (-0.72 to -0.08‰) and Hillside (-1.44 and -1.53‰).

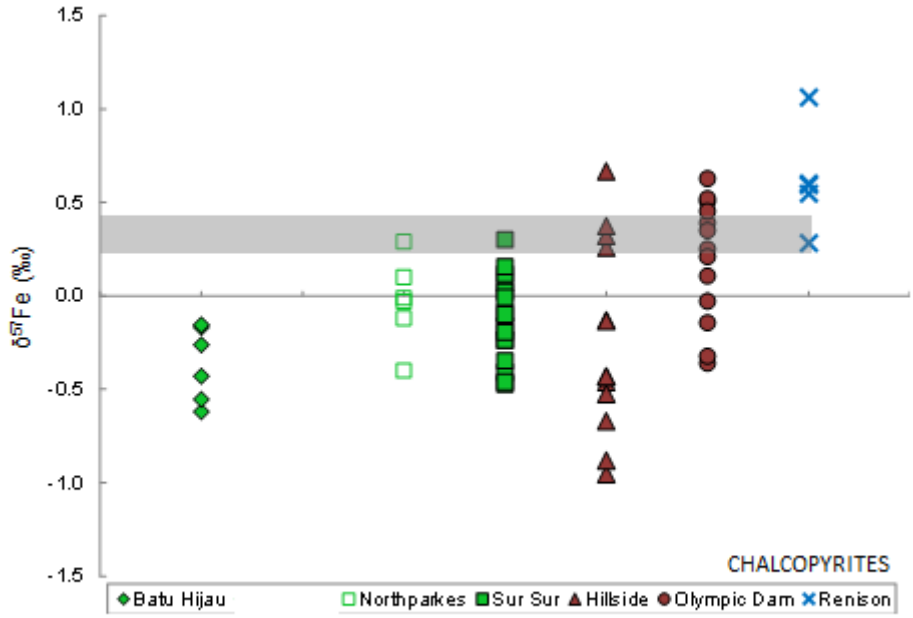

Figure 6.4 Fe isotope values of chalcopyrite separates categorised by deposit type. Northparkes data from Li et al. (2010).

The original premise of this research was to investigate whether minerals sampled from magmatic-hydrothermal deposits associated with isotopically light melts would also have Fe isotope values clustering around relatively light values, compared to minerals from deposits associated with intrusions that are relatively heavy. A-type granites tend to evolve to the heaviest δ^{57}Fe values (Foden et al., 2015), and notwithstanding the debate about the origin of IOCG deposits, the premise predicts that a contribution of heavy iron from a highly differentiated A-type melt/rocks would yield minerals with the heaviest isotopic values. This is clearly not the case in this study, with minerals from Hillside and Olympic Dam area spanning the entire range of δ^{57}Fe values exhibited by both porphyry copper deposits and the Renison Sn deposit. Fe isotope ratios alone, therefore, do not show clusters that distinguish one deposit class from another.

It is clear from Figures 6.1 to 6.4 that the range of δ^{57}Fe values from the intrusions is narrow (~0.25‰) compared to the ranges within and between groups of mineral separates; this suggests that fluid history and mineral formation processes have the greater influence over iron isotope fractionation between minerals. Moreover, given the differing tectonic settings of the 2 porphyry copper deposits (see Chapters 3 and

4), and the difference in magmatic oxidation state that underpins the differences between development of a Cu-Au from a Cu-Mo deposit (eg Blevin, 2004; Garrido et al., 2002), it is noteworthy that δ^{57}Fe values of magnetite and chalcopyrite separates from both Sur Sur and Batu Hijau are identical; this also suggests that fluid evolution dominate Fe isotope fractionation.

Magmatic-hydrothermal fluid evolution, especially the interdependence of oxygen and sulfur fugacity was discussed in Chapter 3. In particular, wide variation in fS_2 at a given fO_2 can result in significant variation in mineral assemblages and thus significantly influence how Fe isotopes are fractionated. At Renison, widespread pyrrhotite preferentially incorporates the light isotope, so that chalcopyrite has values in between those of magnetite/arsenopyrite, and low δ^{57}Fe pyrrhotite (Wawryk and Foden, 2015). However, at Batu Hijau, magnetite incorporates the heavy isotope, but pyrrhotite is absent, so that chalcopyrite-bornite incorporates the light Fe isotope.

6.3. BARREN AND MINERALISED INTRUSIONS

A second aim of the research was to examine further the hypothesis put forward by Poitrasson and Freydier (2005) and Heimann et al. (2008) to explain isotopically heavy siliceous intrusive rocks, namely the “light fluid hypothesis”. This hypothesis posits that light isotopes of Fe are preferentially partitioned into chloride-rich magmatic-hydrothermal fluids as they exsolve, leaving behind an isotopically heavy “residual” melt, which may be anomalous with respect to igneous rocks that have not undergone volatile loss (Heimann et al., 2008).

A comparison of δ^{57}Fe values between intrusives associated with magmatic-hydrothermal mineralisation (ie have been demonstrated by field and isotopic studies to have contributed magmatic fluids to the mineralising system), and barren intrusions is shown in Figure 6.5. The figure shows a range of δ^{57}Fe values within each category, with overlap between barren and mineralised intrusions. Furthermore, there is now a body of research which demonstrates that fractional crystallisation processes (e.g. Telus et al., 2012, Foden et al., 2015) and physical properties of a melt (e.g. Dauphas et al., 2014) are the dominant processes controlling Fe isotope evolution, although temperature gradients may also be important (eg Huang et al., 2009; Zambardi et al., 2014).

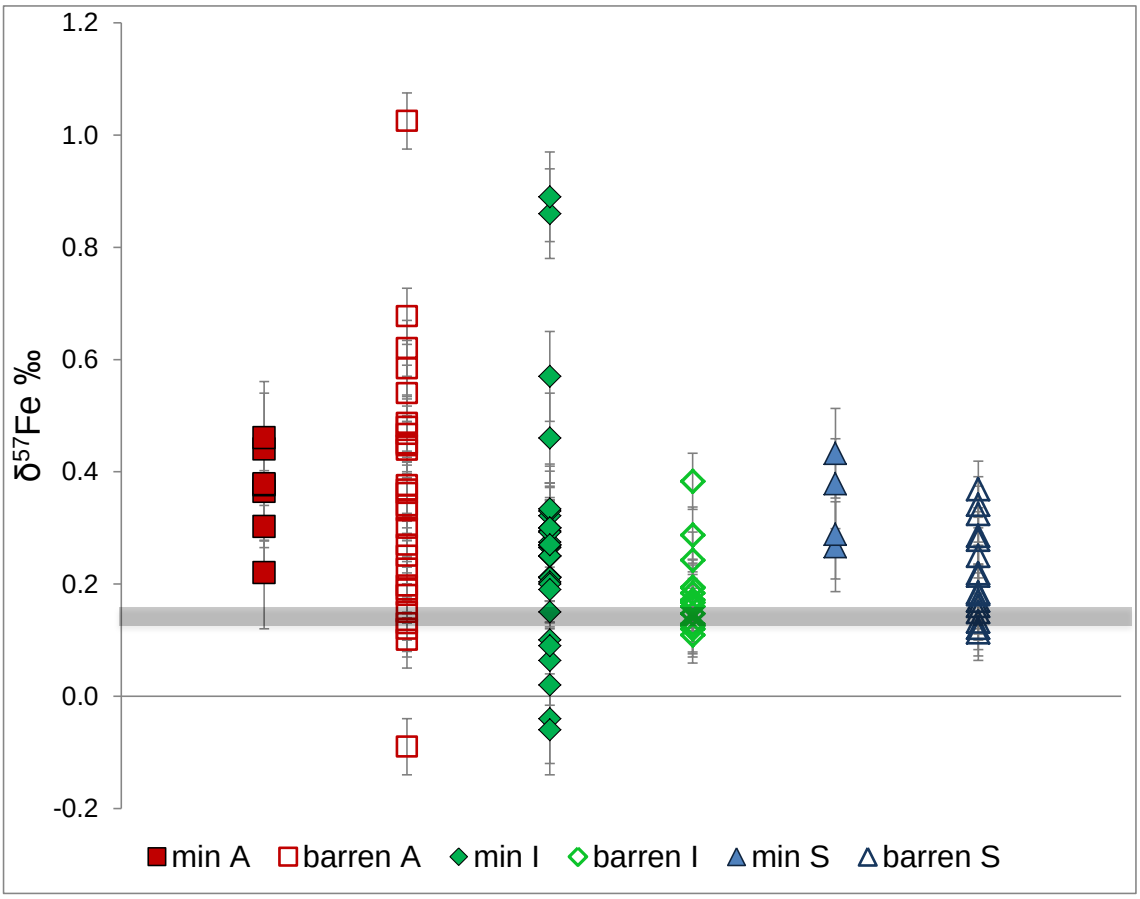

Figure 6.5 Comparison of δ^{57}Fe values of barren and mineralised intrusions. The X-axis is not numerical, and data is divided into A, S, and I type intrusions. Mineralised intrusions are in solid colours, barren intrusions in open symbols. The horizontal, grey shaded bar is the average isotopic value of MORB, shown for comparison. Data for barren intrusions from Foden et al. (2015), Poitrasson and Freydier (2005); Heimann et al. (2008); Telus et al. (2012); Zambardi et al. (2014). Data for mineralised intrusions ('min') from this study; Heimann et al. (2008); Wang et al. (2011); Wang et al. (2015).

6.4. FURTHER RESEARCH

One limitation of this research is that mineral separates were handpicked or separated magnetically, and neither method can achieve 100% separation (see Appendix 1.1). Therefore, any variation in isotopic values owing to growth zonation or mineral inclusions was unable to be assessed (although the closeness of our replicate analysis –see Appendix 1.3– suggests that mineral inclusions are not a significant issue in our samples). So although this study is able to characterise δ^{57}Fe values of mineral groupings between deposits in a broad sense, variability within mineral groups remains subject to many possible interpretations.

One interpretation of variability is that minerals within a paragenetic sequence may have formed by interface coupled dissolution-precipitation (ICDP) reactions. For example, sulfidation reactions can convert magnetite to pyrite (e.g. Qian et al., 2010) or pyrrhotite, or hematite to chalcopyrite (e.g. Zhao et al., 2014). Horn et al. (2006) posited that quantitative dissolution of a primary siderite and precipitation of a secondary hematite retains the isotopic signature of the primary siderite; this type of investigation, for example at Olympic Dam (discussed in Chapter 5) where two fluids were involved in ore formation (eg Rusk et al., 2015), could help to explain the spread of Fe-isotopic values within mineral separates. Thus, experiments to test iron isotope fractionation in sulfidation reactions are needed.

The analysis of growth zones requires in situ analysis either by LA-ICPMS or SIMS (e.g. Horn et al., 2006; Marin-Carbonne et al., 2011; Li et al., 2013; Dziony et al., 2014). In situ analysis of products from mineral formation experiments such as those discussed above, would be a powerful tool to understand further the mechanisms that fractionate Fe isotopes in mineral formation processes. In the case of SIMS integrated isotope studies are possible; for example ^{18}O in quartz and Fe-oxides, and ^{34}S and ^{56}Fe isotopes in coexisting sulfides and oxides within quartz. A difficulty with in situ analyses is the requirement for homogeneous standard samples, which is difficult to achieve with minerals that display extensive solid solution, such as the bornite-digenite series (J. Cliff, per comm). A second direction for future research thus lies in the field of analytical development.

References

Bajwah, Z. U., White, A.J.R., Kwak, T.A.P., Price, R.C. (1995). The Renison granite, Northwestern Tasmania: A Petrological, Geochemical and Fluid Inclusion Study of hydrothermal alteration. Econ. Geol. 90, 1663-1675.

Blevin P. (2004). Redox and Compositional Parameters for Interpreting the Granitoid Metallogeny of Eastern Australia: Implications for Gold-rich Ore Systems. Resource Geology 54, 241-252.

Dauphas, N., Roskosz, M., Alp, E., Neuville, D., Hu, M., Sio, C., Tissot, F., Zhao, J., Tissandier, L., Médard, E., Cordier, C. (2014). Magma redox and structural controls

on iron isotope variations in Earth's mantle and crust. Earth Planet. Sci. Lett. 398, 127-140.

Dziony, W., I. Horn, I., Koepke, J., Steinhoefel, G., Schuessler, J., Hotz F. (2014). In-situ Fe isotope ratio determination in Fe-Ti oxides and sulfides from drilled gabbros and basalt from the IODP Hole 1256D in the eastern equatorial Pacific. Chem. Geol. 363, 101-113.

Foden, J., Sossi, P., Wawryk, C. M. (2015). Fe isotopes and the constrasting petrogenesis of A-, I- and S-type granite. Lithos. 212-215, 32-44.

Garrido, I., Cembrano, J., Sina, A., Stedman, P., Yanez, G. (2002). High magma oxidation state and bulk crustal shortening: key factors in the genesis of Andean porphyry copper deposits, central Chile (31-34 degrees S). Revista Geologica De Chile. 29, 43-54.

Heimann, A., Beard, B. L., Johnson, C. M. (2008). The role of volatile exsolution and sub-solidus fluid/rock interactions in producing high 56Fe/54Fe ratios in siliceous igneous rocks. Geochim. Cosmochim. Acta 72, 4379-4396.

Horn, I., von Blanckenburg, F., Schoenberg, R., Steinhoefel, G., Markl, G. (2006). In situ iron isotope ratio determination using UV-femtosecond laser ablation with application to hydrothermal ore formation processes. Geochim. Cosmochim. Acta 70, 3677-3688.

Li, W., Huberty, J. M., Beard, B. L., Kita, N. T., Valley, J. W., Johnson, C. M. (2013). Contrasting behavior of oxygen and iron isotopes in banded iron formations revealed by in situ isotopic analysis, Earth and Planet. Sci. Lett. 384,132-143.

Marin-Carbonne, J., Rollion-Bard. C., Luais B. (2011). In-situ measurements of iron isotopes by SIMS: MC-ICP-MS intercalibration and application to magnetite crystal from Gunflint chert. Chem. Geol. 285, 50-61.

Poitrasson, F., Freydier, R. (2005). Heavy iron isotope composition of granites determined by high resolution MC-ICP-MS. Chem. Geol. 222, 132-147.

Rusk, B., Emsbo, P., Xavier, R.P., Corriveau, L., Oliver, N., Zhang, D. (2015). A comparison of fluid origins and compositions in iron oxide-copper-gold and porphyry Cu-(Mo-Au) deposits. In Proceedings of PACRIM 2015 Congress, AUSIMM Publication Series 2/2015 271-279.

Syverson, D. D. (2015). Fe and Cu isotope fractionation between chalcopyrite and dissolved metal species during hydrothermal recrystallization: An experimental study at 350C and 500 bars. Abstract OS43A-2012 presented at 2015 Fall Meeting, AGU, San Francisco, Calif., 14-18 Dec.

Telus, M., Dauphas, D., Moynier, F., Tissot, F., Teng, F., Nabelek, P., Craddock, P., Groat, L. (2012). Iron, zinc, magnesium and uranium isotopic fractionation during continental crust differentiation: The tale from migmatites, granitoids and pegmatites. Geochim. Cosmochim. Acta 97, 247-265.

Wawryk C. M. and Foden J., (2015). Fe-isotope fractionation in magmatic-hydrothermal mineral deposits: A case study from Renison Sn-W deposit, Tasmania. Geochim. Cosmochim. Acta. 150, 285-298.

Wawryk, C.and Foden J., (submitted) Fe isotope systematics from the Batu-Hijau Cu-Au deposit, Sumbawa, Indonesia.

Wang, Y., Zhu, X., Mao, J., Li, Z., Cheng, Y. (2011). Iron isotope fractionation during skarn formation - case study of Xinqiao Cu-S-Fe-Au deposit in Middle-Lower Yangtze Valley. Ore Geology Reviews, 43, 194-202.

APPENDIX 1. Procedures for sample preparation, Fe-isotope analysis, and quality control

Appendix 1.1 Sample preparation procedure for Fe-isotope analysis, in the University of Adelaide clean isotope laboratory

- For bulk rock samples of magmatic rocks:
    - Weathered surfaces were removed by cutting with a rock saw
    - Samples were crushed to ~0.5-1cm in a jaw crusher. Crusher was cleaned between samples with compressed air and ethanol
    - Samples were milled to powder in a tungsten-carbide ring mill. The mill was cleaned between samples with compressed air and ethanol
    - XRF analysis of a quartz blank sample showed no Fe contamination, although some Co and Cr was transferred from the ring mill.
- For mineral separates:
    - Weathered surfaces were removed by cutting with a rock saw.
    - Where minerals are coarse grained (>0.5cm) to massive, samples were scratched from fresh surfaces with a tungsten-carbide tipped scribe
    - Where minerals are finer-grained, a wafer was cut using a rock saw, then the wafer was milled in an agate mill, and sieved to a size fraction between 1mm and +125µm.
    - A hand magnet was passed over the samples to remove magnetite.
    - A Frantz magnetic separator was used to separate hematite, bornite, chalcopyrite and pyrite, then checked using a binocular microscope.
    - Frantz current settings (amperes):
        - Hematite: 0.01-0.05
        - Bornite: 0.6-0.9
        - Chalcopyrite: 0.9-1.3
        - Pyrite: >1.3

Dissolution protocol:

- In a 7ml Teflon beaker, about 5-10 mg sample (if a silicate rock), or 0.5-2mg (for sulphides, and oxides) was weighed out.
- Samples were dissolved in reverse aqua regia (0.5ml conc HCl and 1.5ml conc HNO_3) overnight at 140°C on a hot-plate. A strong oxidising agent is required to ensure all Fe is in the Fe^{3+} state, for retention on the ion-exchange resin.
- Samples were evaporated at 140°C to dryness
- Taken up in 2ml of 6M HCl

- Evaporated to dryness at 140°C
- Taken up in 0.5ml of 0.05m HCL
- Insoluble inclusions e.g. zircon, barite, cassiterite and quartz are resistant to aqua regia digestion, and were removed from Fe-solution via centrifuge before loading onto anion-exchange columns.

Preparation of ion-exchange columns using Bio-Rad AG 1X4 200-400 mesh*:*

- 5ml of 6M HCl
- 8ml of 0.05M HCl
- Equilibrate with 0.5ml 6M HCL

Sample Elution:

- Load sample in 0.5ml 6M HCl
- Cu, Ni elution with 4ml 6M HCl
- Fe elution with 3ml 0.05M HCL7
- Dry sample on hotplate and take up in 5m 0.05M HCl for MC ICPMS.

Resin was replaced after 5 uses. A geostandard and procedural blank are prepared simultaneously with the samples.

Appendix 1.2. Check of Fe-Elution chemistry

The aim was to ensure that the resin was not overloaded with Fe, and that elements which can interfere with Fe (Cu, Cr, Co, Ni, Zn) had been removed from the samples prior to MC-ICPMS.

Samples were dissolved at 140° C in reverse aqua regia (3 parts conc HNO_3 to 1 part conc HCl) to oxidise the Fe, and centrifuged to remove insoluble inclusions prior to the column work.

The column chemistry is listed below. The eluent from steps 2-4, and washing steps 5 and 6 were collected for one each of magnetite, bornite and chalcopyrite mineral separates from Batu Hijau ore. The author had noted that after step 4, green-yellow staining remained on the resin, when working with Cu-bearing sulphides, so step 4was repeated; thus a total of 6ml of 6M HCl was used to elute Cu.

Eluents were analysed by Optical Emission Spectroscopy at the CSIRO Analytical Chemistry department at Waite Campus. The concentration of Fe was measured on the Neptune multi collector ICPMS.

Column Procedure:

Sample Elution

8. Load the entire sample (½ ml) on to the top of the resin.
9. Rinse the beaker with 1ml of 6M HCl, and add to the column
10. Cu elution: 3ml of 6M HCl
11. Fe elution: 3ml of 0.05M HCl
    a. Dry down beakers (140°C)
    b. Take the samples up in 5ml 2%HNO_3 for mass spectrometry

Cleaning

12. 5ml of 6M HCl
13. ~7ml of 0.05M HCl
14. Equilibrate with 0.5ml of 6M HCl

Results

Fe elution: Results are shown in Table A2.1, and in the charts below. No Fe has eluted from the column prior to the Fe collection step, showing that the resin was not

overloaded with Fe, with sample weights of 5-7 mg. About 99% of the Fe was recovered in the Fe elution steps, with a small fraction remaining on the columns. Further tests could to be done to see if use of 4-5 ml of acid at step 4 would improve recovery. However, given that internal geostandard GSP2 returns accurate results over the long term, this is probably not necessary.

***Base metal elution**:* Table A2.1 shows that 98% of the Cu from the chalcopyrite sample was eluted in step 2, with the remaining 2% eluted in step 3. Further eluents were below the detection limit of 50ppb using OES. Figure A2.11 shows the good separation of Cu and Fe using the current method.

Cr, Co and Ni all returned results less than the detection limit of 50 ppb. The signal intensity of ^{53}Cr on the Neptune consistently remains around 0.0008V showing effective separation of this element by the resin.

Sample ID	Elution Step	conc Fe (ppm)		%of total Fe	Cu (ppm)
cp1	6M HCl sample vial rinse	0.0004		0.0001%	**539**
cp2	6M HCl base metal elution	0.0021		0.0006%	**11.2**
sample collect	0.05M Fe elution	**336.0**		**99.46%**	<5
cp3	6M HCl wash	1.70		0.50%	<5
cp4	.05M HCL wash	0.13		0.04%	<5
			total [Fe] ppm	**337.83**	
mgt1a	6M HCl sample vial rinse	0.008		0.002%	<5
mgt1b	6M HCl base metal elution	0.004		0.001%	<5
sample collection	0.05M Fe elution	**517**		**99.16%**	<5
mgt2	6M HCl wash	3.89		0.75%	<5
mgt3	.05M HCL wash	0.47		0.09%	<5
			total [Fe] ppm	**521.37**	
bn1	6M HCl sample vial rinse	0.0002		0.0001%	**704**
bn2	6M HCl base metal elution	0.0003		0.0002%	<5
sample collection	0.05M Fe elution	**163.0**		**99.25%**	<5
bn3	6M HCl wash	1.1		0.69%	<5
bn4	.05M HCL wash	0.1		0.06%	<5
			total [Fe] ppm	**164.23**	<5

Table A1 1 Fe and Cu concentrations in eluent steps of ion exchange chromatography , used to separate Fe for mass spectrometry

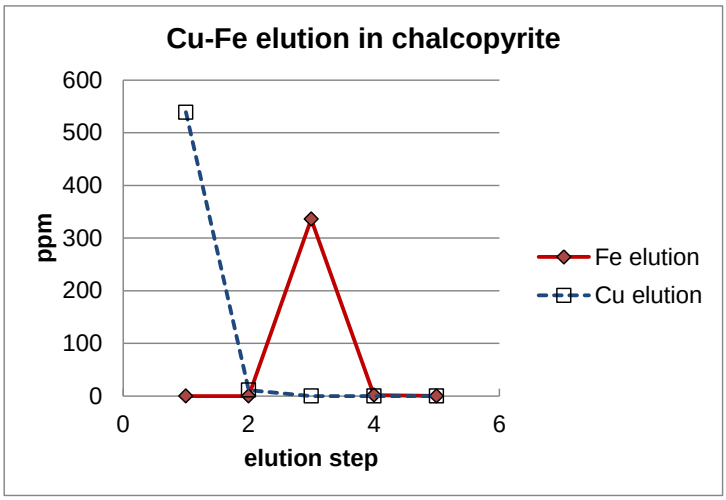

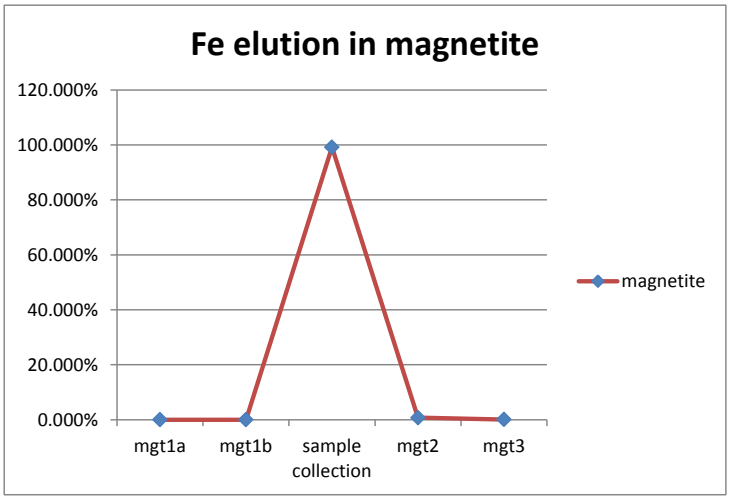

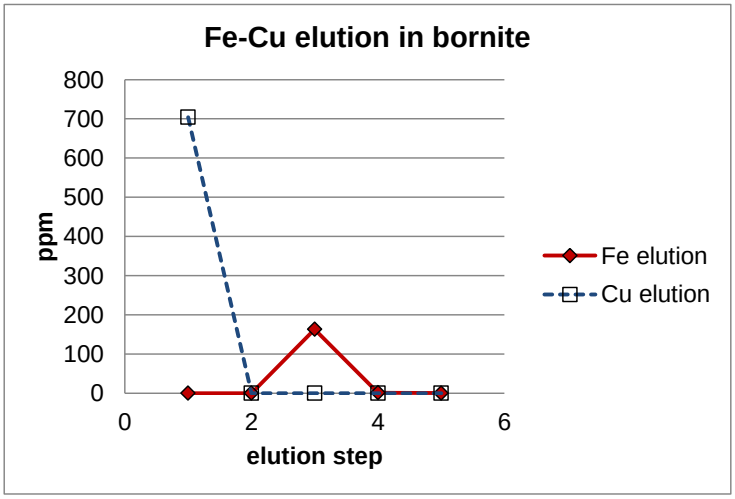

Figure A1 1 Elution profiles for Cu in chalcopyrite, magnetite and bornite.

Appendix 1.3. Performance of Geostandards, procedural blanks and duplicate samples during the period of author's PhD

Geostandards were prepared with each batch of samples. Geostandards comprised:

HEM: The Milhaus hematite, which can be obtained from ETH laboratory in Zurich. This is a pure hematite, so can be used to monitor drift in the multi-collector independent of column chemistry. The long term average, from 127 analyses (from 2009 to 2015; Fig A1.2), is δ^{57}Fe =0.73±0.2‰ (1SD).

GSP2: This is a granodiorite rock obtained from the United States Geological Survey. As a silicate rock this is appropriate to check Fe recovery and purification from the author's silicate rock samples which range from andesite to granite in composition. The long term average, from 75 analyses (from 2012 to 2015; Fig A1.3), is 0.27 ± 0.04‰ (95% confidence interval, CI), comparable to the recommended value of 0.23 ± 0.021‰ (95% CI) published by Craddock and Dauphas (2011).

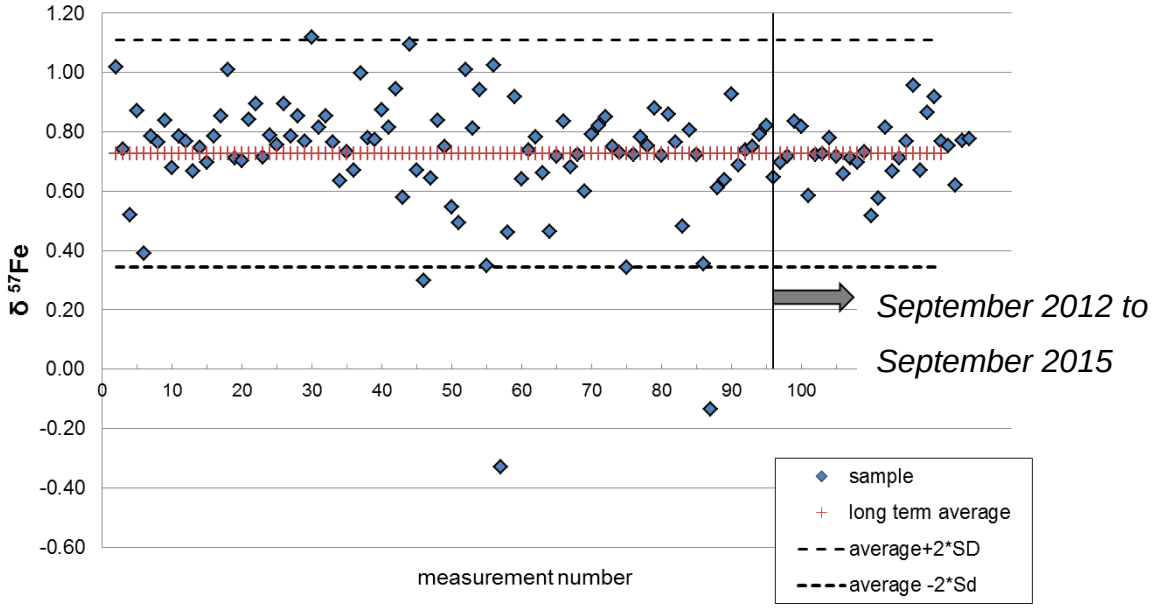

Figure A1 2 Long term analyses of hematite standard

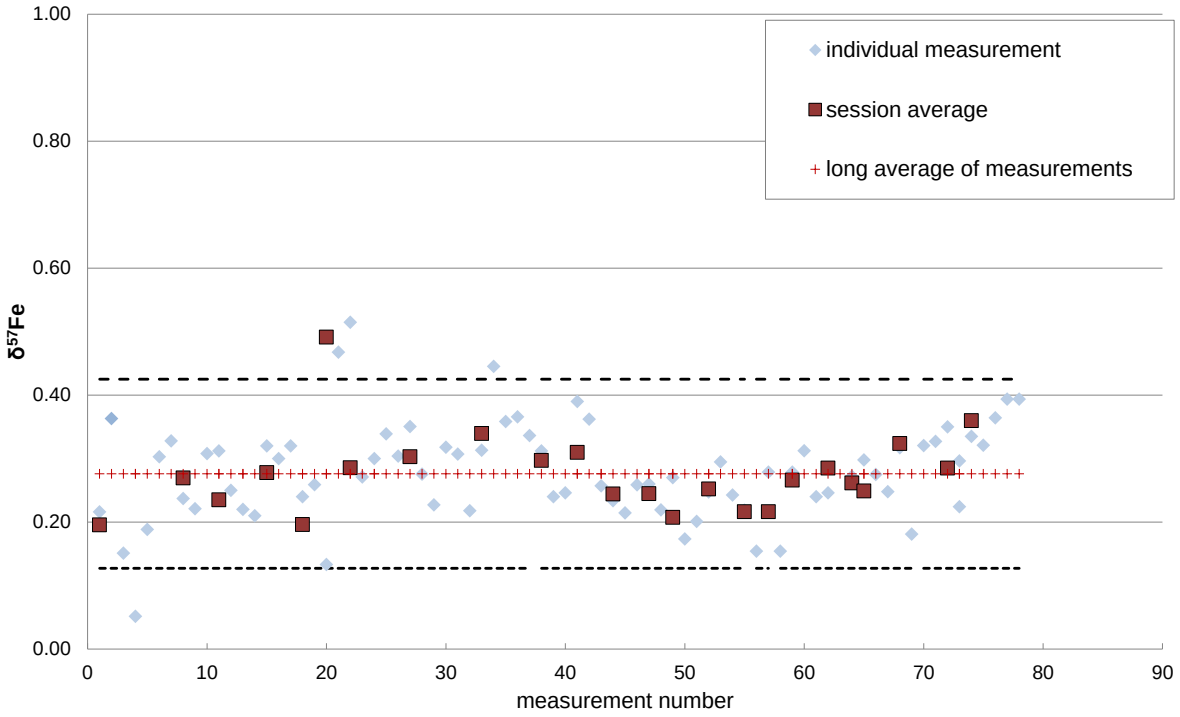

Figure A1 3 Long term analyses of geostandard GSP2. The dashed lines are the 2 times standard deviation of all the individual analyses

Procedural blanks: A procedural blank sample was prepared with each batch of sample dissolution and column chemistry, equating to every 12th sample. The blank consisted of all the dissolution, evaporation and column chemistry steps, but with no sample added. Fe in the procedural blanks averages ~7 ppb. This equates to <0.1% of the total Fe in sample solutions which have [Fe] between 60-700ppm Fe.

Acid blanks used to prepare 3 to 4 ppm solutions for introduction to the Neptune have an average [Fe]=3ppb, or 0.1% of the total signal of a 3 ppm solution.

Sample duplicates: Four duplicate samples were prepared and measured on the Neptune. The samples consisted of Renison Granite (milled whole rock powder), and one each of pyrrhotite, arsenopyrite and pyrite mineral separates. The results are shown in Table A1 2, and illustrated graphically in Figure A1 4. All the samples overlap within analytical error.

Table A1 2 Iron isotope analyses of duplicate samples.

Sample ID	$\delta^{57}Fe$	2SD	$\delta^{56}Fe$	2SD
40612-12po	-0.343	0.077	-0.257	0.030
40612-12po rpt	-0.299	0.050	-0.172	0.030
RB003	0.289	0.093	0.189	0.049
RB003 rpt	0.334	0.018	0.219	0.050
RB024asp	1.191	0.084	0.804	0.018
RB024asp_rpt	1.055	0.004	0.751	0.041
15py	0.58	0.14	0.37	0.12
15py_rpt	0.59	0.09	0.38	0.05

Abbreviations: po = pyrrhote, asp =arsenopyrite, py = pyrite. The duplicate sample is suffixed with "_rpt".

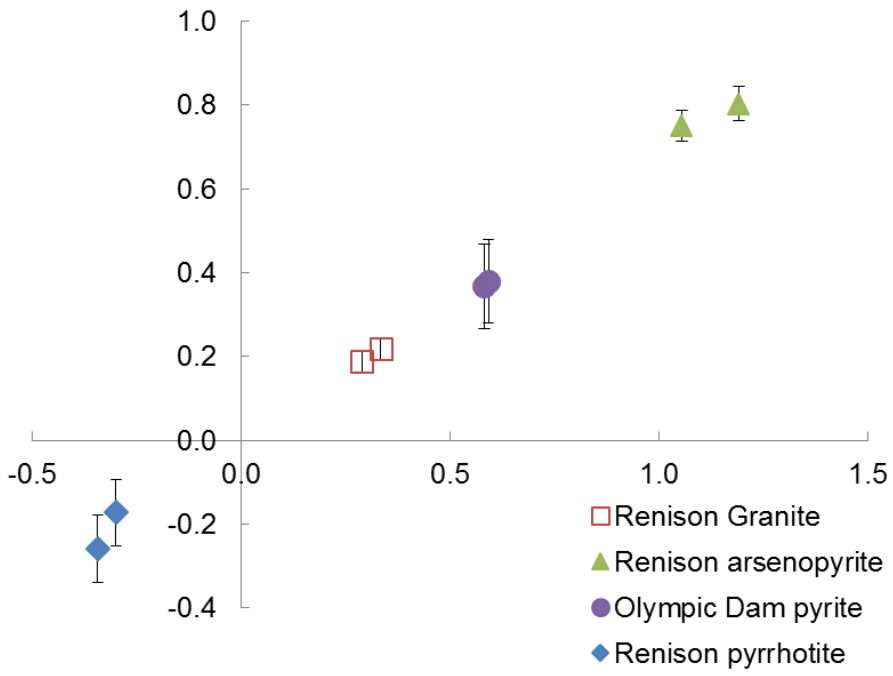

Figure A1 4 Results of duplicate samples. The error bars are the 2 times standard deviation of all the individual analyses; each sample was measured between 3 and 6 times.

Appendix 1.4. Parameters for measuring Fe-isotopes on the Thermo Finnigan Neptune Multi-collector at the University of Adelaide, Waite Campus

Tuning of the instrument-resolution and peak shape

Weyer and Schwieters (2003) authored the seminal work on measuring accurate, high precision Fe isotope measurements with high mass resolution MC-ICPMS, using the Thermo Finnigan Neptune instrument. They demonstrated that polyatomic interferences by argon nitrides, oxides and hydroxides on the Fe signal can be effectively resolved by closing the entrance slit before the electrostatic analyser, i.e. using either “medium” or “high” mass resolution mode. Closing the entrance slit has the effect of creating an interference-free flat plateau on the left of the peak, because the Fe enters the detectors first.

Weyer and Schwieters (2003) also explained the relationship between resolving power (which creates a flat peak) and transmission (signal strength). This translates to requiring a resolution of at least 6,500 in medium resolution mode and peak width of at least 150ppm to achieve accuracy and precision using H-cones in medium resolution mode (Poitrasson, written comm. and Halverson, pers comm.). A typical peak shape from the University of Adelaide Neptune is shown in Figure A4.1.

Monitoring of matrix effects was done by observing the evolution of IRMM14, and variation of Fe isotope and Ni isotope variations during an analytical session. Examples are shown in Figure A4.2 and A4.3.

Cup Configuration:

Cup Number	Species	Position
L4-F	^{53}Cr	93.2
L2-F	^{54}Fe	62.062
L1-F	^{56}Fe	19.052
C	^{57}Fe	
H1-F	^{58}Fe	20.123
H2-F	^{60}Ni	61.31
H4-F	^{61}Ni	90.582

Intake System

- Thermo Standard introduction System (SIS), consisting of glass Scott double pass assembly
- 50 µl/min Teflon nebuliser
- H-geometry skimmer cones and Ni sample cone. For samples with low concentration of Fe, andX-geometry skimmer cone was used
- Medium resolution mode.

Data Acquisition Method

- Uptake time 70-90s
- Rinse time between samples 60s
- Baseline run before each sample
- Run standard-sample-standard bracketing (SSB), using IRMM14
- Spiked with Ni for mass bias correction (normalizing) to exponential law using true fractionation parameter of $^{61}Ni/^{60}Ni$ of 0.04346931
- Correction applied for interference of ^{53}Cr, although column chemistry appears to have effectively removed Cr from samples (signal ~10^{-4} V)
- Samples run in 2% HNO_3. Sample concentration set to achieve ~0.95 V (±10%) on ^{57}Fe and $^{6}1Ni$, and 40V for ^{56}Fe. Using H-cones this is generally ~3-4 ppm Fe. Care was taken to ensure signal intensities were within 10% for both sample and standard solutions and all solutions were prepared from the same batch of nitric acid during a single session (Dauphas et al., 2009).
- 2% HNO_3 acid blank measured at the start, middle and end of the sequence. Acid blanks contribute <1% of the total sample signal. Typical acid blank signals are tabulated below

^{56}Fe	^{57}Fe	^{61}Ni
0.27 V	0.006 V	0.00025 V
0.147	0.0034	0.0005
0.134	0.0032	0.00033

Data recorded

- Signal voltages on each Faraday cup
- Un-corrected ratios $^{56}Fe/^{54}Fe$, $^{57}Fe/^{54}Fe$ and $^{61}Ni/^{60}Ni$
- Normalized $^{56}Fe/^{54}Fe$ and $^{57}Fe/^{54}Fe$
- $\delta^{56}Fe$ and $\delta^{57}Fe$ using mass bias corrected SSB
- Each sample was run a minimum of 3 times.

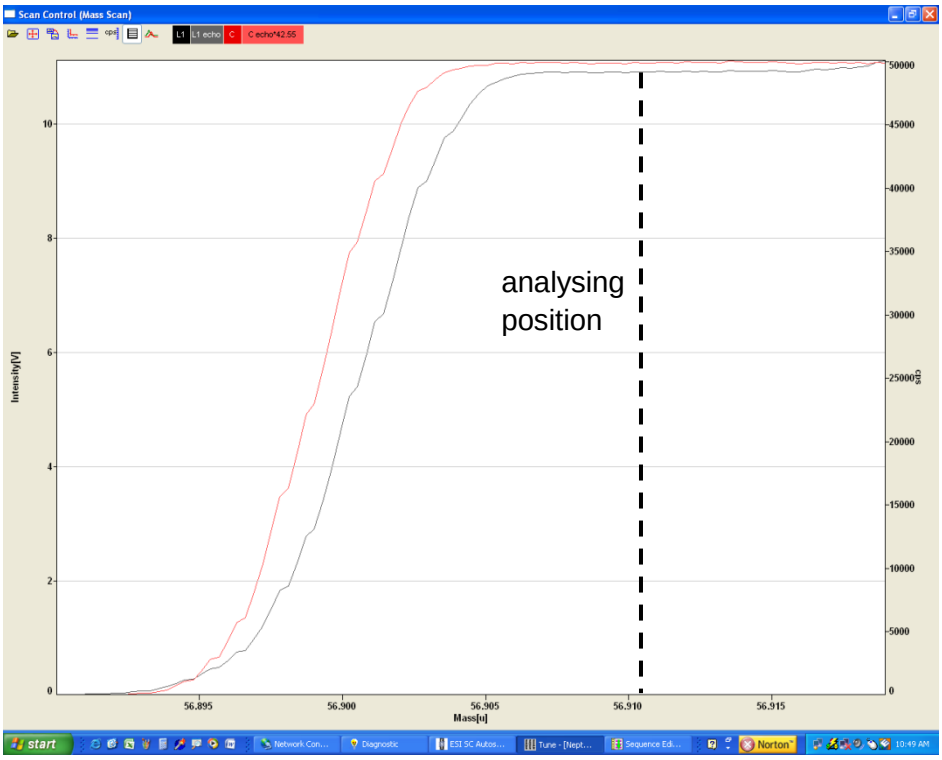

Figure A1 5 Peak shape showing resolution of ~6,600 and peak width ~211 ppm. Isotope ^{57}Fe is the red signal trace, and ^{56}Fe is the black signal trace.

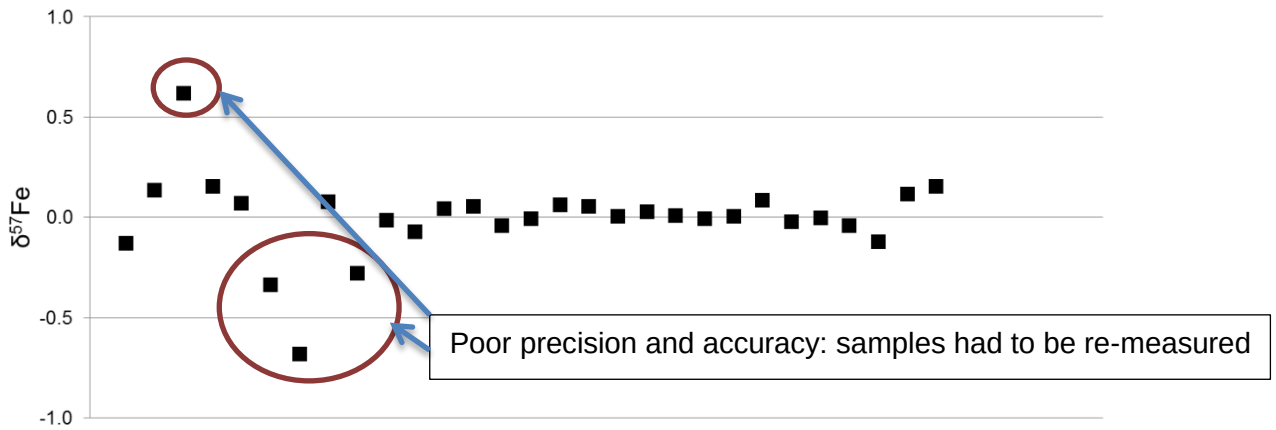

Figure A1 6 Stability of $\delta^{57}Fe_{IRMM14}$ measured during a single session.. IRMM14 measured relative to itself should be very close to 0‰.

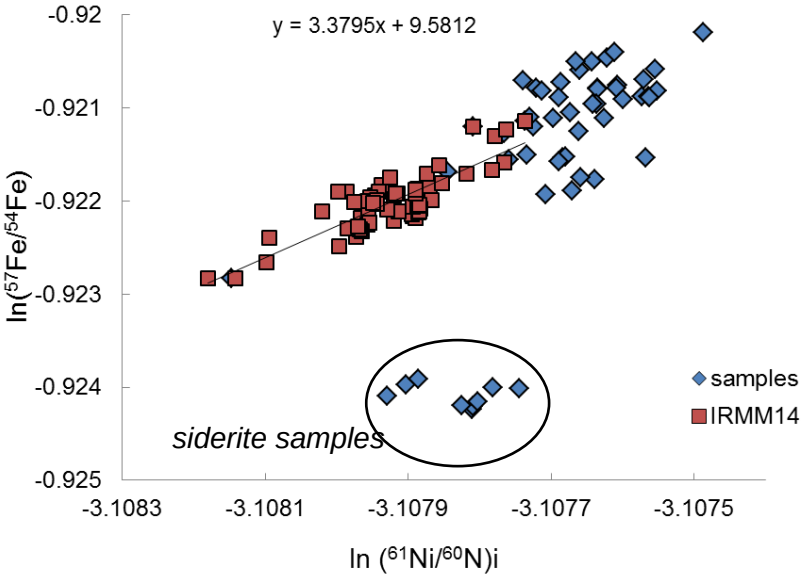

Figure A1 7. Variation of $^{57}Fe/^{54}Fe$ ratios with $^{61}Ni/^{60}Ni$ ratios (natural logs plotted) during a single analytical session. Some siderite samples showed a marked departure from the line, possibly owing to inefficient separation of Ca, and were not used in interpretation of data.

References

Dauphas N., Pourmand A. and Teng, F. Z. (2009) Routine isotopic analysis of iron by HR-MC-ICPMS: How precise and how accurate? Chem. Geol. 267, 175-184.

Poitrasson, F. and Freydier, R. (2005) Heavy iron isotope composition of granites determined by high resolution MC-ICP-MS. Chem. Geol. 222, 132-147.

Weyer S., and Schwieters, J. (2009) High precision Fe isotope measurements with high mass resolution MC-ICPMS. Int. J. Mass. Spectrom. 226, 355-368

APPENDIX 2. Register of samples and thin section collected and stored at the University of Adelaide.

Sample Number	Prospect	Description	Sample Type	Hole ID	Depth	host unit	comments
40612-01	Black Face	massive py	Outcrop			Dol #2	
40612-03	Black Face	massive py	Outcrop			Dol #2	
40612-04	Black Face	massive po	Outcrop			Dol #2	
40612-05	Black Face	massive po	Outcrop			Dol #2	
40612-07	Black Face	massive py	Outcrop			Dol #2	
40612-09	Black Face	massive po	Outcrop			Dol #2	
40612-12	Dunns	massive po	Outcrop			Dol #1	
40612-13	Dunns	massive po	Outcrop			Dol #1	
40612-17	The Battery	intergrown py-po	Outcrop			Renison Bell member	
40612-21	The Battery	massive po	Outcrop			Dol #2	
40612-31	Pine Hill	greisenised granite	Outcrop			PHG	Pine Hill Granite
40612-32	Pine Hill	tourmalinised granite	Outcrop			PHG	Pine Hill Granite
40612-33	Pine Hill	greisen	Outcrop			PHG	Pine Hill Granite
RB001	Renison	porphyritic qtz-fsp-bt granite, more equigranular than at 315m	DD	U4207	383.5	PHG	Pine Hill Granite
RB002	Renison	grey, cg, porphyritic qtz-fsp-bt granite	DD	U4207	315.3	PHG	Pine Hill Granite
RB003	Renison	pale grey, mg q-fs-(bt) granite.	DD	U4382	262.4	PHG	Pine Hill Granite

Sample Number	Prospect	Description	Sample Type	Hole ID	Depth	host unit	comments
RB004	Renison	pale grey, mg q-fs-(bt) granite.	DD	U4382	243.6	PHG	Pine Hill Granite
RB009	King	"distal" sid- altered dolomite	DD	U4390	69	Dol #2	
RB010	King	"distal" sid- altered dolomite	DD	U4388	77.8	RRM	Red Rock Member
RB011	King	mt altered dolomite	DD	U4388	73.8	Dol #2	
RB013	King	sid intergrown with sulphides	DD	U4392	74	Fault	Fault in Dolomite #2
RB016	Rendeeps	as-cp-po	DD	U4602	152.2	CCF	Crimson Creek Fm
RB017	Rendeeps	py-po-(cpy)	DD	U4602	152.4	CCF	Crimson Creek Fm
RB018	Rendeeps	py-aspy	DD	U4602	157.8	CCF	Crimson Creek Fm
RB019	Rendeeps	massive po	DD	U4633	150.27	Fault	Federal Fault in Dolomite #2
RB020	Rendeeps	massive po	DD	U4633	152.8	Dol #2	
RB021	Central Federal	cb-py-aspy-cpy-po vein	DD	U4624	14.9	Fault	Fault in Dalcoath Member
RB022	Central Federal	massive po vein	DD	U4624	75.5	Dol #1	
RB023	Central Federal	cb-mg altered dolomite host rock	DD	U4624	75.9	Dol #1	
RB024	Central Federal	aspy-po in qtz vein	DD	U4624	109.53	Fault	Fault In Crimson Creek Fm

Sample Number	Prospect	Description	Sample Type	Hole ID	Depth	host unit	comments
RB025	Central Federal	massive po-aspy-cpy	DD	U4624	114.25	Fault	Fault In Crimson Creek Fm
RB027	Central Federal	cpy-aspy-py-cb vein	DD	U4627	19	Fault	Fault in Dalcoath Member
RB028	Central Federal	aspy-cpy-cb vein	DD	U4627	47	DM	Dalcoath Member
RB030	Central Federal	sid(?)-cpy-po vein	DD	U4627	102.9	CCF	Crimson Creek Fm

Table A2 1 Samples collected from the Renison Sn-W deposit and surrounds

Drill Hole	Depth_m	Host-rock	Quartz Vein-type	Hydrothermal Alteration	Vein Sulfide Minerals	Au_ppm	Cu_pct	Ag_ppm	Au / Cu	Ag / Au	From	To
SBD031	441.2	Vsst	B	bi-mt	py-cp-(bn)	1	1.19	2.7	0.84	2.70	441	442
SBD031	465.5	Ti	A	strong pgm (bi)-mt	cp-bn-mt	1.34	1.55	4.5	0.86	3.36	465	468
SBD031	566.4	Qde	AB	bi-ep-mt	bn-(mt)	1.05	0.87	2.8	1.21	2.67	564	567
SBD059E	652.1	Ti	A	strong pgm (bi)-mt	bn>>cp	0.34	0.66	1.6	0.52	4.71	651	654
SBD086E	293.2	Qde	A and B	weak-mod pgm bi-mt	A: bn-mt, B: cp>>bn	0.62	1.62	2.8	0.38	4.52	291	294
SBD086E	635.8	Qde	B	weak-mod pgm bi-mt	cp	1.15	1.12	2.2	1.03	1.91	633	636
SBD086E	636.2	Ti	A	weak pgm-ep-bi-mt	bn-cp-mt	1.15	1.12	2.2	1.03	1.91	633	636
SBD086E	714.9	Vsst	A	weak pgm bi-mt	bn-cp	1.89	1.11	3.6	1.70	1.90	714	717
SBD090	266.0	Qde?	A, B, C	weak pgm bi-mt	A:bn-cp, B: cp, C: cp-py	3.39	1.96	8.1	1.73	2.39	265	268
SBD090	381.1	Ti	B	mod pgm bi-mt	cp	0.31	0.16	0.3	1.94	0.97	381	384
SBD103	184.2	Vlbx	B	bi-mt	cp-mt>>bn	0.21	0.27	0.4	0.78	1.90	183	186
SBD103	379.0	Ti	AB	strong pgm (bi)-(mt)	cp-bn-mt, late cp-fractures	1.08	1.41	3.1	0.77	2.87	378	381
SBD103	485.4	Ti	B	bi-chl-ep-mt	bn-cp	1.54	1.16	3.2	1.33	2.08	483	486

Legend:

Rock-types: Qde, equigranular quartz diorite; Ti, Intermediate Tonalite; Vlbx, volcanic lithic breccia; Vsst, volcanic sandstone

Sulfides / Oxides: bn, bornite; cp, chalcopyrite; mt, magnetite; py, pyrite. Minerals listed in order of decreasing abundance, parentheses indicate minor phase

Silicates: bi, biotite; (bi), relict biotite; chl-chlorite; ep, epidote; pgm, pale green mica - sericite/chlorite intergrowth.

Note: sulfide minerals occur as disseminated grains, in altered hornblende sites and in quartz veins; magnetite is much more common as disseminated grains and in altered hornblende sites than in quartz veins.

Refer to Garwin (2000) and Arif and Baker (2004) for explanation of quartz vein terminology at Batu Hijau

Samples are described based on field analysis using a 20X hand-lens. It is recommended that the silicate- and sulfide-mineralogy and sulfide textual relationships be confirmed by viewing the samples through a 50X binocular microscope and reflected-light sections

Table A2 2 Vein samples collected by Batu Hijau mine geologists . Descriptions by S. Garwin

Table A2 3 Rock powders supplied by J. Foden and S. Garwin for Fe-isotope analyses of intrusive rocks. Rock powders returned to S. Garwin

Sample Number	Intrusive Unit	Existing Data	Alteration Zone	Alteration	Sulphides and oxides	Vein type/timing
SBD004-157	Intermediate Tonalite	whole rock and trace, SHRIMP, Ar-Ar	bt			syn, cut by A,B Qtz rinds
97101143	po hbl tonalite	whole rock and trace, amph+mgt EPMA,SHRIMP, Sr-Nd	least altered			
97101144	po hbl tonalite	whole rock and trace, amph+mgt EPMA	least altered			
99050502	QD3	whole rock and trace element	least altered			
99050902	QD3	whole rock and trace element	least altered			
97101030	QD3	whole rock, trace elements,SHRIMP,amph+bi+px+Feox EPMA, Sr, Nd	least altered	local bt-Kspar		early-syn, cut by A and B
SBD120/404m	po dacite (Batu H)	whole rock and trace elements	least altered			
98070736	po andesites±dacites/qtz diorites	fspar+amph+px+mgt EPMA, major elements+Zr	least altered			
BH12	Young Tonalite	Foden's collection, whole rock and trace elements				
BH7	Young Tonalite	Foden's collection, whole rock and trace elements				
BH4	Old Tonalite	Foden's collection, whole rock and trace elements				

Table A2 4 List of samples from the Sur Sur and Rio-Blanco-Los Bronces deposits sampled from the UTAS rock collection

Utas#	Field Number	Collector	Year	Rock Name	Rock Mineral 1	Rock mineral 2	Ore mineral1	Ore mineral2	Ore mineral3	Drill Hole	Depth (m)	Mine/Prospect
149059	CA1		unknown	dacite								Río Blanco
149061				Andesite								
149064	CA8		unknown	dacite								Río Blanco / La Union
150762	46	Frikken Peter	2003	Granodiorite	Quartz	Plagioclase group	Chalcopyrite	Pyrite		TSS 22	37	Sur Sur
150772	94	Frikken Peter	2003	Granodiorite	Quartz	Plagioclase group	Chalcopyrite			DL 139.1	123	Sur Sur
150773	95	Frikken Peter	2003	Granodiorite	Quartz	Plagioclase group	Pyrite	Bornite		DL 139.1 roof	170	Sur Sur
150787	231	Frikken Peter	2003	Andesite	Plagioclase group	Biotite				pendant	Surface	Río Blanco
150788	234	Frikken Peter	2003	Monzonite	Quartz	Plagioclase group				Monolito Mountain	surface	Río Blanco
150795	264	Frikken Peter	2003	Granodiorite	Quartz	Plagioclase group	Chalcopyrite			DDH-734	328.8	Don Luis Sector
150805	279	Frikken Peter	2003	Granodiorite	Quartz	Plagioclase group	Chalcopyrite	Magnetite		DDH-734	386	Don Luis Sector
150812	291	Frikken Peter	2003	Granodiorite	Quartz	Plagioclase group				DDH 734	470.4	Don Luis Sector

150849	492	Frikken Peter	2003	Granodiorite	Quartz	Plagioclase group	Hematite	Chalcopyrite	Pyrite	DL 57	86	Sur Sur
150851	500	Frikken Peter	2003	Granodiorite	Quartz	Plagioclase group	Chalcopyrite	Magnetite		TSS 12	118	Sur Sur
150856	523	Frikken Peter	2003	Granodiorite	Quartz	Plagioclase group	Chalcopyrite	Magnetite		DL 71	98	Sur Sur
150865	MiR9901	Frikken Peter	2003	rhyolite	Quartz	Plagioclase group				DDH-513	134	Río Blanco
150866	Mid9907	Frikken Peter	2003	dacite	Quartz	Plagioclase group				DDH-555	250	Río Blanco
150874	101a	Frikken Peter	2003	Granodiorite	Quartz	Plagioclase group	Chalcopyrite	magnetite	bornite	C-50	26	Sur Sur
150876	102a	Frikken Peter	2003	Granodiorite	Quartz	Plagioclase group	Chalcopyrite	magnetite	Pyrite	C 50	60	Sur Sur
150896	164a	Frikken Peter	2003	Monzonite	Quartz	Plagioclase group				DDH 344	210	Río Blanco
150904	186a	Frikken Peter	2003	Granodiorite	Quartz	Plagioclase group	Chalcopyrite			DL 03	118	Sur Sur
150905	188a	Frikken Peter	2003	Granodiorite	Quartz	Plagioclase group	Chalcopyrite			DL 03	132	Sur Sur
150906	189a	Frikken Peter	2003	Granodiorite	Quartz	Plagioclase group				DL 03	132	Sur Sur
150923	218d	Frikken Peter	2003	Granodiorite	Quartz	Plagioclase group	Chalcopyrite			TSS 22	802	Sur Sur
150931	223a	Frikken Peter	2003	Granodiorite	Quartz	Plagioclase group	Chalcopyrite			TSS 22	305	Sur Sur
150934	224a	Frikken Peter	2003	Granodiorite	Quartz	Plagioclase group	Chalcopyrite			TSS 22	500	Sur Sur

150935	224b	Frikken Peter	2003	Granodiorite	Quartz	Plagioclase group			TSS 22	505	Sur Sur
150939	226a	Frikken Peter	2003	Granodiorite	Quartz	Plagioclase group			TSS 22	730-740	Sur Sur
150950	230b	Frikken Peter	2003	Granodiorite	Quartz	Plagioclase group			DL 64	20-30	Sur Sur
150996	62b	Frikken Peter	2003	Granodiorite	Quartz	Plagioclase group	Chalcopyrite		TSS 22	736	Sur Sur
151004	98b	Frikken Peter	2003	Granodiorite	Quartz	Plagioclase group	Chalcopyrite		DL 139.1	300	Sur Sur
151007	An1c	Frikken Peter	2003	Andesite	Plagioclase group	Biotite			TSS 23		Sur Sur
151012	HGS130a	Frikken Peter	2003	Granodiorite	Quartz	Plagioclase group	Pyrite		DL 139.1	295.1	Sur Sur
151015	O1PF1	Frikken Peter	2003	Monzonite	Quartz	Plagioclase group			DDH 733	343.5	Don Luis Sector
151016	O1PF11	Frikken Peter	2003	Monzonite	Quartz	Plagioclase group			DDH 738	276.5	Don Luis Sector
151019	SS Open pit	Frikken Peter	2003	Granodiorite	Quartz	Plagioclase group			Pit sample		Río Blanco
151021	St1d	Frikken Peter	2003	Monzonite	Quartz	Plagioclase group			DDH 576	109	Río Blanco/ La Union
151029	VHG50a	Frikken Peter	2003	Granodiorite	Quartz	Plagioclase group	Chalcopyrite	chalcocite	DL 03	56	Sur Sur
151030	VHG50c	Frikken Peter	2003	Granodiorite	Quartz	Plagioclase group	Chalcopyrite	chalcocite	DL 03	57.8	Sur Sur
151031	VHG50d	Frikken Peter	2003	Granodiorite	Quartz	Plagioclase group	Chalcopyrite		DL 03	58	Sur Sur

153209	DC-Rhy1-Rhy-1	Davidson, Paul	2003	Rhyolite	Plagioclase group	Quartz	Río Blanco / Los Bronces Cu-Mo deposit

Prospect	sample number	HoleID	Depth From	Rock Type	Ore minerals	Comment
OD Mine	1	RD2495	442.3	RDG		Fresh RDG. Igneous mgt present
fresh granite	2	RD2495	484.6	RDG		Fresh RDG. Igneous mgt present
	3	RD2495	528.3	RDG		mgt-out, incr hem-ser alteration
	4	RD2495	613.3	RDG		Fresh RDG. Igneous mgt present
	5	RD2495	654.1	RDG		less mgt than sample 4.
	6	RD2495	684.5	RDG		ser-hem alteration on edge of fault
	7	RD2495	687.5	RDG		ser-hem alteration within .5m of fault, Kfsp totally replaced
	8	RD2495	701.4	RDG		Fresh RDG. Igneous mgt present
	9	RD2495	793.4	RDG		least altered, salmon-pink Kfsp
	10	RD2495	799.5	RDG		fresh RDG. Igneous mgt present, hem dusting on Kfsp
OD Mine	11	RD2773	2098.1	massive hem	cp-py	top of ore zone, first cut by mine geos.Increasing frequency of hem veinlets and siderite over 20m approaching ore
deeper, early mgt-py	12	RD2773	2181.5	F	cp-py	pervasively silicified Felsic. Early sid-mgt-py overprinted by hem-cp
SE side, edge of deposit	13	RD2773	2182.9	massive hem	cp-py	as above
	14	RD2773	2187.5	massive hem	cp-py	as above
	15	RD2773	2208.2	massive hem	cp-py	as above
	16	RD2773	2224.3	massive hem	cp-py	as above. 1cm cp clots with spec hem halo overprints mgt
	17	RD2773	2234.7	RDG	cp-py	cg cpy overprints siderite-mgt
	18	RD2773	2262.5	RDG	cp-py	bx infill. Sid-py overprint by hem-cp, suls are c.g.
	19	RD2773	2302.5	RDG	cp-py	same as 13-16
	20	RD2773	2326.6	RDG	cp-py	c.g mgt-py, overprinted by hem-cp

Prospect	sample number	HoleID	Depth From	Rock Type	Ore minerals	Comment
	21	RD2773	2093.5	RDG	tr	green/white chlorite altered RDG
Wirrda Well	22	WRD33	404.9	Donnington		massive earthy hem
deeper, early mgt-py	23	WRD33	510.5	Donnington		mixture of earthy and steely hem
	24	WRD33	608.9	Donnington		steely hem, associated with Kfsp alteration
	25	WRD33	714.2	Donnington		steely hem, xcut by spec hem vein
	26	WRD33	843.4	Donnington	tr	mgt altered to spec hem
	27	WRD33	965.5	Donnington	cp-py	mgt vein xcut by spec hem-cpy +cb
	28	WRD33	1087.5	Donnington	cp-py	cg cpy-hem overprints early mgt
	29	WRD33	1276.3	Donnington	cp-py	c.g. cpy-hem, reminiscent of "wispy" chalco at Hillside
	30	WRD33	1404.6	Donnington	cp-py	as above
	31	WRD33	1605	Donnington	cp-py	c.g. cpy-hem overprints py-mgt
	32	WRD33	1819.8	Donnington		siderite-mgt vein
	33	WRD33	1822.7	Donnington	cp-py	cpy-steely hem mineralised clast in bx filled with earthy hem-cp
	34	WRD33	1948.8	Donnington	cp-py	c.g. euhedral py overprinted by cpy
Island Damn!	35	IDD7	493	Wallaroo Gp metaschits		least altered? Massive pink speckled rock, qtz grains in hem matrix
metasediment host	36	IDD7	469.2	Wallaroo Gp metaschits		incr Kfsp and hem alteration
	37	IDD7	465.4	Wallaroo Gp metaschits	py	banded pink/black rock, hematite and c.g. cpy
	38	IDD7	471.2	Wallaroo Gp metaschits		massive hem

Prospect	sample number	HoleID	Depth From	Rock Type	Ore minerals	Comment
	39	IDD7	333.7	Wallaroo Gp metaschits		massive hem xcut by spec hem
	40	IDD7	397.5	Wallaroo Gp metaschits	py	banded hem xcut by cpy clots
	41	IDD7	420.5	Wallaroo Gp metaschits	py	banded hem-py layers
	42	IDD7	424.7	Wallaroo Gp metaschits	py	almost massive py
	43	IDD7	395.8	Wallaroo Gp metaschits	py	py clots, vuggy, vugs filled with spec hem-barite(?)
OD Mine	44	RD2678	427.2	RDG		altered RDG, hem <20%
inside "bt-out" zone	45	RD2678	433.3	RDG	cp-bn(?)	pervasive ser, fg. dissem suls
marginal RDG	46	RD2678	562.5	RDG		more altered than 44, adjacent to mafic dyke
	47	RD2678	632.2	RDG		altered RDG, hem <20%
	48a	RD2678	765.4	RDG		earthy hem altered RDG
	48b	RD2678	765.4	RDG	cp-py	steely hem+sulfides overprints RDG
Oak Dam	49	AD6	699	Donnington		mixture of specular and steely hem
top part of system?	50	AD6	650	Donnington	py	massive hem+cpy stringers
	51	AD6	601	Donnington		massive hem
	52	AD6	694.9	Donnington	py	sulfide blebs in hem
OD Mine	53	RD1988	1678.1	RDG	cp-py	fg dissem suls in hem
anomalous granitophiles	54	RD1988	1728.3	RDG	cp-py	fg dissem suls in hem

Prospect	sample number	HoleID	Depth From	Rock Type	Ore minerals	Comment
	55	RD1988	1773.3	RDG	cp-py	fg dissem suls in hem >1%
	56	RD1988	1815.3	RDG	cp-py	fg dissem suls in hem >1%
	57	RD1988	1891.4	RDG	cp-py	fg dissem suls in hem as matrix around earthy hem clasts
Acropolis	58	ACD1	1095.5	GRV		early mgt veins
GRV hosted	59	ACD1	1039	GRV		early mgt veins
	60	ACD1	968.4	GRV	po(?)	mgt+sulfides
	61	ACD1	928	GRV		massive hematite
	62	ACD1	885	GRV		massive hem
OD Mine	63	RB224	403.5	HEMQ		red earthy
barren core	64	RB224	409	HEMQ		black
	65	RB224	502	HEMQ		massive hem
	66	RB224	820.6	HEMQ		earthy hem
	67	RB224	808	HEMQ		massive hem
OD Mine	68	RU65-8230	6	RDG	cp-py	fg mgt-hem, fg dissem suls
northwest arm at edge of deposit	69	RU65-8230	29.3	RDG		bx RDG, matrix of mgt
sits over A-block	70	RU65-8230	63.2	RDG	cp-py	as above, for 68
	71	RU65-8230	104.2	RDG	cp-py	as above
	72	RU65-8230	161.2	RDG	cp-py	as above
	73	RU65-8230	196.3	RDG	cp	bx RDG, matrix filled with hem-cg cpy
	74	RU65-8230	213	RDG	tr	siderite in hem bx
	75	RU65-8230	237.5	Mafic Dyke?	cp	hem-cpy, fg ore, very confined, sharp contacts with RDG

Prospect	sample number	HoleID	Depth From	Rock Type	Ore minerals	Comment
	76	RU65-8230	257.6	Mafic Dyke?	cp	as above
	77	RU65-8230	363.2	Mafic Dyke?	cp	as above but mgt bearing
	78	RU65-8230	597.1	Gairdner dyke		fresh, cg, magmatic magnetite
	79	RU65-8230	646.1	RDG		mgt-chl altered RDG bx
	80	RU65-8230	667.2	RDG		thin ~2-3mm siderite veins in chl altered RDG
	81	RU65-8230	263.3	RDG		red-pink hem-ser altered "bt-out" granite
	82	RU65-8230	398.3	RDG		red-pink hem-ser altered "bt-out" granite
	83	RU65-8230	698.6	RDG		red-pink hem-ser altered "bt-out" granite
OD Mine	84	RD2749	899.3	RDG		massive hem, few relict granite fragments (qtz)
from barren core to granite	85	RD2749	953.7	RDG		cp-hem ore
varying amounts of hematite altn	86	RD2749	915.2	RDG		granite bx, 30-50% hem clasts. Midway between 84 and 87
close to RD19988	87	RD2749	960.2	RDG		granite bx, 10-20% hem clasts. Midway between 86 and 88
	88	RD2749	1067.4	RDG		pink red altered "bt-out" granite

Table A2 5 List of samples collected from the Olympic Dam mine site. All core samples, milled powders, thin section offcuts and mineral separates have been returned to the mine.

Sample Number	Location	HoleID	Depth From	Host Rock	Description	paragenesis		
14	Le Prena	HDD280	195.04	magnetite skarn	early mt-cpy in magnetite skarn	mgt1	cp1	
12		HDD280	198.21	epidote skarn	hornblende-cpy vein cross cutting epidote skarn	cpy?		
13		HDD280	209.57	magnetite skarn	cpx fragment in magnetite skarn			
1	Zanoni	HDD277	100	magnetite skarn	massive remobilised cpy	cp2		
2		HDD277	178.72	magnetite skarn	massive remobilised cpy	cp2		
3		HDD018W1	263.14	magnetite skarn	massive remobilised cpy, with early(?) py	cp2	py1?	
4		HDD018W1	265.66	magnetite skarn	cpy-hematite replacing early mgt	cpy2	mgt1	hem1
5		HDD018W1	416.4	garnet skarn	garnet clasts in cpy-(py)?	cpy2	py1?	
6		HDD018W1	423.6	garnet skarn	garnet clasts in cpy	cpy2		
7		HDD018W1	431.26	garnet skarn	garnet clasts in cpy	cpy2		
8		HDD018W1	440.7	magnetite skarn	wispy cpy-hem-mag	cp1	mgt1	hem1
9	La Prena?	HDD346	381.45	magnetite skarn	coarse grained allanite cross cuts hematite-magnetite		mgt1	hem1
10		HDD346	383.82	garnet skarn	py-cpy-hem vein x-cuts garnet skarn	cp2	py2?	hem1
11		HDD346	408.08	garnet skarn	cpy-py-hem-mgt	cp2	py1?	hem1
HS391	?	HDD406	391.5	Hillside Syenite	bornite	bn1		
		HDD406	420	magnetite skarn	cpy-hem-mgt early skarn	cp1	mgt1	hem1
15	Dart	HDD381	292.63	magnetite skarn	cpy	cp2		
16		HDD381	300.7	magnetite skarn	wispy cpy-(hem-mag?)	cp1		
17		HDD381	312.71	magnetite skarn	mgt-cpx-amph skarn			

22	?	HDD023		Gabbro	relatively unaltered fine grained gabbro		
23		HDD023		Gabbro	red-rock altered gabbro		
24		HDD023	336.4		banded red-rock altered metasediment	mgt1	hem1
21		HDD023		Gabbro	relatively unaltered fine grained gabbro		
18	?	HDD016	502.5	Hillside Syenite	red-rock altered granite		
20		HDD016	570.09	Hillside Syenite	red-rock altered granite		
19		HDD016	503.5	Hillside Syenite	red-rock altered granite		
HS629				Hillside Syenite	bornite mineralisation		

Table A2 6 Samples collected from the Hillside deposit

Table A2 7 List of thin sections

Deposit	**Sample ID**
Batu Hijau	SBD86E-714.9
	SBD86E-636.2
	SBD86E-293
	SBD59E-652.1
	SBD531-441.2
	SBD103-485
	SBD103-379

Deposit	Sample ID
	SBD103-184.2
	SBD060-266
	SBD031-465.5
Hillside	HS003
	HS005
	HS007
	HS008
	HS014
	HS016
	HS017
Olympic Dam and surrounds	1405_01
	1405_03
	1405_10
	1405_12
	1405_15
	1405_20
	1405_22
	1405_25
	1405_28
	1405_30
	1405_33
	1405_36
	1405_39
	1405_41
	1405_44
	1405_45
	1405_46

Deposit	Sample ID
	1405_50
	1405_51
	1405_55
	1405_57
	1405_58
	1405_61
	1405_64
	1405_67
	1405_70
	1405_72
	1405_74
	1405_77
	1405_85
	1405_87
Renison	40612_06
	40612_23
	40612_25
	40612_29
	40612_30
	40612_31
	40612_32
	40612_33
	40612_34
	40612-12
	RB001
	RB004
	RB011

Deposit	Sample ID
	RB012
	RB013
	RB015
	RB016
	RB017
	RB024
	RB025

APPENDIX 3. Whole rock and assay data for granites and breccias sampled at Olympic Dam

SAMPLE NUMBER	1405_1	1405_3	1405_4	1405_81	1405_5	1405_10	1405_8	1405_9	1405_2	1405_6	1405_80	1405_83	1405_82
Al_pct	6.89	7.27	7.23	6.42	7.03	6.37	7.11	7.79	7.14	7.13	6.62	7.13	7.32
Ba_ppm	745	815	903	1413	821	1062	776	921	836	983	563	706	851
Be_ppm	3.4	3.6	3.9	1.6	3.8	2.5	3.7	4.6	4	2.4	2.8	2.5	2.4
Bi_ppm	0.5	0.5	0.5	0.5	0.5	0.5	0.5	0.5	0.5	0.5	0.5	0.5	0.5
Ca_pct	0.64	0.27	0.63	0.62	0.53	0.79	0.61	0.9	0.67	0.15	1.45	0.14	0.07
Ce_ppm	162	186	146	0.5	179	120	125	164	176	110	169	195	327
Co_ppm	4	9	5	9	3	3	3	4	7	4	6	14	9
Cr_ppm	0.5	0.5	0.5	0.5	0.5	0.5	0.5	0.5	0.5	0.5	0.5	0.5	0.5
Cs_ppm	1.67	1.81	1.38	0.65	1.64	0.93	1.82	1.53	1.65	3.6	3.31	2.99	2.1
Cu_ppm	0.5	102	0.5	133	3	0.5	0.5	0.5	99	10	319	84	88
Dy_ppm	8.48	17.22	9.26	2.9	10.51	35.12	10.09	13.78	11.35	42.65	6.98	8.28	10.89
Er_ppm	5.03	10.6	5.52	2.27	6.27	20.79	6.05	8.4	6.61	26.92	4.21	4.93	7.46
Eu_ppm	1.43	1.97	1.53	0.79	1.56	2.67	1.52	1.93	1.6	2.43	1.32	1.68	1.27
Fe_pct	2.11	1.66	2.04	2.1	2.2	2.27	2.29	2.47	2.6	3.12	3.18	3.23	3.34
Ga_ppm	18.1	18.8	18.7	16.3	19	16.1	19.4	21.3	19.3	16.5	17.6	19.4	19.4
Gd_ppm	8.95	15.35	10.05	1.59	11.16	25.96	10.51	14.07	11.53	27.89	7.29	8.61	7.53
Hf_ppm	7.6	10.2	9.1	7.3	10.1	9.6	11.6	11.1	8.7	11.3	7.8	9	11.3
Ho_ppm	1.79	3.68	1.94	0.69	2.19	7.5	2.11	2.93	2.35	9.49	1.46	1.76	2.49
K_pct	4.51	4.75	4.93	7.06	4.76	3.94	4.65	4.49	4.74	5.81	5.89	6.44	7.24
La_ppm	93	104	83	0.5	109	61	64	71	76	53	103	135	202
Lu_ppm	1.12	1.58	0.92	0.47	1.01	2.66	1.05	1.24	1.17	3.86	0.66	0.8	1.22

SAMPLE NUMBER	1405_1	1405_3	1405_4	1405_81	1405_5	1405_10	1405_8	1405_9	1405_2	1405_6	1405_80	1405_83	1405_82
Mg_pct	0.36	0.5	0.42	0.11	0.43	0.37	0.39	0.5	0.42	0.33	0.8	0.24	0.22
Mn_pct	0.04	0.04	0.04	0.02	0.05	0.08	0.04	0.05	0.06	0.06	0.26	0.02	0.03
Mo_ppm	0.5	0.5	0.5	15	0.5	0.5	0.5	0.5	0.5	0.5	0.5	0.5	0.5
Na_pct	2.52	2.58	2.6	0.16	2.46	2.53	2.61	3.33	2.57	1.59	0.12	0.13	0.11
Nb_ppm	23.1	31.7	24.2	12.5	31	24	32.2	35.6	31.2	29.5	26.6	25.8	34.3
Nd_ppm	62.6	71.8	62.2	8.4	73.4	64.4	63.4	82.4	66.5	46.9	52	65.8	69.7
Ni_ppm	0.5	1	0.5	0.5	0.5	0.5	2	1	2	0.5	0.5	2	0.5
P_pct	0.03	0.05	0.03	0.5	0.04	0.04	0.03	0.04	0.04	0.06	0.05	0.04	0.05
Pb_ppm	17	66	19	13	14	65	25	28	15	9	11	9	9
Pr_ppm	18.72	21.54	18.42	2.96	22.28	17.57	17.41	23.4	19.41	12.83	16.93	22.23	28.21
Rb_ppm	241.7	221.8	252.8	228.5	259.6	204.5	249.4	236.9	223.5	312.2	287	313	284.9
Sb_ppm		1	0.8	1.3	0.9	1	0.8	0.8	0.9	1.4	1.3	1.1	1
Sc_ppm	5	6	5	0.5	6	3	5	6	6	5	5	4	5
Si_pct	33.09	33.35	32.75	34.55	32.92	29.12	32.92	33.25	32.79	32.89	31.2	33.28	32.85
Sm_ppm	10.21	13.64	10.9	1.5	12.49	17.07	11.83	14.96	12.28	14.59	8.32	9.5	6.26
Sn_ppm	3	3	3	3	3	3	3	4	3	3	3	4	5
Sr_ppm	99	90	114	166	96	60	85	129	109	23	46	60	84
Ta_ppm	2.3	3.3	2.6	2	3	2.5	3.3	3.7	2.9	3.2	2.9	3.3	3.2
Tb_ppm	1.43	2.72	1.58	0.38	1.77	5.28	1.7	2.29	1.89	5.99	1.19	1.39	1.64
Th_ppm	51.68	72.03	59.33	44.76	52.36	45.09	50.86	63.13	57.99	67.86	60.28	65.39	52.01
Ti_pct	0.202	0.28	0.223	0.109	0.246	0.208	0.254	0.289	0.262	0.256	0.206	0.218	0.274
Tm_ppm	0.77	1.57	0.85	0.38	0.95	2.98	0.95	1.24	0.99	4.05	0.65	0.78	1.17
U_ppm	9.16	16.47	14.05	45.91	13.67	10.04	12.12	13.05	18.92	10.78	20.09	36.2	19.13
V_ppm	17	34	16	0.5	19	16	24	33	27	20	26	24	23

SAMPLE NUMBER	1405_1	1405_3	1405_4	1405_81	1405_5	1405_10	1405_8	1405_9	1405_2	1405_6	1405_80	1405_83	1405_82
W_ppm	0.5	0.5	0.5	5	0.5	0.5	0.5	0.5	0.5	1	2	2	1
Y_ppm	50.6	106.1	56.9	21.7	62.3	228.5	62.3	87	65.5	268.9	43.2	52.3	75.7
Yb_ppm	5.18	10.25	5.71	2.69	6.48	18.59	6.33	8.23	6.47	24.95	4.28	5.07	7.75
Zn_ppm	45	269	29	39	42	62	34	25	43	55	19	28	44
Zr_ppm	267	379	307	210	363	330	403	381	326	401	276	305	398
Al2O3_pct	13.02	13.74	13.66	12.13	13.28	12.04	13.43	14.72	13.49	13.47	12.51	13.47	13.83
CaO_pct	0.90	0.38	0.88	0.87	0.74	1.11	0.85	1.26	0.94	0.21	2.03	0.20	0.10
Fe2O3_pct	3.02	2.37	2.92	3.00	3.15	3.25	3.27	3.53	3.72	4.46	4.55	4.62	4.78
K2O_pct	5.43	5.72	5.94	8.50	5.73	4.75	5.60	5.41	5.71	7.00	7.10	7.76	8.72
MgO_pct	0.60	0.83	0.70	0.18	0.71	0.61	0.65	0.83	0.70	0.55	1.33	0.40	0.36
Na2O_pct	3.40	3.48	3.50	0.22	3.32	3.41	3.52	4.49	3.46	2.14	0.16	0.18	0.15
P2O5_pct	0.07	0.11	0.07	1.15	0.09	0.09	0.07	0.09	0.09	0.14	0.11	0.09	0.11
TiO2_pct	0.34	0.47	0.37	0.18	0.41	0.35	0.42	0.48	0.44	0.43	0.34	0.36	0.46
SiO2_pct	70.79	71.35	70.06	73.91	70.43	62.30	70.43	71.13	70.15	70.36	66.75	71.20	70.28

SAMPLE NUMBER	1405_44	1405_88	1405_79	1405_47	1405_7	1405_21	1405_46	1405.48a	1405_59	1405_78	1405_87	1405_86	1405_84	1405_45
Al_pct	7.48	6.46	7.37	6.56	6.71	9.26	7.1	6.74	6.41	6.77	2.4	1.26	0.77	0.08
Ba_ppm	507	15317	624	958	351	320	427	185	1937	115	27069	67578	22334	1767
Be_ppm	1.9	1.3	3.1	2.2	3.4	5.7	2.7	3.8	1	1.2	0.6	0.6	0.6	0.7
Bi_ppm	0.5	0.5	0.5	0.5	0.5	0.5	0.5	0.5	10	0.5	5	24	5	40
Ca_pct	0.06	0.09	0.81	0.08	0.12	0.3	0.07	0.17	0.04	6.35	0.79	1.4	5.29	0.08
Ce_ppm	361	545	0.5	152	131	320	156	606	0.5	0.5	604	746	2877	386

SAMPLE NUMBER	1405 _44	1405_ 88	1405_79	1405_47	1405_7	1405_21	1405_46	1405.48a	1405_59	1405_78	1405_87	1405_86	1405_84	1405_45
Co_ppm	19	16	17	32	12	28	23	34	16	43	0.5	0.5	4	156
Cr_ppm	0.5	0.5	0.5	0.5	0.5	0.5	0.5	0.5	0.5	24	0.5	0.5	0.5	0.5
Cs_ppm	4.24	1.13	2.7	2.23	3.49	7.12	3.55	2.9	2.29	0.8	0.96	1.08	0.49	0.09
Cu_ppm	1539	1653	223	369	0.5	886	446	2999	28	458	822	2271	4944	3096
Dy_ppm	44.69	7.58	10.33	8.71	10.44	25.17	7.82	16.73	11.95	12.16	6.11	7.05	14.84	21.51
Er_ppm	28.75	4.65	7.01	5.39	7.58	14.5	4.52	9.91	7.95	6.8	3.97	3.61	7.51	13.2
Eu_ppm	3.15	4.7	1.11	1.32	0.86	4.06	1.42	4.27	1.68	2.19	4.49	6.7	20.77	4.6
Fe_pct	5.1	5.1	5.62	6.27	6.95	7.72	7.74	9.55	11.9	12.28	16.58	24.99	42.48	44.94
Ga_ppm	19.5	14.4	21.2	17.8	22.1	19	17.6	16.6	18.8	25.4	8.8	7	0.5	0.8
Gd_ppm	31.24	9.4	7.41	8.36	6.98	27.78	8.8	18.96	8.81	10.79	7.48	8.08	28.58	27.83
Hf_ppm	10.8	9.4	9	9.4	11.6	15.4	10.1	10.7	10.8	5.6	4.6	6.5	3.1	0.3
Ho_ppm	9.94	1.56	2.35	1.85	2.44	5.21	1.61	3.44	2.65	2.52	1.31	1.62	2.76	4.55
K_pct	5.64	8.05	6.56	5.61	3.97	3.69	4.72	3.57	5.27	0.42	2.25	0.65	0.35	0.05
La_ppm	202	315	68	99	73	148	110	366	82	0.5	367	560	1999	197
Lu_ppm	3.9	0.69	1.05	0.89	1.45	1.96	0.76	1.46	1.21	1.01	0.63	0.62	0.92	2.14
Mg_pct	0.32	0.04	0.86	0.15	0.81	0.14	0.37	0.24	0.2	2.36	0.03	0.03	0.03	0.93
Mn_pct	0.1	0.03	0.16	0.16	0.19	0.04	0.09	0.17	0.04	0.16	0.5	0.5	0.5	1.62
Mo_ppm	0.5	26	0.5	0.5	0.5	26	0.5	7	6	0.5	139	220	457	3
Na_pct	0.14	0.13	0.12	0.12	0.15	0.31	0.16	0.06	0.08	1.44	0.06	0.04	0.03	0.01
Nb_ppm	31.5	22.1	27.4	25.5	34.5	68.4	25.2	92.8	7.1	11	16	25.5	9.7	0.5
Nd_ppm	120.7	125.1	38.7	52	41.3	171.9	68.8	185.8	33.8	26.2	122.7	133.6	572	145.9
Ni_ppm	0.5	3	3	0.5	0.5	0.5	1	4	6	38	5	3	1	7
P_pct	0.06	0.04	0.05	0.03	0.04	0.08	0.04	0.11	0.03	0.14	0.04	0.05	0.1	0.05
Pb_ppm	13	12	9	10	15	37	9	28	18	12	21	42	31	0.5
Pr_ppm	39.19	48.85	12.27	17.25	13.01	47.1	21.16	62.62	11.72	5.78	48.53	55.94	217.31	42.98

SAMPLE NUMBER	1405 _44	1405_ 88	1405_79	1405_47	1405_7	1405_21	1405_46	1405.48a	1405_59	1405_78	1405_87	1405_86	1405_84	1405_45
Rb_ppm	281.7	269.7	316.6	247.6	268.4	227	226.3	179.9	178.7	16.4	83.7	33.3	18.9	2.2
Sb_ppm	0.9	7.3	0.7	1	1.5	1.9	1.3	2.5	1	0.5	64.7	192	125.2	0.7
Sc_ppm	4	3	5	4	6	6	6	0.5	10	35	0.5	0.5	0.5	0.5
Si_pct	30.35	30.94	29.64	30.85	31.77	28.42	30.07	28.93	28.46	22.21	24.84	20.58	9.7	0.92
Sm_ppm	19.77	16.44	6.65	7.77	6.62	30.01	10.21	23.15	6.11	7.95	11	11.21	46.41	30.07
Sn_ppm	4	6	4	4	4	6	3	6	5	2	22	38	78	0.5
Sr_ppm	84	174	50	95	0.5	26	46	156	37	169	335	717	294	22
Ta_ppm	3.2	2.5	3.4	2.7	3.5	4.4	2.7	3	1	1.1	1.7	2.2	0.5	0.5
Tb_ppm	6.56	1.33	1.47	1.43	1.47	4.43	1.36	3.04	1.8	1.96	1.05	1.15	3.43	3.76
Th_ppm	60.96	70.11	70.8	60.02	74.77	67.01	42.38	36.77	45.72	3.67	21.64	20.39	15.53	5.83
Ti_pct	0.261	0.215	0.243	0.22	0.264	0.363	0.218	0.246	0.278	2.002	0.086	0.137	0.047	0.5
Tm_ppm	4.27	0.73	1.06	0.84	1.21	2.1	0.7	1.44	1.19	0.95	0.63	0.83	0.96	2.02
U_ppm	30.54	31.02	18.67	11.08	4.9	33.33	15.42	104.39	15.07	0.85	42.33	54.13	59.69	112.89
V_ppm	25	18	32	23	27	26	26	33	68	444	29	17	13	19
W_ppm	3	19	1	2	3	6	1	40	3	0.5	152	271	637	4
Y_ppm	281.8	40.6	71.6	54.2	75.2	154.1	47.5	100.8	80	73.4	31.8	40.3	91.6	150.7
Yb_ppm	26.71	4.66	7.09	5.62	8.62	13.46	4.73	9.6	7.71	6.04	4.17	4.17	6.17	13.83
Zn_ppm	76	16	40	67	158	131	52	118	138	175	26	83	15	344
Zr_ppm	347	322	314	345	401	555	348	349	393	192	127	187	61	0.5
Al_2O_3_pct	14.13	12.21	13.93	12.39	12.68	17.50	13.42	12.73	12.11	12.79	4.53	2.38	1.45	0.15
CaO_pct	0.08	0.13	1.13	0.11	0.17	0.42	0.10	0.24	0.06	8.88	1.11	1.96	7.40	0.11
Fe_2O_3 pct	7.29	7.29	8.04	8.96	9.94	11.04	11.07	13.65	17.01	17.56	23.70	35.73	60.73	64.25
K_2O_pct	6.79	9.70	7.90	6.76	4.78	4.44	5.69	4.30	6.35	0.51	2.71	0.78	0.42	0.06
MgO_pct	0.53	0.07	1.43	0.25	1.34	0.23	0.61	0.40	0.33	3.91	0.05	0.05	0.05	1.54
Na_2O_pct	0.19	0.18	0.16	0.16	0.20	0.42	0.22	0.08	0.11	1.94	0.08	0.05	0.04	0.01

SAMPLE NUMBER	1405 _44	1405_ 88	1405_79	1405_47	1405_7	1405_21	1405_46	1405.48a	1405_59	1405_78	1405_87	1405_86	1405_84	1405_45
P_2O_5_pct	0.14	0.09	0.11	0.07	0.09	0.18	0.09	0.25	0.07	0.32	0.09	0.11	0.23	0.11
TiO_2_pct	0.44	0.36	0.41	0.37	0.44	0.61	0.36	0.41	0.46	3.34	0.14	0.23	0.08	0.83
SiO_2_pct	64.93	66.19	63.41	66.00	67.97	60.80	64.33	61.89	60.88	47.51	53.14	44.03	20.75	1.97

APPENDIX 4. Polynomial functions for calculating beta factors of minerals.

Theoretical fractionation factors can be derived by spectroscopic and parametric measurements and calculations. These measurements are called 'beta factors' and can be calculated for different temperatures by expanding polynomial functions given in the literature. The polynomial expansions used for calculating beta factors, presented in figures 2.9 and 5.20 in the thesis are summarised below:

mineral	Equation	Reference
pyrite	$T \times 1.2922+(-4.6376\times10^{-3} \times T^2)+(1.6509 \times 10^{-5} \times T^3)$	Blanchard 2009
magnetite	$T \times 0.95706+(-4.7296\times10^{-3} \times T^2)+(4.0703 \times10^{-6} \times T^3)$	Polyakov et al. 2007
pyrrhotite	$T \times 0.4382+(-0.98632 \times 10^{-3} \times T^2)+(0.44611 \times 10^{-5} \times T^3)$	Polyakov and Soultanov (2011)
chalcopyrite	$T \times 0.7463+(-2.6918 \times 10^{-3} \times T^2)+(1.4549 \times 10^{-5} \times T^3)$	Polyakov and Soultanov (2011)
siderite	$T \times 0.555099-(9.29295 \times 10-^{4} \times T^2)+(2.4204 \times 10^{-6} \times T^3)$	Polyakov and Mineev (2000)
hematite	$T \times 1.0542+(-3.1652 \times 10^{-3} \times T^2)+(1.326 \times 10^{-5} \times T^3)$	Polyakov et al. (2007)

$T = 10^6/T^2$ where T is in degrees Kelvin.

REFERENCES

Blanchard, M., Poitrasson, F., Meheut, M., Lazzeri, M., Mauri, F., Balan, E. (2009). Iron isotope fractionation between pyrite (FeS2), hematite (Fe2O3) and siderite (FeCO3): A first-principles density functional theory study. Geochim. Cosmochim. Acta 73, 6565-6578.

Polyakov, V. B., Mineev, S. D., 2000. The use of Mössbauer spectroscopy in stable isotope geochemistry. Geochim. Cosmochim. Acta 64, 849-865.

Polyakov, V. B., Clayton, R. N., Horita, J., Mineev, S. D., 2007. Equilibrium iron isotope fractionation factors of minerals: reevaluation from the data of nuclear inelastic resonant X-ray scattering and Mössbauer spectroscopy. Geochim. Cosmochim Acta 71, 3833-3846.

Polyakov, V. B., Soultanov, D. M., 2011. New data on equilibrium iron isotope fractionation among sulfides: constraints on mechanisms of sulfide formation in hydrothermal and igneous systems. Geochim. Cosmochim. Acta 75, 1957-1974.